

A Thesis Submitted for the Degree of PhD at the University of Warwick

Permanent WRAP URL:

<http://wrap.warwick.ac.uk/93940>

Copyright and reuse:

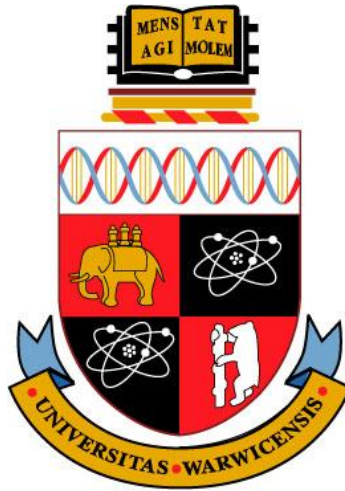
This thesis is made available online and is protected by original copyright.

Please scroll down to view the document itself.

Please refer to the repository record for this item for information to help you to cite it.

Our policy information is available from the repository home page.

For more information, please contact the WRAP Team at: wrap@warwick.ac.uk



EFFECT OF TiB_2 ADDITION ON THE MICROSTRUCTURE AND MECHANICAL PROPERTIES OF Al-Cu-Mg-Ag ALLOY

by

Martha Indriyati

A thesis submitted to The University of Warwick in fulfilment of the requirement for the
degree of Doctor of Philosophy in Engineering

Warwick Manufacturing Group

The University of Warwick

Coventry, United Kingdom

October 2016

CONTENTS

CONTENTS	i
LIST OF TABLES	vi
LIST OF FIGURES	vii
ACKNOWLEDGEMENTS	xv
DECLARATION	xvii
ABSTRACT	xviii
LIST OF SYMBOLS	xix
ABBREVIATIONS	xxi
CHAPTER 1. INTRODUCTION	1
1.1 Research Background	1
1.2 Design Philosophy and Research Scope	4
1.3 Research Aims and Objectives	5
1.4 Hypothesis	6
1.5 Novelty of the Research	6
1.6 Thesis Structure	7
CHAPTER 2. LITERATURE REVIEW	9
2.1 Introduction	9
2.2 The Al-Cu-Mg-Ag Alloy System	9
2.2.1 Precipitate Phases and Age Hardening Behaviour	10
2.2.2 Role of Alloying Elements	14
2.3 TiB ₂ in Aluminium Alloys	15
2.3.1 TiB ₂ as Grain Refiner in Al Alloy	16
2.3.2 TiB ₂ as Reinforcement in Al Alloy	19
2.3.2.1 Material A20X	21
2.4 Hot Deformation	22
2.4.1 Flow Stress Behaviour	23

2.4.2 General Characterisation of Flow Stress Behaviour	24
2.4.3 Processing Map	29
2.5 Recovery and Recrystallisation After Deformation	32
2.5.1 General Theory of Recovery and Recrystallisation	33
2.5.2 Nucleation of Recrystallisation	35
2.5.3 Zener Pinning	41
2.6 Superplasticity	42
2.6.1 Fundamentals of Superplasticity	43
2.6.2 Superplasticity in Metal Matrix Composites	47
CHAPTER 3. EXPERIMENTAL METHODS	51
3.1 Introduction	51
3.2 Materials	52
3.3 Materials Processing	52
3.3.1 Casting	52
3.3.1.1 Casting of 0.2Ti-4.5TiB ₂ Alloy (A20X)	54
3.3.1.2 Casting of 0.2Ti Alloy and Matrix Alloy	55
3.3.1.3 Sampling procedure for Spectroscopy Analysis	56
3.3.1.4 Thermal Analysis (Cooling Curve Determination)	56
3.3.2 Homogenisation	57
3.3.3 Hot Rolling	58
3.3.4 Hot Extrusion	59
3.3.5 Annealing	59
3.3.6 Artificial Ageing	60
3.4. Mechanical Testing	60
3.4.1 Compression Testing	60
3.4.2 Tensile Testing	62
3.4.3 Tensile Testing at Elevated Temperature (Superplastic Forming)	65

3.4.4 Vickers Hardness Testing	66
3.5 Material Characterisation	67
3.5.1 Phases and Chemical Analysis	67
3.5.1.1 Arc Spark Optical Emission Spectroscopy	67
3.5.1.2 Differential Scanning Calorimetry	67
3.5.2 Microstructure Examination	68
3.5.2.1 Metallography Sample Preparation	68
3.5.2.2 Light Optical Microscopy	69
3.5.2.3 Scanning Electron Microscopy	70
3.5.2.4 Energy Dispersive X-Ray Spectroscopy	71
3.5.2.5 Electron Backscattered Diffraction	71
3.5.2.6 Transmission Electron Microscopy	72
CHAPTER 4. STRAIN RATE AND TEMPERATURE DEPENDENCE.....	73
4.1 Introduction	73
4.2 Stress Strain Relationship	74
4.3 Constitutive Analysis	78
4.3.1 Effect of TiB ₂ on the Material Constants	82
4.3.2 Effect of TiB ₂ on the Hot Working Activation Energy	83
4.3.4 Verification of Activation Energy	86
4.4 Processing Map	88
4.4.1 Strain Rate Sensitivity Parameter	88
4.4.2 Development of Processing Maps	89
4.5 Effect of Strain Rate and Temperature on the Microstructure	91
4.6 Summary of the Stress Strain Relationship	100
CHAPTER 5. INFLUENCE OF TiB₂ REINFORCEMENT ON THE AS-CAST AND AS DEFORMED MATERIALS	102
5.1 Introduction	102
5.2 Characterisation of As-Cast Materials	103

5.2.1 Grain Structure of As-Cast Materials	103
5.2.2 Cooling Curves Analysis	104
5.2.3 Secondary Phase Analysis in As-Cast Materials	106
5.3 Characterisation of As-Homogenised Materials	110
5.3.1 Phase Distribution in As-Homogenised Materials	110
5.4 Characterisation of Sheet Materials	111
5.4.1 Load Profiles during Rolling	111
5.4.2 Phase Distribution in Sheet Materials	112
5.4.3 Microstructure Examination of Sheet Materials	114
5.4.4 Deformation Behaviour in 0.2Ti-4.5TiB ₂ Composites	118
5.5 Influence of TiB ₂ on the Extruded Materials	120
5.5.1 Effect of TiB ₂ on the Extruded Materials	120
5.5.2 Grain Structure in the Extruded Materials	120
5.6 Summary of the Effect of TiB ₂ in the As-Cast and As-Deformed Materials ..	124
CHAPTER 6. INFLUENCE OF TiB₂ REINFORCEMENT ON THE STATIC RECRYSTALLISATION	125
6.1 Introduction	125
6.2 Recrystallisation in Compressed Materials	125
6.2.1 Effect of Temperature and Strain Rate on the Recrystallisation	125
6.2.2 Nucleation of Recrystallisation	129
6.3 Recrystallisation in Sheet Materials	132
6.3.1 Effect of TiB ₂ on the Recrystallisation Temperature	132
6.3.2 Effect of TiB ₂ on the Recrystallisation Behaviour	133
6.3.3 Effect of Particle Distribution on the Grain Size	136
6.3.4 Recrystallisation Mechanism in 0.2Ti-4.5TiB ₂ Composite	138
6.4 Recrystallisation in Extruded Materials	142
6.5 Summary of the Effect of TiB ₂ on the Recrystallisation	144

CHAPTER 7. EFFECT OF TiB₂ ON THE MECHANICAL PROPERTIES AND SUPERPLASTIC FORMING ABILITY	146
7.1 Introduction	146
7.2 Tensile Strength	146
7.2.1 Investigation on Ageing Behaviour	146
7.2.2 Measurement of Tensile Strength in Sheet Materials	148
7.2.3 Measurement of Tensile Strength in Extruded Materials	153
7.2.4 Effect of TiB ₂ on the Fracture Surface	154
7.3 Superplastic Forming Ability	155
7.3.1 Superplastic Behaviour Dependence on the Strain Rate and Temperature	156
7.3.2 Strain Rate Sensitivity Parameter	159
7.3.3 Deformation Microstructure of 0.2Ti-4.5TiB ₂ Composite	159
7.3.4 Cavitation Formation	161
7.4 Summary of the Effect of TiB ₂ on the Superplasticity and Mechanical Properties	164
CONCLUSION	169
FUTURE WORKS	171
REFERENCES	172
APPENDIX A	186
APPENDIX B	190
APPENDIX C	192
APPENDIX D	194

LIST OF TABLES

Table 2.1. Proposed crystal structures for the phases in Al-Cu-Mg-Ag system	11
Table 2.2. Chemical composition of A20X alloy based on the AMS standard	22
Table 3.1. Alloy designations and chemical composition of material used in this study; measured in wt.%	52
Table 3.2. Hot rolling schedule	58
Table 3.3. Extrusion process parameter	59
Table 4.1. Material constants in constitutive equation for each material.....	83
Table 4.2. Coefficient of polynomial fit corresponding to the Eq. (4-17) for 0.2Ti-4.5TiB ₂ composites.....	87
Table 4.4. Flow stress (MPa) data of 0.2Ti-4.5TiB ₂ composites at different temperature, strain rate and strain	89
Table 5.1. Comparison of secondary phases' length presented in as-homogenised (HO) condition and sheet materials in solution treated (ST) condition of all studied materials .	114
Table 7.1. Comparison of tensile test data in the studied materials and commercial aircraft alloys	150
Table 7.2. Comparison of tensile test data in the studied materials	153

LIST OF FIGURES

Fig. 1.1. Schematic diagram of research scope	5
Fig. 2.1. Common ageing precipitates existing in the Al-Cu-Mg-Ag alloy recorded with the electron beam parallel to $\langle 110 \rangle$ showing changes in microstructure with ageing at 250°C (a) 5 hrs ageing, Ω plates and occasionally θ and θ' phase, (b) 30 hrs ageing, coarser Ω , θ' and θ phase and S phase and (c) 600 hrs ageing, very coarse Ω phase, large θ' and θ particle and S phase [11]	13
Fig. 2.2. Equilibrium of interfacial energies during heterogeneous nucleation	16
Fig. 2.3. Schematic diagram of the atomic arrangement of Al (lime) and Ti (blue) atoms in the (112) plane of the bulk Al_3Ti intermetallic compound [90].....	19
Fig. 2.4. Stress-strain curves for (a) Al-1% Mg at 400°C which undergo dynamic recovery and (b) 0.68% C steel deformed at $\dot{\epsilon} = 1.3 \times 10^{-3} \text{ s}^{-1}$ which undergo dynamic recrystallisation [30].....	24
Fig. 2.5. Summary of microstructure evolution during dynamic recovery	25
Fig. 2.6. High angle boundaries in compressed specimens of aluminium alloy deformed at 400°C (a) showing serration of high angle grain boundaries in Al-5 wt.% Mg and (b) planar grain boundaries due to the existence of second phase particles which hinder serration formation in Al-2 wt.% Cu [30]	26
Fig. 2.7. Schematic illustration of geometric dynamic recrystallisation (GDRX). Serrated high angle grain boundaries (HAGBs) become closer as deformation progresses while subgrain size remains constant. At some point, impingement of HAGBs occurs, resulting in high angle equiaxed grains [30]	27
Fig. 2.8. Schematic illustration of microstructure evolution during dynamic recrystallisation. (a) - (d) Large initial grain size, (e) small initial grain size. The dotted lines show old grain boundaries [30]	29
Fig. 2.9. Schematic illustration of the constitutive relation of material system as an energy converter (dissipater) where in the general case, material systems are considered as (a) nonlinear energy dissipater, and in this particular case, material system is considered as (b) linear energy dissipater [42].....	30
Fig. 2.10. Processing map of 2124/ SiC_w composites shows percentage of power dissipation efficiency represented as a contour number. The shaded area indicates flow instability	

whereas the rest area corresponds to optimum parameter. The filled circle shows the condition where the extrusion process is conducted [42]	32
Fig. 2.11. Microstructure evolution during annealing (a) recovery process (or continuous recrystallisation process if the grains consist of HAGBs), (b) primary or discontinuous recrystallisation process and (c) transition between discontinuous and continuous recrystallisation processes [113]	33
Fig. 2.12. Schematic illustration of (a) deformation structure at large second-phase particles [114] and (b) growth of nucleus within deformation zone [30]	36
Fig. 2.13. The effect of deformation conditions on PSN [114].....	37
Fig. 2.14. SIBM mechanism illustration (a) single-subgrain SIBM and (b) multiple-subgrain SIBM	39
Fig. 2.15. Schematic TTT diagram for recrystallisation and precipitation in supersaturated aluminium alloys with fast heating to the annealing temperature [30].....	39
Fig. 2.16. Schematic illustration of broad front SIBM sequences where (a) bulging initiates at HAGBs where there is little precipitation, followed by (b) formation of grains due to boundary migration and finally (c) recrystallised grains join up and are separated by low angle grain boundaries [116].....	40
Fig. 2.17. Schematic illustration of elongated particles interaction with boundary and its effect on the pinning pressure with aspect to the ratio [117]	42
Fig. 2.18. Logarithmic plot of stress versus strain rate for superplastic material, where Q_{gb} is the activation energy for grain boundary diffusion, Q_v is the activation energy for volume diffusion, m is the strain rate sensitivity, p is constant and GBS stands for grain boundary sliding [121]	45
Fig. 2.19. Schematic illustration of grain boundary sliding in (a) coarse subgrain size d and (b) fine grain size [122].....	46
Fig. 2.20. Schematic illustration of the forces occurring towards adjacent grains when the liquid phase is present in the grain boundaries [122].....	48
Fig. 3.1. Material processing route from casting to forming including heat treatment processes	51
Fig. 3.2. Schematic illustration of the mould used to produce (a) extrusion ingot, (b) rolling ingot and (c) OES samples.....	53
Fig. 3.3. Samples taken from 0 minutes, 10 minutes and 15 minutes degassing showing smooth and concave surface and no porosity as degassing time increases to 15 minutes ...	55
Fig. 3.4. Examples of cooling curves on Al-Cu alloy	57

Fig. 3.5. Graph exemplifying the homogenisation process.....	57
Fig. 3.6. In-homogeneity of deformation in a compressed specimen [103]	60
Fig. 3.7. Example of aluminium processing map showing the safe region for forming [103]	61
Fig. 3.8. Compression specimen sampling scheme.....	62
Fig. 3.9. (a) Engineering stress-strain curve and (b) true stress-true strain curve [103].....	63
Fig. 3.10. Specimen dimension for tensile testing (a) rectangular specimens and (b) cylindrical specimens	65
Fig. 3.11. Specimen dimensions for superplastic formability test	66
Fig. 3.12. Schematic illustration of DSC concept.....	67
Fig. 3.13. Illustration of hot rolled and extruded specimens with directions: parallel (RD/ED), normal (ND) and transverse (TD) to rolling or extrusion direction. The white area indicates the plane where microstructure examination and hardness were performed and the brown area indicates the plane where the TEM examination was performed.....	69
Fig. 3.14. Schematic representation of linear intercept method performed on the microstructure	70
Fig. 3.15. Experimental set up for EBSD.....	71
Fig. 4.1. True stress-true strain curves of the matrix alloy deformed at (a) 300 °C, (b) 350 °C, (c) 400 °C, (d) 450 °C and (e) 500 °C	74
Fig. 4.2. True stress – true strain curves of 0.2Ti alloy deformed at (a) 300 °C, (b) 350 °C, (c) 400 °C, (d) 450 °C and (e) 500 °C.....	75
Fig. 4.3. True stress – true strain curves of 0.2Ti-4.5TiB ₂ composite deformed at (a) 300 °C, (b) 350 °C, (c) 400 °C, (d) 450 °C and (e) 500 °C.....	75
Fig. 4.4. Effect of the addition of TiB ₂ particles on the flow stress at a strain 0.5 of Al-Cu- Mg-Ag alloys at (a) 10 ⁻³ s ⁻¹ , (b) 10 ⁻² s ⁻¹ , (c) 10 ⁻¹ s ⁻¹ and (d) 1 s ⁻¹	76
Fig. 4.5. Illustration of dislocation interaction in the presence of non-deformable particles at (b-c) low and (d-e) high strain rates [164]	78
Fig. 4.6. Graph of (a) ln (ε) – ln (σ) and (b) ln (ε) – σ of 0.2Ti-4.5TiB ₂ material	81
Fig. 4.7. Plots of (a) ln (ε) – ln [sinh (ασ)] and (b) ln [sinh (ασ)] – 1/T for 0.2Ti-4.5TiB ₂ ..	84
Fig. 4.8. Relationship between Zener-Hollomon parameter with flow stress for (a) matrix alloy; (b) 0.2 Ti alloy and (c) 0.2Ti-TiB ₂ composite	86
Fig. 4.9. Correlation between predicted flow stress and experimental flow stress of the 0.2Ti-4.5TiB ₂ composite showing the accuracy between both experimental data and predicted data	87

Fig. 4.10. Log stress vs log strain rates of (a) matrix alloy; (b) 0.2Ti alloy and (c) 0.2Ti-4.5TiB ₂ composite.....	88
Fig. 4.11. Processing map at strain of 0.5 of (a) matrix alloy; (b) 0.2Ti and (c) 0.2Ti-4.5TiB ₂ composite.....	91
Fig. 4.12. Orientation map (left) and misorientation profile (right) of as-homogenised (a) matrix alloy, (b) 0.2Ti and (c) 0.2Ti-4.5TiB ₂	93
Fig. 4.13. Orientation map (left) and misorientation profile (right) of compression test specimen deformed at 300°C, 10 ⁻¹ s ⁻¹ (a) matrix alloy, (b) 0.2Ti and (c) 0.2Ti-4.5TiB ₂	94
Fig. 4.14. Orientation map (left) and misorientation profile (right) of compression test specimen deformed at 500°C, 10 ⁻³ s ⁻¹ (a) matrix alloy, (b) 0.2Ti and (c) 0.2Ti-4.5TiB ₂	95
Fig. 4.15. The phase distribution of 0.2Ti-4.5TiB ₂ composite upon deformation at 300°C with strain rates of 10 ⁻¹ s ⁻¹ showing a homogenous distribution of TiB ₂ particles around the grain boundaries which occasionally contain Al ₇ Cu ₂ Fe particles.....	97
Fig. 4.16. (a) IPF maps and (b) band contrast of the 0.2Ti-4.5TiB ₂ composite deformed at 300°C, 10 ⁻¹ s ⁻¹ , showing recrystallisation in the area of clustered TiB ₂ (indicated as black areas) and Al ₃ Ti particles. On the band contrast map, HAGBs (>15°) are indicated with red lines, MAGBs (8 - 15°) are indicated with blue lines and LAGBs (<8°) are indicated with magenta lines.....	98
Fig. 4.17. IPF map of the 0.2Ti-4.5TiB ₂ composite deformed at 500°C with a strain rate of 10 ⁻³ s ⁻¹ showing dynamic recovery and localised dynamic recrystallisation. Black area indicates TiB ₂ particles and/or clusters	99
Fig. 4.18. Percentage of DRX and DRV of 0.2Ti-4.5TiB ₂ composites	99
Fig. 5.1. As-cast microstructure of (a) matrix alloy showing a dendritic microstructure, (b) 0.2Ti alloy, (c) 0.2Ti-4.5TiB ₂ composite showing finer grains and (d) grain size comparison between matrix alloy, 0.2Ti and 0.2Ti-4.5TiB ₂ composite showing a decreasing of the grain diameter by addition of Ti and TiB ₂ particles	104
Fig. 5.2. Cooling curves showing no undercooling was measured with addition of TiB ₂ particles	105
Fig. 5.3. Composition of constituent elements with respect to Al composition in (a) Al ₃ Ti; (b) Al ₇ Cu ₂ Fe and (c) Al ₂ Cu	107
Fig. 5.4. SEM examination including EDX map of Cu, and Fe of the matrix alloy.....	108
Fig. 5.5. SEM examination and EDX map of Cu, Fe and Ti of the 0.2Ti alloy	109
Fig. 5.6. SEM examination and EDX map of Cu, Fe, Ti and B of the 0.2Ti-4.5TiB ₂ composite	109

Fig. 5.7. TiB ₂ string thickness distribution along grain boundaries	110
Fig. 5.8. As-homogenised microstructure of (a) matrix alloy, (b) 0.2Ti alloy and (c) 0.2Ti-4.5TiB ₂ showing needle-shaped Al ₇ Cu ₂ Fe on the grain boundaries for all three studied materials, and TiB ₂ and Al ₃ Ti particles on the 0.2Ti-4.5TiB ₂ composite.....	111
Fig. 5.9. Load profile during rolling experiment showing higher load for 0.2Ti-4.5TiB ₂ composites.....	112
Fig. 5.10. Phase distribution of as-rolled (a) matrix alloy, (b) 0.2Ti alloy and (c) 0.2Ti-4.5TiB ₂ composite.....	113
Fig. 5.11. As-rolled microstructure of (a) matrix alloy, (b) 0.2Ti alloy and (c) 0.2Ti-4.5TiB ₂ composite showing shear band and matrix bowing around secondary particles..	115
Fig. 5.12. IPF maps (top), misorientation profiles (middle), and {111} pole figure (bottom) of as-rolled materials of (a) matrix alloy, (b) 0.2Ti alloy and (c) 0.2Ti-4.5TiB ₂ composites	117
Fig. 5.13. (a) Recrystallised grains observed in the vicinity of Al ₃ Ti particles on the as-rolled microstructure of the 0.2Ti-4.5TiB ₂ composite and (b) misorientation profile adjacent to the Al ₃ Ti particle (point A to point B).....	118
Fig. 5.14. (a) Comparison of grain and subgrain thickness, (b) misorientation profile	119
Fig. 5.15. Comparison of extrusion pressure for each studied material showing a higher extrusion pressure for the 0.2Ti-4.5TiB ₂ composite	120
Fig. 5.16. Microstructure of as-extruded materials taken from the outer surface (left images) and the centre (right images) of (a-b) matrix alloy, (c-d) 0.2Ti alloy and (d-e) 0.2Ti-4.5TiB ₂ composite.....	121
Fig. 5.17. Comparison of grain thickness on the specimen surface and at the centre of the specimen showing finer grain thickness at the surface	122
Fig. 5.18. (a) TiB ₂ string/cluster thickness and (b) Al ₃ Ti particle size distribution comparison between as-cast and as-extruded condition	123
Fig. 6.1. Effect of temperature and strain rate on the microstructural development after solution treatment at 540°C for 2 h on the materials deformed at temperature of 300°C with a strain rate of 10 ⁻¹ s ⁻¹ (left) and 500°C with a strain rate of 10 ⁻³ s ⁻¹ (right); (a-b) matrix alloy, (c-d) 0.2Ti alloy and (e-f) 0.2Ti-4.5TiB ₂ composite.....	126
Fig. 6.2. Comparison of misorientation profile of as-compressed and as-annealed 0.2Ti-4.5TiB ₂ specimens deformed at 500°C with a strain rate of 10 ⁻³ s ⁻¹	127
Fig. 6.3. (a) Recrystallised grain size following annealing at 540°C for 2 h as a function of compression parameter showing larger grains on the subsequent annealed specimen which	

was deformed at high temperature and a low strain rate (low Z); (b) recrystallised grain size as a function of flow stress.....	128
Fig. 6.4. (a) Annealed microstructure and (b) grain size distribution of the 0.2Ti-4.5TiB ₂ composite deformed at 300°C, 10 ⁻¹ s ⁻¹ , showing heterogeneity of recrystallised grains....	130
Fig. 6.5. Microstructure of the 0.2Ti-4.5TiB ₂ composite previously deformed at 500°C at a strain rate of 10 ⁻³ s ⁻¹ and subsequently annealed at 540°C for 2 h. Black areas indicate TiB ₂ particles	131
Fig. 6.6. Schematic illustration of recrystallisation kinetics of the matrix alloy and the 0.2Ti-4.5TiB ₂ composite, showing retardation of the recrystallisation temperature by the addition of TiB ₂ particles	132
Fig. 6.7. IPF map of (a) matrix alloy, (b) 0.2Ti alloy and (c) 0.2Ti-4.5TiB ₂ composite showing a fully recrystallised structure upon annealing at 540°C for 2 h.....	134
Fig. 6.8. TiB ₂ particle size distribution in 0.2Ti-4.5TiB ₂ composites.....	135
Fig. 6.9. Linear intercept grain size distribution of (a) matrix alloy; (b) 0.2Ti alloy and (c) 0.2Ti-4.5TiB ₂ composite	137
Fig. 6.10. {111} pole figures of all alloys in the (a) matrix alloy; (b) 0.2Ti alloy and (c) 0.2Ti-4.5TiB ₂ composite upon annealing at 540°C for 2 h.....	138
Fig. 6.11. IPF maps derived from in-situ experiments at temperatures of (a) room temperature, (b) 275°C, (c) 300°C, (d) 335°C for 30 minutes, (e) 335°C for 1 h, (f) 375°C and (g) misorientation profile comparison, (h) SRX vs SRV percentage during in-situ EBSD scanning	140
Fig. 6.12. Phase map (left) and band contrast map (right) of the 0.2Ti-4.5TiB ₂ composite heated in the hot stage EBSD at 375°C showing fine recrystallised grains in the vicinity of Al ₃ Ti particles and TiB ₂ clusters.....	141
Fig. 6.13. Illustration of principal microstructural evolution during annealing of material containing bimodal particles, showing grain boundary pinning by small particles, whilst large particles accelerate recrystallisation [198]	142
Fig. 6.14. IPF Maps of (a) matrix alloy; (b) 0.2Ti alloy and (c) 0.2Ti-4.5TiB ₂ composite showing fully recrystallised structures upon annealing at 540°C for 2 h.....	143
Fig. 6.15. Recrystallisation frequency comparison of the matrix alloy, 0.2Ti and 0.2Ti-4.5TiB ₂ composite, showing inhibition of recrystallisation in the 0.2Ti-4.5TiB ₂ composite	144

Fig. 7.1. (a) Ageing profile of the 0.2Ti-4.5TiB ₂ composite aged at several temperatures; (b) Ageing behaviour comparison of the matrix alloy, 0.2Ti alloy and 0.2Ti-4.5TiB ₂ at 175°C.....	147
Fig. 7.2. Ω precipitate observed on the 0.2Ti-4.5TiB ₂ composites aged at 175°C for 16 hours.....	148
Fig. 7.3. Comparison of Engineering stress vs Engineering strain curves showing a higher ultimate tensile strength and lower ductility achieved by the addition of TiB ₂ particles to the Al-Cu-Mg-Ag alloy.....	149
Fig. 7.4. (a) Illustration of data taken for the strain-hardening-exponent calculation; (b) True stress vs True Strain curves showing a higher flow stress of 0.2Ti-4.5TiB ₂	150
Fig. 7.5. Engineering stress vs engineering strain curve at 200°C.....	153
Fig. 7.6. Engineering stress vs engineering strain curve of extruded product showing a higher UTS was achieved in the 0.2Ti-4.5TiB ₂ composite than the other two materials ..	154
Fig. 7.7. Fractography of (a-b) matrix alloy; (c-d) 0.2Ti alloy and (e-f) 0.2Ti-4.5TiB ₂ composite	155
Fig. 7.8. The stress-strain relationship of 0.2Ti-4.5TiB ₂ composite deformed at (a) 450°C, (b) 475°C, (c) 500°C, (d) 525°C and (e) 550°C.....	156
Fig. 7.9. Flow stress vs strain rate relationship of (a) matrix alloy, (b) 0.2Ti alloy and (c) 0.2Ti-4.5TiB ₂ composite.....	157
Fig. 7.10. Elongation vs strain rate relationship of (a) matrix alloy, (b) 0.2Ti alloy and (c) 0.2Ti-4.5TiB ₂ composite.....	158
Fig. 7.11. (a) IPF map of 0.2Ti-4.5TiB ₂ deformed at 475°C at a strain rate of $5 \times 10^{-1} \text{ s}^{-1}$; (b) Recrystallised vs subgrain structure percentage showing a higher percentage of substructure, indicating recovery was dominant during deformation.....	160
Fig. 7.12. Magnified area of the deformed structure showing grain boundary bulging	161
Fig. 7.13. Microstructure evaluation showing cavitations' nucleation on the Al ₃ Ti and TiB ₂ particles; and crack propagation across Al ₃ Ti particle.....	162
Fig. 7.14. SEM image and EDX map of Al, Cu, Fe and Ti showing cavities nucleated at Al ₃ Ti particles and TiB ₂ particles which were associated with the Cu and Fe constituents	163
Fig. 7.15. Fracture surface on the specimens deformed at (a)-(c) 475°C, $5 \times 10^{-1} \text{ s}^{-1}$ which has the highest ductility and (b)-(d) 525°C, $5 \times 10^{-1} \text{ s}^{-1}$ which has low ductility	164
Fig. 7.16. DSC results of the 0.2Ti-4.5TiB ₂ composite showing endothermic reaction at the temperature of 535°C	165

Fig. 7.17. EDX map (Cu, Fe and Ti map) of specimen with highest ductility which was deformed at 475°C with a strain rate of $5 \times 10^{-1} \text{ s}^{-1}$, showing the existence of Cu and Fe constituents in the vicinity of TiB_2	166
Fig. 7.18. Fracture surface of specimens with low ductility which was deformed at 525°C with a strain rate of $5 \times 10^{-1} \text{ s}^{-1}$	167

ACKNOWLEDGEMENTS

The author is so grateful for the opportunity and every support that have been given to her during her PhD. Hence, the author would like to express her gratitude to the following people for their contribution in the completion of this work.

First of all, I would like to thank The University of Warwick for giving me the opportunity and Aeromet International Ltd. for the financial support to this project. Their support throughout my PhD is most appreciated. Furthermore, I am so grateful for my supervisors, Prof. Dr. Richard J. Dashwood and Dr. Vit Janik for their trust in giving me the opportunity to do this project and for their tremendous guidance during my PhD. The completion of this thesis would be impossible without their help and support.

I am thankful for a number of people from Aeromet International Ltd., Dr. Harpinder Singh Pull, Dr. John Forde, Mr. Bill Stott and Mr. Steve Ashworth, who have always been supportive during the completion of this work. Their willingness to support me in their busy time is greatly appreciated. Not to forget the contribution of Swinden Technology Centre Rotherham, George Ibbeson and Peter Dutton, for allowing me to use their rolling facility and for their great help in carrying out rolling process.

I am greatly indebted to Mr. Richard Keyte C.Eng for his tremendous help in casting, rolling and extrusion as well as for the knowledge sharing. His willingness to share his expertises, answer my various questions and give invaluable inputs to this project is very much appreciated. I am grateful for Dr. Hiren Kotadia for his support and encouragement as well as for the knowledge sharing throughout the work in this thesis. Furthermore, the completion of this work would have been so much difficult without a help from Dr. Mike Keeble and Dr. Evan Mogire from Buehler who always provided good inputs for this project. Their willingness to spend their time for a long discussion with me in their busy schedules, share their vast knowledge and give invaluable suggestions to this project is highly appreciated.

I am grateful for every person who always willing to help me during my labworks and for their hardwork in preparing my test samples; John Pillier, Paul Johnson, Darren Woon, Dave Cooper, Lewis Curry, Stefan Kousoulas, Zac Parkinson, Martin, Darren Stewardson and Darren Grant. Their kindness and support is much appreciated.

The contribution of the following people is also deeply acknowledged; Dr. Carlos Moreno for the training in the static Instron machine as well as for the friendship; Scott Taylor for sharing his knowledge in material preparation and for the training in dynamic Instron machine; other PhD and EngD fellows, Dr. Hamzah Alharti, Dr. Elspeth Keating, Dr. Prasun Choksi, Balaguru Balasubramaniam. In addition to that, I am so thankful to Prof.Dr. Brian Ralph for his willingness to do proofreading of this thesis.

Furthermore, my PhD life would have not been so much fun without the supportive and optimistic friends around me, Dr. Liping Zhang, Dr. Shamsiah Awang, Lorena Santamaria, Dr. Simon Davies, Dr. Annirudha Gupta, Dr. Sneha Singh, and Alexander Garrido Rios. I would like to thank you all for the sweet friendship and all of your support. I am also indebted to my friend, Reza Miftahul Ulum, for sharing the PhD spirit and for his full support in providing me a bunch of good journals which I could not access from here.

Morover, I am deeply indebted to my family, Walfreddy Nixon and my bestfriend, Eva Rida Meilyna Simatupang, for their endless long-distance support, motivation and prayer. I could not have done this far without their support. The last but not least, my highest gratitude is to my Lord and Saviour, Jesus Christ, for without Him, I am nothing.

DECLARATION

This thesis is submitted in partial fulfilment of the requirements for the degree of Doctor of Philosophy and describes work carried out from October 2012 to October 2016. Unless otherwise indicated, the research described is my own and not the product of collaboration. No part of this thesis has been submitted to any other university, or as any part of any other submission to the University of Warwick.

ABSTRACT

The influence of addition of 0.2 wt.% Ti + 4.5 wt.% TiB₂ particles on the workability and static softening behaviour of Al-Cu-Mg-Ag matrix alloy has been compared with matrix alloy, Al-Cu-Mg-Ag, and Al-Cu-Mg-Ag alloy containing 0.2 wt.% Ti. In this study, the workability has been explored through compression test, rolling and extrusion. Furthermore, a mechanical property in tension, both in room temperature and elevated temperature was also carried out. Detailed characterisation on the distribution of TiB₂ particles as well as Al₃Ti particles in each of material processing stages i.e. casting, homogenisation, rolling and extrusion are presented.

The flow stress behaviour obtained from compression testing showed a similar trend for all three materials in which the flow stress increases with decreasing temperature and increasing strain rates. In all test conditions, 0.2Ti-4.5TiB₂ composites exhibited the highest flow stress of all materials. Interesting finding was obtained in which with increasing temperature and decreasing strain rates, 0.2Ti-4.5TiB₂ composites exhibited closer flow stress with other two alloys. Owing to the existence of TiB₂ clusters around grain boundaries and triple joints as well as blocky Al₃Ti particles in the as-cast conditions which will increase strain hardening during deformation, this finding was not expected. This result indicates that at higher temperatures and low strain rates, the addition of TiB₂ particles would not give a significant influence to the deformation mechanism. Dynamic recovery was observed in all test conditions of matrix alloy and 0.2Ti alloy. In contrast to that, in 0.2Ti-4.5TiB₂ composites, dynamic recrystallisation was observed upon low temperature and high strain rate deformation, while dynamic recovery with localised dynamic recrystallisation was observed upon high temperature and low strain rate deformation.

Another interesting finding was achieved regarding static softening behaviour of 0.2Ti-4.5TiB₂ composites. Recrystallisation was retarded in 0.2Ti-4.5TiB₂ composites. Large and elongated recrystallised grains were observed following annealing of the rolled product of 0.2Ti-4.5TiB₂ composites. Furthermore, fine recrystallised grains were observed in the vicinity of Al₃Ti particles and TiB₂ clusters. This result was also unexpected since owing to the high volume fraction of secondary particles in the composites, one would expect high recrystallisation rates due to potential nucleation in the vicinity of secondary particles. This behaviour was explained in terms of the distribution of TiB₂ particles. TiB₂ particles were found pinning the grain boundaries during annealing, inhibiting grain boundary migration and hence leading to the retardation of recrystallisation. Consequently, a large recrystallised grain size was observed in the 0.2Ti-4.5TiB₂ composites. On the contrary, more equiaxed recrystallised grains were observed in the matrix and 0.2Ti alloy. In addition to that, a deformed structure was retained following annealing of extruded 0.2Ti-4.5TiB₂ composites, suggesting retardation of recrystallisation.

Regarding the mechanical properties, higher tensile strength was observed in 0.2Ti-4.5TiB₂ composites, both at room temperature as well as at a temperature of 200°C. Furthermore, concerning the superplastic behaviour of the composite, a limited processing window was observed in which the highest elongation of 151% was obtained at the temperature of 475°C. Elongation was decreased with further increasing temperature. This was postulated as being due to liquation at higher temperature.

LIST OF SYMBOLS

A_0	original cross section
α	material constant
β	material constant
d_s	subgrain size
D_0	original grain size
D_R	recrystallised grain size
ε	strain
$\dot{\varepsilon}$	strain rate
ε_c	critical strain
ε_{cr}	critical compressive strain
ξ	instability parameter
%EL	elongation percentage
H	grain thickness
γ_{lp}	liquid/particle interfacial energy
γ_{sp}	solid/particle interfacial energy
γ_{ls}	liquid/solid interfacial energy
k	material constant
l_f	fracture length
l_0	original gauge length
m	strain rate sensitivity
η	power dissipation
n	strain hardening exponent
n_s	number of particles interacted with grain boundary
P_D	driving pressure

P_Z	Zener pinning pressure
Q	activation energy
Q_{gb}	activation energy for grain boundary diffusion
Q_v	activation energy for volume diffusion
Q_{HW}	activation energy for hot working
σ_p	peak stress
σ	flow stress
%RA	reduction in area
R	universal gas constant
S	engineering tensile strength
S _y	engineering yield strength
T_i	incipient melting temperature
T_s	solidus temperature
T_{gb}	traction force
V_f	volume fraction
VHN	Vickers hardness value
X_v	volume fraction of recrystallised grain
Z	Zener-Hollomon

ABBREVIATIONS

AMS	Aerospace Material Specification
ASTM	American Society for Testing and Materials
AMCs	aluminium matrix Composite
Al ₃ Ti	titanium aluminide
Al ₂ O ₃	aluminium oxide
BSE	backscattered electron
CVM	cluster variation method
DMM	dynamic materials model
DRX	dynamic recrystallisation
DRV	dynamic recovery
DSC	differential scanning calorimetry
dSRX	discontinuous static recrystallisation
EBSD	electron backscattered diffraction
ECAP	equal channel angular pressing
EDS	energy dispersive X-ray spectroscopy
GB/GBs	grain boundary/ies
GBS	grain boundary sliding
GDRX	geometric dynamic recrystallisation
HAGBs	high angle grain boundaries
HSRS	high strain rate superplasticity
ISS	internal stress superplasticity
LAGBs	low angle grain boundaries
MAGBs	medium-angle grain boundaries
MMCs	metal matrix composites

ND	normal direction
OES	optical emission spectroscopy
OM	optical microscopy
PBDs	particle deformation bands
PSN	particle stimulated nucleation
RD	rolling direction
SIBM	strain induced boundary migration
SiC	silicon carbide
SEM	scanning electron microscopes
SFE	stacking fault energy
SPF	superplastic forming
SRX	static recrystallisation
SRV	static recovery
TEM	transmission electron microscope
TiB ₂	titanium diboride
TiC	titanium carbide
TMP	thermomechanical processing
TTT	time temperature transformation
T6 temper	solution heat treated and then artificially aged
T8 temper	solution heat treated, cold worked and then artificially aged

CHAPTER 1

INTRODUCTION

1.1. Research Background

Aluminium and its alloys are known as one of the most important engineering materials after steel. Besides their excellent properties such as light weight, good corrosion resistance, ductility, and strength [1–3], their versatility makes them more extensively used compared to other materials. It allows them to be formed into a variety of shapes through a range of different manufacturing processes, from traditional techniques such as casting to advanced techniques such as additive layer manufacturing.

Despite many emerging advanced manufacturing technologies, bulk metal forming processes are still being widely used in various industries. Their ability to produce large scale complex-shape products has made them become a special attraction to many industries. In addition to that, bulk metal forming processes offer time-efficient production as well as cost effectiveness. There are several types of bulk metal forming processes, such as rolling, extrusion, forging, and drawing. Among those processes, rolling and extrusion are the most commonly used processes in industry. A variety of shapes from standard semi-finished products e.g. plates, sheets, and rods, to complex shapes can be produced by rolling and extrusion. In contrast to extrusion which is usually used to obtain a final product with tight dimensional accuracy, rolling is used mainly to produce a semi-finished sheet product which will be further formed into a final product.

Currently, industries have been facing competitive challenges to manufacture complex structures from sheet metal that meet cost and product goals. With the advantages of producing near-net complex-shape components in a one step process and eliminating unnecessary joints and rivets [4], superplastic forming (SPF) is now becoming a major interest to many industries. The SPF processing also allows higher formability which leads to a decreasing amount of material waste through better material utilisation. Therefore, rolling, extrusion, and SPF processes have been used in a wide variety of industries, from automotive to aerospace due to their versatility and cost effectiveness.

Along with improvements in the performance of aircraft, the progress of materials has also been increased. Breakthroughs in material technologies have been made to meet aircraft industrial demands. It is expected that the lighter, stronger, better fatigue resistant, more damage and heat resistant materials, both metallic and composites, will become a trend in the development of next generation aircraft, both in airframe and engine development [5].

One of the most commonly used materials for aircraft applications are Al-Cu-Mg alloys (2xxx series Al alloys [6]). Al-Cu-Mg alloys are used extensively in aircraft structures due to their high specific strength and modulus at relatively high operating temperature [7]. Their properties are defined by the existence of fine coherent precipitates and dispersoids. Their ability to get heat treated to control the morphology and distribution of those precipitates and dispersoids enables them to be produced in a variety of microstructural conditions. As a result, it permits the fulfilment of specific design requirements. However, alloys based on the Al-Cu-Mg alloys have some limitations such as low fracture toughness and poor damage tolerance. Literature study [8–10] showed that the addition of Ag to Al-Cu-Mg alloys is able to overcome those disadvantages. Improvements in age hardening have been discovered by addition of trace Ag (~0.1%) to the Al-Cu-Mg alloy. It is due to the formation of a fine and uniform dispersion of a hexagonal plate-like precipitate, Ω (Al_2Cu) on the $\{111\}_\alpha$ plane, an active plane in the Al matrix. Because of the apparent stability of Ω precipitates, Al-Cu-Mg-Ag alloys also showed promising creep properties up to 200°C [8,9,11,12]. Creep is known as one of the important properties in aircraft, such as aircraft skin. Although the air temperature is very low, however, due to aircraft's high speed, the friction between the air and the skin could create local heating in the certain area. For example, it is reported that in the Concorde aircraft, the temperature at the nose cone can reach up to 128°C, 105°C at the tail and 91 – 97°C at the wings [13]. Moreover, the addition of Ag to the ternary Al-Cu-Mg system reduces the formation of precipitate on the grain boundary (GB), which leads to the increment of toughness when the alloys are subjected to ageing. Furthermore, it also decreases the probability of intergranular failure during forming [7]. Therefore, in recent years, aircraft industries have shown their interest in Al-Cu-Mg-Ag systems because of their outstanding mechanical properties, thermal stability and creep resistance at elevated temperatures.

Another promising material for aircraft applications are aluminium-based matrix composite (AMCs). AMCs have been an attractive research topic in the aircraft industry

due to increased strength-to-weight ratio and strength-to-cost ratio, high modulus and thermal stability. The addition of high strength/elastic modulus ceramic particles such as TiB_2 (titanium diboride) [14–16], SiC (silicon carbide) [17–19] and Al_2O_3 (aluminium oxide) [20–22] to an aluminium-based matrix offers a unique combination of strength, stiffness, wear resistance and elevated temperature stability.

Over other traditional particulate reinforcement materials, TiB_2 has shown superior properties. It has a high melting point (2790°C), high hardness (960 HV) and high modulus of elasticity (530×10^3 GPa) [23]. Literature [24,25] indicated that TiB_2 exhibits good resistance to elevated temperature plastic deformation and is thermodynamically stable in liquid aluminium. Therefore it avoids the formation of brittle products at reinforcement-matrix interfaces which reduces mechanical properties of the composites. Furthermore, addition of > 0.15 wt.% Ti in the 4-5 wt.% TiB_2 containing Al alloys allows the formation of Al_3Ti particles. It has been known that Al_3Ti particles are more potent grain refiners than TiB_2 . Thus, a large number of Al_3Ti particles are suspended along with TiB_2 in the liquid metal prior to solidification. On solidification, Al_3Ti particles will rapidly nucleate a large number of aluminium grains and as TiB_2 particles are pushed to the grain boundaries, the grain growth is inhibited. Consequently, the addition of > 0.15 wt.% Ti in the TiB_2 containing Al alloys not only increases the yield strength by refining the grains, but also maintains ductility of the alloys as the remaining Al_3Ti particles will be engulfed by the advancing growth [26].

Because of the excellent properties of Al-Cu-Mg-Ag alloy and TiB_2 particles as particulate reinforcement, this present research will be focused on TiB_2 reinforced Al-Cu-Mg-Ag alloys. Aeromet International LTD has developed A20X alloy, a casting product of Al-4.5Cu-0.27Mg-0.75Ag-0.2Ti-4.5 TiB_2 . As a result of a combination of good elevated temperature properties of the Al-Cu-Mg-Ag alloy due to the presence of Ω phases as well as improvements in strength yet maintaining ductility due to grain refining and engulfing Al_3Ti by introducing free Ti and TiB_2 , it is hypothesised that the wrought product of A20X will show high mechanical properties attractive to potential aerospace applications. Therefore, in this study, the workability of the A20X alloy was explored through rolling, extrusion and superplastic forming with subsequent detailed materials characterisation through conventional and in-situ characterisation methods.

1.2. Design Philosophy and Research Scope

AMCs are recognized as important structural materials. However, owing to the presence of particulate reinforcements, particularly in high volume fractions, AMCs suffer from lower ductility during the forming process compared to the monolithic alloys. Apart from the casting defects in the billet and impurities, the presence of TiB_2 particles is the critical property in the present material as it will influence the workability of the AMCs. Consequently, a clear understanding on the effect of TiB_2 particles on the material's workability is important.

In order to design processing parameters, it is important to understand the dependency of workability on temperatures, strain rates and level of strain. In this research, workability of Al-4.5Cu-0.27Mg-0.75Ag-0.2Ti-4.5 TiB_2 composites (A20X) was investigated through compression testing followed by the inspection of the deformed specimens. The flow stress resulted from compression testing enables us to analyse the resistance of the materials to deformation with respect to the deformation parameter. Processing maps which define regions that allow crack-free forming in terms of strain rate and temperature were developed.

Moreover, microstructural features such as the degree of recrystallisation, grain and/or subgrain size and shape, and crystallographic texture [27] play an important role in controlling properties of AMCs. The importance of understanding the effect of TiB_2 particles on those features has led this present research to carefully study the deformation and static softening behaviour of A20X on the rolled and extruded product with the aim of improving the performance and design of further processing steps, such as superplastic forming, stamping etc. The superplastic forming ability of A20X was also assessed. However, as the main focus in this thesis is about rolling and extrusion, the effect of TiB_2 on the superplastic forming will be discussed very briefly.

It has been identified [15,26,28,29] that the presence of free Ti in the TiB_2 containing Al alloys will give a significant impact on the microstructure and mechanical properties. In addition to that, the existence of precipitates will also have a significant influence on those aspects. For example, a complex interaction between precipitation and recrystallisation has been observed [30]. Considering that the Al matrix used in this research is an Al-Cu-Mg-Ag based alloy which contained various types of precipitates, it is expected that these

precipitates will influence the A20X softening mechanism. Thus to avoid misleading conclusions, two additional alloy, Al-Cu-Mg-Ag alloys and Al-Cu-Mg-Ag alloys with addition of 0.2 wt.% Ti were chosen as comparative materials to give a clear understanding about the effect of TiB₂ in this present research. The scope of the study in this thesis is schematically described in Fig. 1.1.

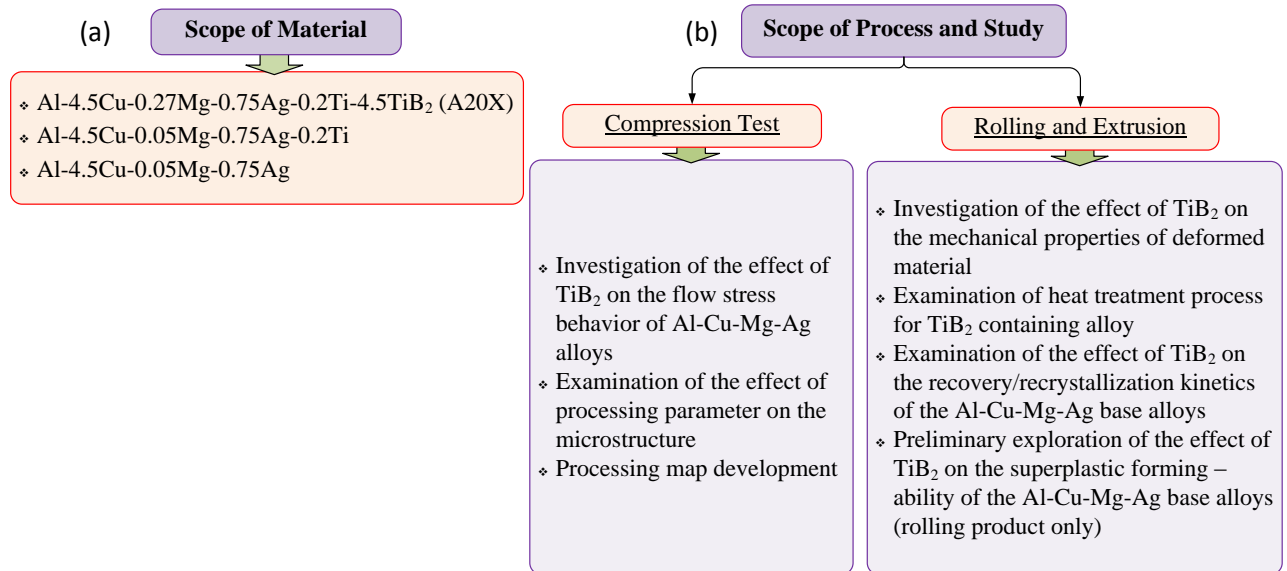


Fig. 1.1. Schematic diagram of research scope

1.3. Research Aims and Objectives

It is the aims of this research to investigate the role of TiB₂ particles on the workability, softening mechanism and mechanical properties of high strength Al-Cu-Mg-Ag base alloy. Fulfilment of those aims requires a critical selection of experimental design which has specific objectives:

- To identify a safe processing window of the TiB₂ reinforced Al-Cu-Mg-Ag alloy by developing a processing map which utilises elevated temperature uniaxial compression testing on cylindrical samples machined from homogenised material
- To determine the effect of TiB₂ reinforcement by assessing the properties of Al-Cu-Mg-Ag base alloy in the different areas below:
 - Grain size control
 - Flow stress
 - Recovery and recrystallisation

- Tensile strength
- To investigate superplastic forming ability of TiB_2 reinforced high strength Al-Cu-Mg-Ag alloy

1.4. Hypothesis

A hypothesis has been made for this present research with respect to the research aims and objectives. The addition of TiB_2 to the high strength Al-Cu-Mg-Ag is expected to restrict its processing window compared to the matrix alloy. It is suspected that this composite will be very sensitive to deformation parameters. During forming, the existence of hard particles of TiB_2 and Al_3Ti will lead to higher dislocation density around them which might lead to the localised strain. The stress concentration created around the particles might cause particle detachment, initiating void formation. This will reduce the workability of the composites, leading to a decrement of the processing window. Consequently, it is important to investigate its safe processing parameter to avoid crack formation during forming. Furthermore, increasing of the flow stress during deformation is also expected with the existence of those particles.

Regarding the softening mechanism, the author in this thesis expects that the existence of TiB_2 and Al_3Ti plays a certain role during static softening depending on their size and or cluster sizes, interparticle spacing and deformation parameters. If the particle/cluster sizes are less than $1\text{ }\mu\text{m}$ and closely spaced, it is expected to retard or completely inhibit recrystallisation and pin the grain boundaries. However, if the particle/cluster size is more than $1\text{ }\mu\text{m}$ and highly spaced, recrystallisation is expected. This is due to a higher dislocation density created around the big particles ($> 1\text{ }\mu\text{m}$), meaning that higher stored energy will be localized around the particles during deformation. This later on will induce a higher recrystallisation degree during annealing.

1.5. Novelty of the Research

The main objective of this research is to understand the effect of TiB_2 reinforcement on the workability and static softening mechanisms including mechanical properties of Al-Cu-Mg-Ag alloy. Even though many researchers have worked on the in situ TiB_2 reinforcement Al alloys [31–35], very few researchers have worked on the specific high strength Al-Cu-Mg-Ag alloys. There is some research reporting the processing map of

other particulate (Al_2O_3 , SiC_p , SiC_w , TiC) reinforced aluminium alloys [36–42], but no report found on the processing map and softening mechanism of particular TiB_2 reinforced high strength Al-Cu-Mg-Ag alloys. The combination of high strength of the Al-Cu-Mg-Ag based alloy and TiB_2 reinforcement has its own challenge to be developed into wrought product. A processing map provides the optimum zone for hot workability and instability regions information. That information is important in designing ‘defect free’ process conditions and parameters for hot deformation. Apart from that, the softening mechanism gives information about recovery and recrystallisation behaviour which is important in designing further processing steps for previously deformed material. In this present research, in situ EBSD was conducted, providing real time investigation on the role of TiB_2 during annealing. The consolidation of industrial scale rolling and extrusion process and advanced material characterisation conducted in this study provides information on plastic deformation and softening mechanisms during industrial scale processing.

1.6. Thesis Structures

This thesis begins by highlighting the advantages of TiB_2 as a reinforcement particle and the excellent properties of Al-Cu-Mg-Ag alloys, including the reason why it is examined. It is followed by the literature review and fundamental theory utilised in interpretation of the results. The experimental methods section introduces all testing and deformation processes conducted in this research as well as each technique used to characterise the materials.

The result chapters start from Chapter 4, a study of strain rate and temperature dependence of the AMCs and comparative materials to understand the effect of TiB_2 on the deformation process. Processing maps which define the safe processing window are provided in this chapter. The role of TiB_2 on the solidification process during casting, together with their influence on the sheet and extruded material are briefly discussed in Chapter 5.

Chapter 6 describes the effect of the distribution, size and volume fraction of TiB_2 in the wrought materials on the recrystallisation behaviour during annealing. Recrystallisation kinetics are measured and the underlying mechanism is revealed. The mechanisms are explained by taking into consideration the distribution of each particle and the cluster. The results chapter is ended with Chapter 7, focusing on mechanical properties in the as peak-

aged condition. These properties are the hardness and tensile strength at ambient temperature and 200°C. Furthermore, preliminary test result of superplasticity is also explained in this chapter.

CHAPTER 2

LITERATURE REVIEW

2.1. Introduction

This chapter includes a review of literature and fundamental theories which will be utilised in the interpretation of the results. The subchapters will guide the reader to a review of the role of each alloying element on the material behaviour and properties. Furthermore, the influence of TiB_2 particles in the aluminium alloys and aspects concerning recrystallisation and recovery are described. Finally, an introduction to superplastic forming together with the role of reinforcement particles during superplastic forming is given.

2.2. The Al-Cu-Mg-Ag Alloy System

The demand for high strength Al alloys has led to the development of Al-Cu-Mg-Ag alloys. Al-Cu-Mg-Ag alloys were initially developed by Polmear *et al* [2,43–45] in the early 1960's to replace conventional 2000 (Al-Cu-Mg) alloys. With a mechanical strength that can exceed 500 MPa at room temperature and almost 400 MPa at 200°C, Al-Cu-Mg-Ag alloys provide superior properties compared to other 2000 series Al alloys. The emphasis was focused on high Cu:Mg ratio quaternary alloys since they exhibited higher properties at high temperature. Early research [46] on the addition of 0.4 wt.% Ag to the Al-4Cu-0.3Mg alloy discovered an unexpected result of promising creep performance at 125°C when it was tested at the underaged condition. This observation has driven detailed investigation on Al-Cu-Mg-Ag alloys. Composition design experiment based on the commercial alloy 2219 (Al-6.3Cu-0.3Mn) was conducted by I.J. Polmear and M.J. Couper [47] in which a small amount of Mg and Ag were added. A significantly improved tensile property was obtained with a nominal composition of Al-6.3Cu-0.45Mg-0.4Ag-0.3Mn-0.2Zr. It was reported that the extruded product of that alloy aged at T6 temper (solution heat treatment followed by artificial ageing) showed a higher yield strength of around 467 to 520 MPa compared with 290 MPa and 390 MPa respectively for 2219-T6 and 2618-T6 in similar extruded form [6,47]. The same tendency in fatigue properties was also observed. Furthermore, 10 times longer stress rupture life than 2000 series alloys was

recorded during accelerated creep testing at 180°C. Preliminary tests on stress corrosion resistance also revealed a higher resistance compared to 2000 and 7000 series alloys.

Following those studies, a comprehensive programme to test a series of industrially cast and extruded Al-Cu-Mg-Ag alloys was initiated by collaboration between French and Australian research groups [48]. This work confirmed that these alloys aged to T6 temper (8 h at 185°C) revealed higher creep performance at 150°C and 180°C compared with either a T6 or T8 (solution heat treatment, cold work and then artificial ageing) temper of other competing 2000 series Al alloys such as 2219, 2024, 2618 and 2048. The optimum composition was exhibited to be Al-5.6Cu-0.45Mg-0.45Ag-0.3Mn-0.18Zr. Moreover, a high creep resistance was also observed in the United States when it was tested at 107°C and 135°C.

With these superior properties, alloys based on the Al-Cu-Mg-Ag system are very attractive for an application where high strength and creep resistance are major concerns, such as in aircraft. The high heat resistance, high ballistic properties and high damage tolerance properties of Al-Cu-Mg-Ag alloys make them possible to be applied in the next generation of supersonic transport airplanes and armoured tanks [43]. Consequently, Al-Cu-Mg-Ag alloys will continue to be of interest to aircraft and defence industries. Since the materials studied in this research consist of a high Cu:Mg ratio in their alloy composition, the discussion in this present section will be limited only to high Cu:Mg ratio alloys.

2.2.1. Precipitate Phases and Age Hardening Behaviour

The high strength levels attained by addition of trace Ag (~0.1 wt.%) to high Cu:Mg ratio Al-Cu-Mg alloys derive mainly from the existence of hexagonal-shaped plate-like Ω (Al_2Cu) precipitates. The increment of strength comes from the fact that this phase precipitates as a fine and uniform dispersion on the $\{111\}_\alpha$ planes, the principle glide plane in the Al matrix, thus inhibiting dislocation movement more effectively. Furthermore, the ability of this phase to maintain close coherency with the matrix up to approximately 200°C enhances the creep resistance of the quaternary alloy [9,10,12]. Stemming from those facts, as the target industrial application of this present work is for the aircraft application, which requires high strength and creep resistance properties, Al-Cu-Mg-Ag based alloys were chosen as the studied material in this work.

Several experiments have been conducted with regards to developing optimum properties of Al-Cu-Mg-Ag alloys. One of the most important inventions was conducted by Polmear and Couper [47]. In their research, Al-6.3Cu-0.5Mg-0.5Ag-0.5Mn-0.2Zr was cast and extruded. Several solution treatments from 520°C – 540°C and ageing temperatures from 175°C – 205°C were subjected to the extruded alloy in order to find the optimum heat treatment parameters. In their case, liquation was found in the microstructure at a temperature of 530°C and the optimum ageing temperature was found to be 195°C for 7 hours. Their method and inventions were used as a base line in developing heat treatment parameters for the current studied material. However, since the alloy's composition used in this study is slightly different, meaning that the solubility level is also different, it is expected that the heat treatment parameters will also be different from their results.

Table 2.1. Proposed crystal structures for the phases in Al-Cu-Mg-Ag system

Phase	Proposed Structure	Lattice Parameter	Ref.
θ	Body centred tetragonal	$a=b=0.6066 \text{ nm}$, $c=0.487 \text{ nm}$	[49]
θ'	Body centred tetragonal	$a=b=0.404 \text{ nm}$, $c=0.58 \text{ nm}$	[50]
θ_m	Tetragonal	$a=b=0.6066 \text{ nm}$, $c=0.496 \text{ nm}$	[51]
Ω	Monoclinic	$a=b=0.496 \text{ nm}$, $c=0.848 \text{ nm}$	[52]
	Hexagonal	$a=0.496 \text{ nm}$, $b=0.859 \text{ nm}$, $c=0.848 \text{ nm}$	[53]
	Orthorhombic	$a=0.496 \text{ nm}$, $b=0.859 \text{ nm}$, $c=0.848 \text{ nm}$	[9]
S	Body centred orthorhombic	$a=0.4 \text{ nm}$, $b=0.923 \text{ nm}$, $c=0.714 \text{ nm}$	[54]

It is now clear that the improvement in strength in the quaternary alloy, Al-Cu-Mg-Ag alloy, is due to the existence of the Ω phase. Various theories have been proposed regarding the crystal structures of the Ω phase [52,53]. This is because the structure of the Ω phase has close similarity with other structures, particularly with the θ phase when it is aged at high temperature. This led to a misleading interpretation. For example, a tetragonal phase was observed by Garg and Howe [55] when an Al-4Cu-0.5Mg-0.5Ag (wt.%) alloy was aged at high temperature of 250°C and 350°C. This phase was then designated as θ_m . However, it was later re-designated as θ phase by Chang and Howe [12] based on the fact that it has the same composition as the equilibrium phase (Al_2Cu). Although the structure of the Ω phase still remains under question, it is recognised that the θ_m , θ and Ω phases have nearly the same lattice parameter. Later on, it was finally concluded that the Ω phase possesses a face-centred orthorhombic structure with an orientation relationship with the aluminium matrix of $\{111\}\alpha//\{001\}\Omega$, $[10\bar{1}]\alpha//[010]\Omega$, $[1\bar{2}1]\alpha//[100]\Omega$ [9,56]. Table 2.1

provides the proposed lattice parameters of those precipitates along with other precipitates present in the Al-Cu-Mg-Ag alloy system such as θ' and S phase.

As well as Ω phase's crystal structure, its nucleation and growth remains uncertain since several mechanisms have been proposed [9,11,44,51,56–62]. The current understanding of its nucleation process involves Mg-Ag co-clusters during the early stages of ageing [49,63]. These clusters associate with Cu to form $\{111\}_\alpha$ GP zones which then transform into the Ω phase by forcing out the Ag and Mg. Ringer *et al* [49], for example, observed Mg-Ag co-clusters during 15 s of ageing at 180°C. This indicates that Mg-Ag has a strong interaction since no Mg-Cu co-cluster was observed during early ageing of Al-Cu-Mg-Ag alloys as it was observed in the ternary alloy. After 30 s of ageing, they examined that Mg and Ag were associated with Cu to form the Ω phase. Similar results were obtained by Zhu *et al* [64] who conducted a cluster variation method calculations (CVM) to analyse the Ω phase nucleation precursors stability by the addition of trace Ag to the ternary Al-Cu-Mg alloys. They reported that the Mg-Ag cluster has to be associated with Cu to be elastically viable on $\{111\}_\alpha$. It was proposed that the precipitation of Ω phase was facilitated by Mg and Mg-Ag co-clusters [49,64]. Due to strong interaction, it appears that the role of Ag is to act as an effective trap for Mg atoms, resulting in Mg-Ag co-clusters, which act as effective nucleation sites for Ω precipitates.

Regarding the evolution of microstructure during ageing, TEM and SAED studies observed the formation of fine and uniform GP zones and θ'' on $\{001\}_\alpha$ during the early stages of precipitation of Al-Cu-Mg-Ag alloys aged at 180°C. It was followed by the formation of the $\{111\}_\alpha \Omega$ at the expense of the $\{001\}_\alpha$ precipitates. As a result, a fine and uniform dispersion of Ω precipitates and coarsely dispersed θ' precipitates nucleated on dislocations present after quenching [49]. The Ω phase was observed nucleated on low angle grain boundaries in preference to θ' even when the $\{001\}_\alpha$ habit plane of θ' is closer to the grain boundary plane than the $\{111\}_\alpha$ habit plane of Ω precipitates [51]. In the presence of cold working prior to ageing, the size and density of Ω precipitates are decreased, whereas the density of θ' precipitates is increased, resulting in a reduction in hardening response [65,66]. This suggests that the $\{001\}_\alpha \theta'$ phase is less effective in strengthening i.e. retarding dislocation motion compared to the $\{111\}_\alpha \Omega$ phase. The dislocations introduced during cold working prior to ageing will impede the clustering process and alter the vacancy content which may be a precursor to Ω nucleation [65].

Furthermore, the dislocations introduced during cold working will also provide the heterogeneous nucleation sites for competing precipitates such as θ' , leading to the decrement of size and density of Ω phase. Considering these investigations, in this study, no cold work prior to ageing was applied as the strength is one of the important properties that has to be achieved considering its application is for aircraft.

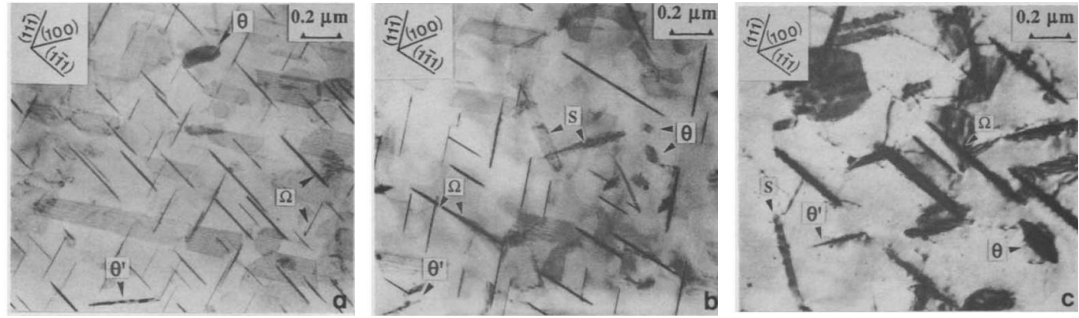


Fig. 2.1. Common ageing precipitates existing in the Al-Cu-Mg-Ag alloy recorded with the electron beam parallel to $\langle 110 \rangle$ showing changes in microstructure with ageing at 250°C (a) 5 hrs ageing, Ω plates and occasionally θ and θ' phase, (b) 30 hrs ageing, coarser Ω , θ' and θ phase and S phase and (c) 600 hrs ageing, very coarse Ω phase, large θ' and θ particle and S phase [11]

Literature studies [11,65,67–69] showed that the distribution of fine uniform Ω precipitates are affected by several factors. For example, the presence of S (Al_2CuMg) phase precipitates affected the number density and stability of the Ω as reported by Ringer *et al* [11] and Hutchinson *et al* [67]. This is because the formation of S precipitates during ageing consumes magnesium which will decrease the number of Mg atoms required for the formation of Ω . Consequently, the formation and stability of Ω phase are hindered. Prolonged ageing at 250°C for 2400 hours showed dissolution of the Ω phase [11]. This finding correlates with the result of Mukhopadhyay [70] who illustrated the partitioning of silver to S-phase precipitates. As the stable S precipitates coarsen, magnesium and silver are consumed from the adjacent matrix and Ω interfacial layers which leads to the dissolution of Ω phase. This will further the formation of S-phase and θ -type precipitates towards their equilibrium volume fraction, while furthering the dissolution of Ω phase. Consequently, future alloy design must account for this competitive precipitation. As treatment at elevated temperature will further the formation of the S phase while hinder the nucleation and stability of the Ω phase, careful control of the composition and heat treatment are required to minimise the formation of S precipitates. These drove the current

research in designing the ageing temperature not higher than 200°C to avoid the formation of S phases. Hence it prevents the decrement of strength.

Moreover, the thermal stability of the Ω phase is also limited by the thickness of individual plates. Studies [11,67] show that the coarsening resistance of Ω plate in silver containing alloys is compromised when the plate thickness reaches or exceeds 13 nm (when artificially aged at 250°C). At this critical thickness, dislocations are accommodated at the plate periphery which reduces the misfit strain. As a result, the barriers for ledge nucleation decreases, facilitating more rapid plate thickening which ultimately degrades the potent strengthening effects of the precipitates. Fig. 2.1 shows the morphology of each phase present in Al-Cu-Mg-Ag alloys when aged at 250°C.

2.2.2. Role of Alloying Element

The interaction among each element in Al-Cu-Mg-Ag alloys systems determines their ageing response. This will affect the resulting mechanical properties. The paragraphs below explain the effect of each element in this alloy system.

Cu. Elevated temperature strength increases but elongation decreases by increasing the Cu content. Cu contributes to the formation of Ω and θ' phases, the pre-dominant hardening phases in Al-Cu-Mg-Ag alloys, via diffusion of Cu atoms. Due to a high binding energy between Cu atoms and vacancies in Al-Cu-Mg-Ag alloys, Cu atoms will bond with vacancies during quenching, promoting the diffusion of Cu atoms and hence enhancing the nucleation and precipitation of Ω phases. Consequently, it will raise the alloy strength [71].

Mg. Addition of Mg increases the strength of the alloy. In the ternary Al-Cu-Mg alloys, Mg binds with vacancies and generates a high density of GP zones and θ'' precipitates which will accelerate the precipitation kinetics of the alloys. In the presence of Ag, Mg forms Mg-Ag co-clusters which will promote the formation of the Ω phase by reducing the strain energy associated with the formation of the Ω phase on the {111} matrix plane [60,72,73].

Ag. Ag acts as an effective trap for Mg atoms, forming Mg-Ag clusters which act as precursors to the formation of Ω precipitates. It raises the nucleation kinetics of Mg clusters by decreasing their elastic strain energy during nucleation. This Mg and Ag combine with Cu and segregates to the interface boundary of Al | Ω . By comparing the

atomic radii of Mg – Ag and Al – Cu, the presence of Mg and Ag in the interface reduces the strain that arises from the difference in interplanar spacing in the two phases, stabilising the interface and enhancing the bonding, hence increasing the coarsening resistance of the Ω phase. Ag is only present in the interface boundary of Al | Ω and not within the Ω plate or at the disordered plate peripheries, indicating the presence of Ag is not necessary for the precipitation although it enhances the precipitation kinetics of Ω precipitates [9,49,60,64,67,73,74].

Si. The high binding energy between Si and Mg limits the Mg available for the formation of pre-precipitate Mg-rich clusters along $\{111\}_\alpha$ which act as nucleation sites for Ω precipitates, resulting in a decreasing volume fraction of Ω precipitates. Additionally, the presence of Si shifts the metastable and equilibrium phase boundaries which may lead to the instability of the Ω phase. As a result, the θ' , S and/or σ precipitates formation enhances, whereas the formation of Ω precipitates is limited [62,68,75]

Ti. Addition of Ti up to 0.6 wt.% results in inhibition of the GP zone formation and a lowering of the precipitation temperature of Ω , resulting in the enhancement of Ω precipitates. Finer and denser Ω and θ' precipitates were observed by a Ti addition which leads to increasing tensile strength [76].

TiB₂. Addition of TiB₂ promotes finer grain size in as-cast material which leads to the improvement in yield and ultimate tensile strength, while maintaining the ductility [14,16,26,77].

2.3. TiB₂ in Aluminium Alloys

For decades, TiB₂ has been used widely as a grain refiner in the aluminium industry. It promotes the formation of a fine equiaxed microstructure by suppressing the columnar and twin columnar grain growth [78]. A large grain size provides poor castability and mechanical properties. In contrast, finer grain size leads to the improvement in mechanical properties due to reduction of the size of defects such as micro-porosity and second-phase particles [78].

Several ways exist to introduce titanium and boron to the aluminium melt, such as by a salt mixture of K₂TiF₆ and KBF₄ in which the titanium and boron formed as a consequence of

the reaction of aluminium with salt mixtures and by addition of Al-Ti-B master alloy. In terms of Al-Ti-B master alloys variants, the Al-5Ti-1B master alloy is the most commonly used due to optimum grain refining properties. The presence of 2.8% excess Ti over the stoichiometric ratio of TiB_2 (i.e. 2.2 : 1 in wt.%) in Al-5Ti-1B leads to the formation of Al_3Ti which acts as nuclei for grains, providing a larger fraction of nucleation sites and optimizing the grain refinement [79].

2.3.1. TiB_2 as Grain Refiner in Al alloys

The solidification mechanism of Al in the presence of inoculants is explained by the heterogeneous nucleation in which its nucleation kinetics are influenced by interfacial energy as described in Fig. 2.2. The interfacial energy reaches its equilibrium when

$$\gamma_{lp} = \gamma_{sp} + \gamma_{ls} \cos \theta \quad (2-1)$$

Where γ_{lp} , γ_{sp} , and γ_{ls} are the liquid/particle, solid/particle and liquid/solid interfacial energy respectively and θ is the contact angle. To be amenable to act as a potent nucleation site, the particles should wet the nucleating solid, which means the contact angle has to be as low as possible. This situation can be achieved if γ_{sp} and/or γ_{ls} is low and/or γ_{lp} is high.

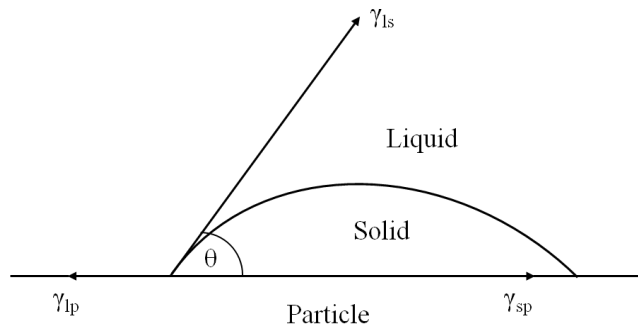


Fig. 2.2. Equilibrium of interfacial energies during heterogeneous nucleation

Several theories were developed regarding the mechanism of grain refinement by addition of TiB_2 in aluminium [80–85]. However, until now, the exact mechanism of grain refinement is still not clear. The grain refinement theory was first described by carbide-boride particle theory which explains that insoluble TiB_2 acts as heterogeneous nucleation sites in the melt. However, by looking at the crystallographic structure of TiB_2 which has hexagonal structures in which does not have any correlation with any crystallographic

planes of the aluminium, the validity of this theory is doubted. Further research which observed that no undercooling was needed to nucleate aluminium with the existence of aluminides, while borides needed some [81,86]; and no orientation relationship between borides and α -Al [87] confirmed the invalidity of this theory. Moreover, the carbide-boride particle theory then indisputably by duplex nucleation theory which was proposed by Mohanty and Gruzleski [85] as they observed the borides are pushed to the grain boundaries and no grain refinement was observed in the absence of Ti solutes. This suggests that the aluminium and borides has a large lattice discrepancy, indicating that borides are a poor nucleant.

Furthermore, another theory called peritectic theory was proposed by Mondolfo [80]. He observed that instead of TiB_2 , Al_3Ti acts as a nucleation site for α -Al via the peritectic reaction ($0.15\% \text{ Ti}$), $\text{L} + \text{Al}_3\text{Ti} \rightarrow \alpha\text{-aluminium}$. This theory was supported by other experimental observations. For example Maxwell and Hellawel [86] observed little or no undercooling during α -Al nucleation in the existence of Al_3Ti as compared to TiB_2 which suggests that Al_3Ti is a more potent nucleant than TiB_2 . Furthermore, experimentation conducted by Davies *et al* [87] observed Al_3Ti in the centre of the grain indicating that Al_3Ti may serve as a nucleant. However, fading effect was observed at the hypoperitectic concentration in which the grain size increases with increasing holding time as the aluminides dissolve [83], indicating poor grain refinement effectiveness. This shows that at the hypoperitectic titanium concentration, Al_3Ti does not act as the nucleation sites for the aluminium, except for the very short holding time. Hence, this theory does not suitable and fails to explain the grain refinement at the hypoperitectic titanium concentration.

Following those, Backerud *et al* [88] and Vader *et al* [89] proposed peritectic hulk theory which identifies Al_3Ti as a better nucleant than TiB_2 . This theory suggested that the borides form a shell around the aluminides, decreases the dissolution rate of aluminides and hence increases the stability of the aluminides. The aluminides will then dissolve and leave a cell of liquid with approximately a peritectic composition [90]. And α -Al is formed by the peritectic reaction. Although this theory is supported by some other experiments, however, some of the aspects in this theory are also questionable. For example, to be amenable to create a sheel around aluminides and slowly dissolve Al_3Ti particles, borides needs to dissolve first in the melt, so that they can reprecipitate on the more slowly dissolving Al_3Ti particles. This seems impossible since borides are very stable in the

aluminium melts, compared to the Al_3Ti , particularly at the hypoperitectic concentration. As has been explained above that fading effect is occurred at the hypoperitectic titanium concentration. Even in the master alloy, the dissolution of Al_3Ti is still quick and it only takes minutes to dissolve it [83]. Furthermore, the observation by Mayes *et al* [91] who identified the existence of TiB_2 at the centre of Al_3Ti particles by TEM studies also opposed this theory. Consequently, the peritectic hulk theory is not valid.

Another theory, hypernucleation theory [92], suggested α -Al nucleated via segregation of Ti atoms to the TiB_2 particles, leading to the formation of a pre-existing solid aluminium with high titanium from which solid aluminium grows. Moreover, it was claimed that the solute elements present in expense to nucleation particles in the alloy affects the grain refinement as proposed by solute theory [86,93]. It was claimed that the presence of solute elements on heterogeneous nucleation tend to restrict the grain growth, allowing more nucleation substrates to be active before recalescence [83,84]. However, there was no significant experiment that can prove the validity of this theory.

Following that, Mohanty and Gruzleski [85] proposed duplex nucleation theory as has been explained above. Among all of the theories which have been explained above, this theory appears as the most attractive one, although it still has some weaknesses. They suggested that during solidification, solute Ti will segregate to the melt/ TiB_2 interface, forming Al_3Ti layer on the surface of the TiB_2 particles. This Al_3Ti layer will then nucleates the grain [85,94]. The existence of the Al_3Ti layer on the surface of TiB_2 particles described in this theory implies that the Ti content in the melt is more than the solubility limit of Ti in the Al, 0.15 % (hyperperitectic), to allow the occurrence of peritectic reaction. However, this theory proposed that Al_3Ti layer was also formed in the interface of TiB_2 and α -Al in the alloys which lied in the hypoperitectic composition. This leads the author of this thesis to the question. They claimed that the evidence for the occurrence of Al_3Ti layer in the hypoperitectic concentrations is based on an extrapolation of observations at the hyperperitectic concentrations, making it as weak evidence. Furthermore, the latest experiments by Fan *et al* [90] which attempted to clarify the grain refinement mechanism observed the existence of a (112) Al_3Ti two-dimensional compound (DC), a Ti-rich monolayer, on the (0001) TiB_2 surface (Fig. 2.3). They identified that the potency of TiB_2 to nucleate the grains was significantly improved by the formation of a monolayer of Al_3Ti DC on their surface.

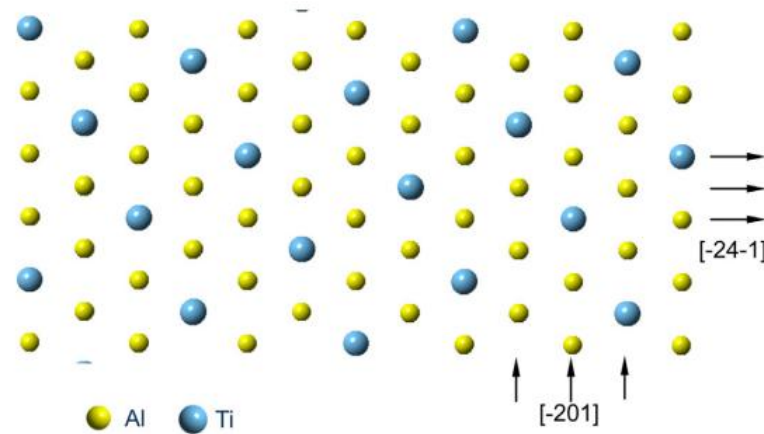


Fig. 2.3. Schematic diagram of the atomic arrangement of Al (lime) and Ti (blue) atoms in the (112) plane of the bulk Al_3Ti intermetallic compound [90]

Although the mechanism of grain refinement by TiB_2 is now still unclear, it is noted that the TiB_2 particle is a good nucleant and the existence of free Ti increases its nucleation potency. To be able to act as an effective nucleation site, an inoculant should have a melting point higher than the alloy being solidified and initiate freezing at very small undercooling. Additionally, a sufficient number of inoculants should be distributed uniformly throughout the material. Other than that, it should be fast acting, which means a short time required to reach ultimate grain size (optimum contact time), and demonstrate insignificant fading during long holding times. In the case of a Al-Ti-B master alloy grain refiner, fading is observed in long holding times due to dissolution of Al_3Ti and agglomeration of TiB_2 particles. Additionally, the existence of certain elements i.e. Cr, Zr, Li and high levels of Si was observed to have an adverse effect on the grain refining efficiency of Al-Ti-B master alloys, which is known as the poisoning effect. It is believed that the reaction between those particular elements and grain refining nucleants causes poisoning. For examples, zirconium present in the alloy was found to form ZrB_2 which coats TiB_2 particles, reducing the nucleation potency of TiB_2 . Furthermore, substitution of titanium in Al_3Ti by zirconium was also reported [79,95].

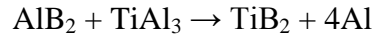
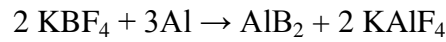
2.3.2. TiB_2 as Reinforcement in Al alloys

TiB_2 has been known as an outstanding reinforcement particle and has been used as a reinforcement in aluminium matrix composites (AMCs) for several decades [24]. In contrast to other particulate reinforcement particles, TiB_2 particles do not react with molten

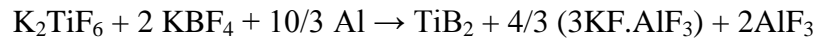
aluminium, preventing the formation of a brittle phase at the interface of reinforcement/matrix. Other reinforcement particles, such as SiC and Al_2O_3 tend to form brittle Al_4C at high temperature and Al_2MgO_4 in the magnesium containing aluminium alloys respectively. Investigation on A356 alloy by Wood *et al* [96] showed that A356- TiB_2 composites exhibited better properties compared to A356-SiC composites even with a much higher volume fraction of SiC. Furthermore, the addition of TiB_2 also gives the increasing wear properties of the aluminium alloys. A 15 vol% of TiB_2 added to Al showed the same wear properties as carbon steel [23]. Mandal *et al* [16] also reported the increasing of wear resistance of Al-4.0Cu by the addition of TiB_2 particles. Furthermore, Siddhalingeswar *et al* [32,97,98], in their research of mushy state rolling of Al-4.5Cu reinforced by 5 wt.% TiB_2 also reported the increment of mechanical properties with addition of TiB_2 . A 7.5 – 10% increment of ageing kinetics as well as higher tensile strength was observed with the addition of TiB_2 particles. Apart from grain refinement, the enhancement of mechanical properties achieved in their study was attributed to the homogeneous distribution of Cu atoms, higher matrix dislocation density produces and thermal expansion coefficient difference between Al and TiB_2 particles.

TiB_2 reinforced AMCs can be produced either by ex-situ or in-situ processes. An ex-situ process is conducted by the addition of TiB_2 powders to the melt, while an in-situ process utilises the chemical reaction between added chemical substances and the aluminium melt to produce TiB_2 . Compared to an ex-situ process, an in-situ process offers stable interfaces between aluminium/ TiB_2 and free impurity, providing strong bonding between them which leads to the higher mechanical properties. For those reasons, most of the TiB_2 reinforced AMCs are produced by an in-situ process, including A20X master alloy, the studied material in this current work.

The production of TiB_2 reinforced AMCs by an in-situ process is developed based on a salt-reaction process to produce Al-Ti-B grain refiner master alloy. It involves the reaction between salt mixtures K_2TiF_6 and KBF_4 , and liquid aluminium. During production of Al-Ti-B master, K_2TiF_6 and KBF_4 react with molten aluminium to produce the intermediate compound 3TiAl_3 and AlB_2 in which the reaction between those compounds results in releasing Ti and B ions into liquid aluminium. The reaction sequences during production of Al-Ti-B master alloys are as follows [99]:



In the in-situ production of TiB_2 AMCs, salts of potassium hexafluorotitanate, K_2TiF_6 , and potassium tetrafluoroborate, KBF_4 , are introduced into a stirred aluminium melt with an atomic ratio in accordance with $\text{Ti}/2\text{B}$. It was proposed that the reaction during in-situ production is as follows [100]:



2.3.2.1. Material A20X

A20X alloy is TiB_2 reinforced AMC developed by Aeromet Int. LTD via an in-situ process. It is a aluminium copper (Al-Cu) based alloy which is a modified version of A201 alloy where the complex castability issues associated with aluminium copper based alloys such as shrinkage porosity, segregation and hot tearing have been eliminated. Those properties have been achieved due to addition of a small amount of Ti particles resulting in alteration of the solidification mechanism of the alloy. The addition of more than 0.15% wt of free Ti not only decreases the grain size by the combination effect of TiB_2 and TiAl_3 particles, but also alters the material solidification behaviour and feeding mechanism resulting in an improvement of castability of this alloy [26].

The addition of more than 0.15 wt% of free Ti to an Al-Cu alloy which contained 4 – 5% TiB_2 allows the formation of TiAl_3 particles. During the solidification process, TiAl_3 particles rapidly nucleate a very large number of aluminium grains. Grain growth is inhibited by the TiB_2 particles as they are pushed to the grain boundaries. As not every TiAl_3 particles will nucleate a grain during the solidification process; the remaining TiAl_3 particles will be engulfed by the advancing growth instead of being pushed. In addition to that, the formation of TiAl_3 particles enables the formation of highly grain refined structures even in slow cooled sections. It means that the grain size obtained is fine enough to allow mass feeding to occur even at slow cooling rates. Consequently, the addition of 0.15 wt% of free titanium facilitates further savings in terms of feed metal, resulting in increases in material yield and increases in material and energy efficiency [11]. However, although the existence of TiB_2 and Al_3Ti particles is beneficial for the as-cast material

properties, it could give some problems during forming as the stress during forming will be concentrated at the particle which could initiate a crack. For this reason, careful control and design of forming parameters have to be maintained. Consequently, owing to this unknown effect of TiB_2 and Al_3Ti particles during forming, particularly in hot working, it is one of the aims of this thesis to optimise the hot working parameters.

This new high strength aluminium cast alloy has been registered at the Aluminium Association as AA205 and designated as AMS4471 for investment casting and AMS4482 for sand casting by AMS Technical Committee “D” and the SAE Aerospace Council. Due to its enhanced properties with a typical yield strength up to 440 MPa, tensile strengths of 500 MPa and elongation of 3 – 5% [101], this alloy can compete with 2000 and 7000 series alloys. The composition of this alloy based on the Aerospace Material Specification (AMS) standard is presented in Table 2.2.

Table 2.2. Chemical composition of A20X alloy based on the AMS standard

AMS Number	Chemical Composition					
	Al	Cu	Ti	B	Ag	Mg
AMS 4471 (A205.0/TiB ₂ /3p-T7P/investment cast)	rem	4.6	3.4	1.4	0.75	0.27
AMS 4482 (A205.0/TiB ₂ /3p-T7P/sand cast)	rem	4.6	3.4	1.4	0.75	0.27

2.4. Hot Deformation

This present section focuses on the deformation mechanisms with regards to the flow stress behaviour. Restoration or softening process occurring during deformation are also explained in this section whereas static softening process occurred during annealing after deformation will be described in the next section. Recovery and recrystallisation occurring during deformation are termed as dynamic recovery (DRV) and dynamic recrystallisation (DRX), respectively, to differentiate them from the static softening processes. Dynamic recovery involves the formation of subgrain/low angle grain boundaries as a result of dislocation climb, cross slip and glide. No new grains are formed during the dynamic recovery process. In contrast, dynamic recrystallisation process involves the formation of new grains originating at the existing high angle grain boundaries. Metal with a high stacking fault energy (SFE) such as aluminium undergoes only dynamic recovery since partial dislocations are very close to each other, allowing rapid dislocation climb and cross

slip [102]. In contrast, metal with low SFE experiences dynamic recrystallisation. However, in very high purity aluminium alloy, dynamic recrystallisation was observed [30].

2.4.1. Flow Stress Behaviour

It is well-known that the workability of a material is characterised by its flow stress. Flow stress can be defined as the stress required for plastically deforming the material [103]. The flow stress of the material can be measured in several ways, such as tension, compression and torsion [104]. Among all of them, compression and torsion tests are widely used to explore flow stress of bulk materials in order to investigate their hot deformation behaviour. Tensile testing is mainly applied for sheet materials and the fact that it experiences severe necking limits its application only to the low strain deformation investigations ($\epsilon \leq 0.3$). In contrast to the tensile test, compression and torsion tests have the ability to carry out the test under large strains which is similar to those in metal working. Thus it produces a representative microstructure as in metal working. Compared to the plane strain compression test, a torsion test allows flow stress identification at larger strains which enables them to simulate multistage rolling up to 20 passes ($\epsilon \geq 5$) whilst a compression test is only limited to less than half that ($\epsilon \leq 1.5$) due to friction [104,105]. However, it is difficult to get uniform strains by a torsion testing. On the other hand, it requires complex equipment as well as stress calculation which then further restricts its applications. Considering those reasons and available equipments in our laboratory, compression tests were conducted in this study to examine the flow stress behaviour of the studied materials. Although compression testing experiences barrelling phenomena because of friction, the use of proper lubrication is able to eliminate this problem and could extend its application up to a strain of 2.0 [27].

The behaviour of material during high temperature deformation can be analysed from the flow stress curve resulting from the test. However, it should be supported by microstructure examination in order to avoid misleading conclusions. Materials undergoing dynamic recovery exhibit a rise to a plateau followed by a steady state flow stress as seen in Fig. 2.4a. At the initial stage of deformation, dislocation density rises significantly. At this point, the rate of work hardening exceeds dynamic softening which leads to the rapid increase in flow stress. The increment of dislocation density provides a high driving force for the recovery so that the rate of recovery increases. During this period, low angle

boundary microstructures and subgrains are formed. As the deformation progresses, the rate of work hardening and recovery will reach a dynamic equilibrium at a certain strain and the dislocation density will remain constant. Consequently, a steady-state flow stress is obtained [30].

In the case of dynamic recrystallisation, the stress-strain curve generally shows a broad peak instead of plateau as it appears in the materials which experience only dynamic recovery (Fig. 2.4b). Under deformation at high temperature and low strain rates, materials which undergo dynamic recrystallisation might reveal multiple peaks at the low strain in their stress-strain curve as shown in Fig. 2.4b. Furthermore, it is of important to analyse critical deformation/strain (ϵ_c) in dynamic recrystallisation as it indicates the initiation of recrystallisation. This critical strain (ϵ_c) takes place prior to the peak stress (σ_p) of the stress strain curve. Generally, the value of critical strains tends to decrease progressively with decreasing stress, although the enhancement of critical strain rate might occur again under low strain rates during creep testing [30].

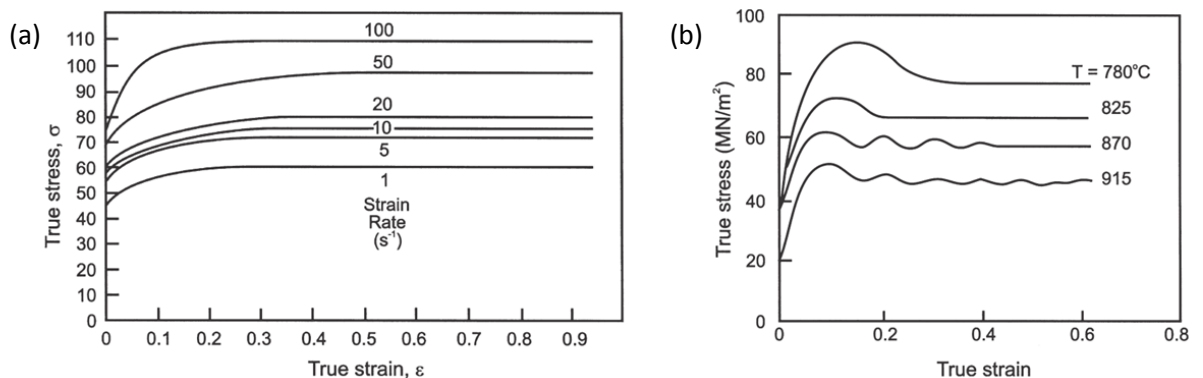


Fig. 2.4. Stress-strain curves for (a) Al-1% Mg at 400 $^{\circ}C$ which undergo dynamic recovery and (b) 0.68%C steel deformed at $\dot{\epsilon} = 1.3 \times 10^{-3} s^{-1}$ which undergo dynamic recrystallisation [30]

2.4.2. General Characterisation of Deformed Microstructures

The evolution of microstructure during deformation involves the generation and migration of dislocation loops and subsequent interaction as well as storage and recovery of dislocations. As described above that due to the high SFE of Al, dynamic recovery (DRV) is more likely to occur in aluminium. Similar to static recovery (SRV), the DRV process is

characterised by the formation of low angle boundaries which leads to the formation of subgrains. Rearrangement of dislocations happened during dynamic recovery results in more organised dislocations within the subgrain boundaries. The difference between SRV and DRV is that the applied stress during deformation induces an additional driving force for the movement of dislocations at low angle grain boundaries. Those of the opposite sign will migrate to the opposite direction leading to dislocation annihilation in the opposing boundaries and triple-junction boundary interactions [30]. That phenomenon allows the subgrains to remain equiaxed during deformation. As the deformation temperature increases, the subgrains formed increase in size and become more equiaxed and sharper. Apart from dislocation migration, subgrain might also reorient themselves during hot deformation. Observation with X-ray diffraction confirmed that they were misoriented by a few degrees about a common grain orientation [106]. This indicates that subgrain boundaries are transient features which repeatedly rearrange.

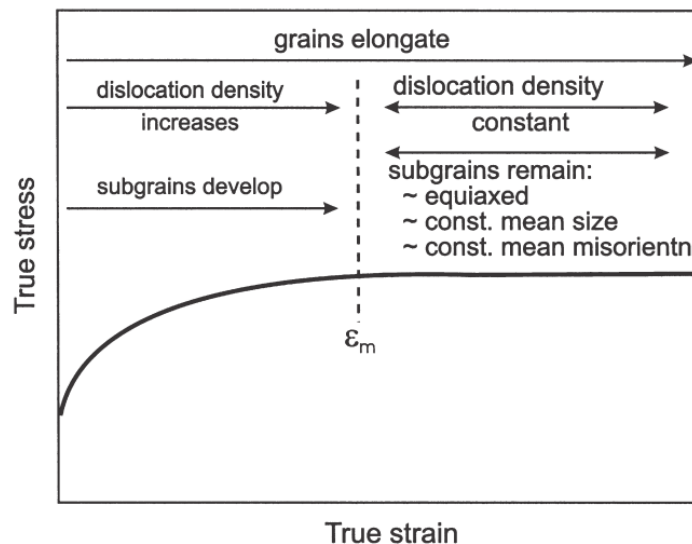


Fig. 2.5. Summary of microstructure evolution during dynamic recovery

The evolution of microstructure during dynamic recovery is summarised in Fig. 2.5. As both work hardening and dynamic recovery take place during hot deformation, repetitive formation and elimination of subgrain boundaries occur. As a result, the density of unbound or ‘free’ dislocations in subgrains will keep constant, leading to the steady state. It is noticed that the subgrain structure usually reach its steady state after a strain of 0.5 to 1 [30]. This subgrain structure determines the flow stress and can be defined by Z , thus:

$$d_s^{-1} = a + b \log Z \quad (2-2)$$

where d_s is a subgrain size, a and b are material constants.

Along with the formation of subgrain structures as a result of the dynamic recovery process in hot deformation, serrations can appear along the grain boundaries (GBs). This mainly occurs because of the grain boundary migration. Tension on the substructure's boundaries and variation of local dislocation density created during hot deformation will force grain boundaries to migrate for a short distance; resulting in serrated GBs (Fig. 2.6a). Subgrain size (which is influenced by temperature and strain rate) and the alloying elements in the alloy will affect the occurrence of serrations. Grain boundary serrations are not observed in the materials containing second phase particles because local GBs migration is inhibited by the second phase particles as shown in figure Fig. 2.6b.

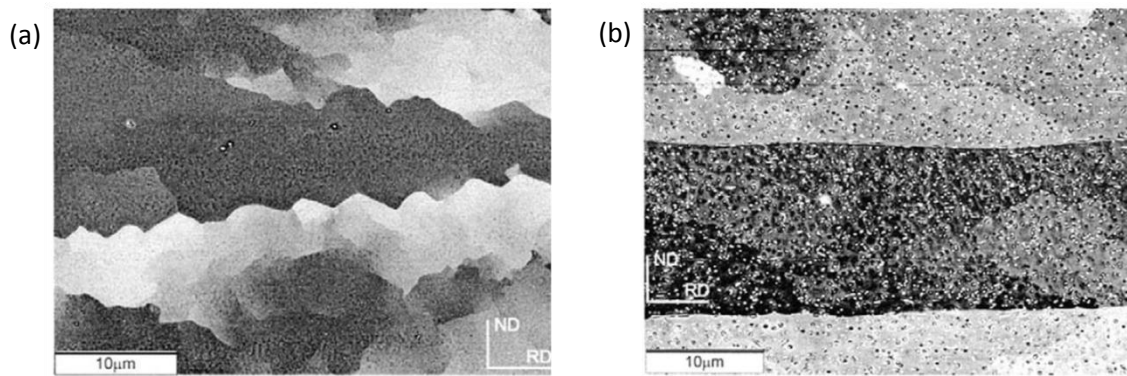


Fig. 2.6. High angle boundaries in compressed specimens of aluminium alloy deformed at 400°C (a) showing serration of high angle grain boundaries in Al-5 wt.% Mg and (b) planar grain boundaries due to the existence of second phase particles which hinder serration formation in Al-2 wt.% Cu [30]

If the material is subjected to a large strain, the formation of grain boundary serrations can lead to what is referred to as geometric dynamic recrystallisation (GDRX) [30,107,108]. When a large strain is applied to the material, the original grains become elongated as shown in Fig. 2.7. As the strain increases, the original grains become thinner and the serrated GBs come close to each other (Fig. 2.7a). The subgrain size will remain constant since it is independent of strain. At the some point, the serrations of opposite boundaries can come into contact which leads to the separation of the original grains by high angle grain boundaries which appears as equiaxed grains. Since the formation of these high angle

equiaxed grains does not occur by the nucleation of new stress-free grains, this process does not correspond to dynamic recrystallisation [30].

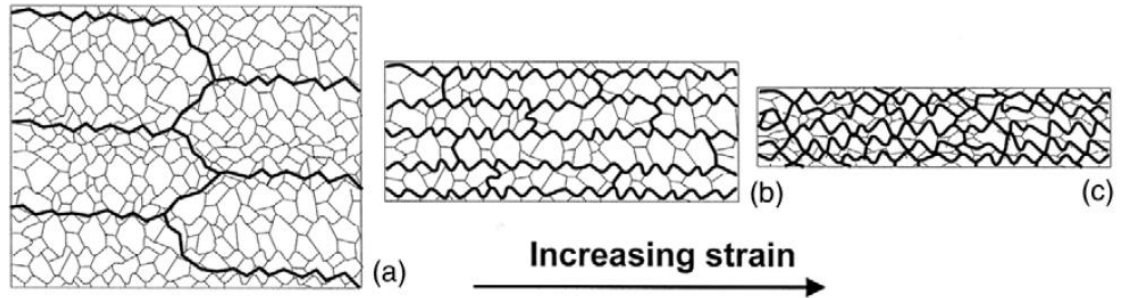


Fig. 2.7. Schematic illustration of geometric dynamic recrystallisation (GDRX). Serrated high angle grain boundaries (HAGBs) become closer as deformation progresses while subgrain size remains constant. At some point, impingement of HAGBs occurs, resulting in high angle equiaxed grains [30]

The existence of geometric dynamic recrystallisation (GDRX) will be influenced by the size of original grain (D_0) and deformation conditions. It is known that under deformation, the final grain thickness in the normal direction (H) will depend on the strain (ϵ) and the initial grain size (D_0), which can be calculated as

$$H = D_0 \exp(-\epsilon) \quad (2-3)$$

If we assume that the pinching off the grain during GDRX occurs when the subgrain size (d_s) is equal to the grain thickness (H), then the critical compressive strain (ϵ_{cr}) for the GDRX can be defined as

$$\epsilon_{cr} = \ln\left(\frac{K_1 D_0}{d_s}\right) \quad (2-4)$$

where K_1 is a constant of the order of unity.

The critical compressive strain (ϵ_{cr}) for GDRX can also be calculated in terms of flow stress, which is

$$\epsilon_{cr} = \ln(\sigma D_0) K_2 \quad (2-5)$$

where K_2 is the material constant.

Furthermore, the occurrence of GDRX also depends on the strain rate and temperature of deformation, which means the Zener-Hollomon parameter. GDRX does not occur until large strain when the materials are deformed at high Z (high stresses) since the subgrain size is small, whereas at low Z (low stresses), GDRX occurs at smaller strains [30]. The relationship between GDRX and Z can be calculated as

$$\varepsilon_{cr} = \ln \left(Z^{\frac{1}{m}} D_0 \right) + K_3 \quad (2-6)$$

In contrast to GDRX, new grains are formed during dynamic recrystallisation (DRX), which is also known as discontinuous dynamic recrystallisation, as a result of very high boundary mobility. The DRX process normally initiates from the old grain boundaries which is described schematically in Fig. 2.8a. New grains are nucleated at the boundaries of the growing grain (Fig. 2.8b). As the process continues, a thickening band of recrystallised grains as shown in Fig. 2.8c is formed. If the initial grain size (D_0) and recrystallised grain size (D_R) are significantly different, a ‘necklace’ structure of grains may be formed (Fig. 2.8b-c) and finally the material will become fully recrystallised (Fig. 2.8d). In contrast to static recrystallisation, grain growth does not occur in the dynamic recrystallisation process and the mean size of dynamically recrystallised grains remains constant as recrystallisation continues [30].

The existence of large second phase particles in the material affects the DRX process as it may act as a stimulant/nucleus for DRX (particle stimulated DRX). Dislocations accumulated at the particles during deformation will induce the formation of small highly misoriented grains next to large second-phase particles. This will only occur if the materials contain large particles and are deformed at lower temperatures with high strain rates (high Z). In addition to that, rotation of subgrains which are located adjacent to the pre-existing grain boundaries might occur during straining, leading to the formation of new grains with high angle grain boundaries. This phenomenon is called rotation recrystallisation [30].

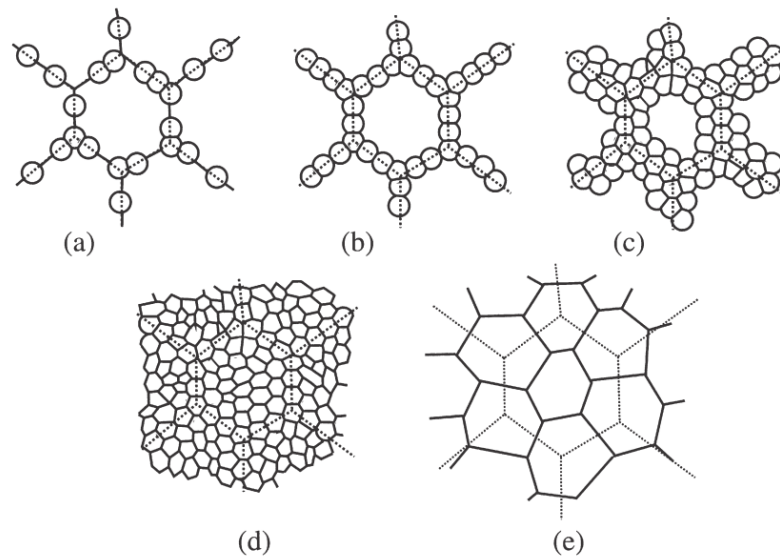


Fig. 2.8. Schematic illustration of microstructure evolution during dynamic recrystallisation. (a) - (d) Large initial grain size, (e) small initial grain size. The dotted lines show old grain boundaries [30]

2.4.3. Processing Map

There were two motivations in developing a processing map; one is to evaluate the effect of processing parameters such as flow stress, temperature, strain rate and strain on the microstructural evolution. Another one is to integrate the process simulation using a finite element model which is developed based on the mechanics of large plastic flow with material behaviour [109,110]. Industrially, a processing map is useful to analyse a manufacturing process such as optimise the process parameters, control the product properties and avoid defects such as edge cracks and internal cavities.

The map was first developed by Frost and Ashby [111,112], known as a Deformation Mechanism Map, by plotting normalised stress vs. homologous temperature showing the dominant area of each flow mechanism. The Deformation Mechanism Map was fundamentally developed to evaluate creep mechanisms; hence it is applicable only for lower strain rates. Following that, Raj [38,42] extended the concept of Ashby's map to construct a processing map by considering strain rates and temperature as direct variables, allowing higher strain rates to be evaluated. The map is constructed using the Dynamic Materials Model (DMM). DMM was developed based on the fundamental principals of continuum mechanics, physical system modelling and irreversible thermodynamics [109].

In this model, the work piece which undergoes hot deformation is considered as a nonlinear dissipater of power. It means that during deformation, the work piece will dissipate a power and no significant energy will be stored. Furthermore, its response to the deformation variables such as strain, strain rate and temperature is considered to be nonlinear [109].

The instantaneous power dissipated at a given strain rate is considered as two parts: G co-content, representing the temperature rise, and J co-content (Fig. 2.9a), representing dissipation through metallurgical processes [36]. The total power (P) of those can be calculated as:

$$P = G + J = \bar{\sigma} + \dot{\epsilon} \quad (2-7)$$

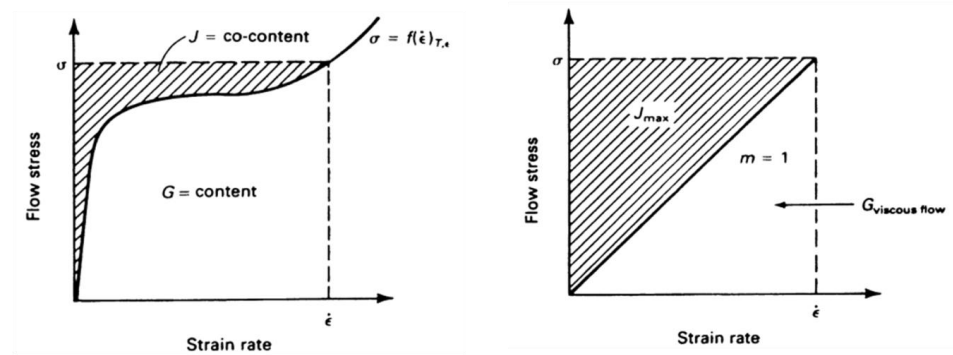


Fig. 2.9. Schematic illustration of the constitutive relation of material system as an energy converter (dissipater) where in the general case, material systems are considered as (a) nonlinear energy dissipater, and in this particular case, material system is considered as (b) linear energy dissipater [42]

The value of power partitioning between G and J is dependent on the constitutive flow behaviour of the material and is defined by the strain rate sensitivity (m) of flow stress since:

$$\frac{dJ}{dG} = \frac{\dot{\epsilon} d\bar{\sigma}}{\bar{\sigma} d\dot{\epsilon}} = \frac{\dot{\epsilon} \bar{\sigma} d \ln \bar{\sigma}}{\bar{\sigma} \dot{\epsilon} d \ln \dot{\epsilon}} \approx \frac{\Delta \log \bar{\sigma}}{\Delta \log \dot{\epsilon}} = m \quad (2-8)$$

And thus m is a power partitioning factor. At a given temperature and strain, the instantaneous value of J co-content can be evaluated by:

$$J = \int_0^{\bar{\sigma}} \dot{\bar{\epsilon}} d\bar{\sigma} = \frac{\bar{\sigma} \dot{\bar{\epsilon}} m}{m + 1} \quad (2-9)$$

The value of J reaches its minimum when $m = 1$ (Fig.2.8b). Consequently,

$$J_{max} = \frac{\bar{\sigma} \dot{\bar{\epsilon}}}{2} \quad (2-10)$$

This leads to the chief measure of the power dissipation capacity of the material, the dimensionless parameter called efficiency of power dissipation, η :

$$\eta = \frac{J}{J_{max}} = \frac{2m}{m + 1} \quad (2-11)$$

A deformation process has to be conducted on the area where the maximum efficiency of power dissipation occurred in order to prevent structural instabilities such as flow localization. Those microstructural instability regions (Fig. 2.10) are discovered by mapping the instability parameter $\xi(\dot{\epsilon})$, which can be calculated as

$$\xi(\dot{\epsilon}) = \frac{\partial \ln[m/(m + 1)]}{\partial \ln \dot{\epsilon}} + m < 0 \quad (2-12)$$

Thus by combining the power dissipation map, which reveals the safe processing regimes, and the instability map, which defines the boundary of safe processing parameters, a processing map is established. Figure 2.9 shows an example of a processing map of 2124-SiC_w composites. There are several areas in the processing map in which is used for interpretation of the processing map, including the dynamic recrystallisation (DRX), superplastic, wedge cracking and adiabatic shear bands domain. The DRX domain generally has maximum efficiency of dissipation about 30 – 35% for low SFE materials, 40% for medium SFE materials and 50 – 55% for high SFE materials. The superplastic domain is characterised by a high efficiency of power dissipation of about >60% and a sharp increasing of efficiency with declining strain rate which is characterised by closer contour in the processing map [109]. The processing map defines dynamic recovery (stable flow) and dynamic recrystallisation as safe deformation regimes which are free from microstructural defects or flow instability.

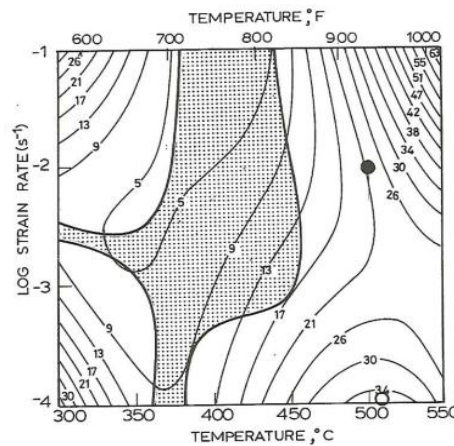


Fig. 2.10. Processing map of 2124/SiC_w composites shows percentage of power dissipation efficiency represented as a contour number. The shaded area indicates flow instability whereas the rest area corresponds to optimum parameter. The filled circle shows the condition where the extrusion process is conducted [42]

2.5. Recovery and Recrystallisation after Deformation

This current section focuses on the static annealing processes which occur during heat treatment after deformation. A recovery process can be defined as microstructural changes occurring prior to recrystallisation in which the properties are partially restored to the original value prior to deformation [30]. Recovery process occurs homogeneously throughout the whole of the microstructure, whereas primary recrystallisation involves the formation of a new strain-free grains only in a certain areas of the microstructure and this recrystallised grain will grow much larger than the rest of the microstructure (Fig. 2.11b). For this reason, primary recrystallisation is also known as ‘discontinuous recrystallisation’ in order to distinguish it from ‘continuous recrystallisation’ which involves the formation of fine-grained microstructure consisting of high angle grain boundaries (HAGBs). This continuous recrystallisation process typically occurs at a large strain and elevated temperature with a low initial grain size (Fig. 2.11c) to induce a high density of HAGBs. The difference between both processes is that continuous recrystallisation does not involve any ‘nucleation’ and ‘growth’ of recrystallised grains, and the end result is same as the recovered microstructure as shown in Fig. 2.11a.

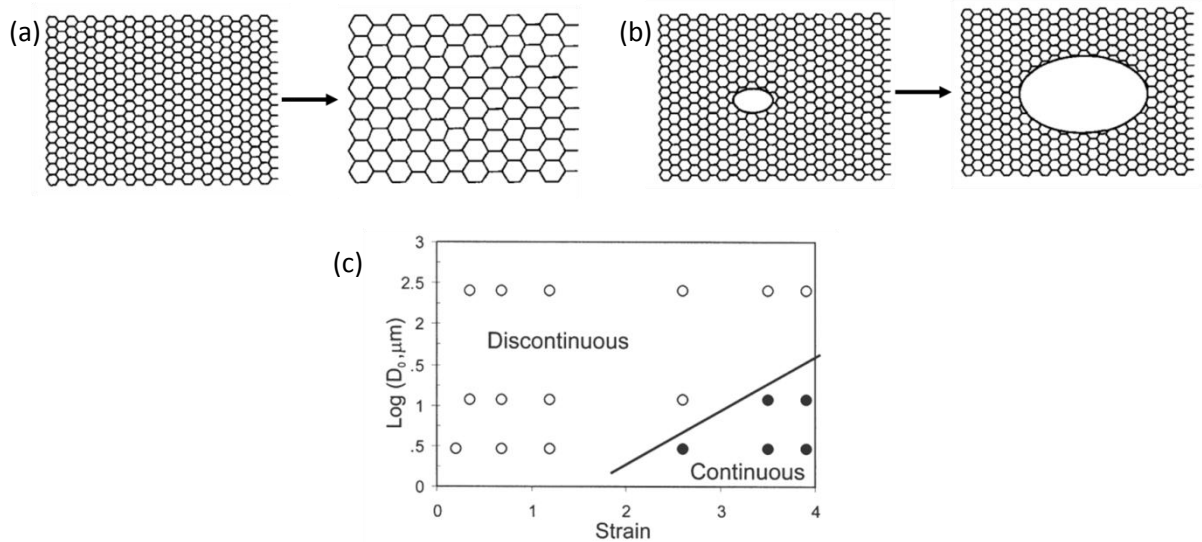


Fig. 2.11. Microstructure evolution during annealing (a) recovery process (or continuous recrystallisation process if the grains consist of HAGBs), (b) primary or discontinuous recrystallisation process and (c) transition between discontinuous and continuous recrystallisation processes [113]

2.5.1. General Theory of Recovery and Recrystallisation

Recovery and recrystallisation occurred during annealing are termed as static recovery (SRV) and static recrystallisation (SRX) respectively in order to distinguish them between dynamic processes. Static recovery involves a dislocation mechanism which consists of a rearrangement of statistically stored dislocations into a lower energy more regular configuration. In contrast to dynamic recovery, the dislocation mechanism in static recovery is only driven by the internal stress of the substructures. It should be highlighted that static recovery involves no HAGBs migration.

Static recovery is characterised by two phenomena of microstructural evolution which includes polygonisation and a growth of subgrains [30,102]. The term polygonisation refers to the arrangement of dislocations into regular form of lower energy configurations or low angle grain boundaries (LAGBs). In the case of large strain deformation which leads to dislocation tangles formation, annealing induces the formation of subgrains. The mechanism of subgrain formation involves dislocation annihilation and reorganisation into a more stable structure of lower energy or LAGBs. The typical steps of the recovery process on the large strain deformed materials containing dislocation tangles includes a) cell formation, b) annihilation of dislocations within the cell interior by incorporating them

in the cell walls, c) subgrain formation and d) subgrain growth. The sequence of these steps depends on the material and processing parameters during deformation and annealing. In the materials which experience dynamic recovery during deformation in which subgrain structures are already well developed after deformation, annealing will then lead to coarsening of subgrain structures. Some of the material properties that favour dynamic recovery include high stacking fault energy which accelerates dislocation climb and low solute content which minimises dislocation pinning. Furthermore, large deformation strains which increase stored energy and driving force for recovery and high deformation temperatures also induce subgrain formation during deformation.

It is relatively complex to measure recovery kinetics since it involves several concurrent atomistic mechanisms and it can only be described by using empirical relationship [30]. Subgrain growth, on the contrary, can be predicted by considering the initial subgrain size and annealing time with equation

$$D^n - D_0^n = c_1 t \quad (2-13)$$

where n is a constant, c_1 is a temperature-dependent rate constant and D_0 is the initial subgrain size at $t = 0$ (before annealing). The subgrain growth of deformed materials is driven by the energy stored in the deformed state, whereas the rate of its growth is influenced by the existence of pinning particles. Furthermore, subgrains' coarsening also depends on the local texture. If the surroundings subgrain have a similar orientation, it limits the boundary mobility and hence decreases subgrain growth. The subgrain misorientation during annealing also depends on the orientation in the microstructure in which higher orientation gradients induces higher boundary mobility leading to the formation of subgrains with higher misorientation average [30].

The common discontinuous recrystallisation (dSRX) or also known as primary recrystallisation is associated with the formation of a new dislocation-free grain structure in a deformed material by the development and migration of HAGBs which are induced by the stored energy of plastic deformation [114]. Recrystallisation occurs in a competition with recovery as the driving force for both of them originates from the same source; the stored energy resulting from deformation in the form of dislocations or LAGBs. Two conditions need to be fulfilled in order to induce dSRX, which are 1) the presence of a mobile high-misorientation boundary or rearrangement of defects and 2) higher driving

force in order to allow boundary migration rather than retarding forces due to particle pinning or segregation [102]. Those conditions will depend on the material properties, deformation conditions and annealing temperature. In general, a low annealing temperature allows recovery at the expense of recrystallisation. Recrystallisation process can be described as a function of annealing time, t , by

$$X_v = 1 - \exp(-kt^n) \quad (2-14)$$

Where X_v is the volume fraction of recrystallised grains, k and n is the constant [115].

2.5.2. Nucleation of Recrystallisation

Nucleation of recrystallisation during annealing is dependent on several factors such as the strain applied during deformation, the existence of second-phase particles and the annealing temperature. Generally, to enable a nucleus to grow and become a recrystallised grain, there has to be an orientation gradient to allow the formation of HAGBs and a high driving force to overcome the pinning pressure of fine particles. Additionally, the presence of a special orientation relationship between the nucleus and surrounding matrix induces migration of the recrystallisation front by increasing its mobility [30].

Nucleation for recrystallisation can be originated from several nucleuses such as GBs, transition bands, shear bands and second-phase particles [30]. In the two-phase aluminium alloy, the existence of second phase particles which may be in the form of dispersed particles present during deformation or precipitates during subsequent annealing as well as ceramic reinforcement in the MMCs play an important role during recrystallisation on the subsequent annealing following deformation. It is their volume fraction, size, shape and spacing which define recrystallisation behaviour [30].

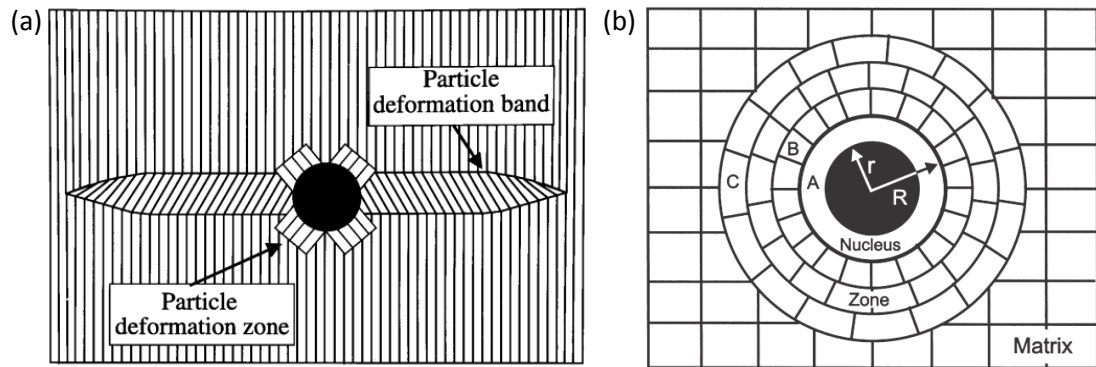


Fig. 2.12. Schematic illustration of (a) deformation structure at large second-phase particles [114] and (b) growth of nucleus within deformation zone [30]

In the materials containing second-phase particles larger than $1\mu\text{m}$, particle stimulated nucleation (PSN) mechanisms normally occur. PSN is also found on slightly smaller particles if they are clustered and deformed at high strain rates [30]. During deformation, a high dislocation density and large orientation gradient are created around the particles. These will then act as nucleation sites for recrystallisation. Furthermore, a deformation zone is formed in the vicinity of the particle and it extends from the particle surface for a distance about one particle diameter. The orientation of these deformation zones may also be altered about 10 degrees from the adjacent matrix. Apart from that lattice misorientation, it is found that small deformation bands (particle deformation bands or PBDs) which can extend to a distance of more than ten particle diameters may be formed at the particles (Fig. 2.12). These bands are developed by the interaction of the particle with the surrounding matrix, which then rotate towards stable orientations during deformation [114]. It is noted that the recrystallised grain will not grow beyond the deformation zone unless the critical particle size is exceeded. Normally, only one grain nucleates in the deformation zone, although it may be possible to have more than one nucleus if the particle size is very large.

In the PSN mechanism, nucleation of a new grain does not necessarily occur at the particle surface (Fig. 2.12b~ A), but it also can be originated at the pre-existing subgrain within the deformation zone, either in the centre of the zone (Fig. 2.12b~ B), or at the periphery (Fig. 2.12b~ C). The mechanism involves rapid migration of subgrain boundaries within the deformation zone which leads to the formation of a HAGB due to a large orientation gradient. The growth of the grain may stop when the deformation zone is consumed.

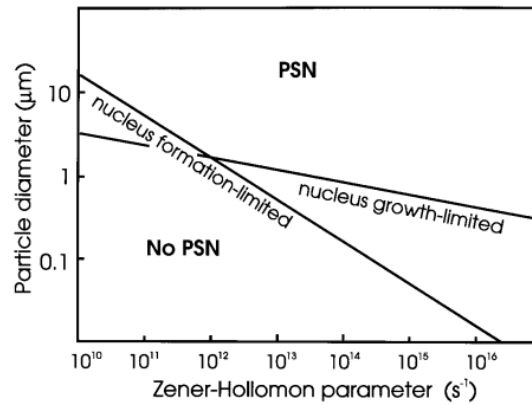


Fig. 2.13. The effect of deformation conditions on PSN [114]

PSN occurs if the temperature in which the deformation occurs is below a certain temperature and the strain rate during deformation exceeds a minimum value [30]. These conditions prevent the plastic strain relieving on the particle/matrix interface occurring via diffusion and hence minimise substructure's recovery. In reverse, the presence of particles induces a high dislocation density during deformation, producing a high driving force for recrystallisation. Fig. 2.13 explains how deformation conditions in terms of temperature and strain rate affected the PSN. Furthermore, PSN is also controlled by the total strain, annealing temperature and presence of second phases. The presence of large particles in the materials as well as high annealing temperature and high strain will favour PSN.

Another important factor that influences the efficiency of PSN is the distribution of second-phase particles. High efficiency nucleation occurs in the materials containing large, widely spaced particles. Whereas, in the materials containing closely spaced particles or if growth of nuclei is affected by a fine dispersion of particles, the nucleation efficiency tends to decrease. In the case of bimodal particle distribution, as the material studied in this present research which contains both large particles Al_3Ti and small particles TiB_2 , the PSN efficiency will depend on the driving pressure (P_D) and Zener Pinning pressure (P_Z). The large particles will act as nucleation sites, whereas the small particles whose spacing is close enough tend to pin boundary migration. This pinning effect within deformation zones around coarse particles due to the existence of small particles will alter the critical particle size for nucleation and the final recrystallised grain size. Under this condition, the critical particle size for nucleation is defined by:

$$d_g = \frac{4\gamma_b}{P_D - P_Z} \quad (2-15)$$

where γ_b is the stored energy, P_D is the driving pressure and P_Z is the pinning pressure.

In addition to PSN, nucleation can also occur via a strain induced boundary migration (SIBM) mechanism. This mechanism is mainly found after low strain deformation or high temperature deformation. SIBM involves the formation of bulging on the prior grain boundary due to the difference in dislocation content (or stored energy that involves subgrain size) between two sides of a HAGB. Once the concave boundary is formed, the region behind the migrating boundary will have a lower dislocation density [30]. Furthermore, since the bulged boundary is formed on the pre-existing boundary, the orientation of new recrystallised grain will be similar with the old grains from which they have grown.

There are two forms of SIBM mechanism, which are single subgrain SIBM and multiple subgrain SIBM. Single subgrain SIBM happens in the materials whose subgrain structure is well recovered in which the stored energy between two grains is somewhat similar. Hence, in single subgrain SIBM, the existence of stored energy difference between two grains is not necessary, but the existence of subgrain with critical size in the vicinity of grain boundary. The subgrain size, subgrain size distribution and the boundary energies of the subgrain in two grains will then define single subgrain SIBM. This single subgrain SIBM mechanism does not involve any substructure drag as illustrated in Fig. 2.14a. On the other hand, the multiple SIBM mechanism involves several subgrains (or a large number of dislocations) in which the bulging boundary on the concave side is connected to the lower side of the advancing high angle grain boundaries (HAGB) or low angle boundaries. The driving force of the bulging formation in multiple SIBM is driven from the dislocation content difference across the boundary. This particular mechanism is characterised by the existence of some substructure and a low dislocation density as shown in Fig. 2.14b [30]. As the bulge enlarges which means that the area of the boundary is raised, the dislocation or the length of the boundary connected to the concave boundary remains steady. Consequently, the restraining force on the bulging boundary due to substructure pressure is decreased. Moreover, the SIBM mechanism is influenced by the subgrain misorientation and size on each side of the HAGB as they will define which preferred SIBM mechanism will occur. If the subgrain misorientation is higher than 1° and

the grains have similar stored energy, the single SIBM mechanism occurs. On the contrary, if the subgrain misorientation is lower than 1° or the poor dislocation cells are formed, multiple SIBM occurs. In the case of second-phase particles present in the materials, multiple SIBM is favoured since those particles will pin the boundary leading to the increment in driving pressures.

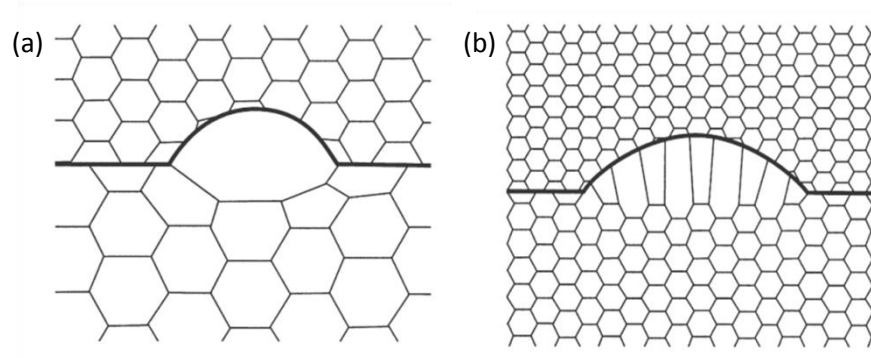


Fig. 2.14. SIBM mechanism illustration (a) single-subgrain SIBM and (b) multiple-subgrain SIBM

It is worth noting the effect of precipitates during recrystallisation considering the material studied in this present research is based on the Al-Cu-Mg-Ag alloys which have a high tendency of precipitation to occur. In the alloy in which involves precipitation process, the situation is very complex since the recrystallisation may occur in parallel with precipitation. The interaction between precipitation and the recrystallisation process during annealing (with fast heating to annealing temperature) is described in a TTT diagram as shown in Fig. 2.15.

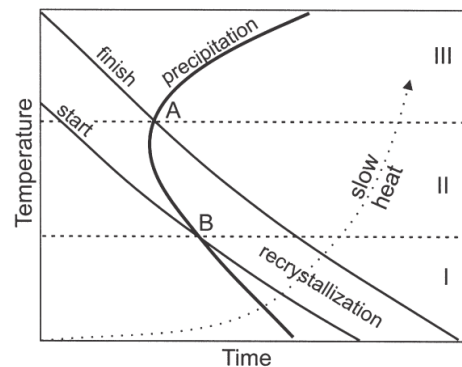


Fig. 2.15. Schematic TTT diagram for recrystallisation and precipitation in supersaturated aluminium alloys with fast heating to the annealing temperature [30]

In the materials in which the subsequent annealing may involve a precipitation process, the behaviour of recrystallisation can be divided into three regions. Region I, where significant precipitation has occurred before recrystallisation ($T < T_B$), the recrystallisation is inhibited. The precipitates formed will pin the high and low angle boundaries, retarding recrystallisation. Prolonged heating at the annealing temperature will induce particle coarsening or transformation to the equilibrium phase which can lead to recrystallisation at the HAGBs, deformation heterogeneities or large second-phase particles. This recrystallisation occurs via broad front SIBM (Fig. 2.16) in which bulging occurs on the HAGB regions consisting of less precipitates. These nuclei grow along the deformation direction (e.g. rolling direction) until their boundaries meet. And finally, the recrystallised grains are formed and separated by a LAGB. These types of recrystallised grains can reach several hundred micrometers in length.

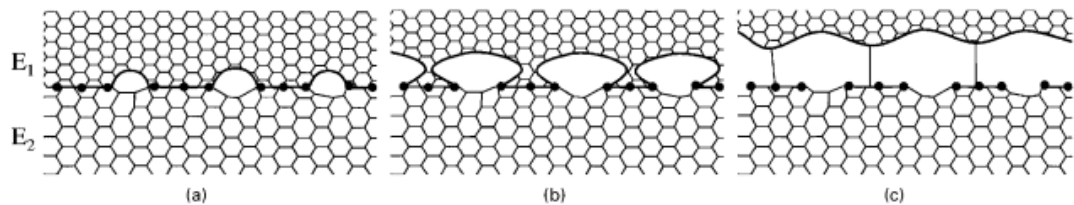


Fig. 2.16. Schematic illustration of broad front SIBM sequences where (a) bulging initiates at HAGBs where there is little precipitation, followed by (b) formation of grains due to boundary migration and finally (c) recrystallised grains join up and are separated by low angle grain boundaries [116]

The recrystallisation behaviour in Region II ($T_A > T > T_B$) involves the precipitation and recrystallisation at the same time. Recrystallisation in this region is strongly dependent on the annealing temperature. At the temperature right above T_B , only a small number of recrystallisation existed, however, at higher temperature, recrystallisation is dominated and it may reach full recrystallisation as the temperature reaches T_A . In the Region III where $T > T_A$, recrystallisation occurs prior to the precipitation and hence the second-phase particles has no influence in this recrystallisation mechanism. Discontinuous recrystallisation similar to a single phase alloy occurs in this region [30].

2.5.3. Zener Pinning

The existence of second-phase particles and/or fine particles in the microstructure plays an important role during recrystallisation as their existence on the GBs results in the inhibition of grain growth and recrystallisation due to grain boundary pinning. Many theoretical studies have investigated the grain boundary pinning effect, however, most of the studies which explain grain boundary pinning are based on the theory developed by Zener. Zener approaches grain growth inhibition in which the pinning force exerted by spherical particles on a randomly positioned grain boundary is equated with the grain boundary curvature force for grain growth [117,118]. The maximum Zener pinning pressure when the particle is in contact with a boundary is given by

$$P_Z = \pi r \gamma \quad (2-16)$$

where r is the radius of the pinning particle and γ is the surface energy per unit area of boundary [117,119,120]. The number of particles which interact with a grain boundary (n_s) can be calculated as

$$n_s = \frac{3V_f}{4\pi r^2} \quad (2-17)$$

Hence, the Zener pinning pressure can be defined as

$$P_Z = n_s P_Z = \frac{3V_f \gamma}{2r} \quad (2-18)$$

where V_f is the volume fraction of the particles.

The driving force for the grain growth was assumed to be $2\gamma/R_0$. This force, however, relates to a contracting spherical surface with no attached interfaces [119]. Hence, the critical maximum grain radius where the grain growth would be entirely suppressed:

$$R_C = \frac{4r}{3V_f} \quad (2-19)$$

Zener pinning is influenced by several factors such as particle size, strength, shape, coherency and distribution. For example, the shape of particles affects the local pinning pressure when in contact with a boundary. The pinning force decreases with increasing

aspect ratio when the elongated particles meet the boundary with their long axis perpendicular to the boundary plane (Fig. 2.17~ case 1). On the other hand, when the elongated particles and boundary are in contact with the long axis of particles facing the boundary, the pinning pressure increases with increasing aspect ratio (Fig. 2.17~ case 2) [117].

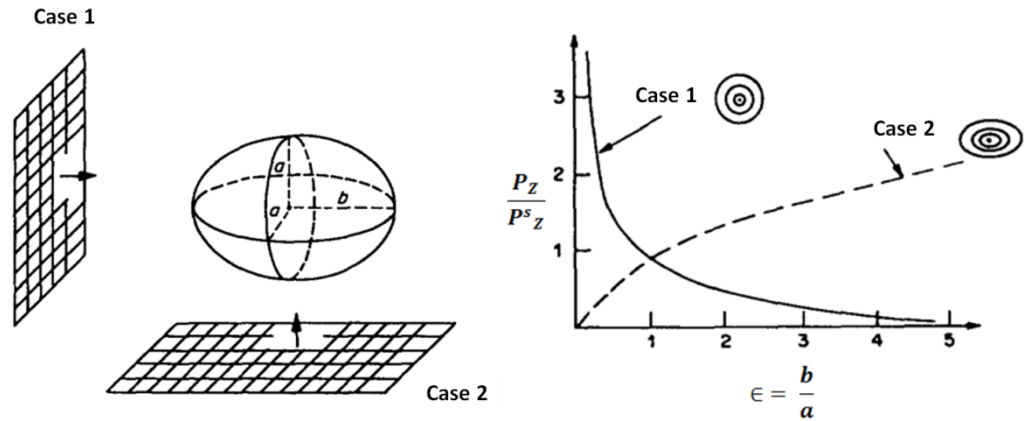


Fig. 2.17. Schematic illustration of elongated particles interaction with boundary and its effect on the pinning pressure with aspect to the ratio [117]

2.6. Superplasticity

Superplasticity is defined as the ability of materials to undergo very large tensile strains prior to failure under a specific range of deformation condition [121,122]. It is characterised by the formation of fine-stable grain size (5 – 15 μm) when the materials are deformed at temperature $\geq 0.5 T_m$ (in degrees Kelvin) with slow strain rates, usually in the range of $10^{-4} \text{ s}^{-1} - 10^{-2} \text{ s}^{-1}$ [102]. In general, materials which undergo more than ~200% elongation under uniaxial tension are considered as superplastic materials, although some researchers proposed a different number, such as Langdon [123] and Pilling with his co-workers [124] who proposed that superplasticity should be nearer 400% and exceeding 800% at hot working temperatures, respectively. Nevertheless, it should be highlighted that elongation depends on the specimen geometry and the cavitations formed during superplastic forming may lead to premature failure.

Strain rate plays an important role during deformation as it strongly affects the flow stress of superplastic materials. The relationship between the strain rate and flow stress is described with a constitutive equation

$$\sigma = k\dot{\epsilon}^m \quad (2-20)$$

Where σ is the flow stress, k is a constant, $\dot{\epsilon}$ is strain rate and m is the strain-rate-sensitivity of flow stress. Superplastic materials are characterised by a high value of strain-rate-sensitivity $m \geq 0.3$, although for many superplastic metallic materials, normally their strain-rate-sensitivity is within the range of 0.4 – 0.8. Strain-rate-sensitivity refers to the ability of material to resist the neck propagation during tensile deformation which leads to the high tensile strain characteristic of superplastic materials.

2.6.1. Fundamentals of Superplasticity

Grain boundary sliding is known as a basic mechanism for superplastic flow. However, sliding between two grains cannot be achieved without the necessity for accommodation at the triple junction which leads to the crack initiation due to differential sliding. The accommodation mechanisms include diffusion and/or dislocation process which also define the kinetics of superplastic flow. In contrast to creep whose life is extended by introducing larger grains, fine grains are necessary for superplasticity to facilitate accommodation by intergrain slip, hence decreasing differential sliding.

Superplasticity is not always possible to characterise only by fine grain size. To be amenable for superplasticity, those fine grains must contain high angle grain boundaries to allow grain boundary sliding. The ease of grain boundary sliding is also affected by the composition of a boundary where a heterophase boundary (a boundary between two grains with a dissimilar chemical composition) favours grain boundary sliding more than a homophase boundary (a boundary between two grains with a similar chemical composition). Furthermore, the grains have to remain stable during superplastic deformation [102,121,122]. To maintain the stability of the fine grains, it is of importance to have secondary phase or particles at the grain boundary. For that reason, materials for superplasticity are usually designed based on the eutectoid, eutectic or monotectoid composition. The solutes present in these compositions enables the materials to be thermomechanically processed to form fine, equiaxed, two-phase structures. The fine and uniform distribution of second phase or particles formed in the material will pin the grain boundary, hence inhibiting the grain growth. Furthermore, the interface between the matrix/second phase or matrix/particles is of importance during superplastic forming since higher stress concentration will be created on those interfaces, leading to the cavitations

nucleation. There is evidence that cavitations initiate from the matrix/second phase or matrix/particles interfaces. For example, nucleation of cavitations has been found at the interface of matrix/hard particle Ag_3Sn when this hard particle is added to a Pb-Sn alloy [125,126]. The same behaviour was also observed in microduplex stainless steel containing $\text{Ti}(\text{C}_3\text{N})$ particles [127]. However, contradictory behaviour was observed in the fine-grained Ti-6Al-4V and hypereutectoid Fe- Fe_3C alloys in which the two phases have almost same strength at the superplastic deformation temperature [128]. This suggests that in order to avoid cavitations, both second phase and matrix should have similar strength. Apart from that, the size, morphology and distribution of the second phase also influences superplasticity. Fine hard particles which are distributed uniformly within the matrix are known to inhibit cavitation by various recovery mechanisms occurring at the surroundings of particles, whereas coarse particles induce cavitations.

There are several ways to develop a fine equiaxed grain size prior to superplastic deformation. In the case of aluminium alloys, superplastic microstructure is developed by applying heavy deformation (heavy cold or warm working) followed by rapid static recrystallisation (SRX). This thermomechanical processing is required to produce high-density areas characterised by high strain energy and misorientation, forming numerous SRX nuclei which then leads to the fine grain structure. Multistage deformation is applied to induce the formation of a cellular microstructure which can be significantly affected by the existence of non-deformable large particles. During annealing, these particles will act as a stimulus to nucleation, raising the recrystallisation kinetics. If precipitates are present in the alloy, it will hinder boundary mobility and impede the SRX process during annealing. Consequently, a treatment based on the SRX process is not suitable for precipitate containing materials, a instead thermomechanical processing (TMP) based on the warm working and precipitation followed by continuous dynamic recrystallisation at the superplastic temperature is preferred [129]. Furthermore, equal channel angular pressing (ECAP) is also commonly used to refine the microstructure. A sub-micro scale grain size could be achieved by ECAP by applying severe plastic deformation without any change in the cross-sectional dimension of the samples. Apart from the deformation process, a fine grain size could also be achieved by the addition of Sc and/or Zr which will improve grain stability at high temperature by retarding the grain growth due to the precipitates formed. However, all of these options are costly, making them not suitable for a large scale superplastic forming of industrial components due to excessive cost.

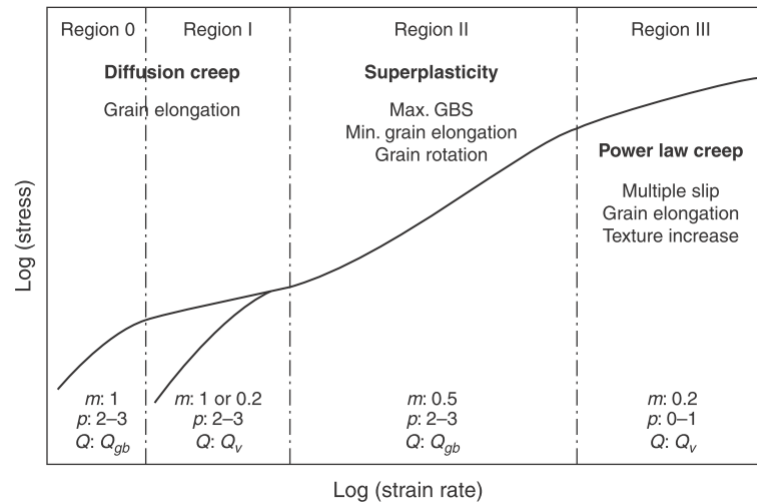


Fig. 2.18. Logarithmic plot of stress versus strain rate for superplastic material, where Q_{gb} is the activation energy for grain boundary diffusion, Q_v is the activation energy for volume diffusion, m is the strain rate sensitivity, p is constant and GBS stands for grain boundary sliding [121]

It has been known that a superplastic material is characterised by high strain-rate sensitivity of flow stress, m [129]. Strain-rate sensitivity can be calculated using Eq. 2-8 which is the tangent/slope of the logarithmic plot of stress and strain-rate curve. In superplastic materials, the slope of $\log(\sigma)$ versus $\log(\dot{\epsilon})$ curve changes with strain-rate and is divided into three regions based on its deformation mechanism (Fig. 2.18), which are:

Region I. This region is known as low strain-rate sensitivity region. The shape of logarithmic stress-strain rate curve resulted from low strain rate test can be varied dependent on their strain rate sensitivity values. The first region lies for the alloys which have m as low as 0.2 or even lower. This region has often proposed as the indication of a threshold stress, the stress required to initiate glide at triple junctions, ledges or particles at grain boundaries (GBs). It has been postulated that grain boundary sliding influenced by segregation of impurities atoms to the GBs is responsible for the mechanism in this region [121]. This proposed mechanism was confirmed by the experimentations on in Zn-22 wt.% Al carried out by Chaudhury and Mohammed [130]. They observed that the existence of this region was affected by the purity level of the alloy as they investigated that this region did not present as the impurities of Zn-22 wt.% Al were declined to a very low levels. On the contrary, the purity levels of the alloy do not give any influence to the Region II and its transition to Region III.

Moreover, diffusion was also proposed to give an influence during deformation flow which could be notified from the slope in Region I in which its tending to unity increases with declining strain rate. On the other hand, another Region terms as Region 0 was developed by Vale *et al* [131,132] which refers to the region in which the m decreases at the beginning and further decreasing results in transition to a slope of 1. This is proposed due to the presence of diffusion-creep which has activation energy of grain boundary diffusion [121].

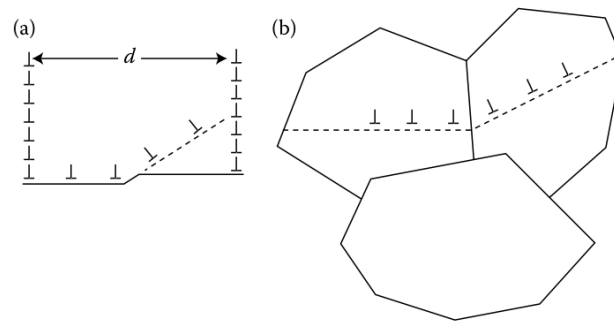


Fig. 2.19. Schematic illustration of grain boundary sliding in (a) coarse subgrain size d and (b) fine grain size [122]

Region II. This region is known as superplastic region in which the grain remains equiaxed over deformation process, where the strain-rate sensitivity is high, $m > 0.3$. In this region, grain boundary sliding (GBS) is responsible for the deformation mechanism [102,121]. During deformation in this region, GBS is accommodated by the dislocation and/or diffusion activity in the vicinity of GBs in which preventing cavitation formation. Cavitation will occur if the GBS takes place on the rigid system.

It is observed that the intergranular dislocation movements did not give any significant contribution to the overall strain. Consequently, materials consisting of large grains do not show superplasticity as dislocation activity and substructures only accumulate within the grains. In contrast to that, fine-grained materials exhibit insignificant intergranular activity except in transition regions from Region II to Region III. Several theories have been developed to understand the mechanism in Region II [131,133]. Alternative dislocation models proposed that the stress concentration due to impediment of GBS can be released by the emission of dislocations from one boundary and by their absorption by another

boundary (Figure 2.23) [124]. The rate of dislocation emission or absorption or the rate at which they cross the grain (glide- or climb-controlled flow) controls the mechanism.

Region III. A high strain rates region where recovery controlled dislocation creep (power law creep) dominates the mechanism. In this region, strain accumulation is occurred due to dislocation glide and it relies on the bypass rate of the obstacles, such as other dislocation, precipitated and solutes. It is proposed that the dislocation climb controls the bypass rate of the obstacles.

2.6.2. Superplasticity of Metal Matrix Composites

It has been observed that metal matrix composites (MMC) show superplasticity when they are deformed either at high strain rates, which refers to strain rates higher than 10^{-2} s^{-1} , or with thermal cycling in which test specimens are thermally cycled between two temperatures. This high strain rate superplasticity (HSRS) phenomenon was initially observed on Al 2124 containing 20 wt.% whiskers of SiC produced by powder metallurgy [134]. Elongation of 300% was achieved when this alloy was deformed at very high strain rates of $3.3 \times 10^{-1} \text{ s}^{-1}$ and a temperature of 525°C which is above the solidus temperature of the 2124 Al matrix (the solidus temperature of 2124 Al is 502°C). It was proposed that the existence of a partial liquid phase may contribute to the superplasticity. In other cases of $\text{SiC}_w/2024$ and $\text{SiC}_w/6061$ composites, superplasticity was observed under non-isothermal test conditions. Elongation of 300% in the $\text{SiC}_w/2024$ and 400% in the $\text{SiC}_w/6061$ were observed when the materials were subjected to thermal cycling of 100°C and 450°C (at 100 s per cycle) at the range of strain rate of 10^{-5} s^{-1} to 10^{-4} s^{-1} . Internal stresses resulting from the thermal coefficient mismatch between the reinforcement and the aluminium matrix is produced under thermal-cycling conditions. On the other hand, $\text{SiC}_w/7475$ composites showed superplasticity only under conditions in which a back pressure was applied. The applied backpressure decreases the cavitations, hence delays fracture in materials.

It is demonstrated that the elongation during HSRS strongly depends on the deformation temperature. It is noted that all of the experiments [135–138] were performed at a temperature near to or above the solidus temperature of the matrix materials. It can also be stated that the materials were tested in the semi-solid state. The liquid phase present in the materials acts as a lubricant to promote grain and particle sliding. This kind of result is expected to prevail, especially in the fine-grained containing materials since the grain

rearrangement which consists of sliding and rotation is easier compared to the coarse grains. Furthermore, the amount of liquid phase present in the materials plays a significant role during superplastic deformation. Earlier investigations [122,134,139–142] revealed that the maximum elongation to failure was achieved at a temperature which is slightly higher than the incipient melting temperature, T_i . Elongation to failure reduces sharply with further temperature increases above the maximum elongation temperature. Fig. 2.20 explains the mechanism behind that phenomenon. At a temperature higher than, yet near to T_i , only a small amount of liquid phase exists in the materials. This liquid phase would segregate either to interfaces between the reinforcement and matrix or to the grain boundaries. When the liquid phase is thin, atoms in the solid state across two neighbouring grains can still experience a traction force, T_{gb} , from each other, hence the grain boundary can sustain the applied tensile force. Additionally, a shear stress can also be transferred across the boundary [136,139]. If the temperature is much higher than T_i where it is closer to the solidus temperature, T_s , the liquid phase is thick as the macroscopic melting starts to occur. At this state, the grain boundary can no longer sustain the tensile force applied since the atoms across two adjacent grains will not experience a traction force anymore. In addition to that, a shear stress cannot be transferred across the boundary which leads to the decrement in ductility [136,139].

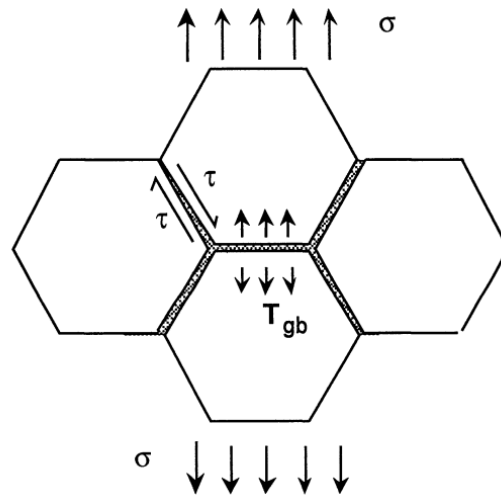


Fig. 2.20. Schematic illustration of the forces occurring towards adjacent grains when the liquid phase is present in the grain boundaries [122]

In contrast to those inventions, later inventions of HSRS in MMC [19,143,144] figured that the maximum elongation to failure occurred in the solid state instead of the semi-solid

state. For example, Zahid *et al* [19] in their experiment on Al 2124 reinforced with particulate SiC exhibited a maximum elongation of 425% when it was deformed at 490°C, where the DSC (differential scanning calorimetry) did not detect the liquid phase at that temperature. Other investigations on TiN_p/2124 Al [144] and SiC_p/6061 [143] exhibited the same tendency where the maximum elongation to failure occurs in the solid regions of the matrix alloy. However, further microstructural investigation under SEM showed the existence of some nodes either at the grain boundaries or reinforcement/matrix interfaces in expense of cavities. This indicated that some liquid phase appears in the material although the temperature is below the incipient melting temperature of the matrix alloy. Following this, it is reported that the existence of ceramic reinforcement affects the solute distribution in an Al alloy [145]. FEM/STEM investigation [146] on the 15 vol.% SiC_p reinforced 2000 series Al alloy (1.45 at.% Cu, 1.67 at.% Mg, 0.12 at.% Zr, 0.1 at.% Mn) exhibited an increasing concentration of Mg and Cu at the SiC/matrix interfaces up to 4.5 and 9 at.% respectively. Both Mg and Cu segregation are expected to decrease the local melting point of the Al matrix near the interface region. Consequently, although those maximum elongation-to-failure temperatures observed lie in the solid state region, due to solute segregation, it may be high enough to cause local melting at the reinforcement/matrix interface, even in the absence of adiabatic heating. Another mechanism was suggested by Imai *et al* [147]. They proposed that the heat generated during deformation is not able to be conducted to the environment due to the very fast deformation process (very high strain rate). This will make the interior temperature of the deformed composite higher than the environment and reach the incipient melting temperature of the composites, hence the liquid phase appears. Apart from those two proposed mechanisms, it could be concluded that the deformation during HSRS is accommodated by grain boundary sliding which is favoured by the liquid phase.

In the case of the internal stress superplasticity (ISS) mechanism due to thermal cycling during superplastic deformation, it is believed that the materials are deformed by slip-creep mechanisms [122]. There are several ways in which an internal stress could be generated. These include thermal cycling of composites where the constituents have different thermal expansion coefficients [148–150]; thermal cycling of polycrystalline pure metals or single-phase alloys which have anisotropic thermal expansion coefficients; and thermal cycling through a phase change [122]. In the case of metal matrix composites, during thermal cycling, internal stresses are generated at the interfaces between the metal matrix and

ceramic reinforcement due to thermal coefficient difference between both constituents, where in this case metal matrix has thermal expansion coefficient a number of times larger than the ceramic reinforcement. The plastic deformation occurred in the metal matrix will relax the internal stresses created on the metal matrix and ceramic interfaces to the value of the local interfacial yield stress of the materials. It is believed that this remaining local yield stress, which is identified as the internal stress, σ_i , which leads to the low applied external stress. As the consequence, macroscopic deformation occurs parallel to the direction of the applied stress. This is because internal-stress superplastic materials can have a strain-rate-sensitivity exponent as high as unity; i.e., they can exhibit ideal Newtonian viscous behaviour [136,139].

CHAPTER 3

EXPERIMENTAL METHODS

3.1. Introduction

This chapter describes the materials studied and experimental techniques used in this present research. Three different variants of Al-Cu-Mg-Ag base alloys were studied to explore the role of TiB_2 on the workability and mechanical properties of the described alloys. The workability behaviour was investigated by applying elevated temperature compression testing, rolling, extrusion and super plastic forming (SPF). Furthermore, mechanical properties were measured by using Vickers hardness and uniaxial tensile test. Optical microscopy (OM), scanning electron microscopy (SEM) equipped by energy dispersive X-ray spectroscopy (EDS), electron backscatter diffraction (EBSD), and transmission electron microscopy (TEM) were used to characterise microstructure evolution. To evaluate chemical composition and phases formed in the alloy, arc spark optical emission spectroscopy (OES) testing was performed. Fig. 3.1 is provided to illustrate the material processing and experimental route in this research.

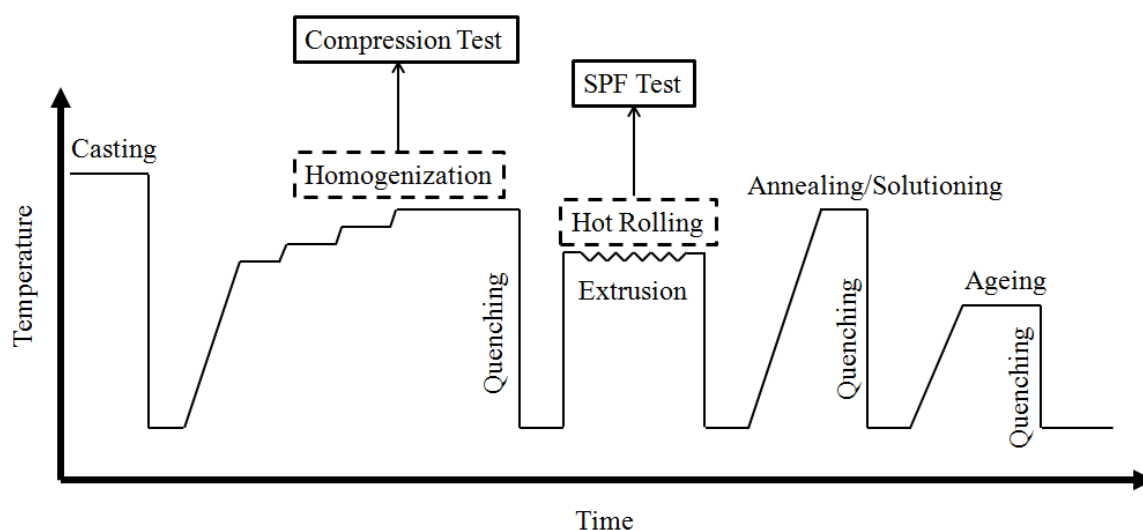


Fig. 3.1. Material processing route from casting to forming including heat treatment processes

3.2. Materials

Three different variants of Al-Cu-Mg-Ag base alloys were studied. They were A20X alloy, an Al-Cu-Mg-Ag alloy reinforced by 4.5 wt.% TiB_2 and contains of 0.2 wt.% free Ti, which will be called 0.2Ti-4.5TiB₂ composites; Al-Cu-Mg-Ag alloy with and without 0.2 wt.% Ti which will be called alloy 0.2Ti and matrix alloy respectively. The main material, A20X, was supplied by Aeromet International PLC in the form of as cast bar. Table 3.1 shows the designations and nominal composition obtained by OES of all three materials used in this present research.

Table 3.1. Alloy designations and chemical composition of material used in this study; measured in wt.%

Alloy	Composition								
	Cu	Mg	Ag	Ti	B	Si	Fe	Mn	Al
A20X (0.2Ti-4.5TiB₂ composite)	4.30	0.21	0.77	3.62	1.44	0.09	0.10	0.02	Rem
Al-Cu-Mg-Ag-Ti (0.2Ti alloy)	4.23	0.05	0.66	0.19	-	0.03	0.29	0.02	Rem
Al-Cu-Mg-Ag (matrix alloy)	4.33	0.06	0.67	-	-	0.03	0.23	0.02	Rem

3.3. Materials Processing

This section provides material processing sequences conducted in this present research, i.e. casting – homogenisation – hot rolling and extrusion – annealing – ageing. All the heat treatment processes in this study were performed in the programmable Lenton air-circulating furnace. In order to monitor the temperature during the heat treatment processes, a type K mineral insulated thermocouple was used in each heat treatment.

3.3.1. Casting

Three types of cast iron moulds which are a cylindrical mould, a rectangular mould and a disk/mushroom-shaped mould were used to produce ingots for extrusion, rolling and spectroscopy analysis respectively (Fig. 3.2). Prior to the casting, the moulds were pre-heated at $\pm 300^\circ\text{C}$. In addition to preventing thermal shock, pre-heating moulds at that

particular temperature prior to casting also serves to provide the same solidification conditions for grain size comparison. Apart from the moulds, all additional equipment used in this casting was also pre-heated at that temperature to prevent thermal shock and to eliminate the moisture. In order to prevent Fe contamination into the melt, all of the equipment was coated with boron nitride. The details of the casting processes for each alloy, including the standard sampling procedure for spectroscopy analysis according to ASTM E716 are described below.

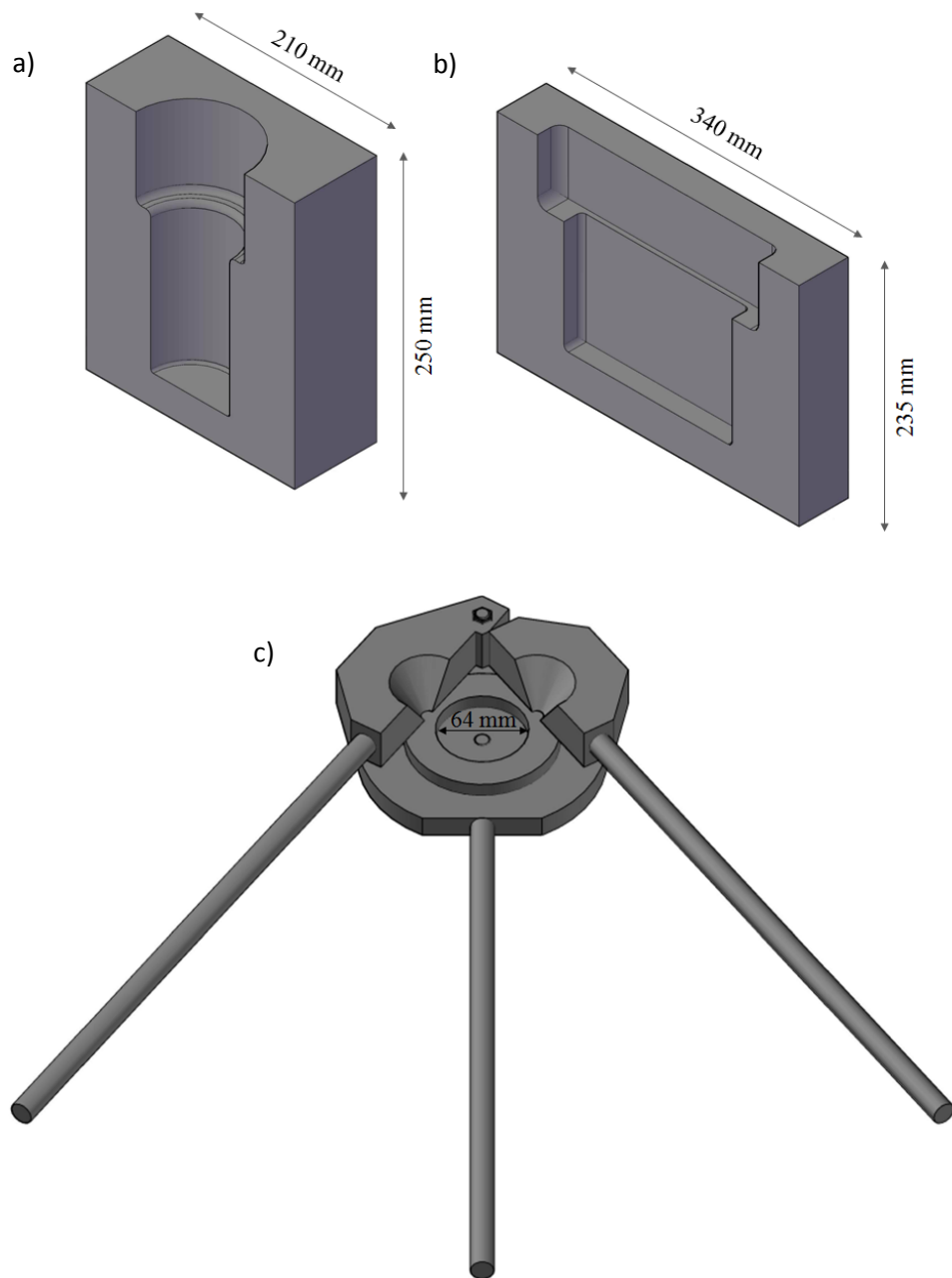


Fig. 3.2. Schematic illustration of the mould used to produce (a) extrusion ingot, (b) rolling ingot and (c) OES samples

3.3.1.1. Casting of 0.2Ti-4.5 TiB₂ Alloy (A20X)

It is essential to eliminate moisture during aluminium casting for safety reasons since it can cause an explosion. Furthermore, the existence of moisture during casting will degrade the properties of the casting product. For these reasons, the boron-nitride-coated graphite crucible used for casting was heated up until the red hot spot showed to eliminate moisture trapped in the molten metal. Following that process, 6 kg of 0.2Ti-4.5TiB₂ master alloy was induction melted and degassed at $775\pm5^{\circ}\text{C}$ with argon to reduce the amount of impurities and hydrogen dissolved in the molten metal. To check the optimum degassing time, samples were taken and vacuumed after 0 minutes, 10 minutes and 15 minutes degassing. An optimum degassed sample will show a smooth concave surface without voids after being vacuumed. In this present research, it was achieved after 15 minutes degassing as shown in Fig. 3.3.

During degassing, the temperature was slowly increased to the casting temperature, 800°C . It has been observed that Al₃Ti particles dissolve ‘moderately quickly’ at 800°C in commercial purity aluminium [151,152]. Thus, in order to minimise the formation of Al₃Ti particles in the alloy, casting was done at 800°C . Apart from that, it is important to keep the temperature below 805°C during degassing as the hydrogen dissolved rate increases above that temperature. Following degassing, the molten metal was immediately cast at 800°C .

To evaluate porosity across the samples and assess the optimum degassing time, degassed samples were sliced and mechanically polished in sequence with #800, #1200 SiC paper, 9µm and 3 µm Metadi Supreme diamond suspension, and 0.05 µm colloidal silica. Samples were subsequently etched with Tucker’s reagent (45 ml HCl + 15 ml HF + 15 ml HNO₃ + 25 ml H₂O) after polishing for macrostructure examination as is shown in Fig. 3.3.

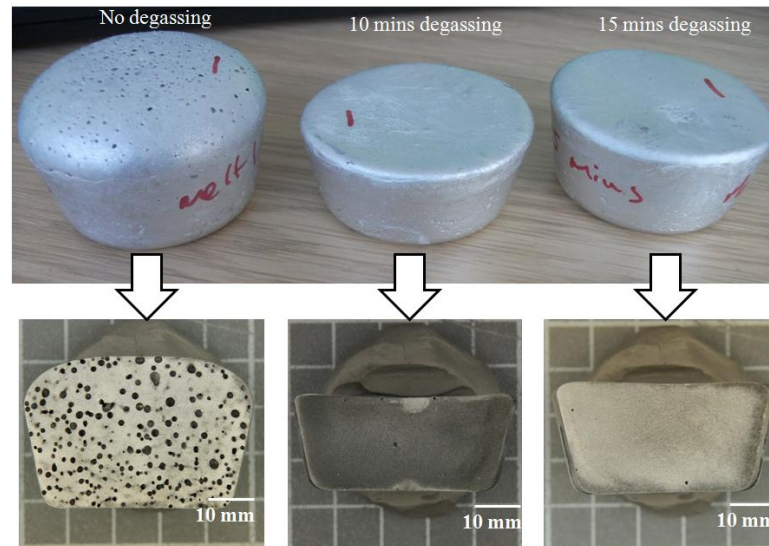


Fig. 3.3. Samples taken from 0 minutes, 10 minutes and 15 minutes degassing showing smooth and concave surface and no porosity as degassing time increases to 15 minutes

3.3.1.2. Casting of 0.2Ti Alloy and Matrix Alloy

Different from the 0.2Ti-4.5TiB₂ alloy which was casted directly using a master alloy provided by Aeromet Int. PLC, 0.2Ti alloy and matrix alloy were cast in house. However, all the process parameters such as molds and all equipment pre-heating temperature, degassing time and temperature, and casting temperatures were kept the same as 0.2Ti-4.5TiB₂ alloy to give the same casting and solidification conditions.

Commercial purity aluminium (99.7 wt.% Al), pure copper, Al-10wt.% Mg, Al-50wt.% Ag and Al-10wt.% Ti master alloy were weighed at a given proportion to make a 6000 ± 100 g melt for each casting. Following the same casting procedure for the 0.2Ti-4.5TiB₂ alloy, a boron-nitride-coated graphite crucible was heated until the red hot spot showed. When the boron-nitride-coated graphite crucible showed the red hot spot, pure Al ingots were fed into the crucible and induction melted. Pure copper and Al-50wt.% Ag master alloy were then added to the melt. Following those processes, the same degassing process as for the 0.2Ti-4.5TiB₂ alloy was performed to the melt. In the case of the 0.2Ti alloy, Al-10wt.% Ti master alloy was added to the melt after degassing. Prior to the addition to the melt, Al-10wt.% Ti master alloy was pre-heated at 500°C to minimise the temperature drop of the melt during its addition. Lastly, Al-10wt.% Mg master alloy was then added to the melt just before pouring. The reason for adding Al-10wt.% Mg master alloy just before pouring is to compensate for loss due to oxidation and/or evaporation of Mg. In order to ensure the

homogenisation of the melt, mechanical stirring was carried out in each master alloy/hardener addition. In addition to that, the temperature was carefully monitored in each step of master alloy addition.

3.3.1.3. Sampling Procedure for Spectroscopy Analysis

The sampling procedure to obtain a chill-cast disk suitable for quantitative optical emission spectrochemical (OES) analysis is based on the ASTM E716. According to that standard, the excited region in the specimen disk is representative of the melt/product and must give a repeatable result close to the reference material used. The repeatability from excitation-to-excitation has to be no more than 2% relative to major elements. Consequently, the sample moulds have to be capable of producing homogeneous chill-cast disks which have smooth surfaces without defects and porosity. There are several types of moulds that can be used to produce samples for spectroscopy analysis, which are book moulds, centre-pour moulds and vacuum moulds. In this present research, a centre-pour mould was used.

A centre-pour mould produces a horizontally cast disk with the sprue over the centre on the back side. The advantage of a central-pour mould is it enables the sample obtained to be excited around the entire annular area. The mould is designed to produce a disk with dimension of 64 diameters and around 6 to 13 mm in thickness. It also has a circular centre recess of 10 to 20 mm in diameter. Not only to facilitate machining during preparation for excitation, the existence of the circular centre recess also promote more uniform solidification of the raised peripheral area.

3.3.1.4. Thermal Analysis (Cooling Curve Determination)

To understand the effect of TiB_2 addition on the solidification of Al-Cu-Mg-Ag alloy, the cooling curve was measured. A 50 mm diameter with 65 – 70 mm height graphite crucible was used to melt 200 grams of each as-cast alloy. The crucible filled with as-cast alloy was placed in the furnace to melt the alloy. To record the temperature during cooling, a Ø3 mm type-K mineral insulated thermocouple was inserted into the melt and connected to the PICO TC-08 data logger. Fast logging (100Hz) was set to record the temperature data to minimise the loss of detail information during actual cooling. The data was then plotted into the cooling curve and thermal analysis was carried out. Fig. 3.4 shows an example of the thermal analysis.

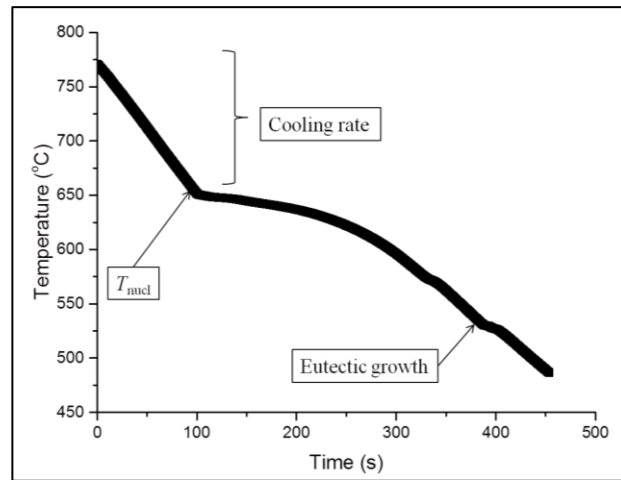


Fig. 3.4. Examples of cooling curves on Al-Cu alloy

3.3.2. Homogenisation

Homogenisation was applied to the as-cast alloy prior to the rolling, extrusion and compression tests. In addition to eliminating the consequences of microsegregation and to increase the properties of casting products, homogenisation is also useful to increase the formability during rolling and extrusion. A heating rate of 50°C/hr was applied during homogenisation with the schedule described in Fig. 3.5. The specimens were then immediately water quenched after homogenisation and stored at a temperature of -20°C to preserve the as-homogenised microstructure.

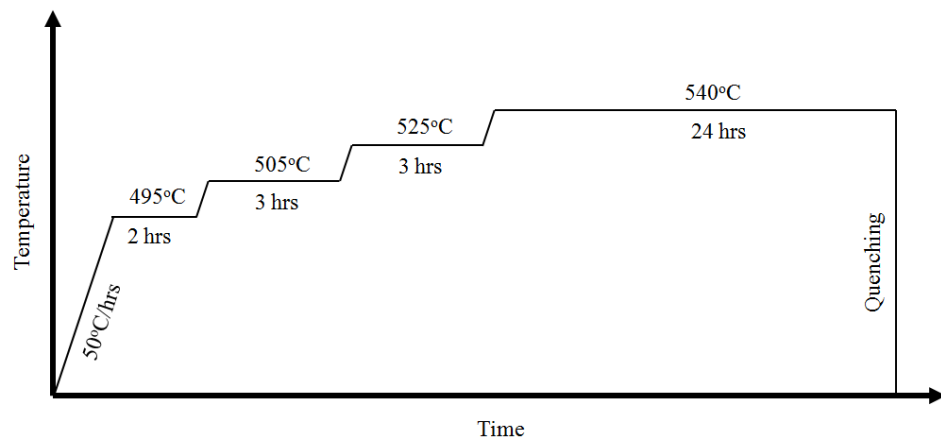


Fig. 3.5. Graph exemplifying the homogenisation process

3.3.3. Hot Rolling

Following the casting, rectangular ingots were scalped and machined into 57.5 mm x 85 mm x 35 mm dimension and homogenised. The homogenised ingots were then pre-heated for 2 hours at 500°C with a heat rate of 50°C/hr and rolled with 11 passes down to ± 1.85 mm thick sheet. A $\varnothing 1$ mm type K thermocouple was inserted into the ingots to measure the temperature during rolling. After 11 passes, the temperature went down to 290°C. The rolling process was conducted on a laboratory scale Lewis rolling mill (rolling diameter 218 mm) at Swinden Technology Centre, Rotherham. The rolling mill is equipped with a numerical control unit, enabling experiment to be performed according to a pre-programmed cycle. In addition to that, it also enables data recording during the actual rolling such as load, torque and rolling mill position for further quantitative analysis. In order to minimize friction during rolling, water soluble lubricant was applied. The rolling schedule is provided in Table 3.2.

Table 3.2. Hot rolling schedule

Pre-heat temperature : 500°C with heating rate 50°C/hrs	
Pre-heat/soak time : 2 hrs	
Pass	Rolling Gap (mm)
1	31
2	24
3	18.5
4	15.5
5	13
6	10.5
7	8
8	6
9	4.5
10	3
11	1

3.3.4. Hot Extrusion

Direct hot extrusion was performed on homogenised cylindrical billets scalped to dimensions of Ø72.5 mm x 120 mm height. The billets were placed in the container and pushed through the Ø16 mm die by the ram pressure. Prior to the extrusion, billets were pre-heated at 450°C for 2 hrs. A type K mineral insulated thermocouple was stacked to the billet to monitor the temperature during pre-heating. Billets were then pressed with a 3 mm s⁻¹ ram speed to produce solid rod profiles. The detailed parameters of extrusion process are described in Table 3.3.

Table 3.3. Extrusion process parameter

Pre-heat temperature	450 °C
Pre-heat/soak time	2 hrs
Container diameter	75 mm
Container temperature	400 – 450 °C
Die diameter	16 mm
Ram speed	3 mm s ⁻¹
Extrusion ratio	22 : 1

In this study, a 5 MN ENFECO hydraulic press was utilised to perform hot extrusion. The press is equipped with heating element, allowing the container and die to be pre-heated at the pre-determined temperature. The press is also equipped with thermo elements which are connected to the digital controller, enabling us to monitor the exit temperature. However, this is only sensitive for flat profiles. Since in this research, rod products were produced, hence the exit temperature could not be monitored. Moreover, the press is also equipped with a cooling unit which enables direct quenching to be performed at the end of deformation. In this present research, direct water quench was performed at the end of deformation for all of the extrusion experiments.

3.3.5. Annealing

Annealing at solution treatment temperature was carried out on the as-wrought products to investigate all phenomena related to the softening mechanisms. Annealing was conducted at a solution treatment temperature of 540°C to study softening mechanisms. Immediately

after annealing, specimens were water quenched to preserve the as-annealed microstructure.

3.3.6. Artificial Ageing

Specimens which have been previously solution treated at 540°C for 2 hours were subjected to ageing at a temperature of 175°C . Both heat treatments, solution treatment and ageing, were carried out with a heating rate of 50°C/hr . In order to study the effect of TiB_2 addition on the ageing response, variation of ageing time up to 24 hours was conducted.

3.4. Mechanical Testing

3.4.1. Compression Testing

Background. Workability is described as the ease with which a metal can be subjected to plastic deformation to achieve the desired shape without any crack formation. In order to evaluate the material's workability, it is important to measure the resistance of deformation (strength) and determine possible plastic deformation before fracture (ductility). Therefore, a material's workability can be specified by its flow stress dependence on its processing conditions (e.g. strain, strain rate, pre-heat temperature, die temperature), its failure behavior and metallurgical transformations that characterise the alloy system to which it belongs [103]. There are several tests which can be used to investigate workability of a material; one of them is a compression test.

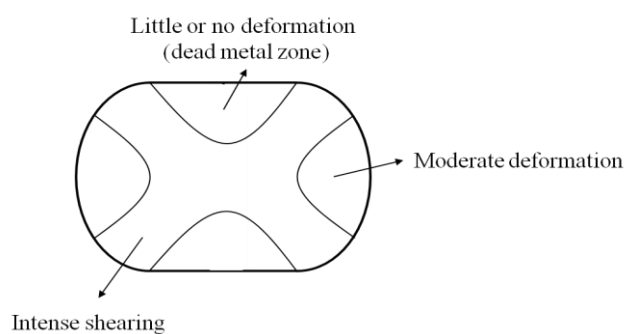


Fig. 3.6. In-homogeneity of deformation in a compressed specimen [103]

Determination of flow stress in compression is performed under isothermal conditions at a constant strain rate and with a minimum of friction in order to minimise barrelling. Therefore, lubrication plays an important role during compression testing. Internal in-

homogeneity of plastic deformation as shown in Fig. 3.6 will occur if insufficient lubrication is applied. Besides applying lubricant, the specimen dimension D_0/h_0 ratio has to be within the range 0.5 to 3 to avoid barrelling and buckling. In addition to that, constant true strain rate to a strain limit of $\varepsilon = 0.7$ is usually applied to avoid further barreling [103]. Not only useful in determining flow stress (σ) and true compressive strain (ε), as explained in Eqs. 3-1 and 3-2, compression test is also useful to determine plastic instability in a material as shown in Fig. 3.7.

$$\sigma = \frac{P}{A} = \frac{4Ph}{\pi D_0^2 h_0} \quad (3-1)$$

$$\varepsilon = \ln\left(\frac{h_0}{h}\right) \quad (3-2)$$

Where P is the deformation force, A is the original cross sectional area of the cylindrical specimen; D_0 is the initial diameter; h_0 is the initial height and h is the final height of the cylindrical specimen.

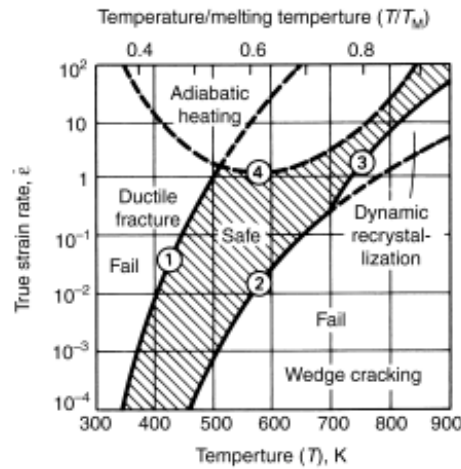


Fig. 3.7. Example of aluminium processing map showing the safe region for forming [103]

Experimental. Cylindrical compression specimens $\varnothing 8$ mm x 10 mm were fabricated from the bottom-top of rectangular ingots as described in Fig. 3.8. Compression tests were performed in a compact tabletop servo-hydraulic testing machine, Instron 8872, which has force capacity up to 25 kN. Variations in temperatures, from 300°C to 500°C and strain rates from 10^{-3} s^{-1} to 1 s^{-1} were applied. The homogenised compression specimens were soaked for 10 minutes at test temperature for equilibrium before it was deformed at a pre-determined strain rate. In order to measure and control the actual temperature, an $\varnothing 1$ mm

type K mineral insulated thermocouple was inserted into the anvil and connected to the Cole-Palmer data logger. Furthermore, boron nitride lubricant was applied to the specimens and anvils surface prior to the test to minimize friction between specimen and anvil during hot deformation. The specimens were compressed to 0.7 strain and quenched in water immediately to preserve the as-deformed microstructure.

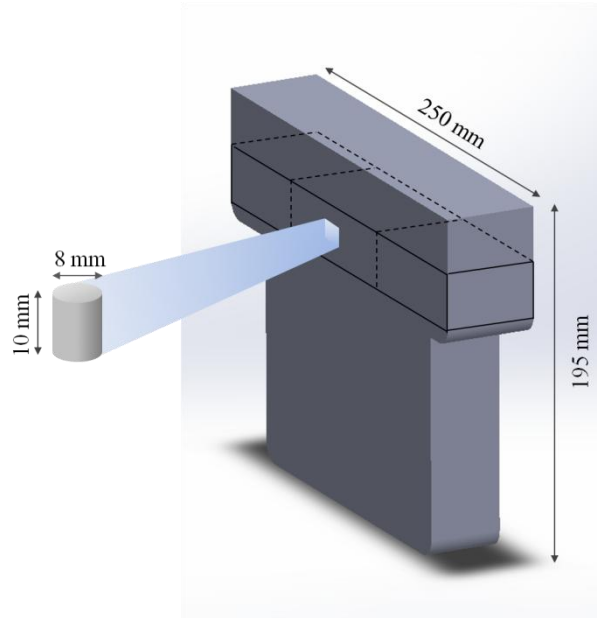


Fig. 3.8. Compression specimen sampling scheme

3.4.2. Tensile Testing

Background. *Engineering tension test* is commonly used to provide mechanical properties in strength of the materials. Strength and ductility properties can be obtained by plotting engineering stress-strain. Tensile strength (S) and yield strength (S_y) information describes strength of materials while ductility is described by percent elongation (%EL) and reduction in area (%RA). Those properties can be calculated by:

$$S = \frac{F}{A_0} \quad (3-3)$$

where F is the instantaneous load applied perpendicular to the specimen cross section (N) and A_0 is the original cross sectional area before any load (m^2 or in^2) is applied.

$$\%EL = \left(\frac{l_f - l_0}{l_0} \right) \times 100 \quad (3-4)$$

where l_f is the fracture length and l_0 is the original gauge length. It is important to note that the %EL value will depend on specimen gauge length since an appreciable fraction of the deformation will be concentrated in the necked region of the specimen. The smaller the l_0 , the greater the fraction of total elongation from the neck and hence the higher the value of %EL.

$$\%RA = \left(\frac{A_0 - A_f}{A_0} \right) \times 100 \quad (3-5)$$

where A_0 is the original cross-sectional area and A_f is the cross-sectional area at the point of fracture.

In addition to engineering stress, the **true stress** value is also important. While an engineering stress-strain curve is only based on the original dimensions, a true stress-strain curve is based on the actual cross-sectional area of the specimens. Hence, the true stress-strain curve increases continuously up to fracture as shown in Fig. 3.9b.

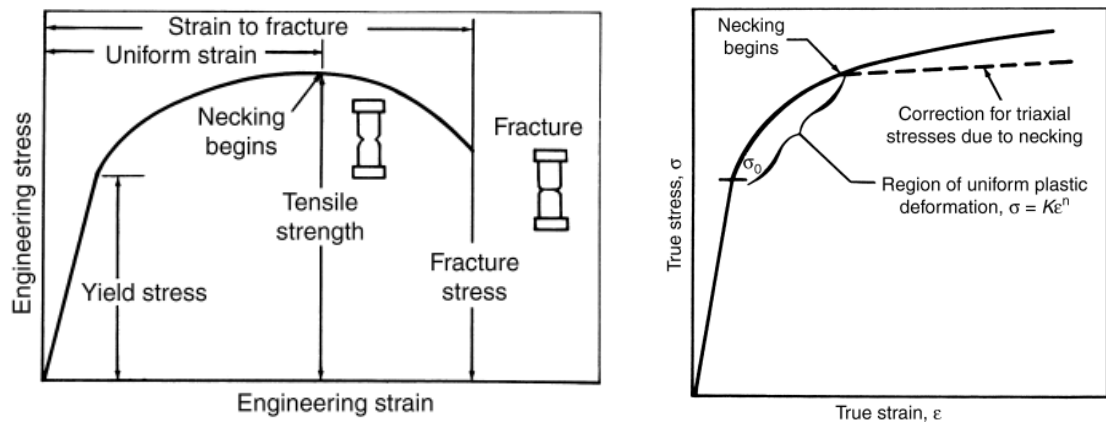


Fig. 3.9. (a) Engineering stress-strain curve and (b) true stress-true strain curve [103]

Further analysis on a true stress-true strain curve generates the strain-hardening exponent (n -value). The n -value is one of the factors that play a crucial role in sheet metal forming. This value is determined from an empirical representation over the range of interest of the true stress-true strain curve. Moreover, the n -value describes how the metal behaves when it is formed. The higher the n -value, the better the formability. As the materials work

harden, their remaining capacity for work hardening decreases. This means that the high strength temper materials typically would have a lower n -value compared to the lower strength temper materials. Some calculations to determine n -value according to ASTM E646 are:

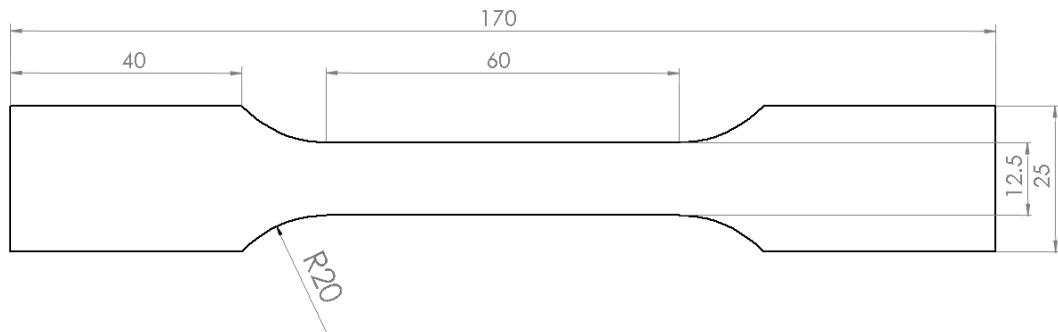
$$\log \sigma = \log K + n \log \varepsilon \quad (3-6)$$

where $\sigma = \sigma (1 + e)$ (3-7)

and $\varepsilon = \ln(1 + e)$ (3-8)

where (σ, ε) is a true-stress versus true-strain pair in the selected interval, σ is an engineering stress and e is an engineering strain.

Experimental. Uniaxial tensile testing was carried out on the Instron 5800R which has 100 kN load capacity, with a cross head speed of $0.175 \text{ mm min}^{-1}$. The tests were employed both at ambient and 200°C , considering the maximum equipment operating temperature (200°C) and the maximum operating temperature in the real application of alloy $0.2\text{Ti}-4.5\text{TiB}_2$ is 215°C if there is a failure. Specimens from rolled sheet were machined parallel to the rolling direction in accordance to ISO 6892-1:2009 which also fulfilled ASTM E646 for n -value determination, while the cylindrical specimens from extruded rod were machined parallel to the extrusion direction in accordance to ASTM B557-14 (Fig. 3.10). A strain gauge extensometer with gauge length of 50 mm with travel distance of 25 mm and 10 mm with travel distance of 5 mm was employed to measure strain on flat specimens and cylindrical specimens respectively.



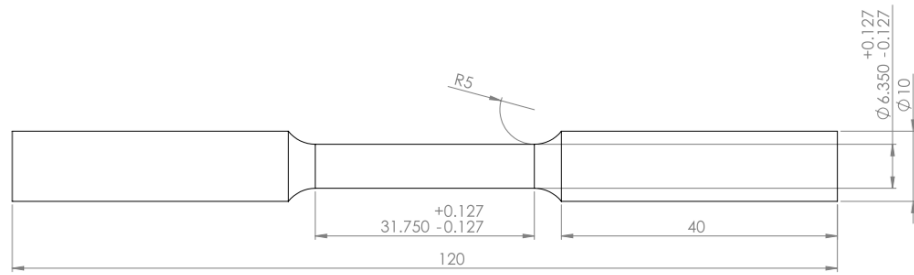


Fig. 3.10. Specimen dimension for tensile testing (a) rectangular specimens and (b) cylindrical specimens

3.4.3. Tensile Testing at Elevated Temperature (Superplastic Forming)

Background. Fine stable grain size and a deformation temperature of $> 0.5 T_m$ are required for superplasticity. In addition to large elongation $> 300\%$, superplastic materials are characterised by high strain-rate sensitivity of flow stress, $m \geq 3$. The m value is defined by the relationship:

$$\sigma = K \dot{\epsilon}^m \quad (3-9)$$

where σ is the steady state flow stress, $\dot{\epsilon}$ the imposed strain rate, and K a material constant.

Experimental. In this present work, tensile testing at elevated temperature was conducted to investigate superplastic formability of all three alloys. A compact tabletop servo-hydraulic testing machine, Instron 8872, was used to perform uniaxial tensile test. The specimens for the SPF test were prepared from rolled sheet parallel to the rolling direction with dimensions illustrated in Fig. 3.11. Furthermore, no heat treatment was applied to the specimens prior to the test. The tests were carried out in a variation of temperature from 450°C to 550°C and strain rate of $5 \times 10^{-3} \text{ s}^{-1}$ to $5 \times 10^{-1} \text{ s}^{-1}$. To introduce static recrystallisation and temperature equilibrium, specimens were soaked at the test temperature for 15 minutes before the test started. A $\varnothing 1 \text{ mm}$ type K mineral insulated thermocouple connected to a digital data logger was inserted into the anvil to measure and control the actual temperature. Once the test finished, specimens were immediately quenched in water to preserve the as deformed microstructure.

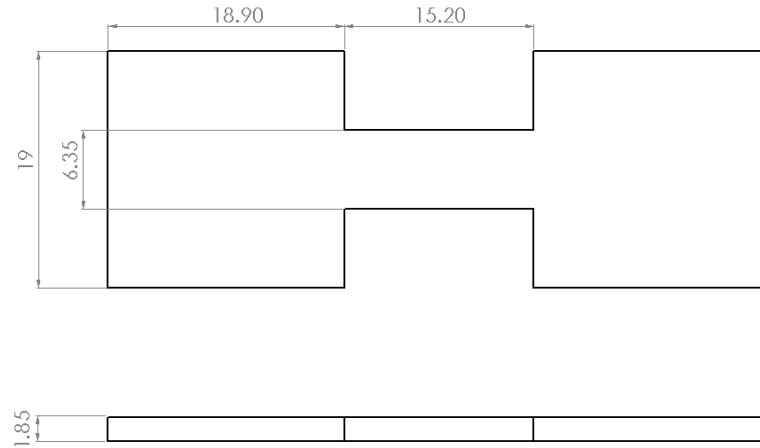


Fig. 3.11. Specimen dimensions for superplastic formability test

3.4.4. Vickers Hardness Testing

Background. Vickers hardness is measured by indentation of a pyramid-shaped diamond tip into the material's surface under a constant applied load. The equation for the Vickers hardness value is:

$$VHN = 1.8544 \frac{P}{d^2} \quad (3-10)$$

where P is the applied force (kgf) and d is the average length of the indentation's diagonals (mm).

Experimental. The Vickers microhardness method with a load of 1 kgf was conducted to measure the hardness of as-cast, as-wrought and aged materials. For wrought materials, hardness was measured in RD/ED-ND planes as illustrated in Fig. 3.13. Prior to the testing, the specimens were ground with #1200 SiC paper and 3 μ m Metadi Supreme diamond suspension to remove the thin surface oxide layer formed during treatments/processing. Mechanically polished the specimens prior to the hardness testing also improves the clarity of Vickers pyramid's edge identification hence increasing the accuracy in the determination of the final hardness. An average of at least 5 indents was calculated to give the final hardness result.

3.5. Materials Characterization

3.5.1. Phases and Chemical Analysis

3.5.1.1. Arc Spark Optical Emission Spectroscopy (OES)

Background. Optical emission spectroscopy using arc and spark excitation is one of the methods for trace metal analysis to determine the chemical composition of metallic materials. In the optical emission spectroscopy (OES), atoms in a specimen are excited by energy which comes from a spark formed between the specimen and electrode. The energy of the spark causes the electrons in the specimen to emit light which is converted into a spectral pattern. The OES analyser will then identify the quality and quantity of material composition by measuring the intensity of the peak spectrum.

Experimental. Disk specimens for composition analysis by OES were machined to 14 % - 22 % depth of original thickness in accordance to ASTM E 716. In this present work, 1.8 mm depth was scalped from the specimens. It was made sure that all of the specimen surface was smooth and free of scuff, pits or inclusions to avoid misleading results. The OES test was performed by Rotech Laboratory Limited and five sparks were applied to each specimen.

3.5.1.2. Differential Scanning Calorimetry (DSC)

Background. DSC measures the temperatures and heat flows associated with the transitions in materials as a function of time and temperature in a controlled atmosphere. It provides quantitative and qualitative information about physical and chemical changes that involves endothermic or exothermic processes, or change in heat capacity. Fig. 3.12 illustrates the concept of DSC.

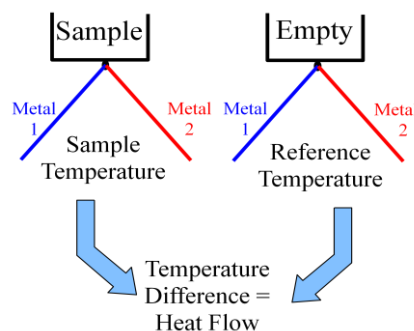


Fig. 3.12. Schematic illustration of DSC concept

Experimental. DSC measurements were performed on the as-rolled sample to study the phase transformation in 0.2Ti-4.5TiB₂ which is related to the superplastic behaviour. DSC measurements were carried out using Netzsch DSC. 14 ± 1 mg of samples were cut and placed inside an alumina crucible. An empty alumina crucible was used as the reference. The temperature and the heat flux between specimen and empty reference crucible were measured directly during the measurement. In order to avoid oxidation during measurements, argon gas was used inside the furnace. The starting temperature is set as 30°C, and then the DSC was heated up to 690°C with a constant heat rate of 10°C/min.

3.5.2. Microstructure Examination

3.5.2.1. Metallography Sample Preparation

One of the critical aspects in microstructural examination in order to get reliable representative data is sampling of microstructure specimens. Thus, to minimise irregularity in microstructure due to processing, all the specimens for microstructure examination were cut from the middle of the bulk specimens, both for cast materials (plate and billet) as well as for wrought materials (rolled sheet and extruded rod). For the rolled/extruded materials, specimens were cut in the RD/ED-ND direction for all microstructure examination as per Fig. 3.13, except for TEM observation where specimens were cut from RD/ED-TD plane. Particularly for compressed specimens, they were cut in half and microstructural examinations were performed in the middle area of the specimens to avoid dead-metal zones.

In this present research, all specimens for microstructural examination were prepared in the same way, except for TEM examination. A precision cutter Isomet 5000 was used to cut the specimens to minimise deformation formed during cutting. Cut specimens were mounted in Bakelite and mechanically polished using #800 and #1200 SiC paper, 9µm and 3µm Metadi Supreme diamond suspension and 0.05 µm colloidal silica. Specimens for grain structure analysis were anodised using Barker's reagent (5 ml 48% HBF₄ + 200 ml H₂O) for ± 60 s with 20 V_{dc} and 0.2 A/cm².

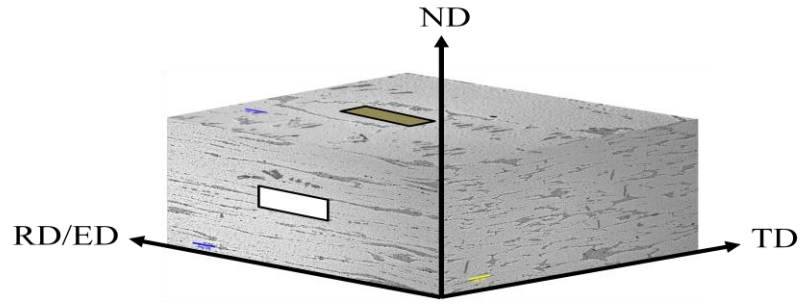


Fig. 3.13. Illustration of hot rolled and extruded specimens with directions: parallel (RD/ED), normal (ND) and transverse (TD) to rolling or extrusion direction. The white area indicates the plane where microstructure examination and hardness were performed and the brown area indicates the plane where the TEM examination was performed.

3.5.2.2. Light Optical Microscopy (LM)

Optical micrograph observations were performed on a Nikon Eclipse MA200 optical microscope. Anodised specimens were examined under polarised light to give colour contrast between each grain. Grain size measurement was then carried out with ImageJ software using intercept method as per ASTM E 112. Fig. 3.14 is provided to illustrate how the grain measurement was conducted.

$$G = (6.643856 \log_{10} N_L) - 3.288 \quad (3-11)$$

where G is the ASTM grain size number, N_L is the number of intercepts per unit length of test line.

where

$$N_L = \frac{N_i}{L} \quad (3-12)$$

where N_i is the number of intercepts counted on the field and L is the total test line length.

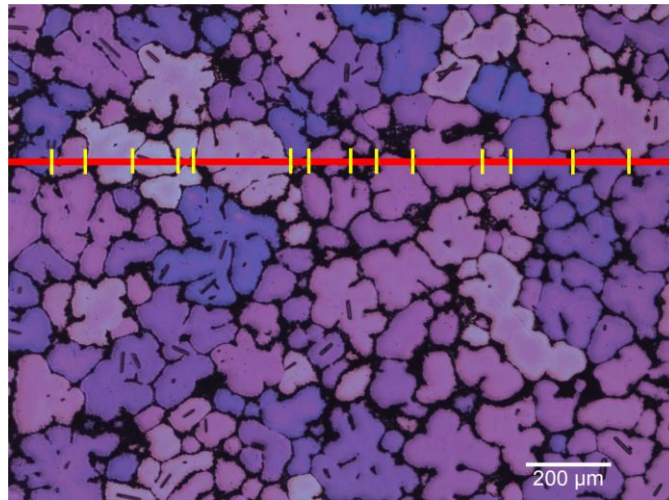


Fig. 3.14. Schematic representation of linear intercept method performed on the microstructure

3.5.2.3. Scanning Electron Microscopy (SEM)

Background. SEM utilises a focused beam of electrons which enables it to reveal levels of details and complexity inaccessible by light microscopy. Electrons which are emitted from the specimen by the action of the scanning beam will be collected by a suitable detector. A secondary electron (SEs) detector will collect SEs, giving an image which is very sensitive to surface condition and slight chemical differences. Furthermore, the lower energy of SEs will be detected by an In-lens detector, generating an image with high surface sensitivity. Thus, an In-lens detector is most suitable for fracture analysis. Moreover, some of the electrons will be backscattered and detected by a backscattered electron (BSE) detector, giving an image which is sensitive to chemical composition.

Experiment. In this present research, SEM was used mainly for characterisation of intermetallics, phase transformations during heat treatment and fracture analysis. A field emission SEM (FE-SEM) Zeiss Sigma with Gemini optics was used to characterise the specimens. Both SEs and InLens lenses were used to investigate microstructure and tensile specimen fracture respectively. 20kV and 5 kV of electron high tension (EHT) were used during imaging with SEs and InLens detector respectively. Furthermore, quantitative analysis of size and volume fraction of Al_3Ti and TiB_2 particles were performed on the fully homogenised and solution treated specimens. It is because the TiB_2 particles sit on the same place as Al_2Cu particle in the non-solutionised specimens which may cause confusion during analysis. ImageJ software was then used for quantitative analysis.

3.5.2.4. Energy Dispersive X-Ray Spectroscopy (SEM/EDX)

Background. X-ray generation is produced by inelastic collisions of incident electrons with electrons in discrete orbital (shell) of atoms in the specimen. As the excited electrons return to lower energy states, they yield x-rays which have fixed wavelengths depending on the elements in the specimens. Thus, specific x-rays are produced for each element in a specimen that is excited by an electron beam.

Experimental. EDX spot analysis and mapping were used to investigate chemical composition and its distribution in each alloy. In addition to that, spot analysis was also done to examine intermetallic or phase composition formed in each alloys. 20kV of EHT with working distance 8.5 mm were applied during all of the EDX analysis.

3.5.2.5. Electron Backscattered Diffraction (EBSD)

Background. The accelerated electrons in the primary beam of the SEM can be diffracted by atomic layers in crystalline materials. These diffracted electrons can be detected when they impinge on a phosphorus screen and generate visible lines, called Kikuchi bands or EBSP's (Electron Backscattered Patterns). EBSD software then processes the Kikuchi bands, indexes to find the best solution that fits the bands and save the data. The experimental set up requires the specimen to be tilted to 70° from the horizontal to allow high numbers of electron to be backscattered as illustrate in Fig. 3.15.

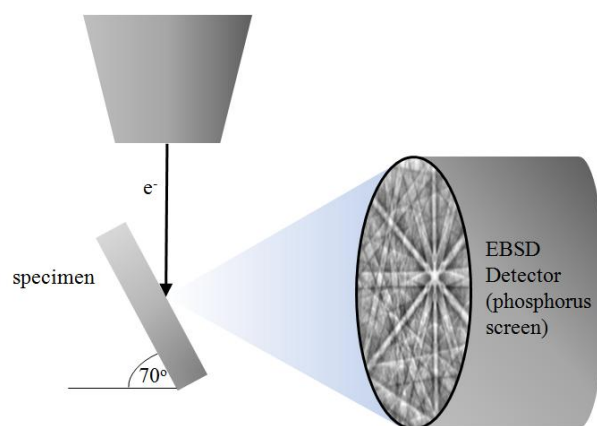


Fig. 3.15. Experimental set up for EBSD

Experimental. Both ambient temperature and hot stage EBSD were performed in this present research to investigate static recrystallisation behaviour on annealed specimens and

in-situ observation of the recrystallisation during annealing respectively. Most of the scans were performed at 300x SEM magnification for as-compressed and as-annealed compression specimens and 500x SEM magnification for the as-wrought and as-annealed rolled/extruded specimens. $\pm 1 \mu\text{m}$ step size and 20KV of EHT was used during the scanning. Furthermore, EBSD hot stage with focus scanning in the area of TiB_2 particles was utilised in order to investigate the role of TiB_2 on the static recrystallisation. The specimens were heated to 540°C , using a Gatan Murano 252 hot stage which mounted directly to the SEM with a heating rate of 5 K min^{-1} with a $0.2 \mu\text{m}$ step size at 5000x of SEM magnification. Specimens were hold for 15 mins at several temperatures while EBSD scan was carried out.

Following the scanning, Channel 5 software was then used for post processing EBSD data. A misorientation grain boundary profile was created and grain and/or subgrain sizes were measured using an intercept method. It is worth to note that the subgrain boundaries were defined as being misoriented $5^\circ - 8^\circ$ to minimise inaccuracy data due to noise, medium angle grain boundaries by $8^\circ < x < 15^\circ$ and high angle grain boundaries by misorientations of $\geq 15^\circ$.

3.5.2.6. Transmission Electron Microscopy (TEM)

Background. TEMs work by using a tungsten filament to produce an electron beam in a vacuum chamber. During bright field imaging, the electron beams will be transmitted through the specimen and then hit a phosphorus screen, CCD or film and produce an image. A brighter image will be produced when the specimen has less density as more electron pass through the specimens. When the specimen has high density, less electrons are able to get through, thus the image produced will be darker. In contrast to bright field imaging, during dark field imaging, a diffracted beam is used to create an image instead of a transmitted beam.

Experimental. In this present research, TEM observation was performed to investigate precipitates formed in the alloys. Hence, only materials in the peak-aged condition were observed under TEM. Specimens for TEM observation were cut from the RD/ED-TD plane. Specimens were then ground down to a thickness in the range of $70 - 100 \mu\text{m}$ and electro-polished until perforation with a Stuers Tenupol 5 in a solution of 30 % HNO_3 – 70% methanol at 17 V. The solution temperature was maintained at -30°C .

CHAPTER 4

STRAIN-RATE AND TEMPERATURE DEPENDENCE ON PLASTIC DEFORMATION

4.1. Introduction

One of the most important aspects to design the hot working parameter is the knowledge of material's flow stress behaviour, which is defined by its strain, strain rate and temperature during deformation. These dependence relationships between flow stress with strain, strain rate and temperature could be described by a constitutive equation. By establishing the relationship between those forming parameters (strain, strain rate and temperature), one can analyse the effect of those parameters on the flow stress of the material. It means that a constitutive equation enables us to predict the forces during forming. Moreover, those forming parameters (strain, strain rate and temperature) not only influence the flow stress behaviour, but also the microstructural evolution. Thus, it is also important to understand the microstructural evolution during forming in order to optimise the forming parameters. This can be predicted by a processing map which provides a region of “safe” and ‘non-safe’ deformation conditions. Consequently, by establishing processing map, it allows us to design hot working parameters which ensures the quality of the part.

In the current work, compression tests at several temperatures (300°C – 500°C) and strain rates ($10^{-3} \text{ s}^{-1} - 1 \text{ s}^{-1}$) were performed on the as-homogenised cast material to identify the material's flow stress behaviour during rolling and extrusion. Attention to the hot deformation behaviour has been made for several aluminium alloys reinforced by ceramic particulates, such as SiC and Al₂O₃ [19,39,41,138,143,153–155]. However, limited research is available on the deformation behaviour of TiB₂ reinforced aluminium alloy, particularly in high strength aluminium alloys. In this chapter, the hot deformation behaviour of TiB₂ reinforced Al-Cu-Mg-Ag in compression is explained. Comparison with other unreinforced material is provided. Furthermore, constitutive equations and processing maps are developed. The objective is to identify the safe processing window of the material by investigating the flow stress and constitutive equations.

4.2. Stress-strain relationship

Fig. 4.1 to 4.3 present a series of representative true stress-true strain curves of the studied materials at various temperatures (300°C to 500°C) and strain rates (10^{-3} s^{-1} to 1 s^{-1}). It is worth noting that at least three reproducibility data were produced in this experiment. The flow stress (σ) of all three alloys followed the same pattern in which a rapid increase to the peak stress (σ_p) was observed at the beginning of the deformation and was followed by either continuous reduction until a certain strain or a 'steady state' conditions as the strain increased. This gives evidence of significant increase of dislocation density at the beginning of deformation which leads to the rapid increase in stress [30]. The steady-state regimes attained in the true stress-true strain curves in this study proves that a constant dislocation density was achieved as a result of equilibrium between work hardening and dynamic softening [30].

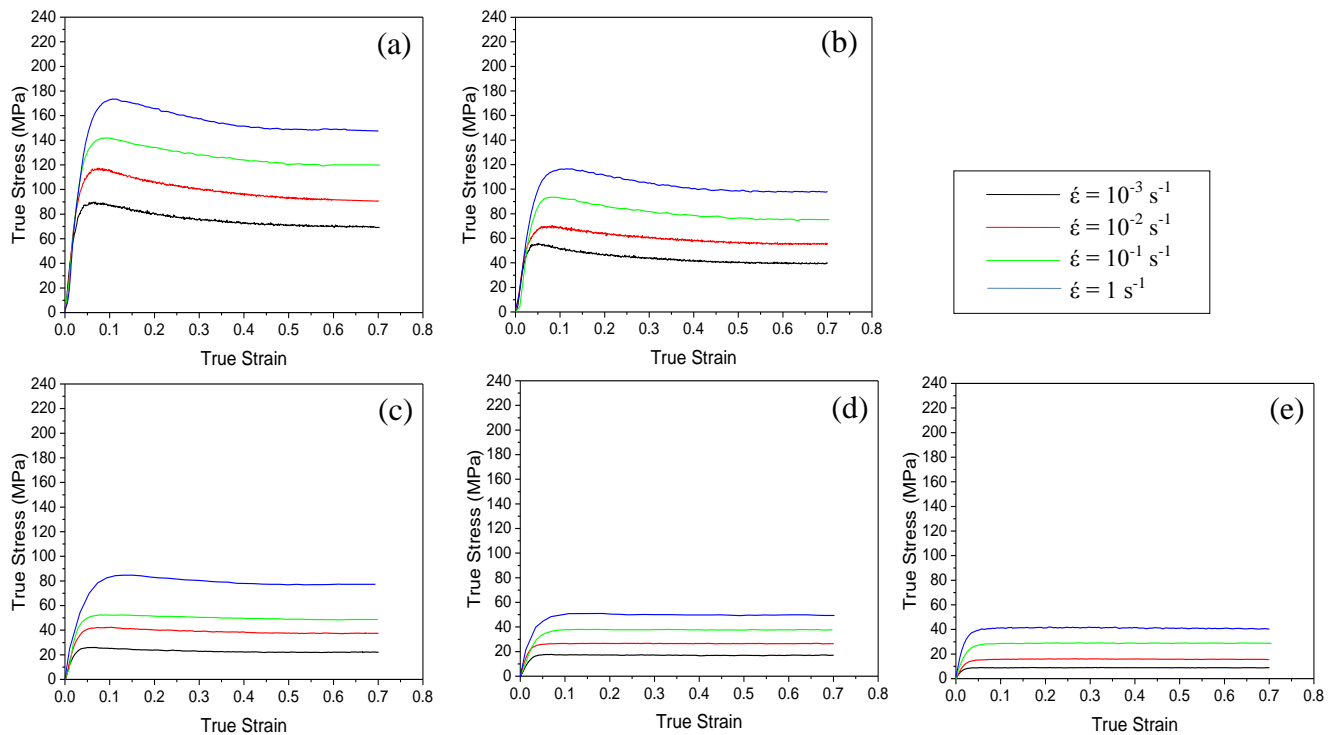


Fig. 4.1. True stress-true strain curves of the matrix alloy deformed at (a) 300°C , (b) 350°C , (c) 400°C , (d) 450°C and (e) 500°C

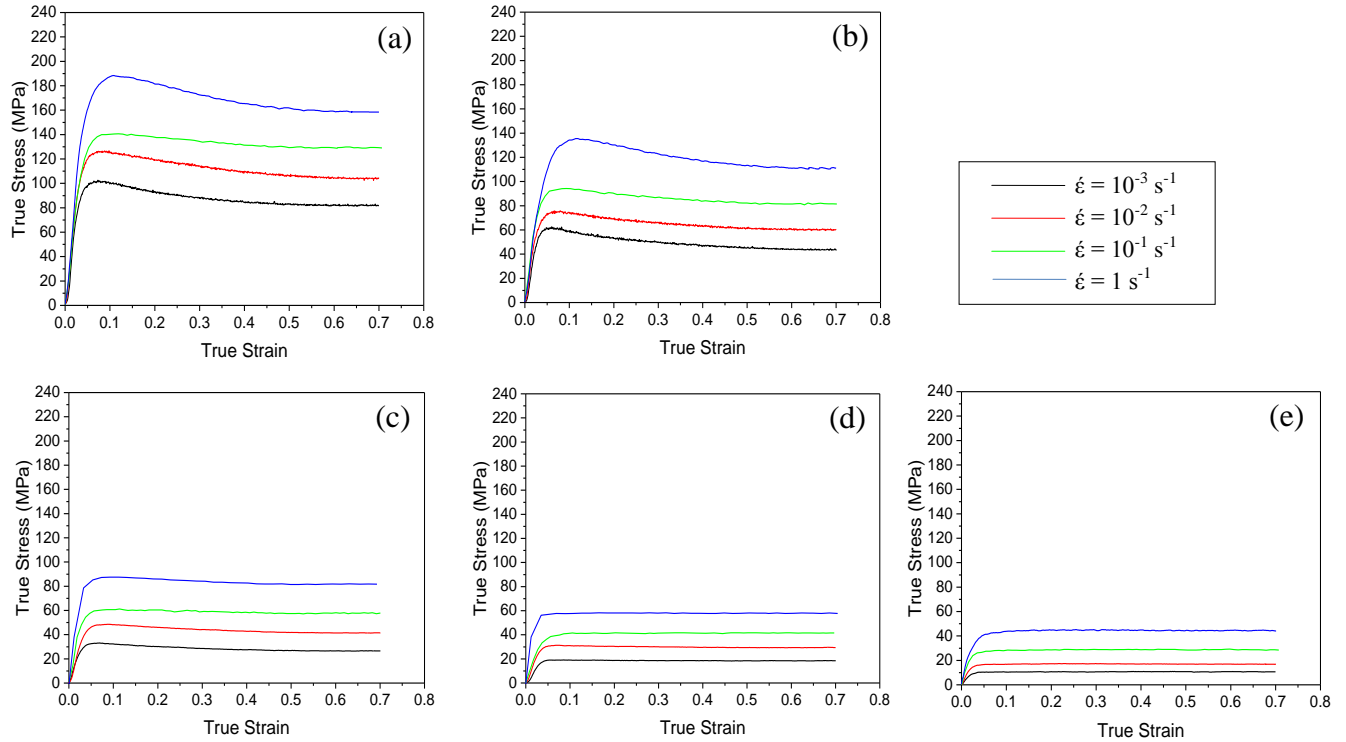


Fig. 4.2. True stress – true strain curves of 0.2Ti alloy deformed at (a) 300°C, (b) 350°C, (c) 400°C, (d) 450°C and (e) 500°C

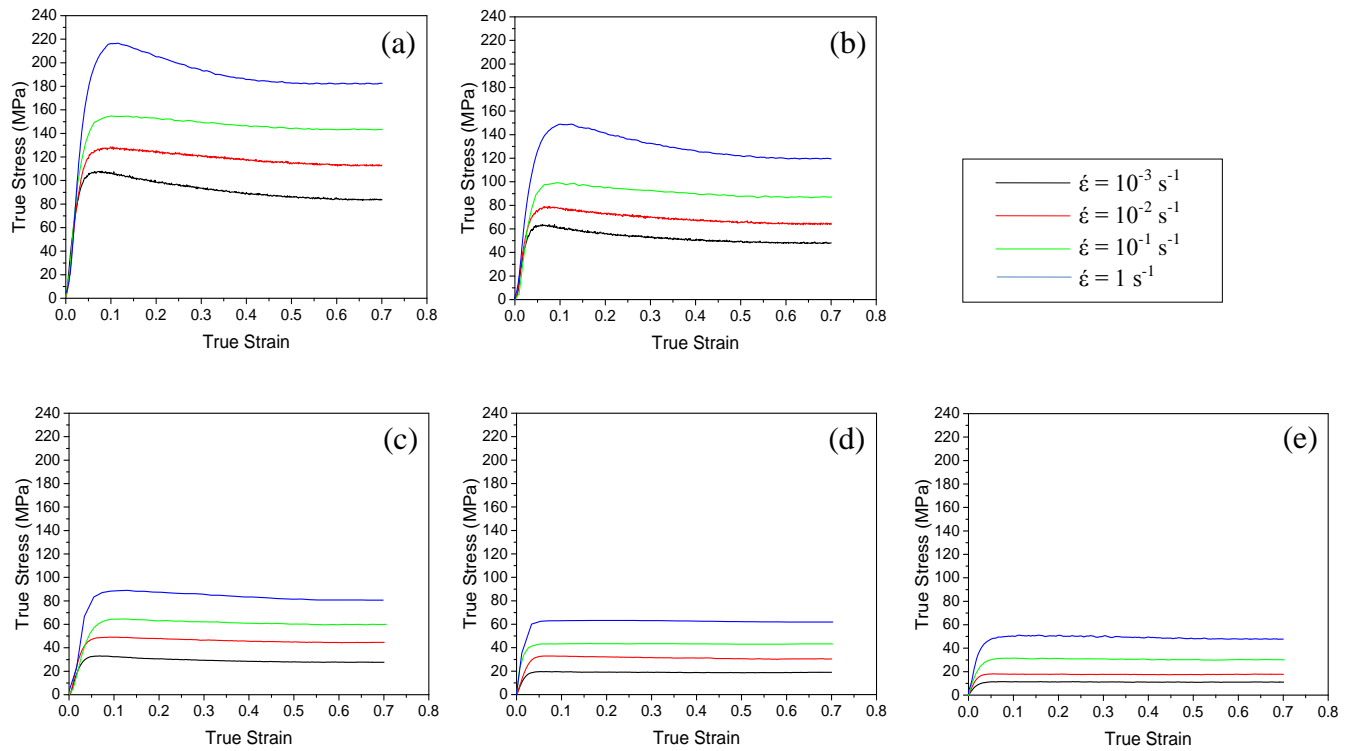


Fig. 4.3. True stress – true strain curves of 0.2Ti-4.5TiB₂ composite deformed at (a) 300°C, (b) 350°C, (c) 400°C, (d) 450°C and (e) 500°C

It has been known [104,156–160] that the flow stress of a material is defined by its deformation strain rates ($\dot{\epsilon}$) and temperatures (T). The true stress-true strain curves obtained in this study clearly showed that the flow stress increased with decreasing temperature and increasing strain rates. This can be explained where declining T and rising $\dot{\epsilon}$, the work hardening is enhanced. According to the literatures [102,161,162], at a given temperature, a higher dislocation density was created with decreasing $\dot{\epsilon}$. This leads to the higher flow stress as T decreased and $\dot{\epsilon}$ increased. For all of the materials studied, the highest flow stress was achieved when the materials were deformed at 300 °C with a strain rate of 1 s⁻¹, whereas the lowest flow stress was reached at a deformation temperature of 500 °C and a strain rate of 10⁻³ s⁻¹.

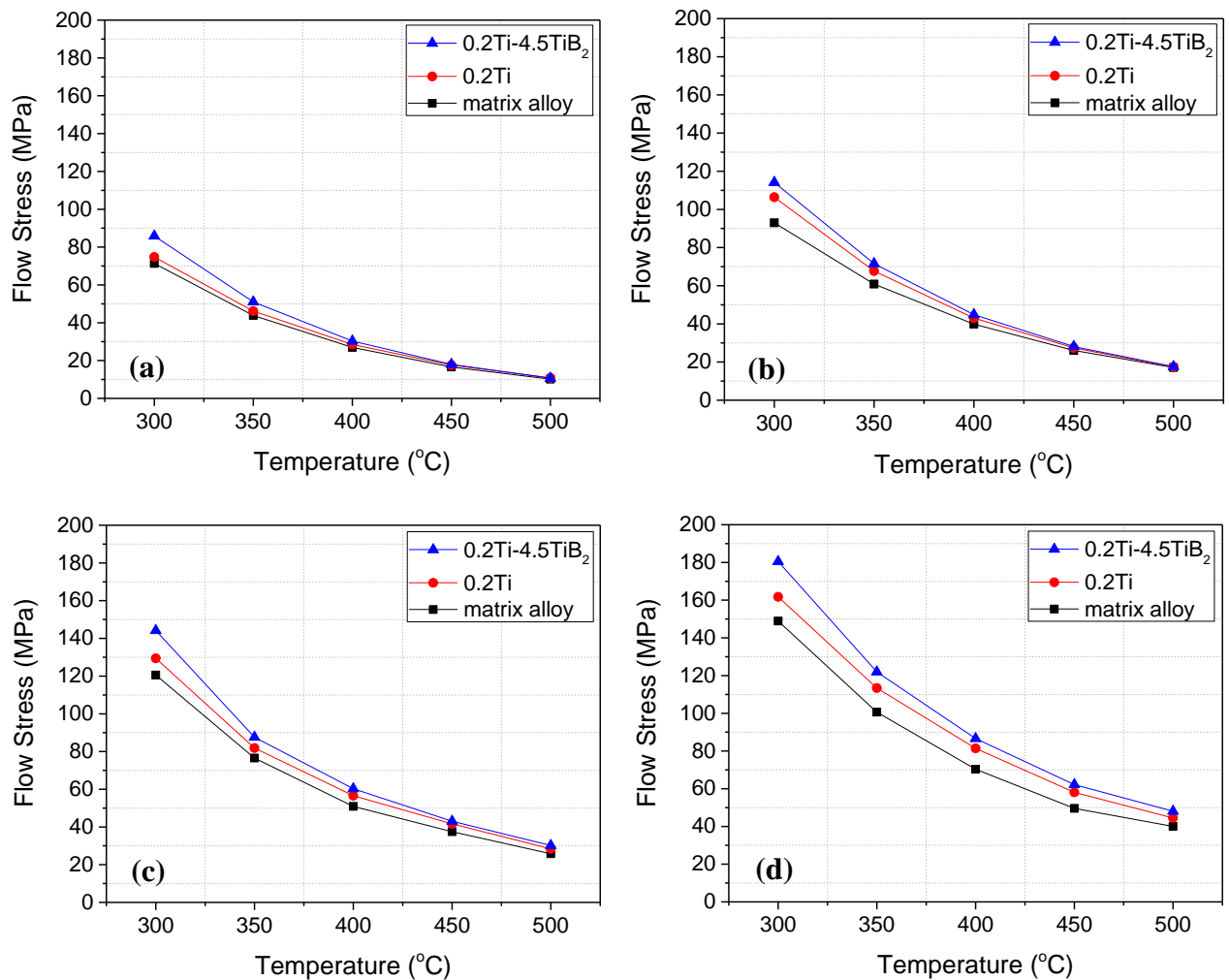


Fig. 4.4. Effect of the addition of TiB₂ particles on the flow stress at a strain 0.5 of Al-Cu-Mg-Ag alloys at (a) 10⁻³ s⁻¹, (b) 10⁻² s⁻¹, (c) 10⁻¹ s⁻¹ and (d) 1 s⁻¹

The stress characteristics derived from the compression tests can be utilised either from the steady state value (σ_s), maximum value (σ_p) if the plateau is slightly decreased, or stress (σ) at a fixed high strain if friction prevents a plateau [163]. Considering the flow stress pattern obtained in this study in which not all the plots showed peak points, especially at high T and low $\dot{\epsilon}$, the steady state regime was used for flow stress (σ) characterisation. In this thesis, σ at strain (ϵ) 0.5 was selected since a steady state value was achieved at this strain. Besides that, this value is large enough for homogeneous deformation to occur and small enough for barrelling, hence minimising the influence of barrelling. The same σ value will be used for the constitutive equation and processing map.

Fig. 4.4 demonstrates the flow stress comparison over temperature for each of the materials. As can be seen from the graph, in most conditions, the flow stress of the 0.2Ti-4.5TiB₂ composite is higher than the other two alloys. This gives evidence that dislocation movement is more hindered by the addition of TiB₂ particles, leading to the higher dislocation density and raising the flow stress. Nevertheless, it was noticed that at a given strain rate, as temperature increases, the flow stress of the 0.2Ti-4.5TiB₂ composites is getting closer to the flow stress of the other two alloys. This result is in good agreement with Leo *et al* [158] in their research on the flow stress behaviour of several types of aluminium composites. They found that at given strain rates, as the temperature increases, the flow stress of the composites gets closer to the matrix alloys and even lower than the matrix alloy. There was no clear explanation given by them for this phenomenon. However, in the case of the present study, the author of this thesis assumed that dynamic softening is responsible for this phenomenon as will later be confirmed by microstructural analysis (section 4.5). It was assumed that the dynamic softening mechanism occurring in the 0.2Ti-4.5TiB₂ composites was capable of decreasing the dislocation density to about the same level as the other two alloys.

The above observation is in accordance with the literature which is illustrated in Fig. 4.5 [164]. Assuming that material containing non-deformable particles is deformed at elevated temperature, dislocations will reach a particle by glide at a rate R_1 , depending on the applied strain rate (Fig. 4.5a). As deformation progresses, more dislocations will be accumulated at the particle which leads to a higher stress concentration at the particle. If these dislocations are able to climb around the particle (Fig. 4.5b), the stress accumulated on the particle will be eliminated at a rate R_2 , depending on the deformation temperature and particle size. If $R_2 > R_1$, the number of dislocations which are removed will be higher

than the number of arriving dislocations (Fig. 4.5c). This will lead to a decrement or even no net accumulated dislocations at particles. Hence, this explains why there was only little difference in the flow stress between 0.2Ti-4.5TiB₂ and the other two alloys as the temperature was increased. This suggests that as temperature increases, there will be little difference in deformation behaviour between the composite and the other two alloys. In other words, at high temperature and low strain rate deformation, the addition of TiB₂ will not give significant influence to the deformation mechanism.

In contrast to that, if $R_2 < R_I$, the number of dislocations which are annihilated/removed will be lower than the number of arriving dislocations (Fig. 4.5e). This will cause a complex dislocation structure at the particle, leading to higher strain hardening [164]. This condition is reflected in the higher flow stress difference between the 0.2Ti-4.5TiB₂ composite and the other two materials achieved as the temperature decreases and strain rate increases.

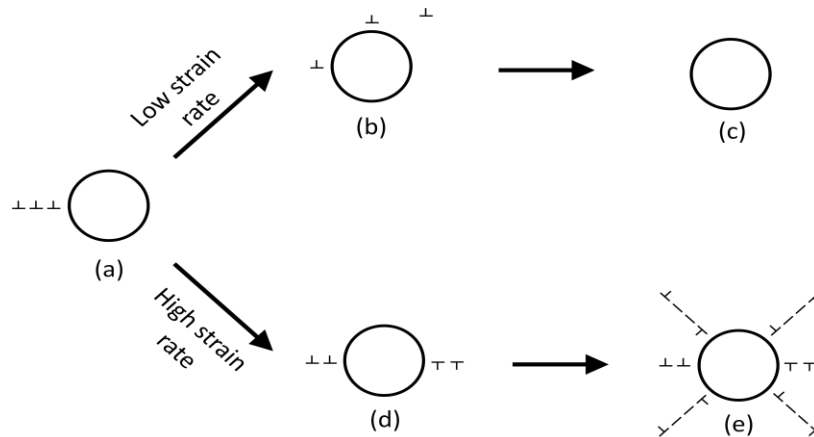


Fig. 4.5. Illustration of dislocation interaction in the presence of non-deformable particles at (b-c) low and (d-e) high strain rates [164]

4.3. Constitutive Analysis

The interdependence of flow stress (σ), deformation temperature (T) and strain rate ($\dot{\epsilon}$), and hence constitutive equations have been used widely in hot working to predict the forces during a forming processes [161,165–168], such as rolling and extrusion. Those deformation temperatures and strain rates together with strain (ϵ) define the degree of

stored energy and thus the microstructural evolution. Hence, by evaluating its constitutive relationship, one can predict not only the forces during deformation but also the deformation mechanism.

The relationship between deformation temperature and strain rate is often described as a single parameter, designated as the Zener-Hollomon parameter (Z) [30,102,104,105,163,169]. As the Zener-Hollomon parameter is a function of deformation temperature and strain rate, it can be employed to analyse the mechanism during deformation. At high values of Z (low temperature and high strain rate), deformation is dominated by work hardening as multiple dislocations are generated, whereas at low Z values (high temperature and low strain rate), a dynamic softening process is dominant. Therefore, in addition to strain, the microstructure after hot deformation will also be dependent on the Zener-Hollomon parameter. The Zener-Hollomon parameter can be defined as :

$$Z = \dot{\epsilon} \exp\left(\frac{Q}{RT}\right) \quad (4-1)$$

where Q is an activation energy, R is the universal gas constant (8.314 J/mol.K), T is the absolute temperature and $\dot{\epsilon}$ is the strain rate. Furthermore, an Arrhenius equation [30,104,159,166] can also be used to express the relationship between strain rate and deformation temperature

$$\dot{\epsilon} = f(\sigma) \exp\left(-\frac{Q}{RT}\right) \quad (4-2)$$

in which the function of $f(\sigma)$ is defined by the degree of stress. For the steady state at a low flow stress data ($\alpha\sigma < 0.8$), $f(\sigma)$ is described using a power law relation (Eq. (4-3)), while an exponential relation (Eq. (4-4)) is utilised to describe steady state condition at high flow stress data ($\alpha\sigma > 1.2$).

$$f(\sigma) = A' \sigma^{n_1} \quad (4-3)$$

$$f(\sigma) = A'' \exp(\beta\sigma) \quad (4-4)$$

where A' , A'' , β and n_1 are material constants.

Those relations were found to be similar with the steady state condition relations for creep, which also occurred as a result of the equilibrium between strain-hardening and dynamic softening process. This similarity led Sellars and Tegart [170] to propose a hyperbolic-sine law equation which covers a wide range of stresses. This hyperbolic-sine law can be expressed as

$$f(\sigma) = A[\sinh(\alpha\sigma)]^n \quad (4-5)$$

Combining Eq. (4-2) and Eq. (4-5), the Arrhenius equation can be expressed as

$$\dot{\varepsilon} = A[\sinh(\alpha\sigma)]^n \exp\left(-\frac{Q}{RT}\right) \quad (4-6)$$

By combining the Zener-Hollomon and Arrhenius equations, the Zener-Hollomon parameter can be expressed as a relation to the flow stress (σ), which is

$$Z = A[\sinh(\alpha\sigma)]^n \quad (4-7)$$

where A and n are the material constants, and α is the stress multiplier which is defined as

$$\alpha = \frac{\beta}{n_1} \quad (4-8)$$

where β and n_1 are the material constant and it could be analysed by substituting the value of $f(\sigma)$ to Eq. (4-2) which gives us the following relationship

$$\dot{\varepsilon} = A'\sigma^{n_1} \quad (4-9)$$

$$\dot{\varepsilon} = A'' \exp(\beta\sigma) \quad (4-10)$$

Taking a natural logarithm of both sides of Eq. (4-9) and Eq. (4-10) gives

$$\ln(\sigma) = \frac{1}{n_1}(\ln \dot{\varepsilon} - \ln A') \quad (4-11)$$

$$\sigma = \frac{1}{\beta}(\ln \dot{\varepsilon} - \ln A'') \quad (4-12)$$

And reconstructing those equations gives us n_1 and β values which can be expressed respectively as

$$n_1 = \frac{(\ln \dot{\epsilon} - \ln A')}{\ln(\sigma)} \quad (4-13)$$

$$\beta = \frac{(\ln \dot{\epsilon} - \ln A'')}{\sigma} \quad (4-14)$$

Hence, considering A' and A'' are constants, n_1 and β values can be determined from the slopes of $\ln(\dot{\epsilon}) - \ln(\sigma)$ and $\ln(\dot{\epsilon}) - \sigma$ graphs at various temperatures, respectively.

Using the experimental results from hot compression testing, all the material constants mentioned above are able to be determined for all the materials investigated in this study. Subsequently, by substituting the flow stress and corresponding strain rate into Eq. (4-11) and (4-12) gives a relationship between flow stress and strain rate. Using 0.2Ti-4.5TiB₂ composites as an example, plots of $\ln(\dot{\epsilon}) - \ln(\sigma)$ and $\ln(\dot{\epsilon}) - \sigma$ were derived as is shown in figure 4.6 and n_1 , β material constants were defined from the slope of these plots respectively. For 0.2Ti-4.5TiB₂ composites, average values of n_1 and β for the range of studied temperature were obtained to be 6.8467 and 0.1217 respectively. Hence, substituting these values to Eq. (4-8) gives the value of α as 0.0177 MPa⁻¹. A similar method was applied to the other materials for defining those material constants. Table 4.1 provides all the material constants including activation energy in the constitutive equations for each of the materials studied in this thesis and their implication towards hot deformation will be discussed below.

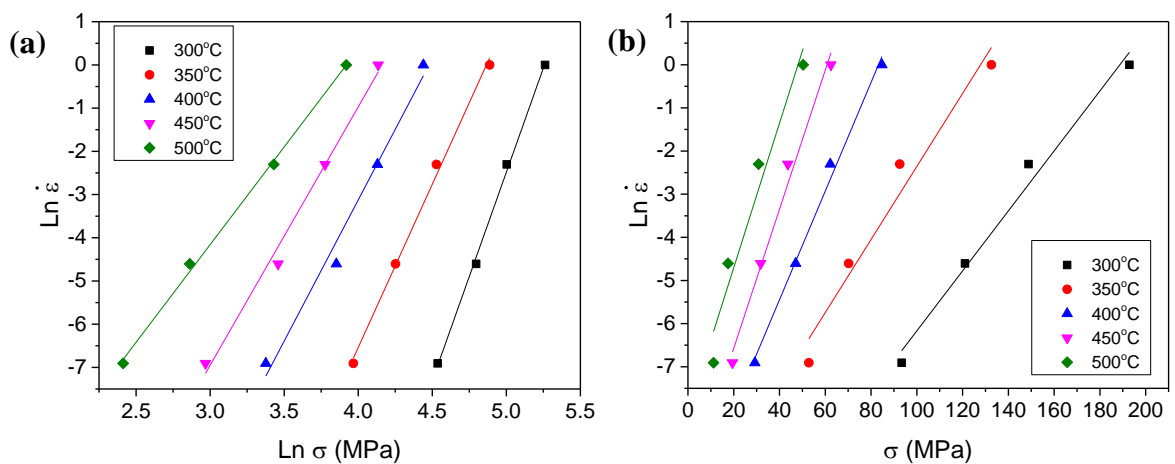


Fig. 4.6. Graph of (a) $\ln(\dot{\epsilon}) - \ln(\sigma)$ and (b) $\ln(\dot{\epsilon}) - \sigma$ of 0.2Ti-4.5TiB₂ material

4.3.1 Effect of TiB₂ Reinforcement on the Material Constants

Beginning with the constant value designated as α . As mentioned earlier the relationship between metal's flow stress and strain rate can be defined either by a power law relation or an exponential relation depending on the degree of stress. At a low stress which falls in the region of $\alpha\sigma < 0.8$, a power relation is favoured, while at a high stress defined as $\alpha\sigma > 1.2$, the flow stress – strain rate relationship is best described with an exponential relation. Therefore, the constant α can be defined as a reciprocal of the flow stress which indicates where the flow stress – strain rate relationship changes from a power to an exponential relationship [165]. It has been known that the flow stress-strain rate constitutive equations were first used to describe deformation mechanisms in creep [104,105,171]. To help addressing the importance of α in hot deformation, creep was used as an analogy since the steady state creep behaviour is similar to the hot deformation behaviour which is controlled by dislocation mobility [165,170]. From Eq. (4-8), we know that the value of α is dependent on the value of n_1 and β . These n_1 and β values define the creep rate as described in Eq. (4-9) and (4-10). Based on those equations, it is evident that for creep, the greater the values of n_1 and β , the greater the creep rate. Furthermore, the creep rate of materials is influenced by several factors such as the existence of a solid solution and second phase particles. During creep deformation, the existence of those particles will impede the mobility of dislocations present, leading to a decreasing of the creep rate [165]. Consequently, the more resistant a material is to dislocation motion, the lower the creep rate, meaning that the lower the n_1 and β value. Furthermore, the value of β has been known to be more sensitive than the value of n_1 [165], and thus the ratio of $\beta:n_1$ decreases with decreasing creep rate. In other words, a lower ratio of $\beta:n_1$ indicates a higher creep resistance. Based on Eq. (4-8), a lower ratio of $\beta:n_1$ will give a lower value of constant α . Consequently, using this creep analogy to the hot working, it could be concluded that the material which has a higher resistance to deformation will have a lower constant α , both in hot deformation as well as in creep [165]. To simplify, the constant α can be defined as the ability of a material to be deformed in which the value increases with increasing ease of deformation.

The constant α for each material provided in Table 4.1 clearly shows that α is decreasing with the addition of Ti and TiB₂ with sequences of $\alpha_{0.2\text{Ti}-4.5\text{TiB}_2} < \alpha_{0.2\text{Ti}} < \alpha_{\text{matrix alloy}}$. As already explained above, the magnitude of α indicates the ability of a material to facilitate

deformation. As will be explained in Chapter 5, finer grains were observed in 0.2Ti alloy and 0.2Ti-4.5TiB₂ composites. Besides a finer grain size, the existence of Al₃Ti and both Al₃Ti and TiB₂ particles were also observed in the 0.2Ti alloy and 0.2Ti-4.5TiB₂ composites respectively. Those aspects will affect the deformation behaviour. During hot deformation, these particles were suspected to hinder dislocation motion, leading to the decrement of deformability. This was supported by the higher flow stress level achieved in the 0.2Ti and 0.2Ti-4.5TiB₂ material ($\sigma_{0.2\text{Ti-4.5TiB}_2} > \sigma_{0.2\text{Ti}} > \sigma_{\text{matrix alloy}}$) as shown in Fig. 4.4, meaning that a greater load was required to deform these materials. Consequently, it is expected, and it was certainly found that the value of α in the 0.2Ti and 0.2Ti-4.5TiB₂ materials was lower than the matrix alloy. From these results, it could be concluded that the constant α value obtained in this study exhibited the correct magnitude order for the particular materials studied in this research.

Table 4.1. Material constants in constitutive equations for each material

Material	α (MPa ⁻¹)	n	A (s ⁻¹)	Q_{HW} (kJ mol ⁻¹)
0.2Ti-4.5TiB ₂	$0.0177 \pm 9.67\text{E-}5$	4.54 ± 0.049	4.68×10^{14}	213 ± 0.093
0.2Ti	$0.0195 \pm 6.68\text{E-}5$	4.56 ± 0.12	1.64×10^{14}	209 ± 0.72
Matrix alloy	0.0216 ± 0.00022	4.56 ± 0.13	1.46×10^{14}	208 ± 0.36

4.3.2 Effect of TiB₂ Reinforcement on the Hot Working Activation Energy (Q_{HW})

Furthermore, one of the most important values that can be derived from hot working is the activation energy (Q_{HW}). In deformation, the activation energy is defined as the free energy barrier to dislocation slipping on slip planes, which indicates the difficulty degree of plastic deformation. This value varies depending on the deformation parameter (range of T and $\dot{\epsilon}$, lubrication etc) and also material composition and microstructure[102]. With increasing solute content in the alloy, the Q_{HW} value increases since the solute will act as an obstacle for dislocation movement during deformation, especially in low temperature deformation. When there is a change in the restoration process which leads to the microstructure changing, for example from DRV to DRX, enhancement of the Q_{HW} value occurs. A higher Q_{HW} value is also observed in the dispersoid material due to dislocation bypassing or particle coarsening leading to the loss in effectiveness [102]. Variation of the flow stress with temperature, especially with decreasing temperature, will reflect in its activation

energy. Materials in which the flows stress increases sharply with decreasing temperature will have a higher activation energy [102]. Consequently, by analysing the activation energy, one can predict the flow stress required at the finishing step of the process, such as rolling or forging. Finally, the activation energy can be calculated by rearranging and differentiating the Arrhenius equation in Eq. (4-6) which is described as:

$$Q_{HW} = R \left[\frac{\partial \ln \dot{\epsilon}}{\partial \ln [\sinh(\alpha\sigma)]} \right]_T \left[\frac{\partial \ln [\sinh(\alpha\sigma)]}{\partial (1/T)} \right]_{\dot{\epsilon}} = RnS \quad (4-15)$$

where σ is the flow stress, n is the mean slope of plots of $\ln(\dot{\epsilon}) - \ln[\sinh(\alpha\sigma)]$ at different temperatures and S is the mean slope of plots of $\ln[\sinh(\alpha\sigma)] - 1/T$ at various strain rates. Using 0.2Ti-4.5TiB₂ data as an example, constants n and S were calculated and the plots are shown in Fig. 4.7. The average results of this calculation for each studied material are provided in Table 4.1.

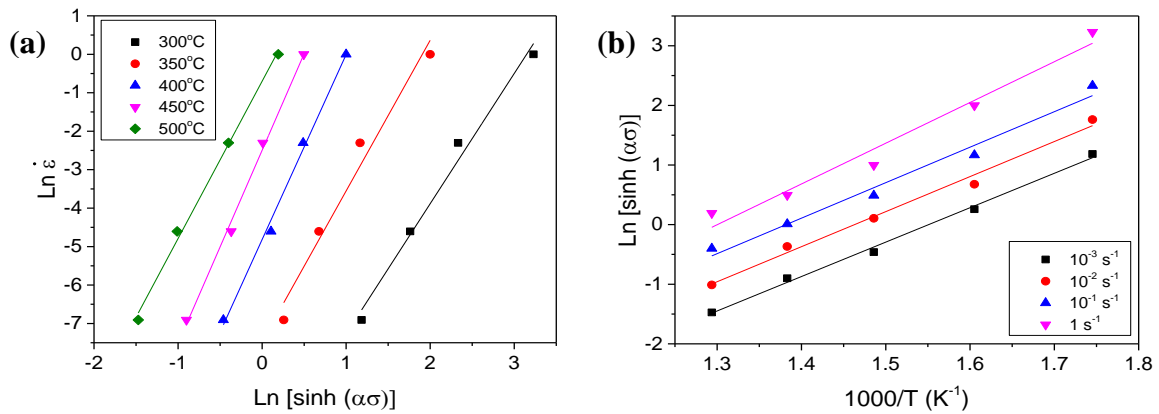


Fig. 4.7. Plots of (a) $\ln(\dot{\epsilon}) - \ln[\sinh(\alpha\sigma)]$ and (b) $\ln[\sinh(\alpha\sigma)] - 1/T$ for 0.2Ti-4.5TiB₂

From Table 4.1, it can be clearly seen that 0.2Ti-4.5TiB₂ has the highest activation energy with the Q_{HW} value of 213 kJ mol⁻¹, followed by the 0.2Ti alloy (209 kJ mol⁻¹) and the matrix alloy (208 kJ mol⁻¹). This indicates that the addition of TiB₂ particles to the Al-Cu-Mg-Ag matrix alloy reduces the ductility of the material and hence increases the resistance of the material to plastic deformation. The higher Q_{HW} value achieved in the 0.2Ti-4.5TiB₂ composite suggests a more complex dislocation interaction due to the existence of TiB₂ particles [102]. This is reflected from the higher flow stress achieved in the 0.2Ti-4.5TiB₂ composites. Furthermore, its more rapid rising to high σ with decreasing T than the other two materials also confirm its higher Q_{HW} achieved in this study. As described before in the

plots of σ - T in Fig. 4.4, a steeper slope was observed in the 0.2Ti-4.5TiB₂ composite as temperature decreases, suggesting a rapid increment of the flow stress with decreasing temperature. From this we can basically predict that the finishing load required to deform the 0.2Ti-4.5TiB₂ composites during rolling will be higher than the other two alloys. And it was indeed observed that the 0.2Ti-4.5TiB₂ composite exhibited a higher finishing load during rolling which will be described in Chapter 5. Hence, in industry, the activation energy could be used to analyse how rapid the flow stress increases with decreasing temperature to the finishing deformation temperature, $0.5 T_m$ (300°C or 200°C), giving an awareness of high finishing forces in rolling or forging [102,105].

Moreover, it is worth comparing the Q_{HW} value achieved in this study with other existing study. Literature study [105,163] shows that the Q_{HW} value of Al of various purity falls in the range of 140 – 160 kJ mol⁻¹. The higher Q_{HW} value resulted in this study suggests that more complex dislocation was occurred during deformation. The existence of precipitates, dispersoids and particles in these materials was suspected to impede dislocation movement during deformation which led to the higher Q_{HW} value than other purity of Al. Furthermore, Liu *et al* [172] in their research about flow behaviour of Al-5.3Cu-0.8Mg-0.5Ag alloy reported the Q_{HW} value of 196.27 kJ mol⁻¹. By comparing this value with the Q_{HW} value of matrix alloy (208 kJ mol⁻¹), it could be concluded that this study is in a good agreement with Liu *et al* [172] study. The slightly higher value obtained in this study was suspected due to different range of test temperature and different concentration of dispersoid and precipitates formed since their volume fraction and size distribution are significantly influenced by their solidification and homogenisation parameters.

Finally, the constant A can be derived by taking the natural logarithm from Eq. (4-7), giving an equation of

$$\ln Z = \ln A + n \ln[\sinh(\alpha\sigma)] \quad (4-16)$$

Hence, the constant A can be calculated by plotting $\ln Z - \ln[\sinh(\alpha\sigma)]$ in which the intercept of this plot gives $\ln A$ values. Fig. 4.8 showed the linear relationship of this plot for each of the studied materials. While the average of constant A values for each of the studied materials is described in Table 4.1.

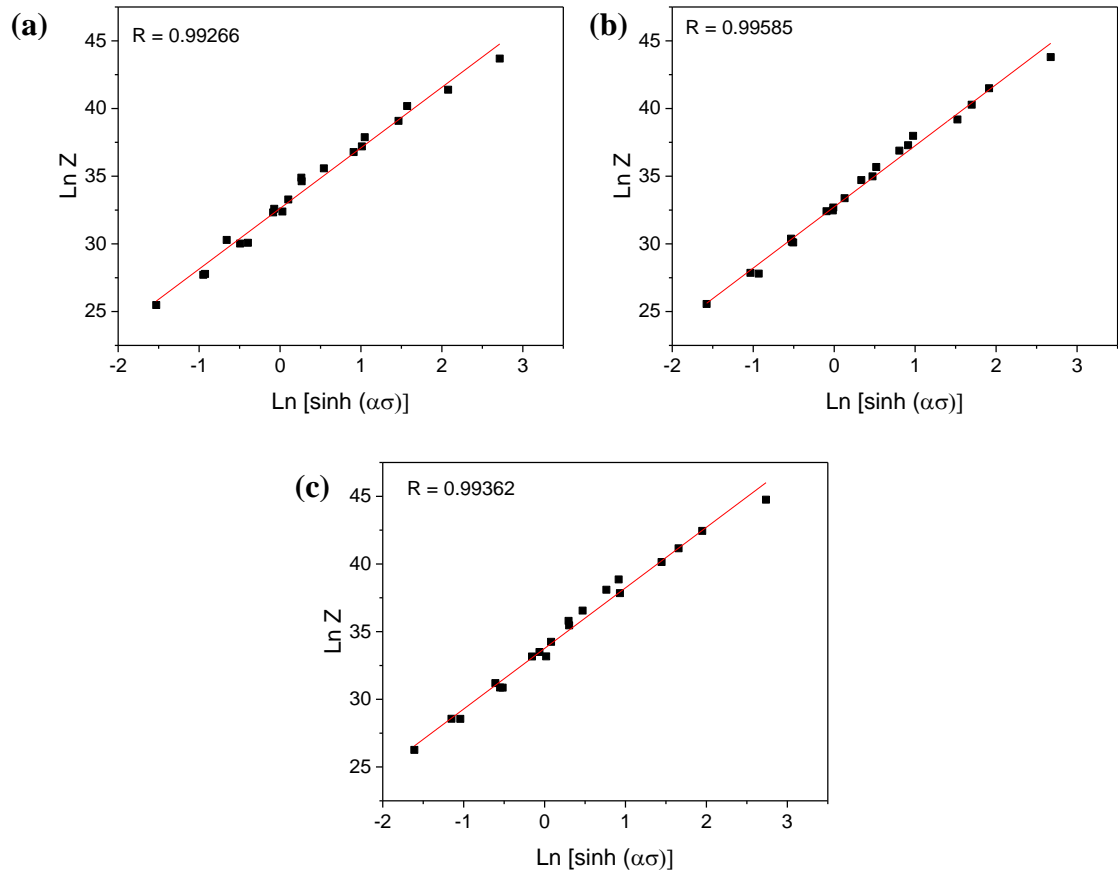


Fig. 4.8. Relationship between Zener-Hollomon parameter with flow stress for (a) matrix alloy; (b) 0.2 Ti alloy and (c) 0.2Ti-TiB₂ composite

4.3.3 Verification of Constitutive Equation

Using the same procedures described above, all the parameters, α , n , Q_{HW} and $\ln A$ for the 0.2Ti-4.5TiB₂ composite can be derived at different true strains. In this thesis, true strain from 0.1 to 0.7 was taken for verifying the constitutive equations. The variations in material constant as a function of true strain were then fitted with a third-order polynomial functions as listed in Eq.(4-17)

$$\alpha = B_0 + B_1\varepsilon + B_2\varepsilon^2 + B_3\varepsilon^3 \quad (4-17)$$

$$n = C_0 + C_1\varepsilon + C_2\varepsilon^2 + C_3\varepsilon^3$$

$$Q_{HW} = D_0 + D_1\varepsilon + D_2\varepsilon^2 + D_3\varepsilon^3$$

$$\ln A = E_0 + E_1\varepsilon + E_2\varepsilon^2 + E_3\varepsilon^3$$

The corresponding coefficients for the above equation are described in the table below.

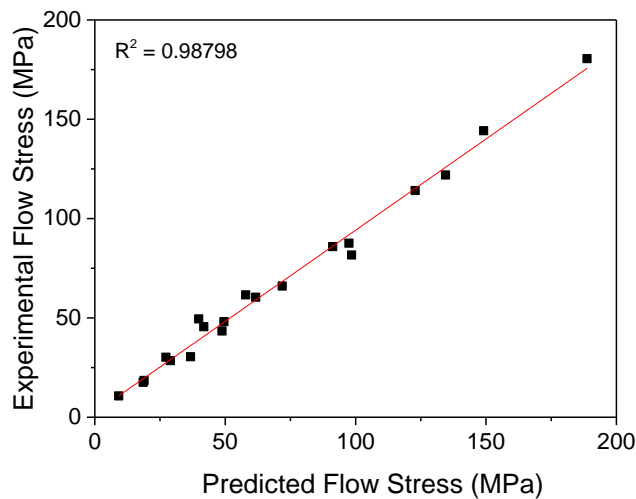
Table 4.2. Coefficient of polynomial fit corresponding to the Eq. (4-17) for 0.2Ti-4.5TiB₂ composites

α		n		Q_{HW}		$\ln A$	
Coef.	Value	Coef.	Value	Coef.	Value	Coef.	Value
B ₀	0.01655	C ₀	4.60412	D ₀	229.99094	E ₀	37.1838
B ₁	0.00219	C ₁	0.06794	D ₁	-77.13412	E ₁	-15.18942
B ₂	0.00976	C ₂	-1.50189	D ₂	82.27679	E ₂	18.5082
B ₃	-0.00225	C ₃	1.41401	D ₃	-32.91167	E ₃	-9.69948

Furthermore, by rearranging Eq. (4-7), the flow stress can be expressed as the Zener-Hollomon parameter as follows

$$\sigma = \frac{1}{\alpha} \ln \left\{ \left(\frac{Z}{A} \right)^{\frac{1}{n}} + \left[\left(\frac{Z}{A} \right)^{\frac{2}{n}} + 1 \right]^{\frac{1}{2}} \right\} \quad (4-18)$$

Using Eq. (4-18), the predicted flow stress was then calculated and plotted against the experimental data as described in Fig. 4.9. It can be clearly seen that the predicted flow stress has a good correlation with the experimental data which is indicated by a correlation coefficient greater than 98%.

**Fig. 4.9.** Correlation between predicted flow stress and experimental flow stress of the 0.2Ti-4.5TiB₂ composite showing the accuracy between both experimental data and predicted data

4.4. Processing Maps

Processing maps of all three materials studied were developed to identify the stable and instable regions during processing. Using the flow stress data derived from compression tests, the processing maps for each of the studied materials were established. The same stress characteristics as for the constitutive equation at a strain = 0.5 were used for processing map calculations to correlate both results.

4.4.1. Strain Rate Sensitivity Parameter

As has been explained in Chapter 2, a processing map was developed based on the strain rate sensitivity (m) for it defines the relative partitioning of power between heat generation and microstructural changes [110]. In addition to that, strain rate sensitivity has also been known as a good indicator for plastic deformation since it is related to the dislocation concept during plastic deformation. Hence, it is worth identifying strain rate sensitivity parameters for each of the materials studied in this thesis.

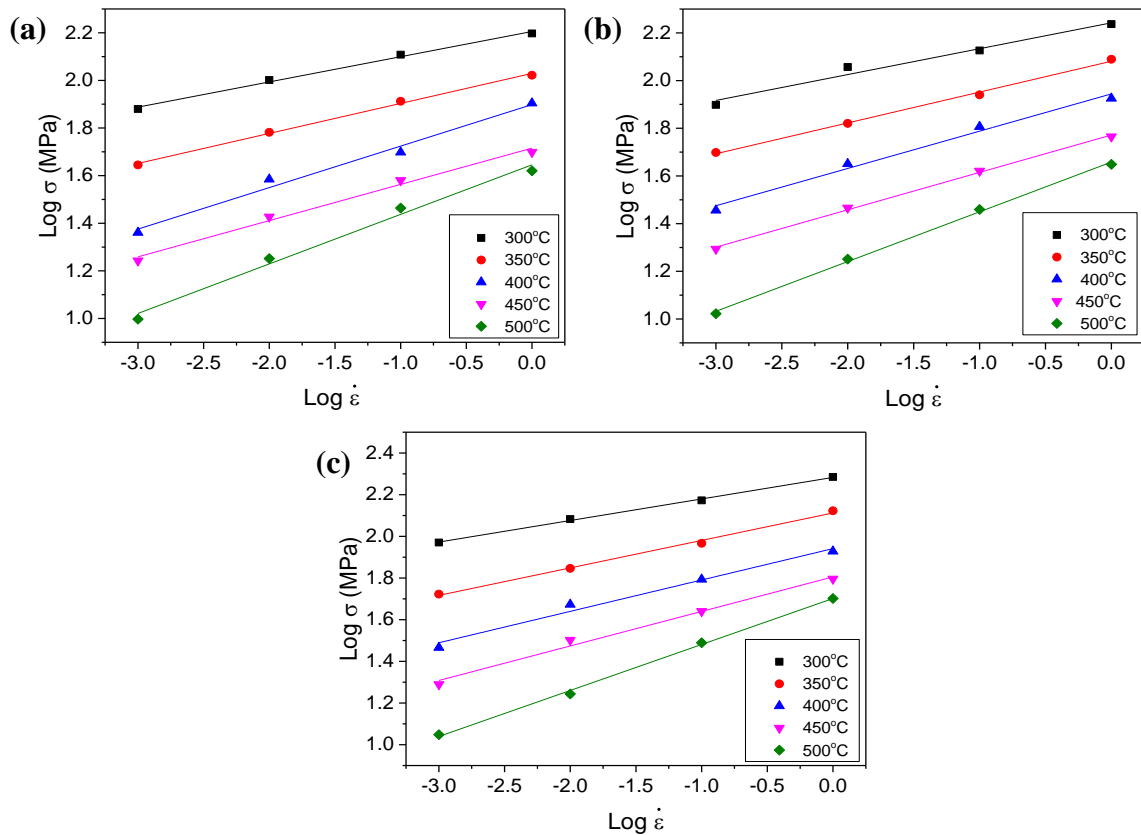


Fig. 4.10. Log stress vs log strain rates of (a) matrix alloy; (b) 0.2Ti alloy and (c) 0.2Ti-4.5TiB₂ composite

Fig. 4.10 shows the log stress vs log strain rates of each of the studied materials. It can be clearly seen that generally, as temperature increases, strain rate sensitivity in each of the studied materials increases as it showed a steeper slope with increasing temperature. Average strain rate sensitivities of 0.16, 0.158 and 0.156 were observed in the matrix alloy, 0.2Ti alloy and 0.2Ti-4.5TiB₂ composites respectively. It is worth noting that, although strain rate sensitivity is generally used to define superplasticity of the material, it is sensitive to the initial microstructure. And hence, the strain rate sensitivity observed in this section can't be really used to define superplasticity of the sheet materials.

4.4.2. Development of Processing Maps

Table 4.3 shows flow stress (σ) values for the 0.2Ti-4.5TiB₂ composite as a function of temperature (T), strain rate ($\dot{\epsilon}$) and strain (ϵ). The other material's flow stress values will be provided in Appendix A. This flow stress data was then processed by using linear interpolation of $\log \sigma$ vs $1/T$ data at a constant strain rate for the adiabatic heating correction. Furthermore, $\log \sigma$ vs $\log \dot{\epsilon}$ data at constant temperature and strain were fitted using a cubic spline function. Subsequently, the strain rate sensitivity (m) was calculated using Eq. (2-8) as a function of strain rate. Using the m value, the efficiency of power dissipation (η) and instability parameter ξ were calculated. The same way of calculation was conducted for other materials and strains. Fig. 4.11 shows the processing map at a strain 0.5 of all studied materials which were developed by superimposing the instability map to the power dissipation map and plotting as an iso-efficiency contour maps. In this thesis, the efficiency of power dissipation (η) was plotted in percent.

Table 4.3. Flow stress (MPa) data of 0.2Ti-4.5TiB₂ composites at different temperature, strain rate and strain

Strain	Strain Rate (s ⁻¹)	Temperature (°C)				
		300	350	400	450	500
0.1	0.001	106.0	61.7	31.8	19.2	11.0
	0.01	127.2	77.8	49.3	33.2	17.9
	0.1	154.7	98.7	64.4	44.3	31.5
	1	212.7	148.9	88.7	63.6	50.1
0.2	0.001	98.6	55.9	30.0	19.0	11.0
	0.01	125.4	73.0	48.2	31.7	18.2
	0.1	152.6	95.4	63.3	44.0	30.9
	1	204.9	141.4	87.3	63.7	51.0

0.3	0.001	93.4	52.8	29.3	19.5	11.2
	0.01	121.1	70.2	47.1	31.8	17.5
	0.1	148.8	92.6	62.2	43.7	30.9
	1	192.9	132.6	84.8	62.5	50.3
0.4	0.001	89.0	50.2	28.7	19.3	11.2
	0.01	116.9	67.7	45.2	30.6	18.0
	0.1	145.8	89.3	60.9	42.8	29.8
	1	184.6	126.2	83.3	61.7	49.4
0.5	0.001	85.9	49.5	28.5	18.5	10.7
	0.01	114.1	66.0	45.5	30.4	17.6
	0.1	144.2	87.6	60.4	43.4	30.2
	1	180.5	121.9	81.6	61.6	48.1
0.6	0.001	84.2	48.5	27.3	19.1	11.2
	0.01	113.6	64.4	44.8	30.6	17.7
	0.1	143.1	86.4	60.3	43.5	30.4
	1	178.9	119.7	80.7	61.7	48.1

It is clear from Fig. 4.11 that the workability of the 0.2Ti-4.5TiB₂ composite is limited to the high temperature and low strain rates, in the range of 400 – 500 °C which is shown by its high efficiency of power dissipation ($\eta > 30$ pct). The highest efficiency of 37 pct was achieved at the domain of 500 °C in the range of strain rates 10^{-2} s^{-1} to 10^{-1} s^{-1} . As temperature decreases, the efficiency of power dissipation decreases. The other two alloys exhibited the same behaviour in which the stable areas were generally observed at high temperatures and low strain rates.

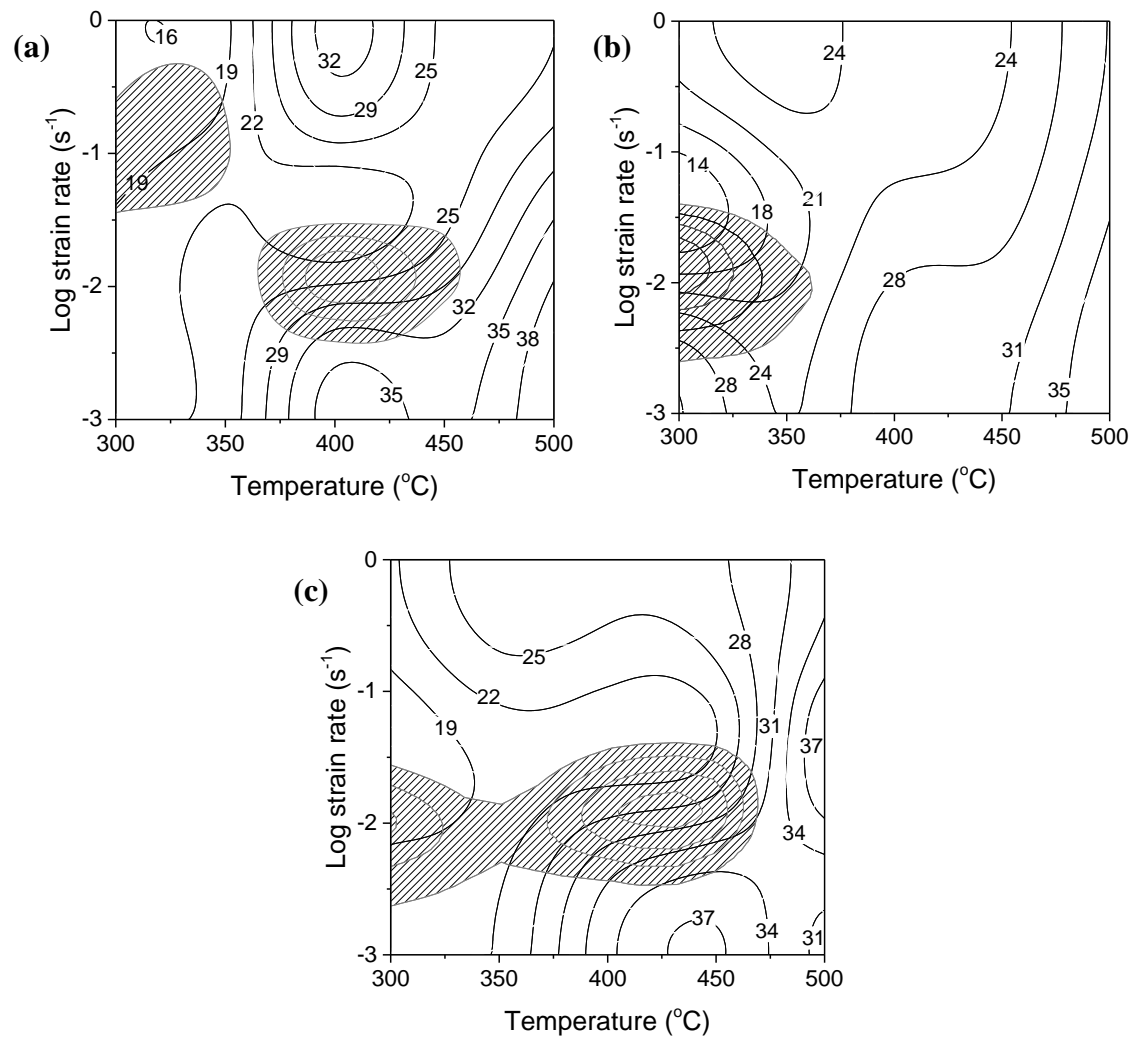


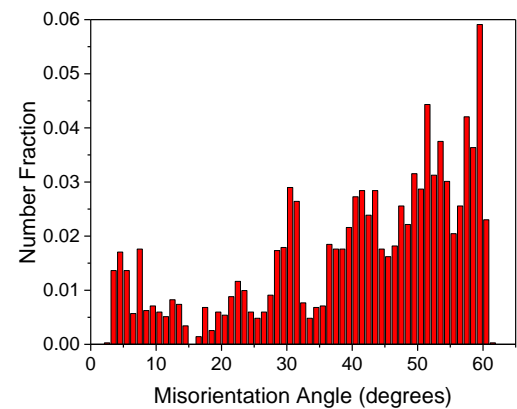
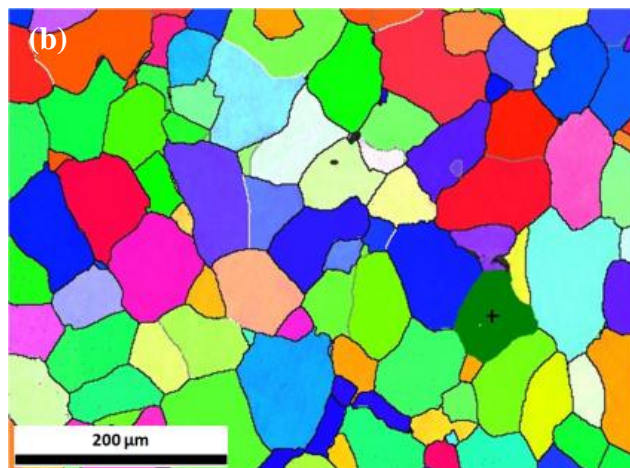
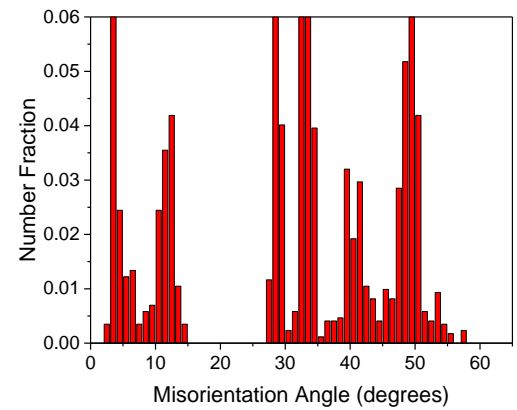
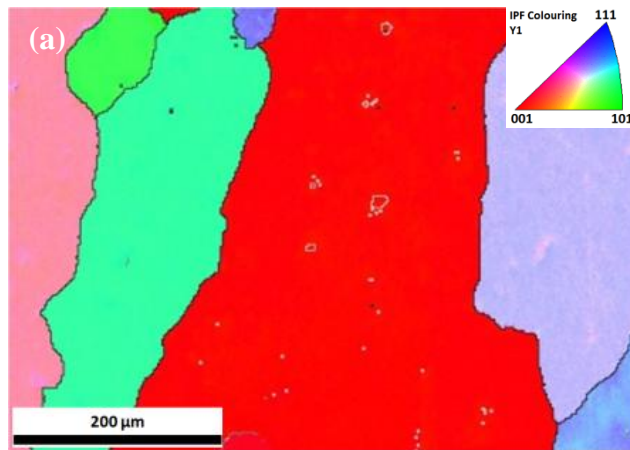
Fig. 4.11. Processing map at strain of 0.5 of (a) matrix alloy; (b) 0.2Ti and (c) 0.2Ti-4.5TiB₂ composite

4.5. Effect of Strain Rate and Temperature on the Microstructure

EBSD analysis was carried out on the deformed specimens of each studied material to investigate the effect of TiB₂ on the deformation mechanisms. Specimens deformed at temperatures of 300 $^{\circ}C$, $10^{-1} s^{-1}$ and 500 $^{\circ}C$, $10^{-3} s^{-1}$ were chosen for observation as a representative of high Z and low Z values respectively in order to understand the effect of temperature and strain rate on the deformation mechanism. In addition to that, as-homogenised orientation maps were also provided to give a better understanding regarding microstructural evolution during deformation.

Fig. 4.12 shows the inverse pole figure (IPF) maps of as-homogenised materials. Furthermore, Fig. 4.13 and Fig. 4.14 show the IPF maps of the deformed microstructure of

each studied material under various deformation conditions after compression to a strain of 0.7. As have already known that the deformation at elevated temperature involves the generation and migration of dislocations as well as the annihilation of dislocations, this leads to the formation of subgrains and grains which indicates the dynamic softening mechanism during deformation. Consequently, in order to understand the mechanism during deformation, in these EBSD maps, low angle grain boundaries (LAGBs), $0 - 8^\circ$ [102], are indicated with grey lines, medium-angle grain boundaries (MAGBs), $8 - 15^\circ$ [102], are indicated with white lines and high-angle grain boundaries (HAGBs), $>15^\circ$ [102], are indicated with black lines. Grain boundaries are characterised by HAGBs, while LAGBs and MAGBs form a subgrain structure [22].



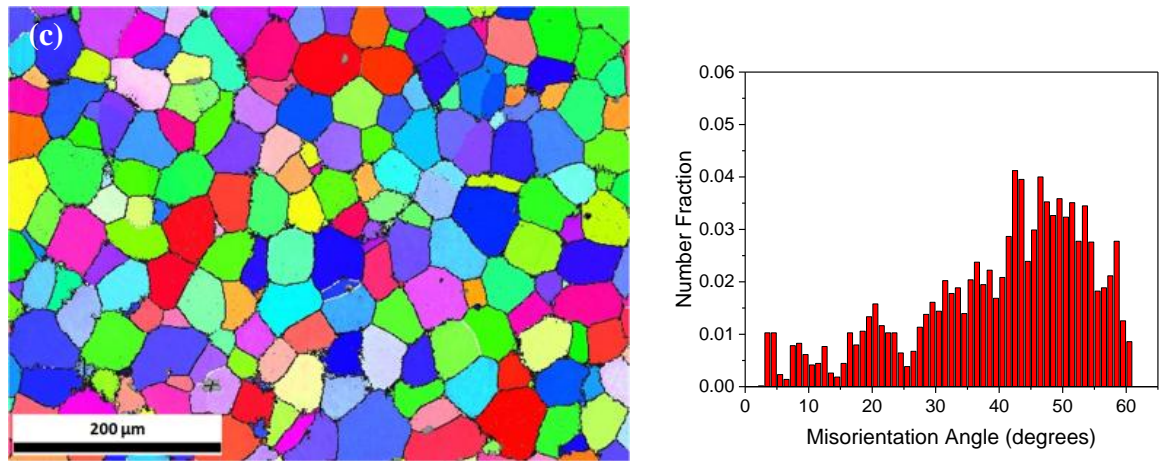
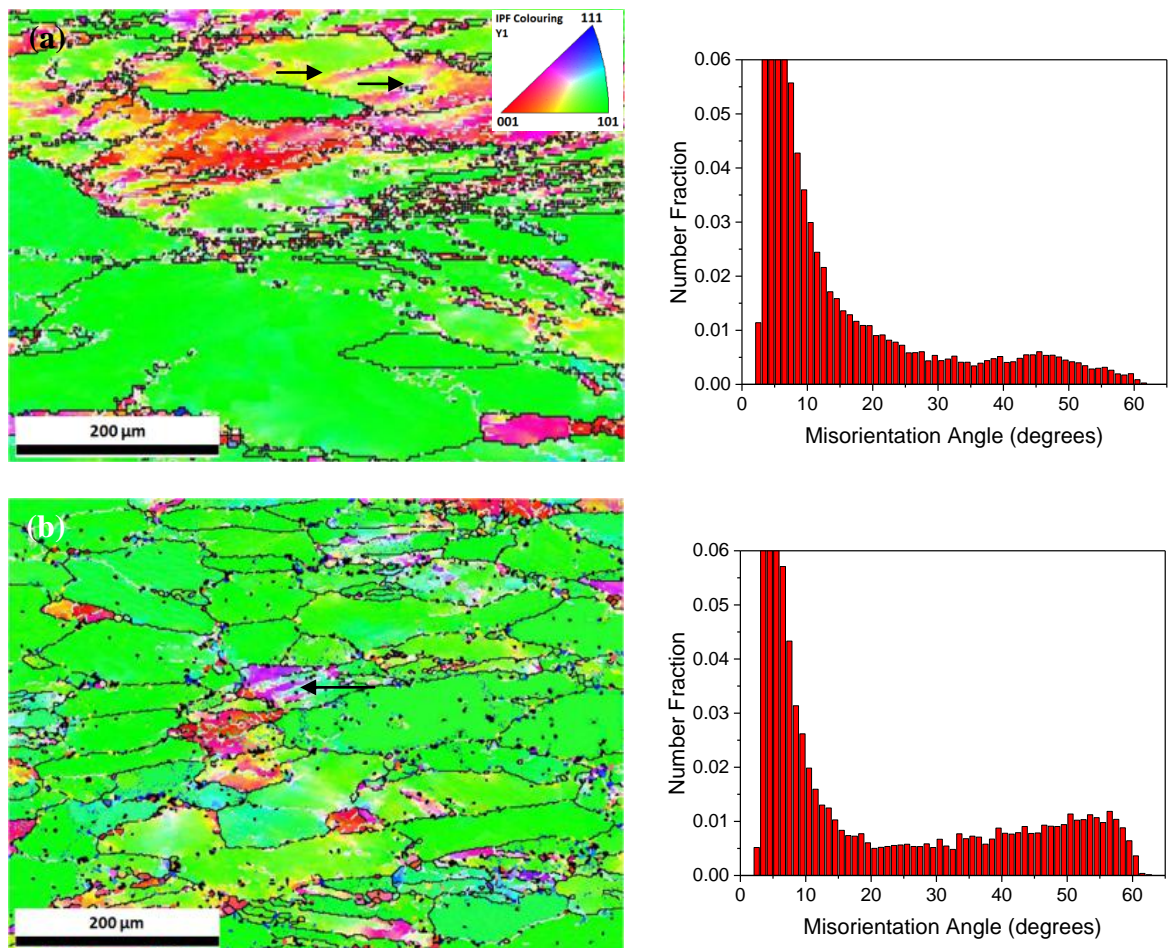


Fig. 4.12. Orientation map (left) and misorientation profile (right) of as-homogenised (a) matrix alloy, (b) 0.2Ti and (c) 0.2Ti-4.5TiB₂



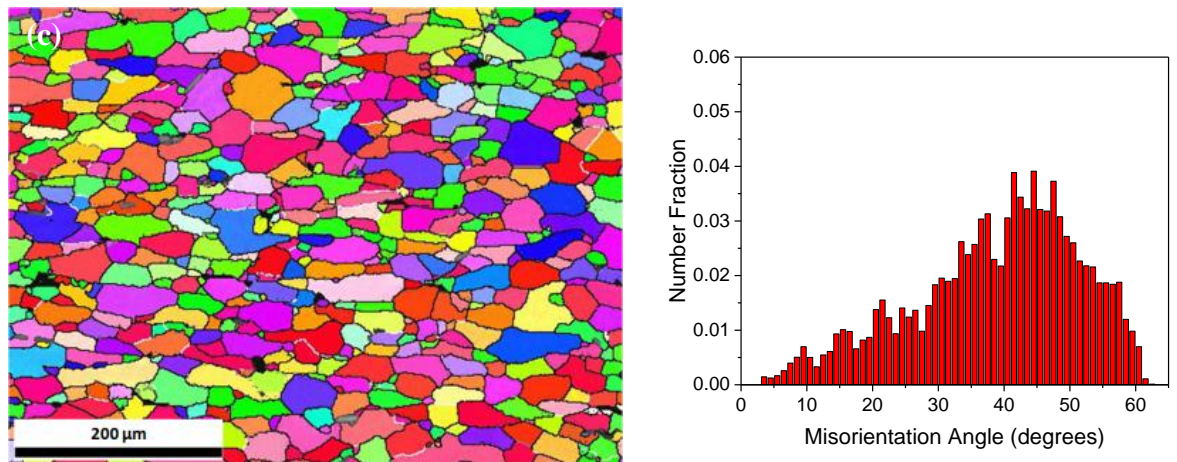
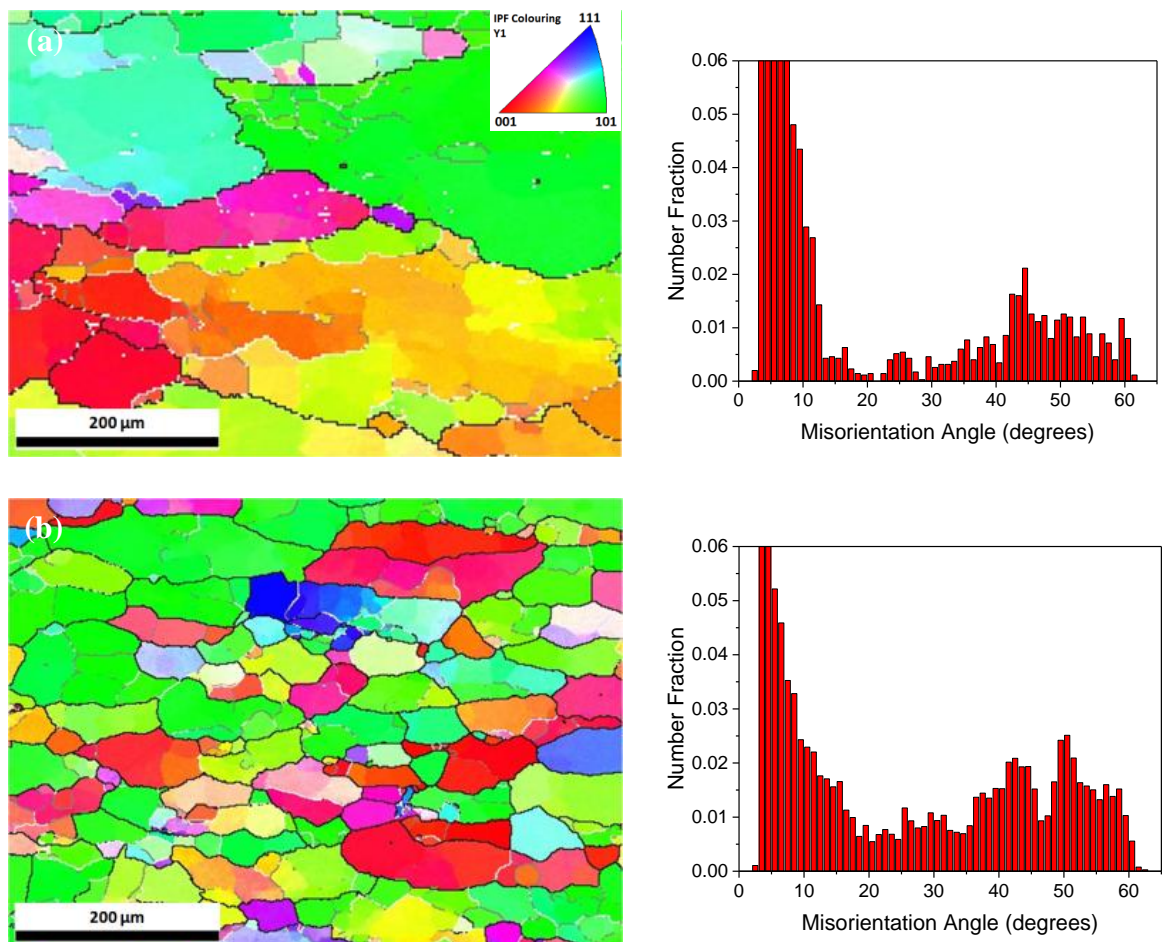


Fig. 4.13. Orientation map (left) and misorientation profile (right) of compression test specimen deformed at 300°C , 10^{-1} s^{-1} (a) matrix alloy, (b) 0.2Ti and (c) 0.2Ti-4.5TiB₂



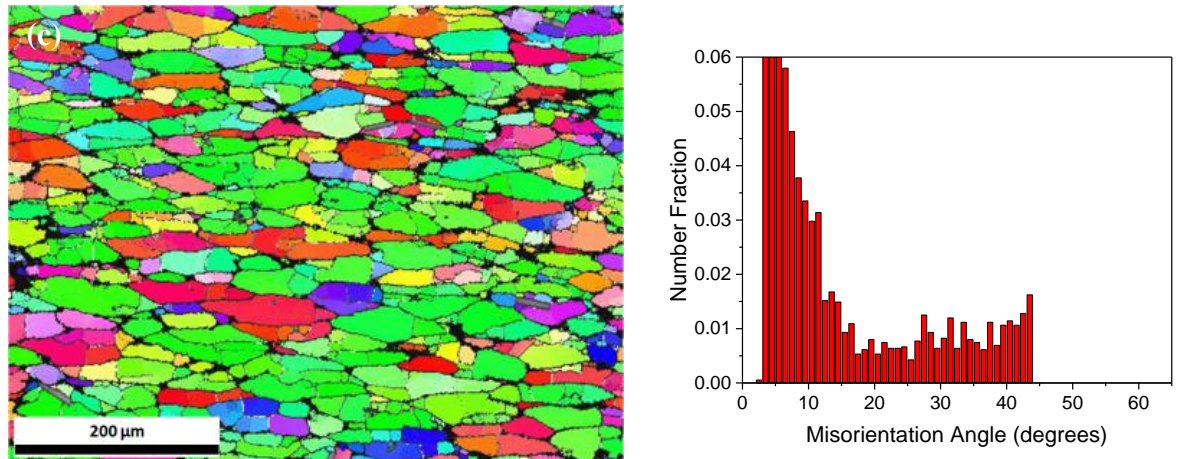


Fig. 4.14. Orientation map (left) and misorientation profile (right) of compression test specimen deformed at 500°C, 10^{-3} s^{-1} (a) matrix alloy, (b) 0.2Ti and (c) 0.2Ti-4.5TiB₂

It can be clearly seen that the as-homogenised structure for all studied materials was dominantly characterised by HAGBs in which their grains have a random crystal orientation. During deformation, these original grains became elongated perpendicular to the compression direction. Upon deformation at 300°C with strain rates of 10^{-1} s^{-1} (high Z), irregular deformation bands (indicated with black arrows in Fig. 4.13a-b) were examined in the original grains of the matrix and 0.2Ti alloy as a result of the occurrence of deformation in different slip systems [30]. Furthermore, a high density of LAGBs was observed in both alloys which indicated the formation of subgrains. In contrast to that, elongated grains which consisted of HAGBs were observed in 0.2Ti-4.5TiB₂ composites. At this deformation condition, it was noted that in the matrix alloy and 0.2Ti alloy, most of the grains rotated their $\langle 110 \rangle$ slip direction parallel to the compression direction, whereas grains with a random orientation were observed in the 0.2Ti-4.5TiB₂ composites.

Moreover, upon deformation at 500°C with a strain rate of 10^{-3} s^{-1} (low Z), a high density of higher angle grain boundaries were observed in the matrix alloy and the 0.2Ti alloy, suggesting the coarsening of subgrains. Whilst in the 0.2Ti-4.5TiB₂ composite, a significant reduction in HAGBs as well as an increment in LAGBs and MAGBs was observed. These indicated a significant formation of subgrains. It was noticed that in all three materials, most of the grains rotated their $\langle 110 \rangle$ slip direction parallel to the compression direction upon deformation at 500°C with a strain rate of 10^{-3} s^{-1} .

The high density of LAGBs observed in the matrix alloy and the 0.2Ti alloy when they were deformed at 300°C with a strain rate of 10^{-1} s^{-1} (high Z) indicated the formation of subgrains which suggested the occurrence of dynamic recovery (DRV). With increasing temperature to 500°C and decreasing the strain rate to 10^{-3} s^{-1} (low Z), a higher density of LAGBs and a lower density of MAGBs and HAGBs than in the as-homogenised microstructure was also observed. Comparing it with high Z deformation, it can be clearly seen that it shows a higher density of MAGBs. This indicated the coarsening of subgrains due to an increment in the degree of dynamic recovery. As temperature increases and strain rate decreases, the subgrains will further recover due to greater time for rearrangement and annihilation of dislocations. This process resulted in enlargement of subgrains which is reflected by the higher density of higher angle grain boundaries [102].

In contrast to the above observations, a high density of grains having misorientation higher than 15° was observed in 0.2Ti-4.5TiB₂ composites at high Z deformations, indicating DRX. This observation is in good agreement with previous researches [102,173,174] in which they also observed highly misoriented dynamic recrystallised grains ($>20^\circ$) when the composite was deformed at high Z. In their experiments, DRX grains were mainly observed in the vicinity of the particles. However, in this study, it was likely that DRX grain was spread throughout the microstructure as shown in Fig. 4.13c. There are two postulations on this. First, the fact that a string of TiB₂ particles (average string thickness of 4 μm) and TiB₂ clusters (average cluster size of 15 μm) homogeneously covered grain boundaries and triple joints respectively in the as-homogenised microstructure (this will be discussed in detail in Chapter 5), will theoretically inhibit dislocation motion during deformation. Moreover, the existence of Al₃Ti particles in the matrix will also influence dislocation motion during deformation. Under such deformation conditions, dislocations are less mobile [175]. Thus, it was expected that a higher dislocation density will be accumulated around the grain boundaries and triple joints as well as in the vicinity of Al₃Ti particles. A higher flow stress observed at high Z deformation proved this higher dislocation density. Hence, there will be a large difference in the accumulated strain level between the area around the string and clusters of TiB₂ particles which are located in grain boundaries, triple joints as well as Al₃Ti particles with the matrix [176]. This will lead to the development of highly misoriented subgrains along the sides of grain boundaries and triple joints, including the edge of Al₃Ti particles. As the strain increases to 0.7, a higher dislocation density will be produced. Grains will be divided into subgrains which are

progressively misoriented to form a number of new grains [177], leading to the homogeneous DRX. Fig. 4.15 gives evidence in which the distribution of the phases upon deformation exhibited the same distribution as in the as-homogenised microstructure which will be discussed in section 5.3.1. Second, the delay time before quenching might induce static recrystallisation, resulting in homogeneous recrystallised grains throughout the volume. On the other hand, the possibility for geometric dynamic recrystallisation (GDRX) was also explored. As explained in Chapter 2, GDRX occurs due to high strain which causes serration of grain boundaries. At some points, these grain boundaries will pinch off, resulting in GDRX grains [107,178]. However, considering the strain in the deformation was only 0.7, it was unlikely that GDRX would occur in this deformation.

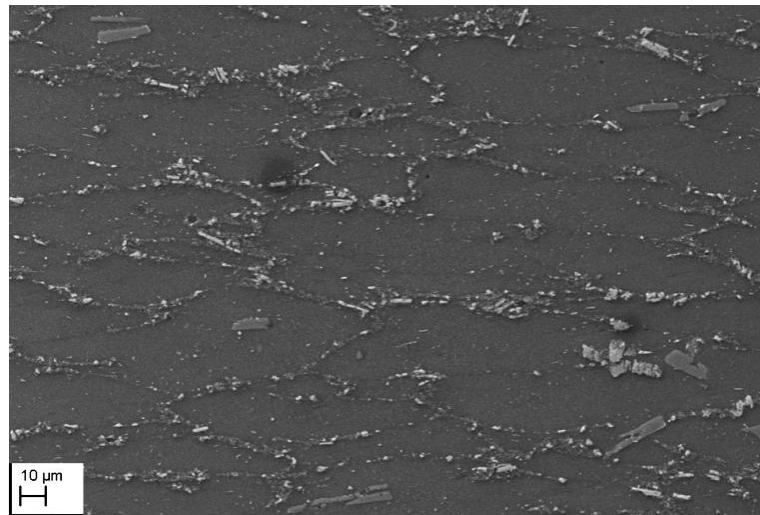


Fig. 4.15. The phase distribution of 0.2Ti-4.5TiB₂ composite upon deformation at 300°C with strain rates of 10⁻¹ s⁻¹ showing a homogenous distribution of TiB₂ particles around the grain boundaries which occasionally contain Al₇Cu₂Fe particles

Nevertheless, regardless of the above of the postulations, Fig. 4.16 confirmed that the existence of TiB₂ particles as well as Al₃Ti particles gives a significant effect on the deformation mechanism. Detailed scanning exhibited small recrystallised grains in the vicinity of TiB₂ clusters and Al₃Ti particles. This observation suggested that a higher dislocation density accumulated around TiB₂ clusters and Al₃Ti particles during deformation, leading to the recrystallisation. Fig. 4.16 is provided to support this postulation.

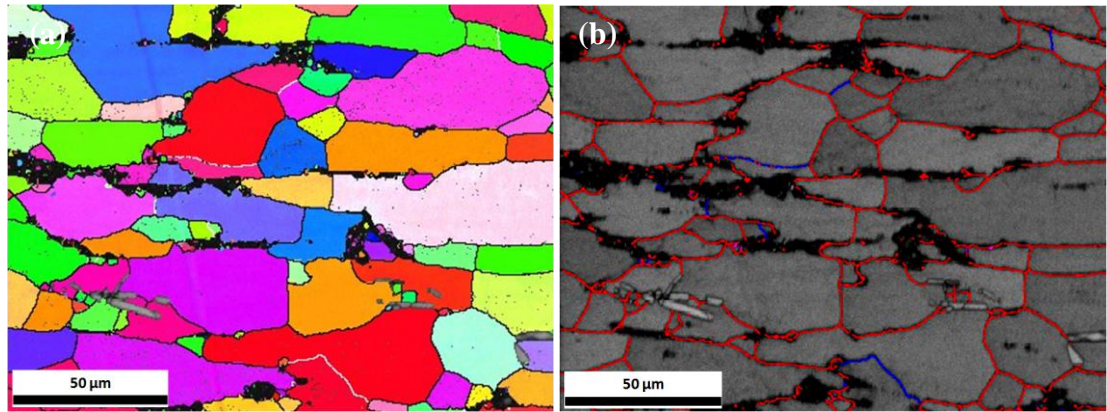


Fig. 4.16. (a) IPF maps and (b) band contrast of the 0.2Ti-4.5TiB₂ composite deformed at 300 °C, 10⁻¹ s⁻¹, showing recrystallisation in the area of clustered TiB₂ (indicated as black areas) and Al₃Ti particles. On the band contrast map, HAGBs (>15°) are indicated with red lines, MAGBs (8 - 15°) are indicated with blue lines and LAGBs (<8°) are indicated with magenta lines.

Furthermore, as temperature increases to 500 °C and strain rate decreases to 10⁻³ s⁻¹ (low Z), significant subgrain formation was observed in the microstructure (Fig. 4.17) as it was reflected from its higher density of LAGBs and MAGBs. In this deformation condition, subgrain rotation might also be involved which is showed by the different orientation of subgrains containing MAGBs. This observation indicated a dynamic recovery (DRV) mechanism. In addition to that, recrystallised grains were also observed in some areas, particularly in the vicinity of clustered TiB₂ and Al₃Ti particles, suggesting localised dynamic recrystallisation (DRX). As the temperature increases and strain rate decreases, there will be longer time for dislocation annihilation to occur, reducing the energy for DRX and hence allowing the occurrence of DRV. A higher dislocation density was expected to be accumulated around TiB₂ clusters and Al₃Ti particles during deformation, providing higher energy for DRX. Thus, DRX grains were mostly observed in the vicinity of TiB₂ clusters and Al₃Ti particles. The same deformation mechanism observed in the composite and the other two studied alloys which also showed a DRV mechanism proved the previous postulation which stated that the addition of TiB₂ particles did not have any significant effect upon deformation at high temperatures and low strain rates. This DRV and local DRX mechanism was responsible for the decrement of the flow stress previously observed with increasing temperature and decreasing strain rates.

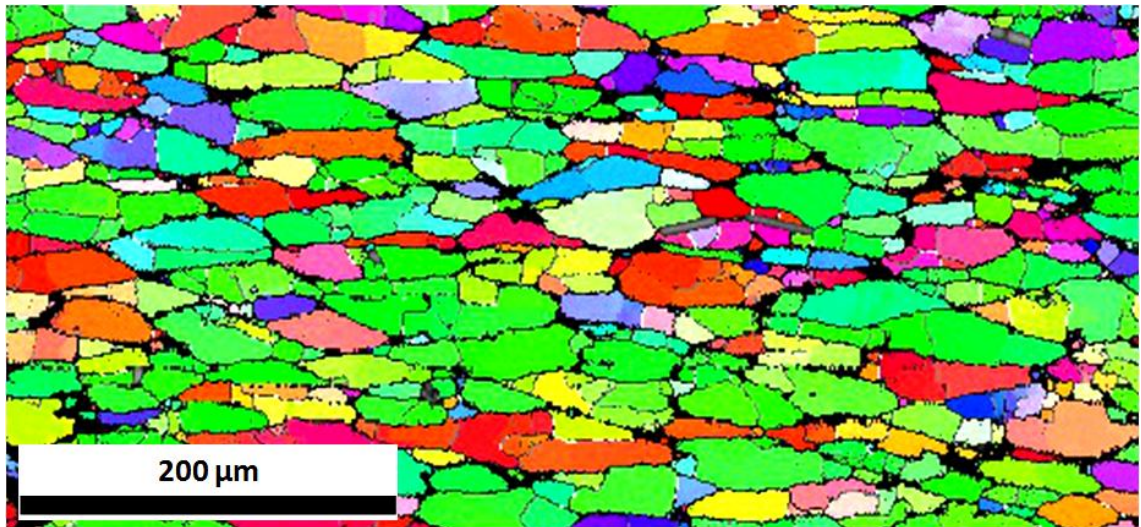


Fig. 4.17. IPF map of the 0.2Ti-4.5TiB₂ composite deformed at 500°C with a strain rate of 10^{-3} s^{-1} showing dynamic recovery and localised dynamic recrystallisation. Black area indicates TiB₂ particles and/or clusters

To sum up, in 0.2Ti-4.5TiB₂ composites, DRX was dominant when the material was deformed at low temperature and high strain rates, whilst DRV was dominant when the material was deformed at high temperature and low strain rates. Fig. 4.18 gives evidence of this postulation in which a higher frequency of DRX was observed on deformation at a temperature of 300°C with a strain rate of 10^{-1} s^{-1} , whilst higher DRV was observed on deformation at temperature of 500°C with a strain rate of 10^{-3} s^{-1} .

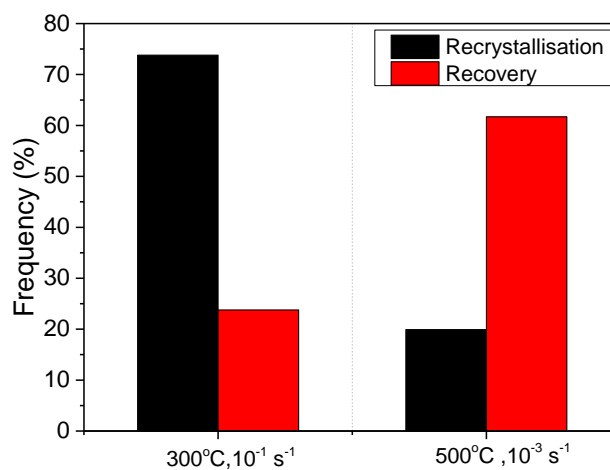


Fig. 4.18. Percentage of DRX and DRV of 0.2Ti-4.5TiB₂ composites

4.6. Summary of the Stress Strain Relationship

Compression tests with several parameters have been carried out on three different materials in this study to explore the workability of the 0.2Ti-4.5TiB₂ composite. In order to understand its mechanism, a comparison with the matrix alloy and 0.2Ti alloy has been conducted. It has been clearly observed that in all deformation conditions, a higher flow stress was achieved in the 0.2Ti-4.5TiB₂ composite than in the other two alloys. This observation was supported by its lower α value and higher Q_{HW} value which suggested its difficulty degree towards plastic deformation. Higher Q_{HW} achieved in 0.2Ti-4.5TiB₂ composite suggested more complex dislocation interaction occurred in the 0.2Ti-4.5TiB₂ composite.

Regarding microstructural evolution, differences in the hot deformation microstructure of the matrix alloy, 0.2Ti and 0.2Ti-4.5TiB₂ composite were noted. However, this discrepancy was more obvious at lower temperature and higher strain rate deformation conditions. Recrystallisation was observed in the 0.2Ti-4.5TiB₂ composite following lower temperature and high strain rate deformation which might indicate a dynamic recrystallisation (DRX) mechanism. The author in this thesis postulated that the existence of strings and clusters of TiB₂ covering grain boundaries and triple junction areas respectively, might increase the dislocation density during deformation, providing a higher driving force for DRX. This was confirmed by the higher recrystallisation rate observed in the vicinity of string and clusters of TiB₂ particles and Al₃Ti particles. On the other hand, dynamic recovery (DRV) was observed as the dominant mechanism in the other two alloys. Furthermore, as temperature increases and strain rate decreases where dislocations are more mobile, the deformation microstructures of all three materials were found to be essentially similar. Dynamic recovery (DRV) was observed in the matrix alloy and 0.2Ti alloy, whilst DRV as well as localised DRX was observed in the vicinity of TiB₂ particles and Al₃Ti particles in the 0.2Ti-4.5TiB₂ composite.

The above observation was reflected from its flow stress behaviour in which the difference of flow stress between 0.2Ti-4.5TiB₂ composites was more apparent following deformation at higher strain rates and lower temperature. As the temperature increases and strain rate decreases, the flow stress of the 0.2Ti-4.5TiB₂ composite was found to get closer to the other two alloys. Consequently, it could be concluded that the addition of

TiB₂ particles to the Al-Cu-Mg-Ag alloy would not have a significant influence when it was deformed at high temperature and low strain rates.

CHAPTER 5

INFLUENCE OF TiB₂ REINFORCEMENT ON THE AS-CAST AND AS-DEFORMED MATERIALS

5.1. Introduction

It is well-known that the annealing behaviour of alloys containing more than one phase is strongly dependent on the volume fraction, size, shape and distribution of the secondary phases. Consequently, before discussing static softening behaviour and its related issues in the next chapter, an analysis of the secondary phase's distribution in the initial materials and its morphology evolution upon deformation is of importance. In this chapter, the analysis of the influence of TiB₂ particles and their distribution as well as other phases formed in different stages of the material's processing i.e. casting, rolling and extrusion are presented.

The analysis of this chapter starts with the examination of the as-cast microstructure. The influence of TiB₂ reinforcement on the as-cast microstructure is revealed. Investigation of the chemical composition to reveal the identity of other phases present in the alloys is reported. Furthermore, the phase distribution in the as-homogenised as well as in the as-rolled and as-extruded microstructure is presented. Apart from that, the morphology of its phases and its evolution upon each stage of material's processing is carefully investigated. Quantitative analysis regarding the secondary phases' volume fraction, size and interparticle spacing is examined, particularly in the as-rolled and as-extruded microstructure, for this defines the static softening behaviour. It is worth noting that it is not the aim of this thesis to study the anisotropy of the materials. For this reason, regarding the microstructural analysis of deformed materials, only the microstructure in the rolling and/or extrusion direction will be examined (ND – RD/ED direction).

On the other hand, in the previous chapter, the flow stress of each material in this thesis has been examined in which the 0.2Ti-4.5TiB₂ composite exhibited the highest value of all materials. The load profile achieved in the rolling and extrusion process and its correlation with the flow stress profile during compression testing is reported.

5.2. Characterisation of As-Cast Materials

It is of importance to characterise the microstructure of as-cast materials, including the phase morphology and distribution for these influence the deformation mechanism and deformed structure which define the mechanical properties of the deformed material. Hence, in this study, optical microscopy and SEM equipped with EDX was utilised to characterise the as-cast microstructure. As already explained in Chapter 2, the addition of TiB_2 particles to the aluminium alloy containing free Ti has been known to have a significant influence on the as-cast microstructure, in which it refines the grain, leading to the enhancement of mechanical properties [85,179]. However, since the focus of this study was on the deformation of TiB_2 reinforced Al-Cu-Mg-Ag alloy, the grain refinement mechanism will not be discussed in detail. In this thesis, the discussion of the as-cast microstructure will be limited in essence to understand microstructural evolution upon deformation.

5.2.1. Grain Structure of As-Cast Materials

Fig. 5.1 shows the optical micrograph images of the matrix alloy, 0.2Ti and 0.2Ti-4.5 TiB_2 composite. Large grains and a dendritic grain structure with average dendrite arm spacing of $51\text{ }\mu\text{m}$ was observed in the matrix alloy (Fig. 5.1a). In contrast to that, a very significant grain size refinement was observed by addition of solute Ti as shown in Fig. 5.1b. This was accompanied by a grain structure that was more equiaxed-like than dendritic. This was supported by the quantitative analysis as shown in Fig. 5.1d. A significant refinement of grain size was evident by the addition of Ti. According to the literature, this alteration of the grain structure and grain size is due to a high segregation ability of solute Ti [94]. During solidification, solute Ti will segregate to the liquid-solid interface, restricting the growth of dendrites and hence leading to the equiaxed-like structure [83,84,180], resulting in a finer grain size. This will be explained in detail later on in the section 5.2.2. Furthermore, further refining and fully equiaxed grains were observed by the addition of both solute Ti and TiB_2 particles as presented in Fig. 5.1c. The average grain sizes of $355\text{ }\mu\text{m} \pm 100.8\text{ }\mu\text{m}$, $84\text{ }\mu\text{m} \pm 16.2\text{ }\mu\text{m}$ and $59\text{ }\mu\text{m} \pm 13.4\text{ }\mu\text{m}$ were achieved in the matrix alloy, 0.2Ti and 0.2Ti-4.5 TiB_2 composite respectively.

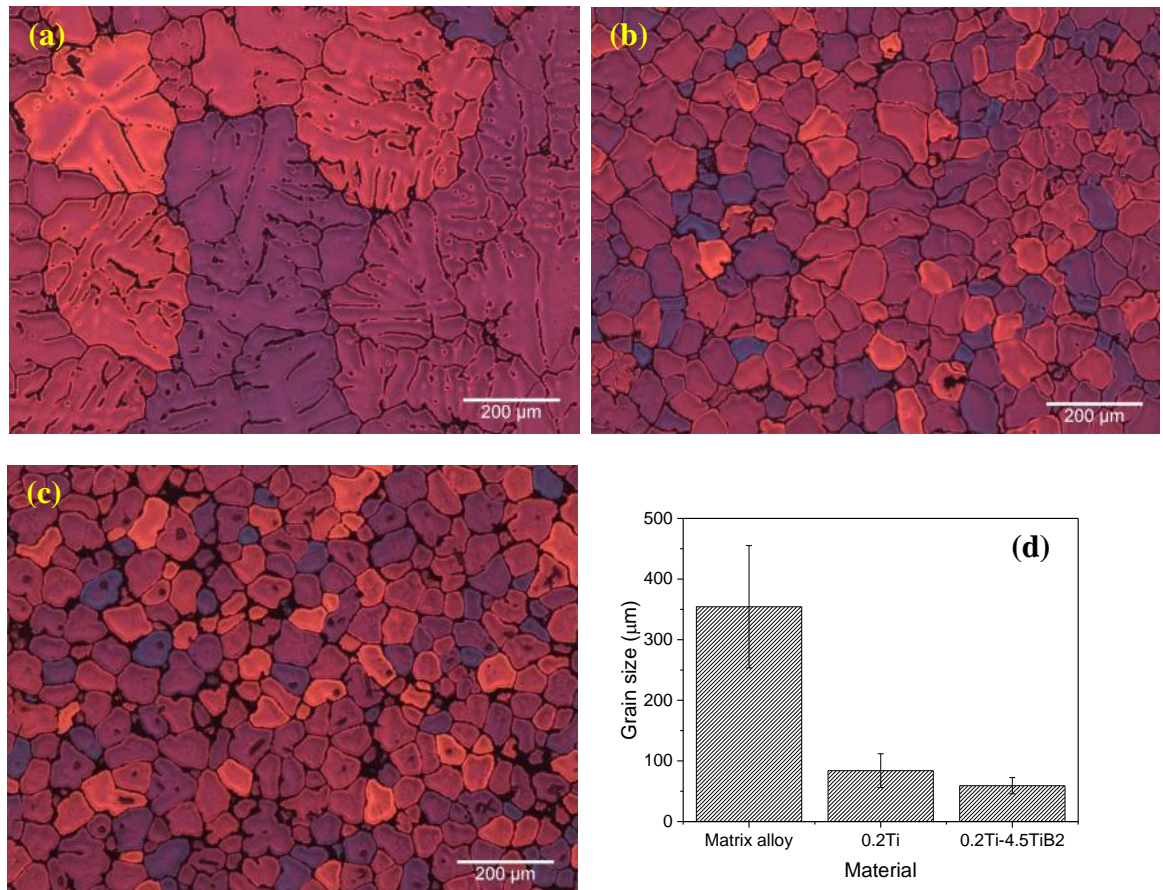


Fig. 5.1. As-cast microstructure of (a) matrix alloy showing a dendritic microstructure, (b) 0.2Ti alloy, (c) 0.2Ti-4.5TiB₂ composite showing finer grains and (d) grain size comparison between matrix alloy, 0.2Ti and 0.2Ti-4.5TiB₂ composite showing a decreasing of the grain diameter by addition of Ti and TiB₂ particles

5.2.2. Cooling Curve Analysis

The finer and equiaxed grains achieved in the 0.2Ti alloy and 0.2Ti-4.5TiB₂ composite were supported by their cooling curve (Fig. 5.2). Undercooling of more than 1°C was observed in the matrix alloy and this reduced to less than 1°C with the addition of Ti. Furthermore, no undercooling was measured with addition of TiB₂ particles. This disappearance of undercooling in the 0.2Ti-4.5TiB₂ composite confirmed that TiB₂ is a good nucleant.

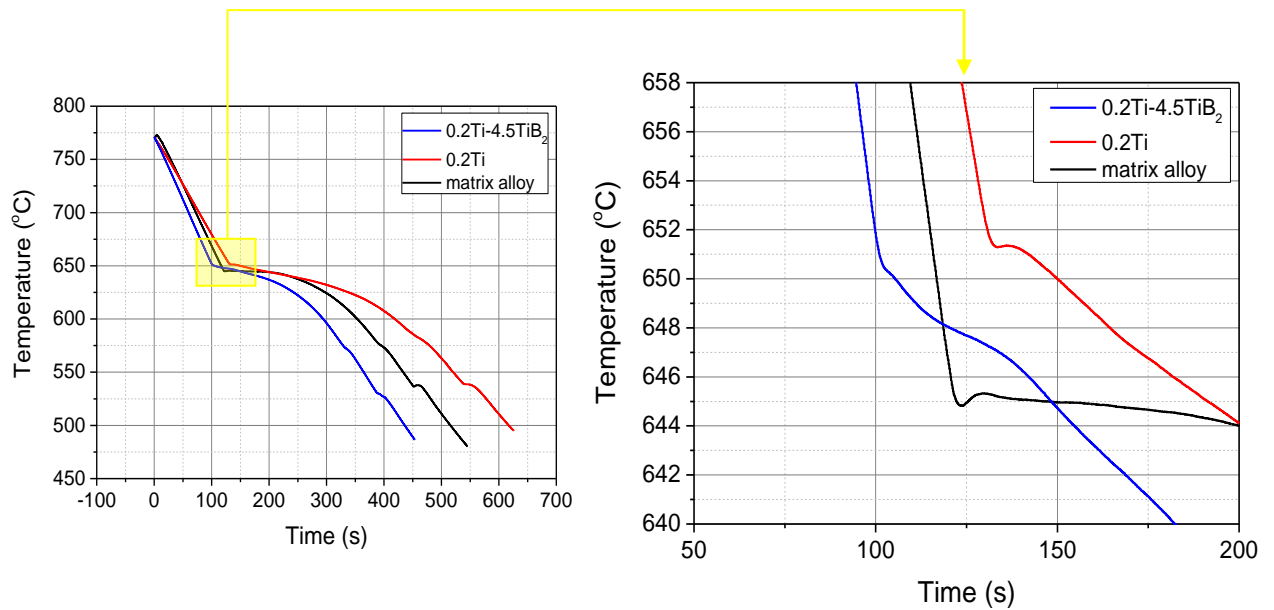


Fig. 5.2. Cooling curves showing no undercooling was measured with addition of TiB_2 particles

In order to explain the relation between undercooling and the grain size achieved upon casting, it is worth briefly discussing some fundamental theory related to nucleation. As we know nucleation is a thermodynamic process and its rate is basically controlled by the magnitude of undercooling, which is the difference between the equilibrium melting temperature, T_m , and the solidification temperature, T_s [94,181]. At the beginning of solidification, nucleation always starts at the cold mould wall and proceeds inwards. Hence, the driving force for the nucleation at the beginning of solidification is derived from the thermal undercooling in the melt at the mould wall. However, this thermal undercooling will be rapidly dissipated and hence, in the absence of solute, no further nucleation will occur although a large number of nucleants are present in the melt. Consequently, columnar grains are achieved [84]. The addition of solute will lead to the occurrence of constitutional undercooling. This means that there will be a maximum region of undercooling in front of the growing grain in which nucleation could occur if the undercooling required for nucleation on the available sites is reached. The more rapid this undercooling is achieved, the more grain growth will be inhibited, resulting in a finer grain size [84,180,182].

According to the literature [80,83,85,183], the addition of solute Ti to the aluminium alloys leads to the formation of Al_3Ti which nucleates a large number of aluminium grains,

resulting in a smaller undercooling region. Hence, a finer grain size is achieved in the 0.2Ti alloy compared with the matrix alloy. With the addition of Ti and TiB_2 particles, it was postulated that TiB_2 particles which act as nucleant particles will be coated by a thin layer of Al_3Ti particles. These Al_3Ti particles will then nucleate a very large number of the aluminium grains. Recent research by Fan *et al* [90] confirmed the formation of an atomic monolayer of Al_3Ti on the TiB_2 surface which improves the nucleation potency of TiB_2 . During nucleation, not all TiB_2 particles will act as nucleating sites for the grains, and hence the rest of the TiB_2 particles will be pushed to the grain boundary, inhibiting the grain growth [26]. This mechanism was believed to be responsible for the absence of undercooling in the 0.2Ti-4.5 TiB_2 composites. Consequently, it leads to the further grain refinement as was explained in the previous section.

5.2.3. Secondary Phases Analysis in As-Cast Materials

High solute levels contained in the materials used in this study led to the formation of variant secondary phases. The existence of these secondary phases will have a significant influence during further material processing i.e. rolling, extrusion, and static softening behaviour. Thus, it is essential to analyse the secondary phases present in the as-cast microstructure before analysing them further in the different material processing stages. In this study, EDX analysis was performed to determine the composition of secondary phases existing in each of the studied materials.

Fig. 5.3 shows the chemical analysis derived from the EDX spot data. In all of the graphs, the constituent elements were plotted with respect to Al composition. The addition of Ti to the aluminium may lead to the formation of intermetallic Al_3Ti particles. EDX spot analysis indeed revealed the existence of blocky Al_3Ti particles in the 0.2Ti alloy and the 0.2Ti-4.5 TiB_2 composite as is illustrated in Fig. 5.3a. All the elements derived from EDX analysis nicely fitted with the superimposed line which represents the Ti composition in Al_3Ti . Furthermore, the existence of Fe impurities in all of the materials studied in this thesis may lead to the formation of Fe-rich intermetallics. EDX spot analysis on the Fe intermetallic composition is presented in Fig. 5.3b. In this graph, Cu and Fe composition was plotted with respect to the Al composition. It was revealed that the composition of the Fe intermetallic which existed in all studied materials was close to the superimposed lines which represent the Cu and Fe composition in $\text{Al}_7\text{Cu}_2\text{Fe}$ intermetallic particles. Some of the data showed deviations which might be due to the effect of other solutes. Based on this

data, it could be concluded that the majority of Fe-rich intermetallics in all of the studied materials is $\text{Al}_7\text{Cu}_2\text{Fe}$. Moreover, eutectic Al_2Cu was also observed in all of the materials. TiB_2 particles (average size of $0.7\ \mu\text{m}$) were clearly observed in the form of clusters at the grain boundaries with eutectic Al_2Cu in the 0.2Ti - 4.5TiB_2 composite. The distribution of each of these secondary phases will be discussed in the section below.

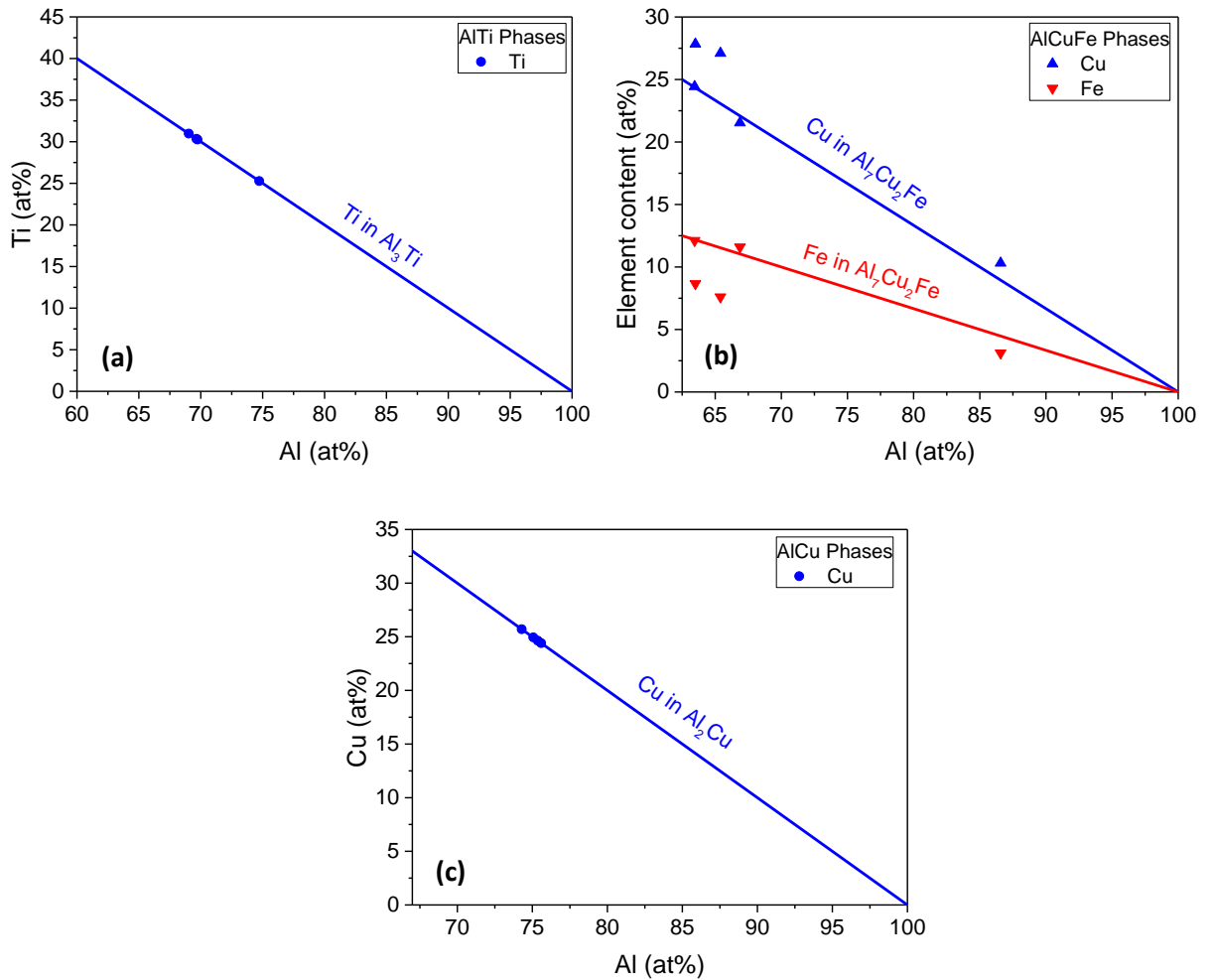


Fig. 5.3. Composition of constituent elements with respect to Al composition in (a) Al_3Ti ; (b) $\text{Al}_7\text{Cu}_2\text{Fe}$ and (c) Al_2Cu

5.2.4. Phases Distribution in As-Cast Materials

Fig. 5.4 and Fig. 5.5 present the distribution of the phases in the matrix alloy and 0.2Ti alloy respectively. It can be clearly seen that Cu and Fe constituents were found segregating to the grain boundaries and formed Al_2Cu and needle-shaped $\text{Al}_7\text{Cu}_2\text{Fe}$ intermetallics as confirmed by EDX analysis in the previous section. The addition of Ti in the 0.2Ti alloy led to the formation of Al_3Ti particles which were occasionally observed in

the middle of the grains. Similar to the 0.2Ti alloy, Al_3Ti particles were also occasionally observed in the middle of the grains in the 0.2Ti-45.TiB₂ composite. TiB₂ particles which have an average size of 0.7 μm were observed in the form of clusters and distributed along the grain boundaries and triple joints of the 0.2Ti-4.5TiB₂ composite. As has been explained before during solidification, not all the TiB₂ particles will nucleate the grains. Thus, the rest of the TiB₂ particles will be pushed to the grain boundaries, inhibiting the grain growth [26]. Therefore, agglomeration of TiB₂ particles formed on the grain boundaries as shown in Fig. 5.6. It was noted that clusters of TiB₂ homogeneously string themselves along the grain boundaries with an average thickness of 4 μm .

Following the above the observation, it was indeed that strings of TiB₂ clusters homogeneously covered grain boundaries; however, variation in the string thickness was observed. In most areas, a thicker string ($\geq 1\mu\text{m}$) which consisted of closely packed TiB₂ particles was observed, while in a few areas, only a thin ($<1\mu\text{m}$) and discontinuous TiB₂ string was observed as illustrated in Fig. 5.7. This random distribution of TiB₂ strings will affect its distribution upon deformation which will further affect the static recrystallisation behaviour of the 0.2Ti-4.5TiB₂ composite. In the triple joint area, thick TiB₂ clusters were observed with an average thickness of 15 μm . Furthermore, similar to the other two materials, Al_2Cu and $\text{Al}_7\text{Cu}_2\text{Fe}$ were found segregating to the grain boundaries and wetting TiB₂ particles which were located on the grain boundaries.

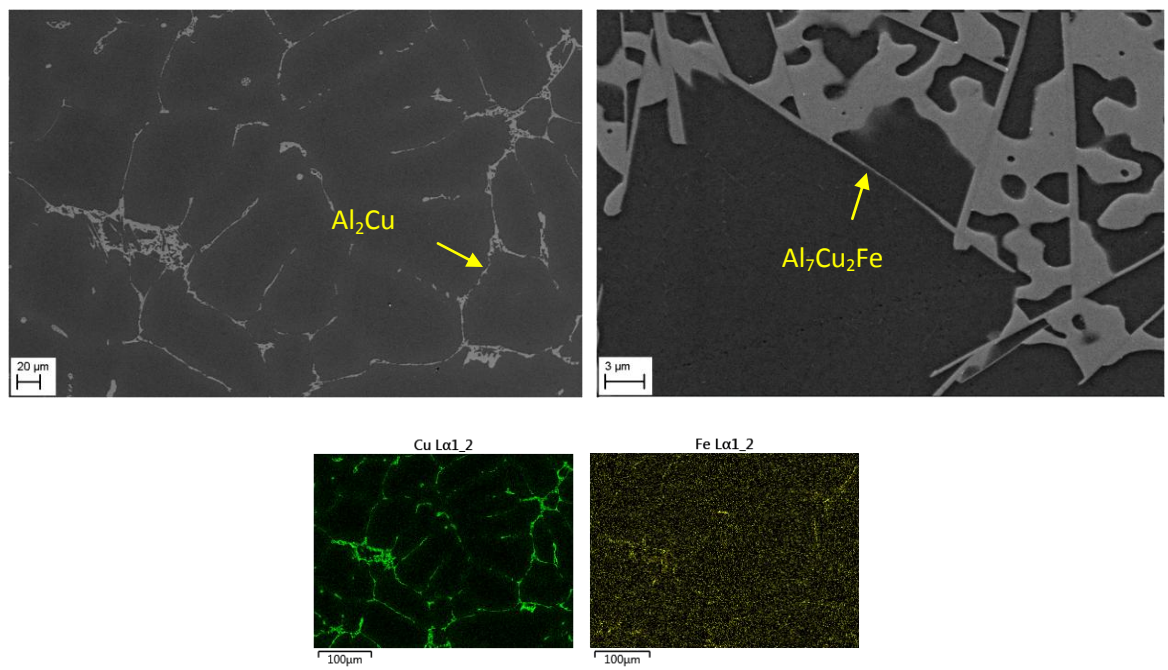


Fig. 5.4. SEM examination including EDX map of Cu, and Fe of the matrix alloy

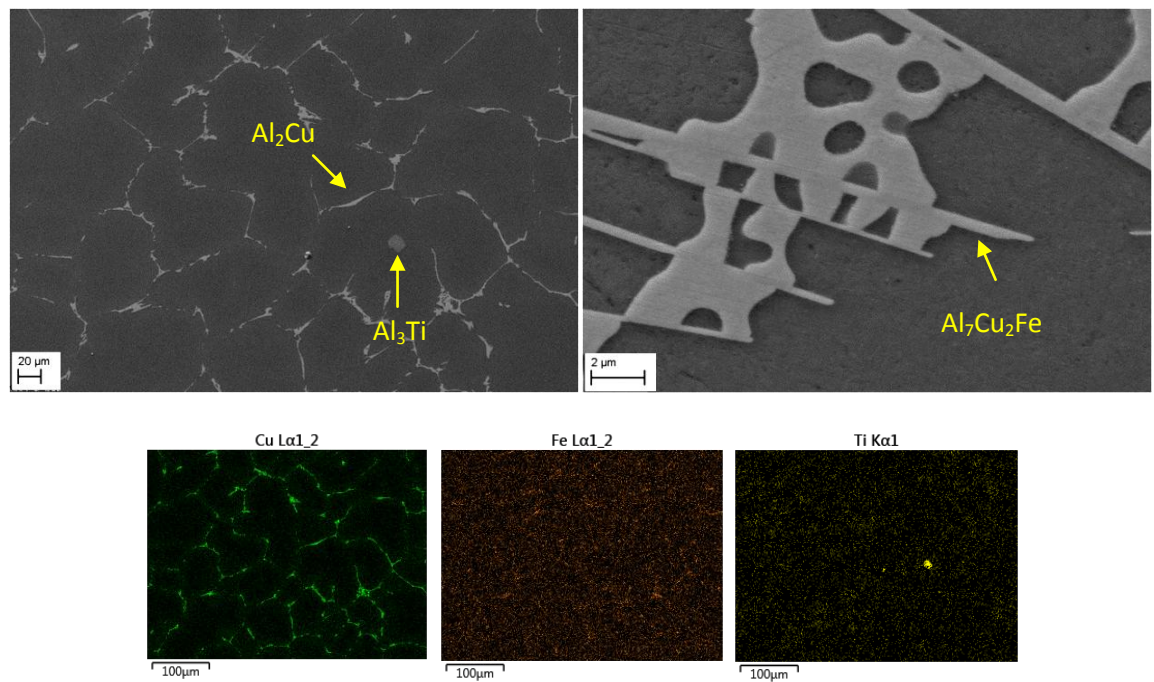


Fig. 5.5. SEM examination and EDX map of Cu, Fe and Ti of the 0.2Ti alloy

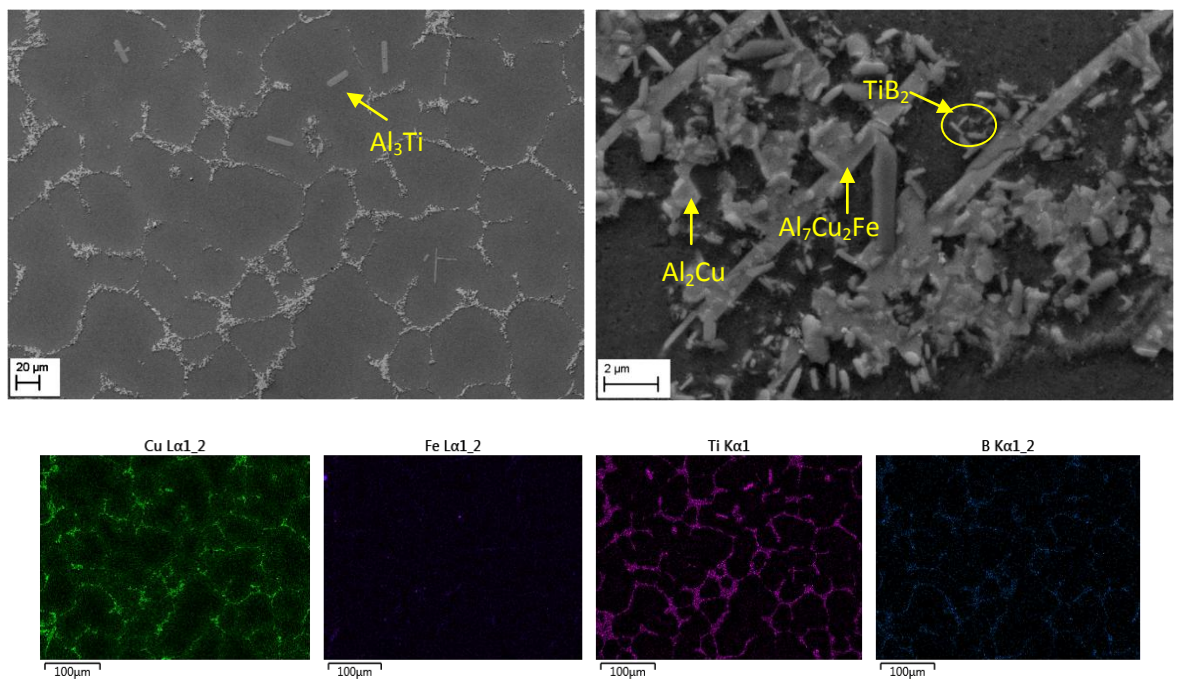


Fig. 5.6. SEM examination and EDX map of Cu, Fe, Ti and B of the 0.2Ti-4.5TiB₂ composite

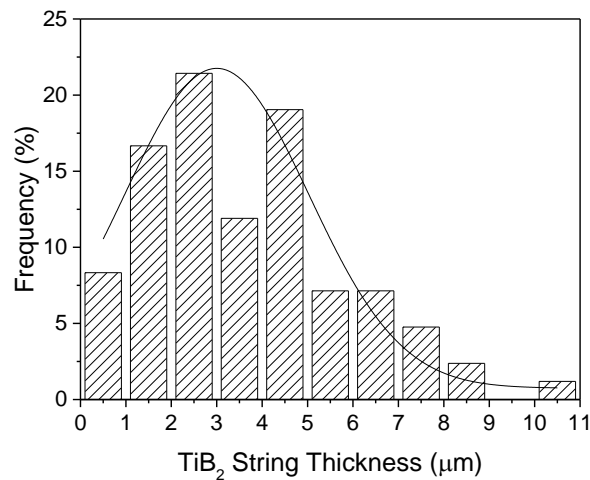
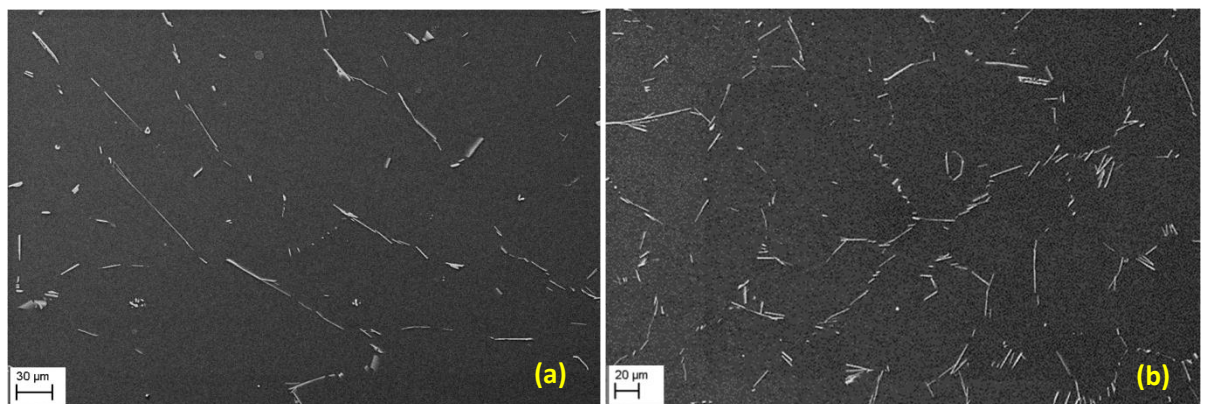


Fig. 5.7. TiB_2 string thickness distribution along grain boundaries

5.3. Characterisation of As-Homogenised Materials

5.3.1. Phase Distribution in As-Homogenised Materials

Following the as-cast characterisation, the as-homogenised microstructure was explored for this influences the workability. Upon homogenisation, the Al_2Cu was found to be dissolved into solid solution in all of the studied materials. In contrast to that, needle-shaped $\text{Al}_7\text{Cu}_2\text{Fe}$ was still observed in the materials. This iron-bearing constituent particle has been known as an un-dissolved constituent. Hence, in addition to the Al_3Ti and TiB_2 particles, the existence of this intermetallic will also influence the workability and mechanical properties of the materials which will be discussed in the related section. Fig. 5.8 shows the as-homogenised microstructure of each studied materials. For brevity, the phase distribution by EDX mapping will be presented in Appendix B.



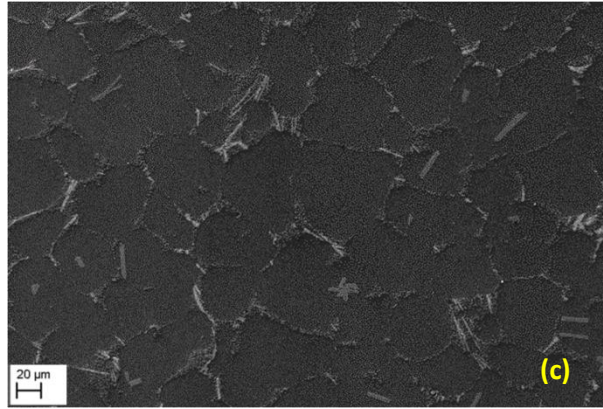


Fig. 5.8. As-homogenised microstructure of (a) matrix alloy, (b) 0.2Ti alloy and (c) 0.2Ti-4.5TiB₂ showing needle-shaped Al₇Cu₂Fe on the grain boundaries for all three studied materials, and TiB₂ and Al₃Ti particles on the 0.2Ti-4.5TiB₂ composite

5.4. Characteristics of Sheet Materials

5.4.1. Load Profiles During Rolling

Fig. 5.9 shows the rolling load profiles obtained during the rolling experiments. Generally, the load was increased with increasing rolling pass which indicated the occurrence of strain hardening in every pass during rolling. As has been explained in Chapter 3, in this study, no re-heating was applied between each pass of the rolling. As temperature decreased in every rolling pass (finishing rolling temperature was 290°C), it was expected that a higher dislocation density was created which led to the higher strain hardening [184]. Consequently, the load increased. Furthermore, comparing the load value between each of the studied materials, in every rolling pass, the 0.2Ti-4.5TiB₂ composites generally showed the highest load of all materials. This is in accordance with the compression results in which the 0.2Ti-4.5TiB₂ composites exhibited the highest flow stress of all materials. Furthermore, the higher finishing load achieved during rolling the 0.2Ti-4.5TiB₂ composite reflected its higher Q_{HW} value achieved during the compression test.

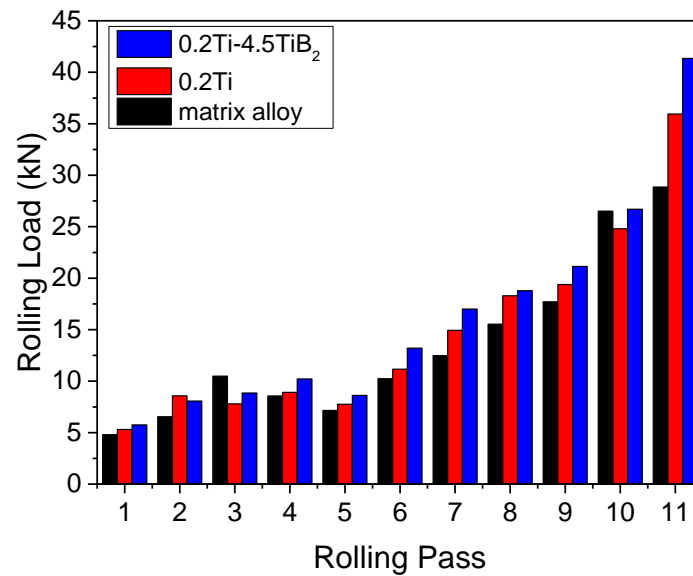


Fig. 5.9. Load profile during rolling experiment showing higher load for 0.2Ti-4.5TiB₂ composites

5.4.2. Phase Distribution in Sheet Materials

SEM examination was carried out to study the evolution of phases after deformation comparison with the as-cast microstructure. Quantitative analysis on the secondary phases' size, their distribution and spacing between the particles, particularly TiB_2 particles, were carried out in order to get a better understanding regarding their effect on the static recrystallisation which will be explained in Chapter 6. It is worth noting that all quantitative analysis was conducted in the solution treated condition to avoid misleading measurements due to high amounts of Al_2Cu present in the as-rolled condition. At least 100 particles were used for particle's size measurement. In terms of the TiB_2 string and cluster measurements, at least 5 zoom images on the TiB_2 areas were taken in several areas in the specimen were used for the measurement. All quantitative analysis was performed using ImageJ software. A similar method was also applied in analysing as-extruded materials.

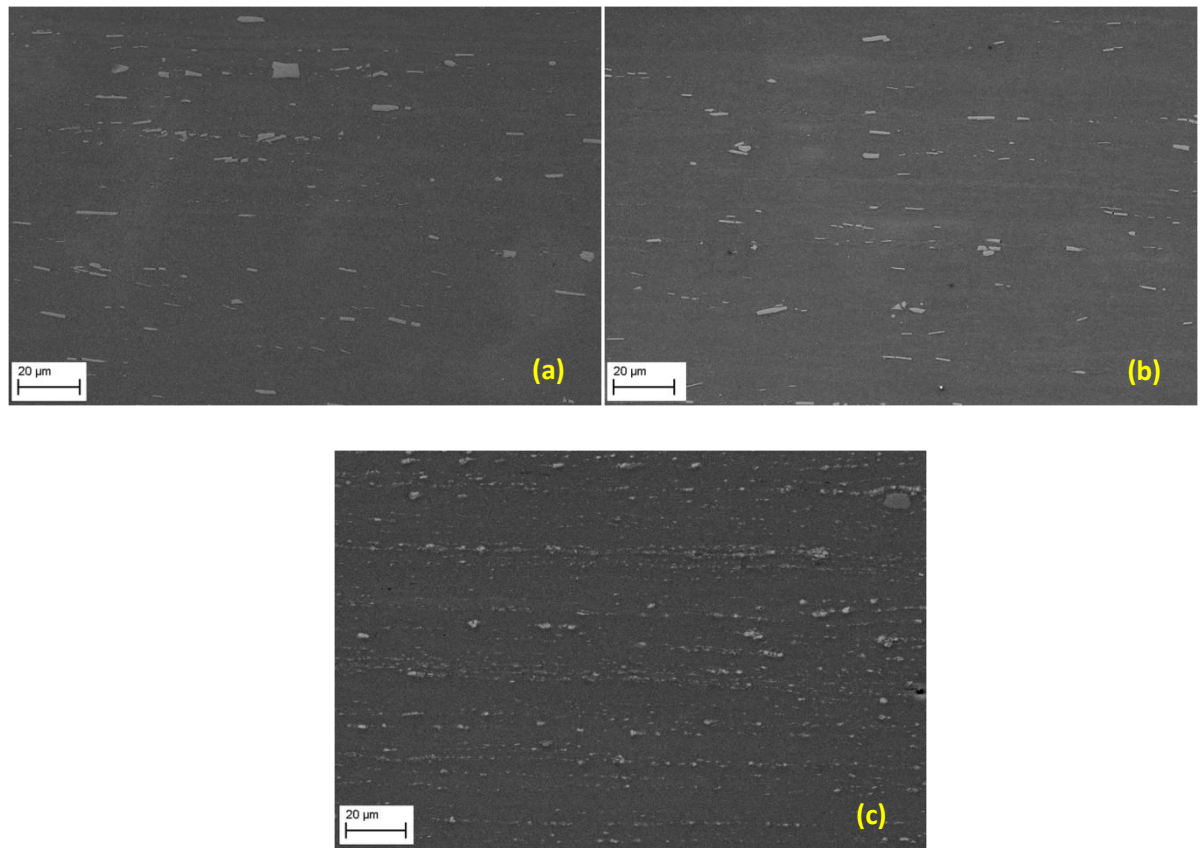


Fig. 5.10. Phase distribution of as-rolled (a) matrix alloy, (b) 0.2Ti alloy and (c) 0.2Ti-4.5TiB₂ composite

Fig. 5.10 shows the phase distribution of the as-rolled specimens. It was clearly observed that $\text{Al}_7\text{Cu}_2\text{Fe}$ intermetallic particles which were present as long-needle-shaped particles in the as-homogenised structure of the matrix alloy and 0.2Ti alloy, after 11 passes of rolling have broken into short-elongated particles and aligned into bands. Similar to both of those alloys, $\text{Al}_7\text{Cu}_2\text{Fe}$ intermetallic particles were also found as short-elongated particles in the 0.2Ti-4.5TiB₂ composites in which they were segregated to the TiB₂ particles. Furthermore, TiB₂ particles were observed to string themselves out along the rolling direction. The clusters of TiB₂ were mostly broken up upon rolling; forming TiB₂ strings with a string thickness which varied from 0.3 μm to 1.5 μm . This variation in TiB₂ string thickness was believed to be due to the random distribution of TiB₂ string thickness along the grain boundaries in the as-cast microstructure. In some areas, closely packed TiB₂ particles were observed with an average interparticle spacing of 470 nm in which they formed a cluster of 3.5 μm . In terms of the size, no broken up TiB₂ particles were observed in this study. In contrast to that, Al_3Ti particles were mostly found broken up during

rolling in both, the 0.2Ti alloy and the 0.2Ti-4.5TiB₂ composite, as was confirmed by quantitative analysis as per Table 5.1. These Al₃Ti particles were observed randomly distributed in both materials' microstructure.

Table 5.1. Comparison of secondary phases' length presented in the as-homogenised (HO) condition and sheet materials in solution treated (ST) condition of all studied materials

Material	Al ₃ Ti Size (μm)		TiB ₂ Size (μm)		Al ₇ Cu ₂ Fe Size (μm)	
	As HO	As ST	As HO	As ST	As HO	As ST
0.2Ti-4.5TiB ₂	18.8	8.2	0.7	0.7	11.3	1.7
0.2 Ti	13.3	8.6	-	-	10.8	3.3
Matrix alloy	-	-	-	-	16.2	4.2

5.4.3. Microstructural Examination of Sheet Materials

Fig. 5.11 illustrates the as-rolled microstructure of each studied material. Pancake and elongated grains with an average thickness of 14 μm, 5 μm and 2.3 μm were observed in the as-rolled matrix alloy, 0.2Ti alloy and 0.2Ti-4.5TiB₂ composite respectively. Shear bands (indicated with black arrows) were clearly seen in the matrix alloy. Although it was not as clear as in the matrix alloy, shear bands were also noticed in the 0.2Ti alloy. In contrast to both alloys, shear bands were not clearly observed in the 0.2Ti-4.5TiB₂ composite. This shear band is basically a result of plastic instability. Several authors [185–188] have observed that the formation of shear bands was related to the chemical composition, initial grain size and rolling temperature. Owing to the same conditions of rolling parameters, the formation of shear bands in this study could be analysed from the chemical composition and initial grain size point of view. Ridha and Hutchinson [189] observed a tendency of an increment of shear bands with increasing initial grain size. It was believed that a finer initial grain size is more prone to dynamic softening during rolling passes, preventing the stress localisation, avoiding the onset of localised shear band deformation [189]. We know that plastic deformation is always related to the dislocation movement [184]. As the strain increases, the dislocation density increases. As a result, dislocation tangles are formed, leading to the development of well-defined cells and subgrains. Materials with a larger initial grain size will have a lower dislocation density, meaning a lower energy to initiate dynamic softening during rolling passes, and hence localisation of stress might occur. A larger subgrain size and a lower density of subgrains will be created. Deformation in-homogeneity will occur as a result of the need to accommodate neighbouring volumes which are deforming with different combinations of

slip [176]. Hence, macroscopic slip in-homogeneity takes place in which is reflected in shear band formation. On the other hand, material with a finer grain size as well as the addition of small secondary particles will lead to the homogeneous slip, preventing the formation of structural in-homogeneities [176]. Furthermore, the higher dislocation density created during deformation of these materials, particularly in the vicinity of secondary particles, will induce a higher degree of dynamic softening, leading to a decrement of stress localisation. Consequently, shear band formation is inhibited [176]. It was indeed observed that the dynamic softening degree in the 0.2Ti-4.5TiB₂ composite was higher than the other two alloys which will be discussed later on.

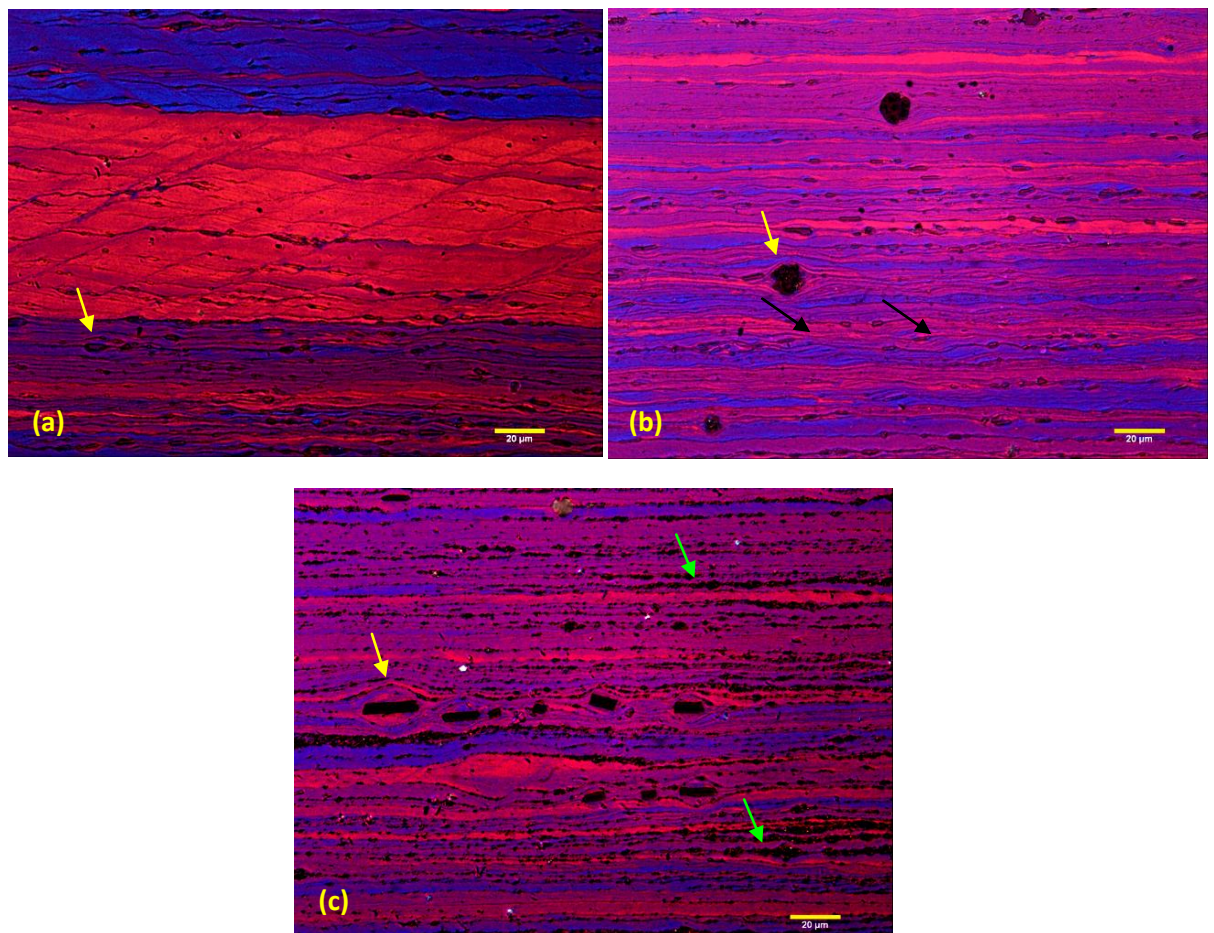
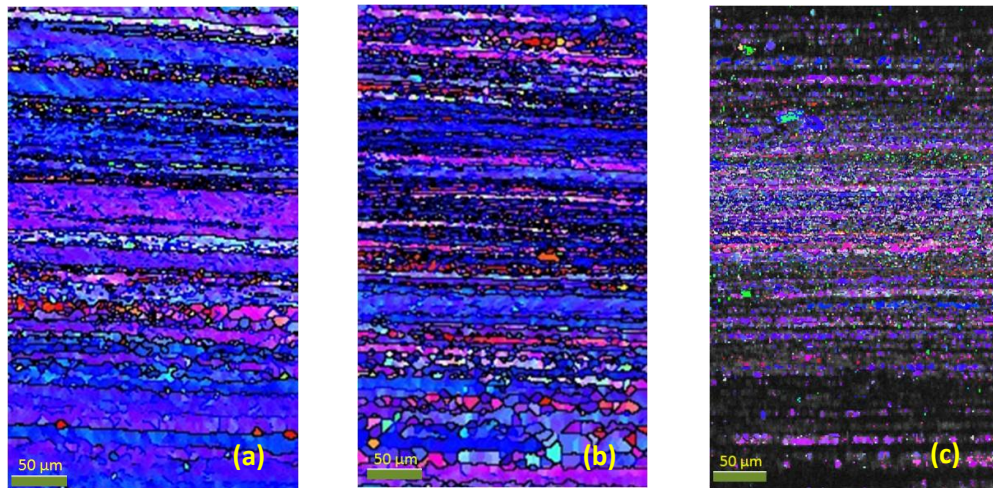


Fig. 5.11. As-rolled microstructure of (a) matrix alloy, (b) 0.2Ti alloy and (c) 0.2Ti-4.5TiB₂ composite showing shear band and matrix bowing around secondary particles

In addition to shear bands, TiB₂ particles which were observed as clusters in the as-cast microstructure were found to string out along the rolling direction upon deformation. However, in some areas, clusters of TiB₂ were still observed. Since the clusters were harder than the matrix, it was expected that their deformation would be less than that of the

matrix. Hence, during rolling, shear flow occurred at the cluster-matrix interface as the matrix flows past the cluster. This shear flow caused the particles adjacent to the cluster-matrix interface to tumble along the cluster interface. As the strain increased, more particles were removed from the cluster interface and transferred to the end of the elongated cluster [176], which appeared like a tail in Fig. 5.11c (indicated with green arrows). After a certain amount of strain, the clusters showed an orientation preference and hence they string themselves out along the rolling direction.

Moreover, matrix bowing (indicated with yellow arrows) was found around Al_3Ti particles and occasionally around bigger $\text{Al}_7\text{Cu}_2\text{Fe}$ particles. This was postulated as a result of stress localisation due to dislocation accumulation around the particles. In this case, these particles were strong enough to resist the deformation stress. Consequently, during deformation, these particles were not deformed, resulting in an accumulation of dislocations around these particles and the formation Orowan loops [30]. All the above observations, such as shear bands, TiB_2 clusters, and matrix bowing around Al_3Ti particles which indicates a higher dislocation density were estimated to have a significant influence on the static softening mechanism. Those observations were expected to have a higher dislocation density, meaning a higher energy is stored. Upon annealing, they tend to promote recrystallisation which will be explained in Chapter 6.



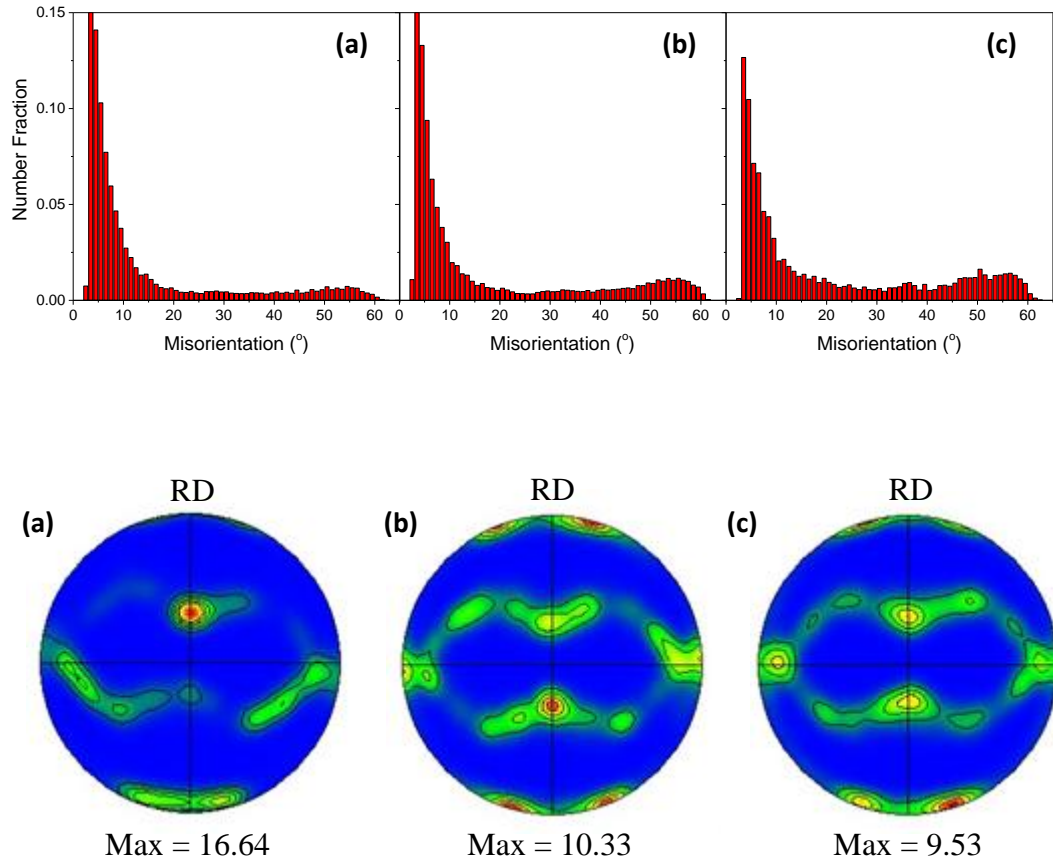


Fig. 5.12. IPF maps (top), misorientation profiles (middle), and $\{111\}$ pole figure (bottom) of as-rolled materials of (a) matrix alloy, (b) 0.2Ti alloy and (c) 0.2Ti-4.5TiB₂ composites

Following the above observations, EBSD analysis was carried out in this study. Fig. 5.12 shows the IPF maps and misorientation profiles as well as $\{111\}$ pole figures of each of the materials in this thesis. It can be clearly seen that a higher fraction of high angle grain boundaries (HAGBs) was observed in the 0.2Ti-4.5TiB₂ composite compared with the matrix alloy and the 0.2Ti alloy. A higher fraction of HAGBs observed in the 0.2Ti alloy was expected due to the existence of Al_3Ti particles which created a local stress, providing higher energy stored for dynamic softening. And hence, this leads to the formation of HAGBs as the strain increases. Similar to the 0.2Ti alloy, a higher HAGBs fraction in the 0.2Ti-4.5TiB₂ composite than in the other two alloys was postulated due to the existence of Al_3Ti particles as well as TiB_2 clusters. Matrix bowing was observed around Al_3Ti particles in the above section which indicated localised stress around the particles was expected to increase the rate of formation of high angle boundaries during deformation. And this was indeed proved by Fig. 5.13 that high angle grain boundaries (HAGBs) were formed in the vicinity of Al_3Ti particles. The deformation mechanism related to this will be

discussed later in section 5.4.4. As the consequences of this heterogeneous deformation microstructure, the 0.2Ti-4.5TiB₂ composite showed the weakest rolling texture among all the materials studied. The pole figure of the 0.2Ti-4.5TiB₂ composite shows a higher orientation spread with a maximum intensity of 9.53, followed by the 0.2Ti alloy with maximum intensity of 10.33, whilst the matrix alloy shows least orientation spread with a maximum intensity of 16.64.

5.4.4. Deformation Behaviour in the 0.2Ti-4.5TiB₂ Composite

In order to understand the deformation mechanism in the 0.2Ti-4.5TiB₂ composite, EBSD scanning in the area adjacent to secondary particles, in this case Al_3Ti and TiB_2 particles, was conducted. Similar to other EBSD analysis, to differentiate between substructure and grain boundaries, in this analysis low angle grain boundaries (LAGBs), 0 - 8° [102], are indicated with magenta lines, medium-angle grain boundaries (MAGBs), 8 - 15° [102], are indicated with white lines and high-angle grain boundaries (HAGBs), >15° [102], are indicated with black lines. A Kuwahara filter was applied in the data processing step in order to reduce noise and enables boundaries determination.

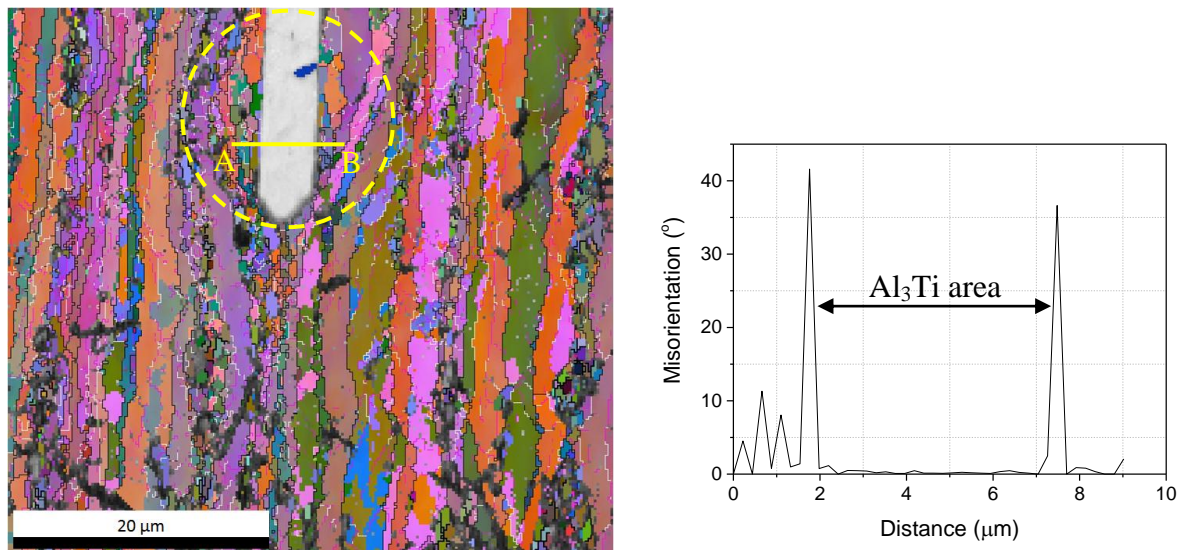


Fig. 5.13. (a) Recrystallised grains observed in the vicinity of Al_3Ti particles on the as-rolled microstructure of the 0.2Ti-4.5TiB₂ composite and (b) misorientation profile adjacent to the Al_3Ti particle (point A to point B)

Fig. 5.13 shows Euler maps of the as-rolled 0.2Ti-4.5TiB₂ composite. HAGBs as well as grain rotation were clearly seen in the vicinity of Al_3Ti particles. Furthermore, a

misorientation line scans adjacent to Al_3Ti particles clearly shows the existence of HAGBs. These give evidence that accumulation of dislocations occurred adjacent to the Al_3Ti particles during deformation, leading to plastic relaxation during rolling passes. Consequently, local lattice rotation and HAGBs were created. Furthermore, owing to the large rolling reduction performed in this thesis (95%), it is worth analysing if geometric dynamic recrystallisation (GDRX) was responsible for the deformation mechanism of the 0.2Ti-4.5TiB₂ composite. As has been explained before (section 2.4.3), GDRX occurs as a result of grain boundary pinch off due to very large strains, resulting in a high density of HAGBs. Consequently, the subgrain size should occur in a similar size as the HAGBs separation [30,114]. In order to confirm the possibility of GDRX, quantitative analysis on HAGB and LAGB spacing was conducted. Fig. 5.14a shows a comparison between HAGB and LAGB spacing. A big gap difference obtained between HAGBs and LAGBs spacing in this study led the author of this thesis to a doubt if the deformation occurred by GDRX. Furthermore, the misorientation profile (Fig. 5.14b) which shows a higher density of LAGBs, inevitably limited the probability of GDRX occurrence. Besides that, without knowing the history of LAGBs and HAGBs fractions between each rolling pass, it is too early to conclude that GDRX occurred during deformation. Therefore, the author of this thesis postulated that in general, recovery occurred during deformation of the 0.2Ti-4.5TiB₂ composite with localised recrystallisation occurring in the vicinity of secondary particles. The occurrence of recovery was confirmed by the high number fraction of LAGBs and localised recrystallisation was confirmed by the HAGBs observed around Al_3Ti particles. However, further detailed analysis, for example with in-situ deformation tests, needs to be conducted to confirm this postulation.

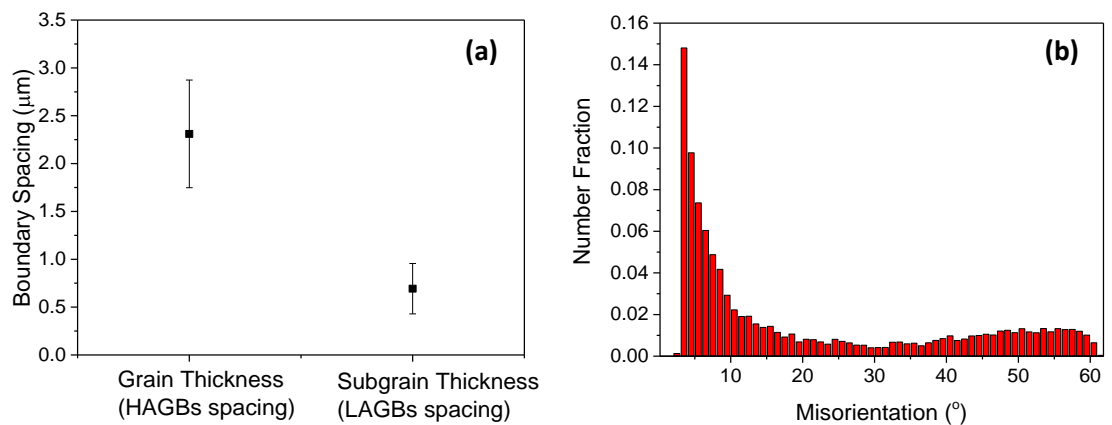


Fig. 5.14. (a) Comparison of grain and subgrain thickness, (b) misorientation profile

5.5. Influence of TiB_2 on the Extruded Materials

5.5.1. Effect of TiB_2 on the Extrusion Pressure

In this study, extrusion experiments were carried out at a temperature 450°C . Fig. 5.15 shows the comparison of extrusion pressure obtained from the extrusion experiments. It was clearly seen that a higher peak extrusion pressure was observed in the $0.2\text{Ti}-4.5\text{TiB}_2$ composite, indicating higher work hardening created at the beginning of deformation in the $0.2\text{Ti}-4.5\text{TiB}_2$ composite. This higher extrusion pressure needed to deform the $0.2\text{Ti}-4.5\text{TiB}_2$ composite reflected its higher flow stress value and lower α value, which indicates its higher capability to resist deformation. The higher Q_{HW} value achieved for the $0.2\text{Ti}-4.5\text{TiB}_2$ composite achieved in compression testing confirmed the complexity of dislocation interaction which reflected in its higher extrusion pressure.

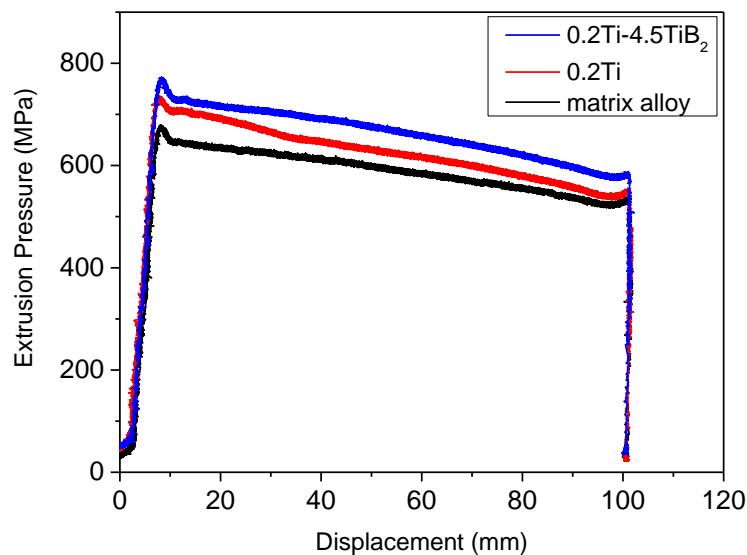


Fig. 5.15. Comparison of extrusion pressure for each studied material showing a higher extrusion pressure for the $0.2\text{Ti}-4.5\text{TiB}_2$ composite

5.5.2. Grain Structure in the Extruded Materials

Fig. 5.16 shows the as-extruded images taken from the surface and middle part of the extruded materials. As we can see from the figure, the microstructure on the surface region consisted of recrystallised grains for all three studied materials. This could be understood since high friction forces occurred at the die-bearing interface during extrusion which

generated heat, causing a higher temperature at the outer surface of the extrusion. This higher temperature provided a higher energy for recrystallisation to occur at the outer surface during deformation [27,190]. Consequently, recrystallised grains were observed at the surface of the extruded specimens. Comparing all three studied materials (Fig. 5.17), the matrix alloy exhibited larger recrystallised grains on the surface than the other two studied materials. This was in accordance with its initial grain size which had a larger initial as-cast grain size compared to the other materials studied.

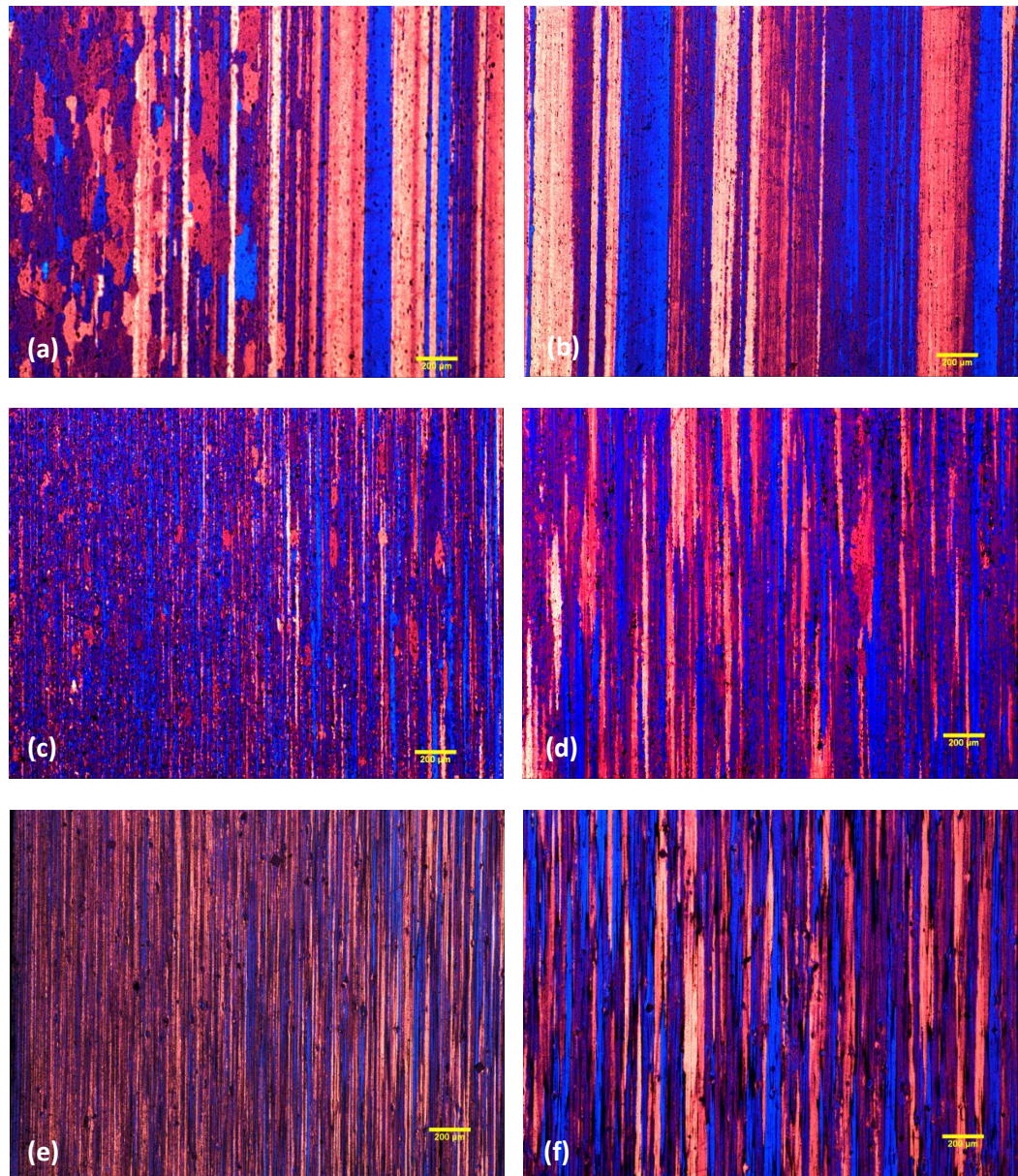


Fig. 5.16. Microstructure of as-extruded materials taken from the outer surface (left images) and the centre (right images) of (a-b) matrix alloy, (c-d) 0.2Ti alloy and (d-e) 0.2Ti-4.5TiB₂ composite

In contrast to that, the microstructure in the centre of the extrusion showed elongated grains parallel to the extrusion direction. Similar with the surface microstructure's trend, the matrix alloy showed larger grains compared to other studied materials because of its larger initial as-cast grains. Apart from that, this variation in grain size obtained in the extrusion is a very common problem. It, however, influences mechanical properties. Hence, in this study, the surface of the extruded materials were machined off and discarded to avoid the influence of recrystallised grains on the mechanical properties.

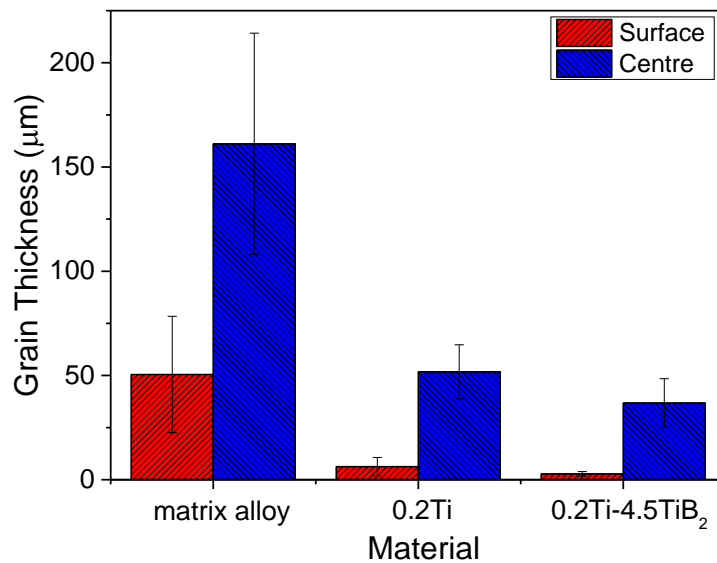


Fig. 5.17. Comparison of grain thickness on the specimen surface and at the centre of the specimen showing finer grain thickness at the surface

Regarding the secondary particles distribution in the 0.2Ti-4.5TiB₂ composite, similar behaviour with the as-rolled microstructure was observed. TiB₂ particles which were observed as clusters in the as-cast condition were found to string themselves out along the extrusion direction. Reduction in the TiB₂ string thickness was evident from Fig. 5.18a. Furthermore, although the effect of extrusion on Al₃Ti particle size was not significant, a decrement of Al₃Ti particles was observed in some areas and it was confirmed by their size distribution as presented in Fig. 5.18b. Upon extrusion, hardly any Al₃Ti particles were found larger than 35 μm. Hence, it was expected that some larger Al₃Ti particles were broken up during the extrusion process.

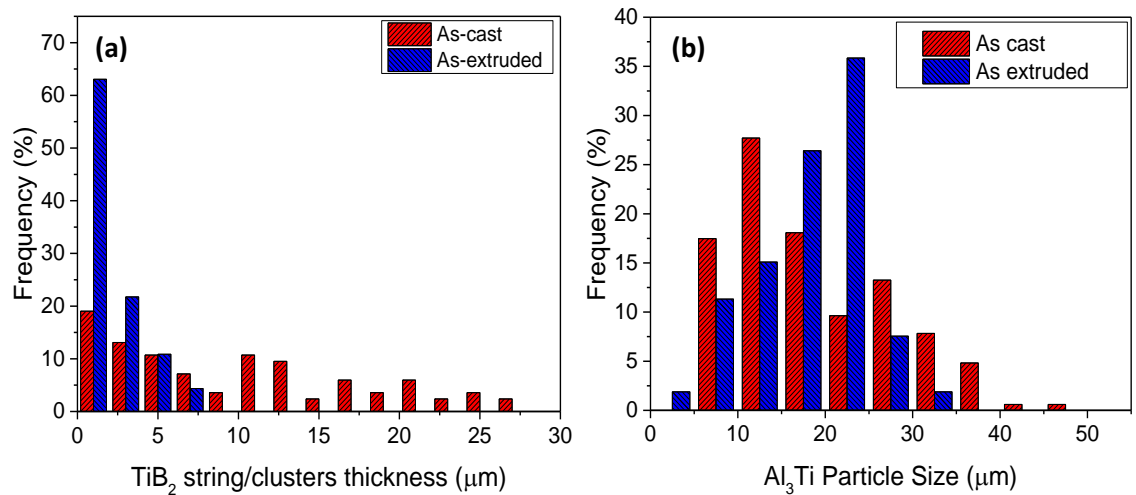


Fig. 5.18. (a) TiB_2 string/cluster thickness and (b) Al_3Ti particle size distribution comparison between as-cast and as-extruded condition

The above examination suggested that the clusters of TiB_2 and Al_3Ti particles were broken-up during deformation. It has been known that the metal flow in extrusion and hence extrusion properties are influenced by many factors such as the type of extrusion, the billet length, container and billet temperature, extrusion ratio, extrusion speed etc [190]. Among those factors, extrusion ratio and extrusion speed give a strong effect on the alignment and breaking-up of the particles and/or their clusters respectively. The extrusion speed applied will define the strain rate during extrusion. We know that the Al_3Ti particles and clusters of TiB_2 are harder than the matrix. Hence, upon deformation, the matrix region will experience a higher strain compared to the particles. From the previous compression results, we know that the matrix alloy has the highest strain rate sensitivity among all the studied materials. Therefore, we could assume that the matrix has a higher strain rate sensitivity compared to the particles. At a given extrusion speed, and hence strain rate, increase in flow stress of the matrix region was expected during deformation in which it forced the deformation at the particles and/or the cluster regions. Thus, it led to the particle break-up and shearing of the clustered regions.

5.6. Summary of the Effect of TiB_2 in the As-Cast and As-Deformed Materials

It has been clearly observed in this study that a finer grain size was achieved in the as-cast microstructure with addition of TiB_2 particles to the Al-Cu-Mg-Ag alloy. Average grain sizes of 355 μm , 84 μm and 59 μm were achieved in the matrix alloy, 0.2Ti and 0.2Ti-4.5 TiB_2 composite respectively. This was attributed to the existence of free Ti which nucleated the grains during solidification as well as the existence of TiB_2 particles around the grain boundaries which inhibited the grain growth during solidification.

There are several phases existing in the as-homogenised microstructure of the materials. Needle-shaped $\text{Al}_7\text{Cu}_2\text{Fe}$ intermetallic particles were observed in all the materials studied, while Al_3Ti particles were observed occasionally in the 0.2Ti alloy and 0.2Ti-4.5 TiB_2 composite. In addition to that, clusters of TiB_2 covering grain boundary areas as well as the triple junction areas were observed in the 0.2Ti-4.5 TiB_2 composite. Upon rolling, $\text{Al}_7\text{Cu}_2\text{Fe}$ as well as Al_3Ti particles were broken into short-elongated particles which were aligned in the rolling direction. Matrix bowing was clearly observed adjacent to those particles which suggested localised stress around the particles. Furthermore, TiB_2 particles which existed as clusters in the as-cast material, upon rolling, string themselves out along the rolling direction and/or extrusion direction, although in some areas, clusters of TiB_2 were still observed. Regarding the deformation mechanism during rolling, it was postulated that recovery was responsible for the deformation mechanism with localised recrystallisation in the vicinity of secondary particles. On the other hand, similar behaviour with the as-rolled microstructure was observed in terms of Al_3Ti particles and TiB_2 clusters upon extrusion. A decrement of Al_3Ti particles and TiB_2 string thickness was evident after extrusion.

In terms of the load required to deform each material, a higher finishing load was obtained during rolling of the 0.2Ti-4.5 TiB_2 composite compared to the other two alloys. Furthermore, a higher extrusion pressure was also obtained in the 0.2Ti-4.5 TiB_2 composite. This is in a good agreement with the Q_{HW} and flow stress values achieved in the previous chapter in which the 0.2Ti-4.5 TiB_2 composite showed the higher values of Q_{HW} and flow stress.

CHAPTER 6

INFLUENCE OF TiB_2 REINFORCEMENT ON THE STATIC RECRYSTALLISATION

6.1. Introduction

The previous chapter has explained the phases existing and their distribution in each of material processing steps i.e. as-cast, as-rolled and as-extruded materials which were hypothesised as influencing static recrystallisation (SRX) behaviour upon annealing. In this chapter, SRX behaviour and its dependency on the distribution, size and spacing of secondary particles present in the materials is discussed. A proposed SRX mechanism in the 0.2Ti-4.5TiB₂ composite is explained. Furthermore, the role of Al₃Ti and TiB₂ particles in SRX behaviour of the 0.2Ti-4.5TiB₂ composite is revealed.

As has been explained in section 3.3.5, all the materials studied in this thesis were annealed at a standard solution treatment temperature for the 0.2Ti-4.5TiB₂ composite, 540°C, for SRX observation. Nonetheless, the effect of TiB₂ on the recrystallisation temperature is revealed. Apart from discussing the SRX behaviour of sheet and extruded materials, the effect of deformation parameters, i.e. strain rates and temperature on the SRX behaviour is also explained in terms of compressed specimens. An important finding regarding the dependency of SRX with the flow stress has been observed which could be beneficial to industry.

6.2. Recrystallisation in Compressed Materials

6.2.1. Effect of Temperature and Strain Rate on the Recrystallisation

Following compression testing which was discussed in Chapter 4, specimens deformed at 300°C, 10⁻¹ s⁻¹, representing a high Z condition (low T and high $\dot{\epsilon}$) and 500°C, 10⁻³ s⁻¹, representing a low Z conditions (high T and low $\dot{\epsilon}$), were solution treated at 540°C for 2 h, an industrial standard solution treatment parameter. In this study, EBSD was utilised to examine the static softening behaviour. Similar to the previous examinations, in this analysis, low angle grain boundaries (LAGBs), 0 - 8° [102], are indicated with grey lines,

medium-angle grain boundaries (MAGBs), $8 - 15^\circ$ [102], are indicated with white lines and high-angle grain boundaries (HAGBs), $>15^\circ$ [102], are indicated with black lines.

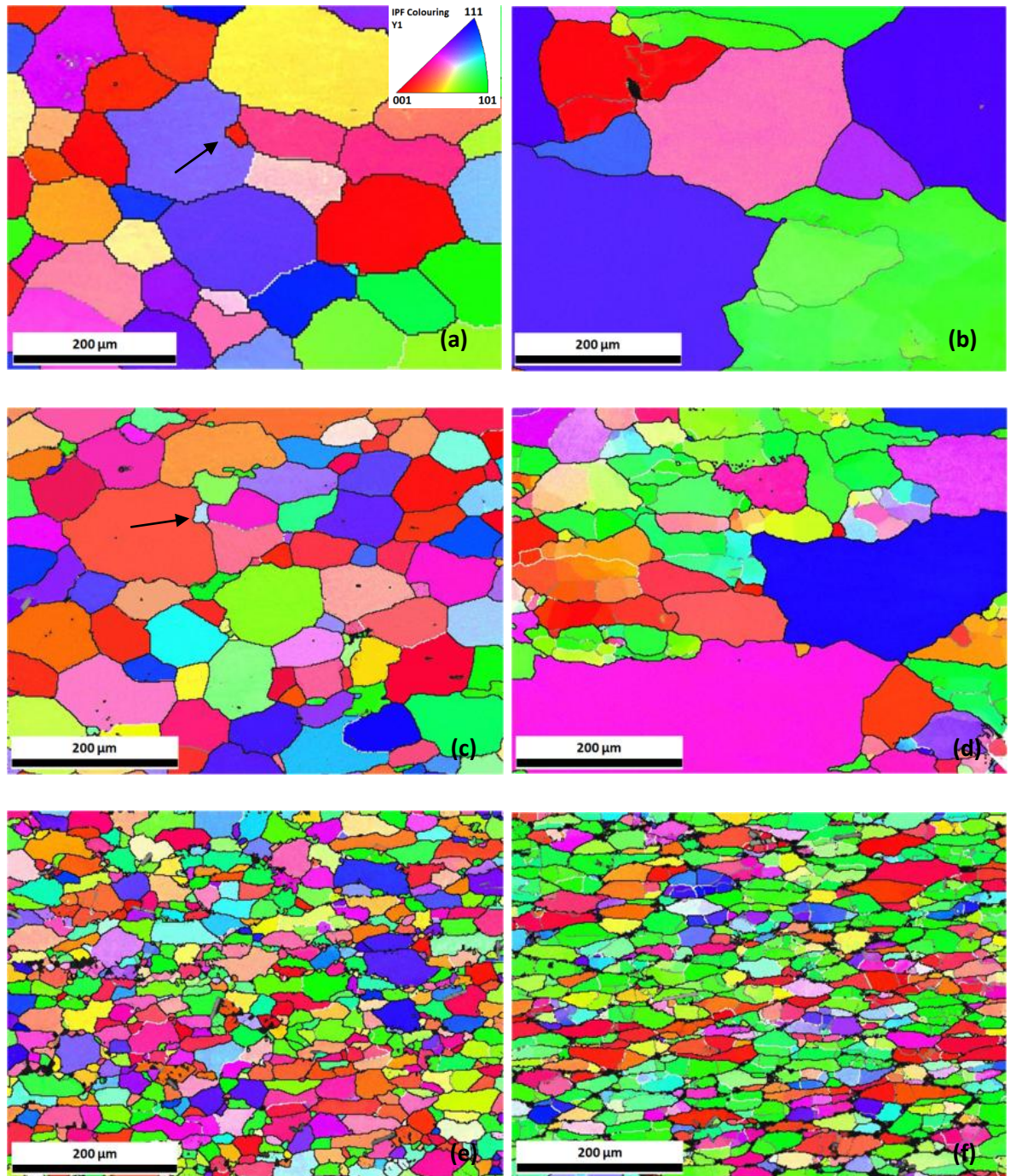


Fig. 6.1. Effect of temperature and strain rate on the microstructural development after solution treatment at 540°C for 2 h on the materials deformed at temperature of 300°C with a strain rate of 10^{-1} s^{-1} (left) and 500°C with a strain rate of 10^{-3} s^{-1} (right); (a-b) matrix alloy, (c-d) 0.2Ti alloy and (e-f) 0.2Ti-4.5TiB₂ composite

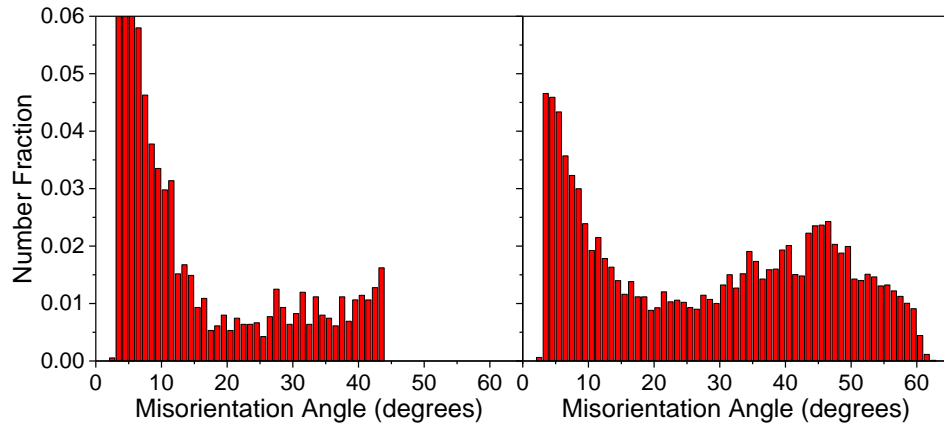


Fig. 6.2. Comparison of misorientation profile of as-compressed (left) and as-annealed (right) $0.2\text{Ti}-4.5\text{TiB}_2$ specimens deformed at 500°C with a strain rate of 10^{-3} s^{-1}

Compared with the as-compressed microstructure which has been described in Chapter 4, it can be clearly seen that in general, all of the studied materials were generally fully recrystallised following annealing at 540°C for 2 h. This was indicated by as-annealed boundaries which mostly consisted of HAGBs as shown in Fig. 6.1. This was confirmed by the misorientation profile (which is listed in Appendix C for brevity) which showed an increment of HAGBs following annealing at 540°C for 2 h. However, an interesting finding was observed in the $0.2\text{Ti}-4.5\text{TiB}_2$ composite. If we compared its microstructure with the as-compressed as presented in Chapter 4, a significant change in the grain orientation was evident following annealing of a specimen deformed at 300°C , 10^{-1} s^{-1} . A fine grain structure was observed along the grain boundaries of the $0.2\text{Ti}-4.5\text{TiB}_2$ composite suggesting recrystallisation occurred following the annealing treatment. In contrast to that, the deformed microstructure seemed to be retained following annealing of the specimen deformed at 500°C , 10^{-3} s^{-1} as no significant change was observed in this microstructure. However, by comparing the misorientation degree between as-deformed and as-annealed microstructures, a lower density of LAGBs and a higher density of MAGBs and HAGBs (Fig. 6.2) were observed in the as-annealed microstructure. This might suggest a coarsening of subgrains and/or recrystallisation.

Furthermore, coarsening of the grain size was evident following subsequent annealing of a deformed specimen at high temperature and low strain rate as shown in Fig. 6.3a. A coarser grain size was achieved in all studied materials following annealing of the specimen deformed at 500°C with a strain rate of 10^{-3} s^{-1} (low Z) compared to the specimen

deformed at 300°C with a strain rate of 10^{-1} s^{-1} (high Z). According to the literature [30,175], a higher dislocation density was created during deformation at a low temperature and high strain rate (high Z) compared to the deformation at high temperature and low strain rate (low Z). The higher flow stress achieved during deformation at high Z as described in Chapter 4 gave evidence to this theory. This higher dislocation density obtained during deformation leads to the higher stored energy, providing a higher driving force for static recrystallisation (SRX) on subsequent annealing. And hence, finer grains were achieved on the subsequent annealing of a specimen deformed at 300°C with a strain rate of 10^{-1} s^{-1} . In contrast to that, dislocations are more mobile during deformation at low Z conditions, leading to dislocation annihilation [30,102]. This was reflected in the low flow stress achieved on deformation at low Z as has been explained in Chapter 4. Moreover, extensive dynamic recovery (DRV) observed on the deformed specimen also supported this postulation. As a result, less energy will be stored as a driving force for SRX, and hence coarse grains were observed upon annealing of a specimen deformed at 500°C with a strain rate of 10^{-3} s^{-1} . In other words, the amount of recovery occurring before recrystallisation during annealing in this particular deformed specimen was dominant, resulting in coarser grains. The same results was observed in previous observations by Sheppard [191] and M. Ferry [192].

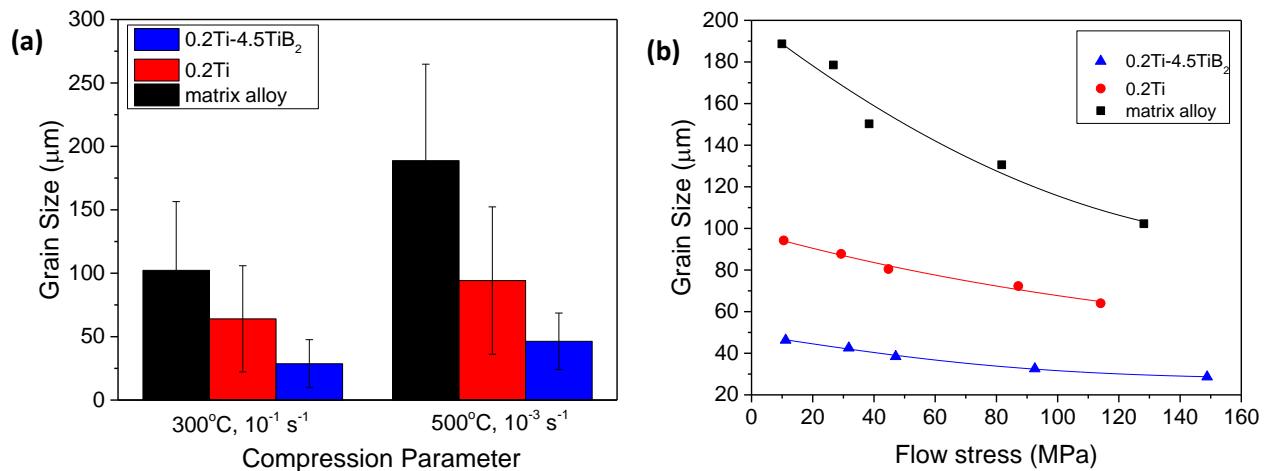


Fig. 6.3. (a) Recrystallised grain size following annealing at 540°C for 2 h as a function of compression parameter showing larger grains on the subsequent annealed specimen which was deformed at high temperature and a low strain rate (low Z); (b) recrystallised grain size as a function of flow stress

The above observation leads the author of this thesis to the hypothesis in which the static recrystallisation behaviour of the prior hot deformed specimen is related to its flow stress. Consequently, Fig. 6.3b is presented to investigate this hypothesis. It can be clearly seen that in all the studied materials, a higher flow stress achieved during deformation led to finer recrystallised grains on subsequent annealing. Similar observations were also obtained in earlier research by Sheppard and Vierod [191]. They stated that the flow stress achieved on deformation is related to the energy stored for static recrystallisation upon annealing. It has been observed by them that any decrement in the flow stress resulted in a decrement in the driving force for static recrystallisation. Consequently, it could be understood why coarser grains were achieved on the as-annealed specimen following deformation at a low flow stress levels. This observation could be very useful for industry in which if the stress is kept low during processing, nucleation will be retarded and a coarse microstructure and/or retainment of the deformed microstructure will be obtained during subsequent heat treatment.

6.2.2. Nucleation of Recrystallisation

It has been known that during annealing after hot deformation, nuclei for recrystallisation can be formed at various sites, depending on its hot deformation parameters and initial microstructure [175]. In the matrix alloy and 0.2Ti alloy, fine recrystallised grains at grain boundaries (indicated with black arrows in Fig. 6.1a-c) were evident upon annealing following deformation at a low temperature and a high strain rate (high Z). This suggests that recrystallised grains might nucleate at grain boundaries during annealing of a specimen deformed at high Z . Shear bands observed on the as-compressed specimen might also act as nuclei for recrystallised grains. Furthermore, recrystallised grains were also estimated nucleating in the vicinity of Al_3Ti particles in the 0.2Ti alloy. Upon annealing after hot deformation at high temperature and low strain rates (low Z) in which recrystallisation was sluggish, indicated by coarse grains, the nucleation sites were estimated to be the initial grain boundaries. As has been explained above, a high amount of recovery was expected to occur before recrystallisation during annealing in this specimen which led to the retardation of recrystallisation. Consequently, recrystallised grains observed upon annealing in this specimen were estimated to be a result of subgrain boundary migration which transform into grain boundaries during annealing.

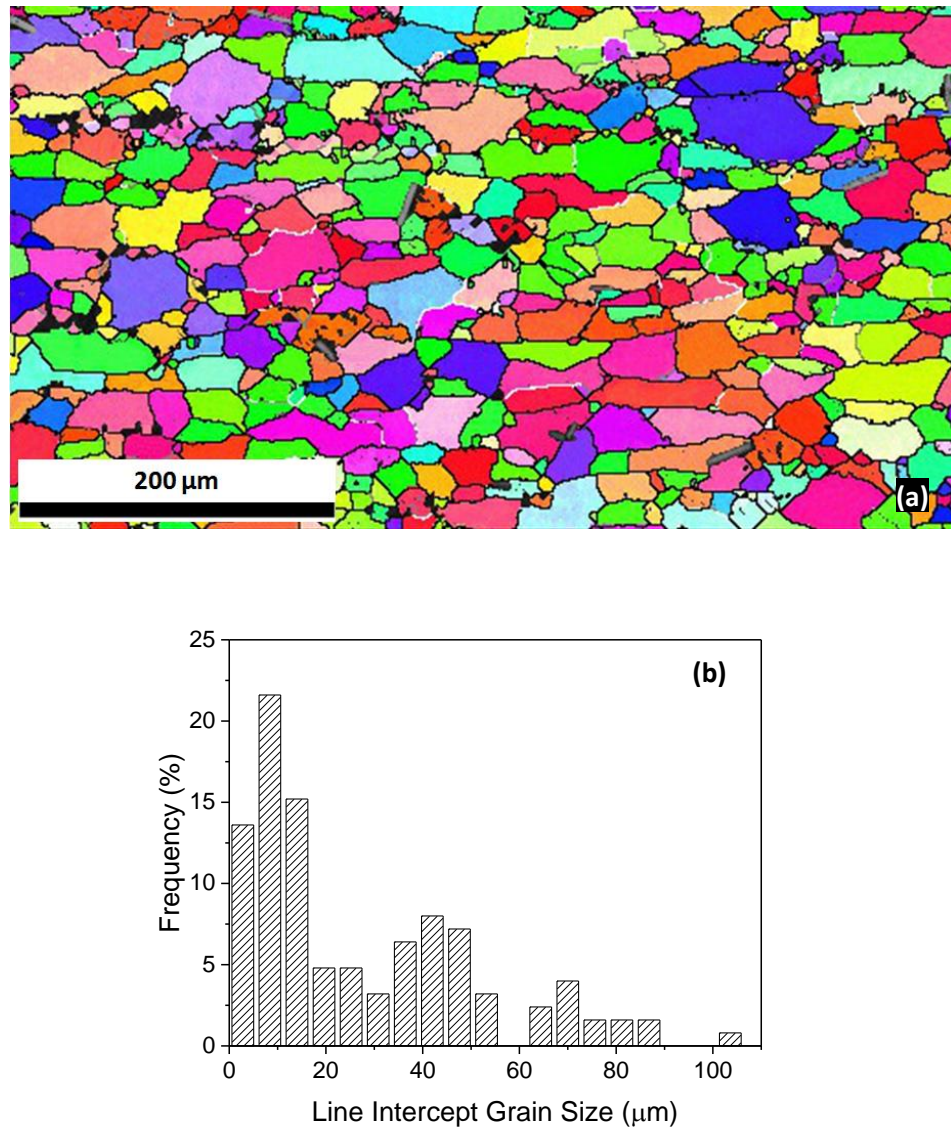


Fig. 6.4. (a) Annealed microstructure and (b) grain size distribution of the 0.2Ti-4.5TiB₂ composite deformed at 300°C, 10⁻¹ s⁻¹, showing heterogeneity of recrystallised grains

On the other hand, in the 0.2Ti-4.5TiB₂ composite, fine recrystallised grains were observed nucleating in the vicinity of clusters of TiB₂ particles located at the grain boundaries upon subsequent annealing of specimen prior hot deformed at high Z as is shown in Fig. 6.4a. Compared with the other two alloys, it was noted that heterogeneous recrystallised grains were obtained in the 0.2Ti-4.5TiB₂ composite as illustrated in Fig. 6.4b. Fine recrystallised grains were mainly observed at the grain boundaries, whereas in other areas, large recrystallised grains were observed. Heterogeneous recrystallised grains achieved upon annealing of this particular specimen were hypothesised due to heterogeneous deformation zones which occurred during deformation. The area adjacent to the TiB₂ clusters at grain

boundaries was postulated to have a higher accumulated strain. In addition to that, the discrepancy of thermal expansion between TiB_2 clusters and the matrix will create local deformation at the interfaces. On the subsequent annealing, subgrain boundaries will be formed in this area and convert into recrystallised grains [176,193].

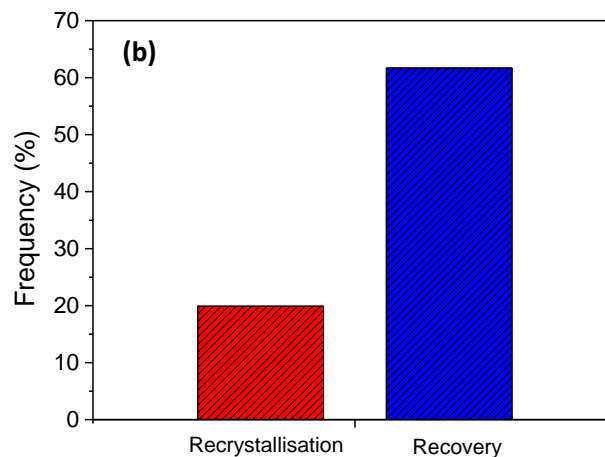
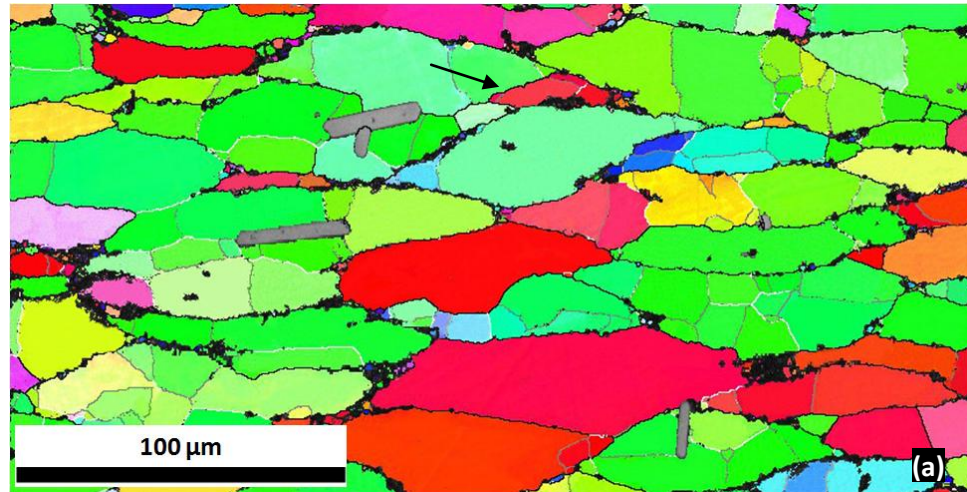


Fig. 6.5. Microstructure of the 0.2Ti-4.5TiB₂ composite previously deformed at 500 °C at a strain rate of 10^{-3} s^{-1} and subsequently annealed at 540 °C for 2 h. Black areas indicate TiB_2 particles

In contrast to that, similar to the other two alloys, with increasing deformation temperature and decreasing strain rate, nucleation tended to be less effective in the 0.2Ti-4.5TiB₂ composite. It was proved by Fig. 6.5 that recovery dominated following annealing of a specimen deformed at high temperature and a low strain rate. Discontinuous

recrystallisation was suppressed during annealing. Fig. 6.5 shows the microstructure of the annealed microstructure of the material deformed at a high temperature and a low strain rate which contained a mixture of HAGBs and LAGBs. It was noted that the HAGBs were mostly observed associated with TiB_2 clusters (indicated with a black arrow). As was explained in Chapter 4, deformation at this temperature and strain rate involved the formation of subgrains. Highly misoriented subgrains were observed adjacent to TiB_2 clusters upon deformation and hence during annealing, these subgrains will convert into new grains.

6.3. Recrystallisation in Sheet Materials

6.3.1. Effect of TiB_2 Addition on the Recrystallisation Temperatures

Hot stage EBSD was carried out on the matrix alloy and the 0.2Ti-4.5TiB₂ composite to study the effect of TiB_2 addition on the recrystallisation temperature. The scan was conducted from room temperature to 540°C as described in Fig. 6.6. It was observed that recrystallisation started at a temperature of 345°C in the matrix alloy, whilst in the 0.2Ti-4.5TiB₂ composite; recrystallisation started at a temperature 375°C. This result suggested the recrystallisation was delayed by the addition of TiB_2 particles. As the temperature was increased to 540°C, both materials showed a fully recrystallised grain structure.

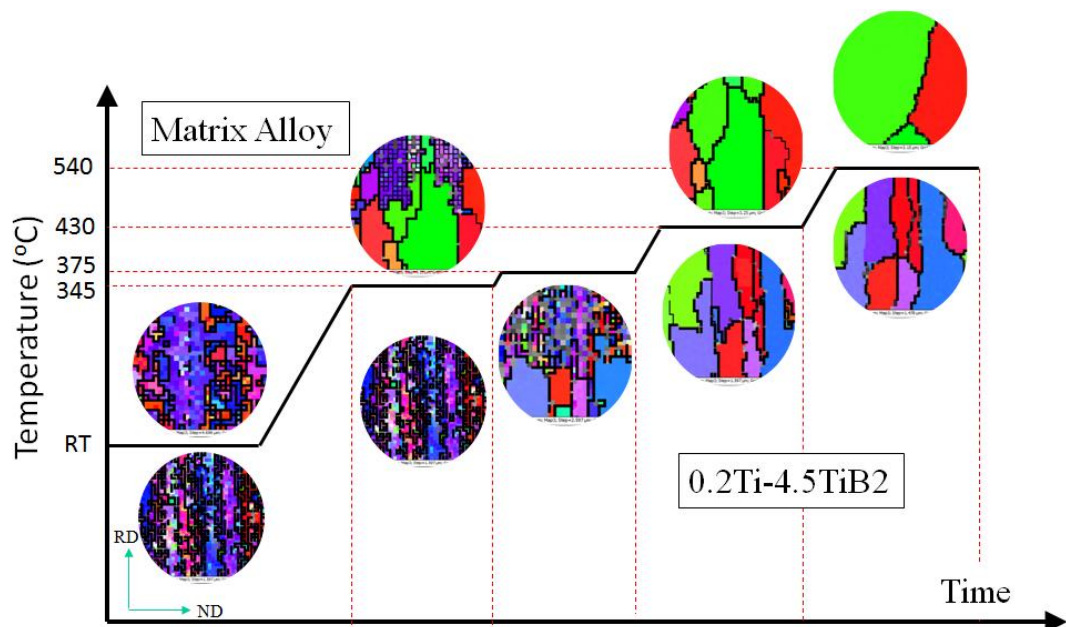


Fig. 6.6. Schematic illustration of recrystallisation kinetics of the matrix alloy and the 0.2Ti-4.5TiB₂ composite, showing retardation of the recrystallisation temperature by the addition of TiB_2 particles

From Chapter 5, we know that both of the sheet materials, the matrix alloy and the 0.2Ti-4.5TiB₂ composite, contain secondary particles in their microstructure. A homogeneous distribution of Al₇Cu₂Fe was found in the matrix alloy, whilst it was found to be segregated to the interface of TiB₂ particles in the 0.2Ti-4.5TiB₂ composite. Besides that, Al₃Ti and TiB₂ particles also existed in the 0.2Ti-4.5TiB₂ composite. Therefore, the existence of these particles might influence the recrystallisation kinetics. It has been known that in materials containing secondary particles, the rate of the recrystallisation is strongly influenced by the particle distribution. Closely spaced particles tend to retard or even completely inhibit recrystallisation, whilst large and widely spaced particles tend to accelerate recrystallisation [30]. It has been observed that the transition between accelerated to retarded recrystallisation is generally dependent on the particle's volume fraction (F_v) and particle's radius (r). Retardation of recrystallisation occurs when the parameter F_v/r is greater than $\sim 0.2 \mu\text{m}^{-1}$. If F_v/r is less than this value, acceleration of recrystallisation will occur, even if the particles are not large enough for particle stimulated nucleation (PSN) recrystallisation to occur [30,194].

Following the above review, the F_v/r value for each of the materials was calculated. The F_v was calculated using a systematic manual point count according to ASTM E562. The F_v/r value of the Al₇Cu₂Fe particles in the matrix alloy is $0.012 \mu\text{m}^{-1}$. While Al₃Ti and TiB₂ particles in the 0.2Ti-4.5TiB₂ composite are $0.0031 \mu\text{m}^{-1}$ and $0.24 \mu\text{m}^{-1}$ respectively. Therefore, based on these calculations, Al₇Cu₂Fe as well as Al₃Ti particles in the matrix alloy and 0.2Ti-4.5TiB₂ composite respectively, were found to accelerate recrystallisation, whilst TiB₂ particles in the composite were found to retard recrystallisation. Hence, the 0.2Ti-4.5TiB₂ composite exhibited a higher recrystallisation temperature during in-situ annealing. In addition to that, in some areas, TiB₂ particles were later on (section 6.3.4) observed to pin the grain boundaries during in-situ annealing, suggesting an inhibition of grain boundary migration. And hence, it leads to the retardation of recrystallisation. This observation will be further discussed later.

6.3.2. Effect of TiB₂ Addition on the Recrystallisation Behaviour

Following the above observations, ex-situ observation under EBSD was carried out on each of the materials to investigate the influence of TiB₂ addition on the recrystallisation behaviour. Fully recrystallised grains were observed in all the studied materials upon annealing at a solution treatment temperature of 540°C for 2 h. However, a clear

discrepancy was observed between recrystallised grains of the 0.2Ti-4.5TiB₂ composite and the other two alloys as shown in Fig. 6.7. A more equiaxed grain structure was observed in the matrix alloy (grain aspect ratio: 0.6) and the 0.2Ti alloy (grain aspect ratio: 0.38), whilst a large elongated grain structure parallel to the rolling direction was observed in the 0.2Ti-4.5TiB₂ composite (grain aspect ratio: 0.15). These highly elongated grains observed in the 0.2Ti-4.5TiB₂ composite might be due to the existence of TiB₂ strings which are elongated in the rolling direction. This might constrain grain boundary migration normal to the rolling direction. Furthermore, the coarser recrystallised grains observed in the 0.2Ti-4.5TiB₂ composite suggested the retardation of recrystallisation due to the addition of TiB₂ particles. This might be attributed to the limited nucleation sites existing in the 0.2Ti-4.5TiB₂ composite.

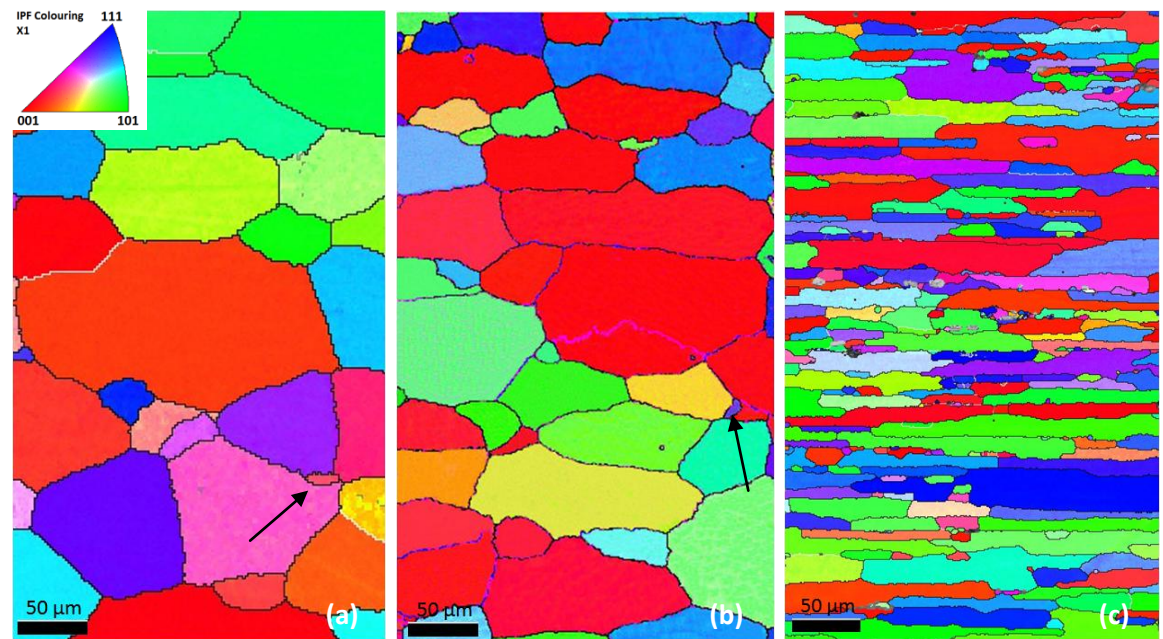


Fig. 6.7. IPF map of (a) matrix alloy, (b) 0.2Ti alloy and (c) 0.2Ti-4.5TiB₂ composite showing a fully recrystallised structure upon annealing at 540 °C for 2 h

It is well-known that the recrystallisation behaviour after deformation of a material is strongly dependent on its deformation structure. In two-phase materials like the materials studied in this thesis, the recrystallisation behaviour is strongly defined by the particle's volume fraction and their shape as well as their spacing [30,195]. The interparticle spacing could be calculated using several methods [196]. In this thesis, nearest-neighbour distance

(Δ) which is defined as the average centre-to-centre distance between any particle and its neighbouring particle was used for interparticle spacing calculations [196]. Nearest-neighbour distance on a plane (Δ_2) was utilised in this thesis and can be calculated by:

$$\Delta_2 = 0.500 N_A^{-1/2} \quad (6-1)$$

Where N_A is the number of particles per unit area on any plane section which can be calculated by

$$N_A = \frac{3 F_V}{2\pi r^2} \quad (6-2)$$

Where F_V is the particle volume fraction and r is the radius of the particle.

As has been explained in Chapter 5, large $\text{Al}_7\text{Cu}_2\text{Fe}$ particles with an average size of $4.2 \mu\text{m}$ and $3.3 \mu\text{m}$ were observed in an as-rolled matrix alloy and 0.2Ti alloy respectively. These particles were distributed homogeneously with average interparticle spacing of $7 \mu\text{m}$. Matrix bowing which indicated accumulation of dislocations was clearly observed in the as-rolled materials as explained in Chapter 5. Consequently, during annealing, besides grain boundaries and shear bands observed in the matrix alloy and 0.2Ti alloy, $\text{Al}_7\text{Cu}_2\text{Fe}$ particles were also estimated to promote nucleation, inducing particulate stimulated nucleation (PSN). Furthermore, the existence of Al_3Ti particles in the 0.2Ti alloy was also estimated as promoting PSN. Owing to these large number of nucleation sites in the matrix alloy and the 0.2Ti alloy, it could be understood why more equiaxed recrystallised grains were observed in both alloys.

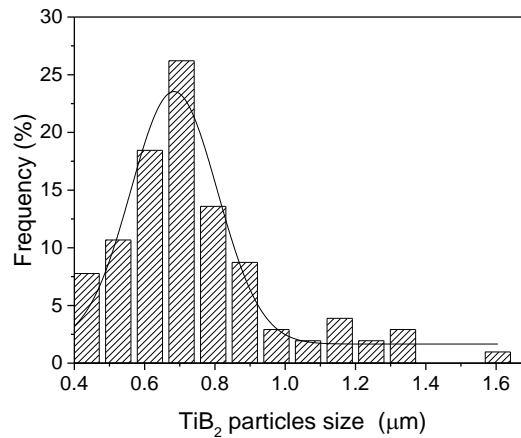


Fig. 6.8. TiB_2 particle size distribution in 0.2Ti-4.5TiB₂ composites

In contrast to both the other alloys, TiB_2 particles with an average size of $0.7\ \mu\text{m}$ which existed in the as-rolled $0.2\text{Ti}-4.5\text{TiB}_2$ composite were too small to act as PSN nuclei. To be amenable to cause PSN, there has to be a deformation zone around the particle and the matrix has to have enough stored energy for a nucleus to grow away from the particle [30,192]. Furthermore, PSN has been known to occur at particles with a diameter greater than $1\ \mu\text{m}$ [30]. Fig. 6.8 illustrates the distribution of TiB_2 particles size in the $0.2\text{Ti}-4.5\text{TiB}_2$ composite. It can be clearly seen that most of the particles sizes fall below $1\ \mu\text{m}$. Although TiB_2 particles were found as strings with a range of thickness from $0.3\ \mu\text{m}$ to $1.5\ \mu\text{m}$, the author of this thesis postulated that the high level of deformation experienced by matrix shearing in the TiB_2 string zone was recovered during annealing and hence there was no adequate strain left to generate recrystallised grains in this region. In addition to that, the distribution of TiB_2 which is relatively closely-spaced across the string (average interparticle spacing $1.7\ \mu\text{m}$) will inhibit grain boundary migration, leading to retardation of recrystallisation and hence resulting in coarse recrystallised grains. Detailed analysis on the effect of TiB_2 particle on the inhibition of grain boundary migration will be discussed later in section 6.3.4.

6.3.3. Effect of the Particle Distribution on the Grain Size

It was noted that a more homogeneous recrystallised grain size distribution was observed in the matrix alloy and the 0.2Ti alloy compared to the $0.2\text{Ti}-4.5\text{TiB}_2$ composite. This might be attributed to the more homogeneous deformation microstructure achieved in both materials. As was explained in the previous chapter, homogeneous shear bands as well as $\text{Al}_7\text{Cu}_2\text{Fe}$ particles distribution were observed in the matrix alloy and the 0.2Ti alloy. Matrix bowing observed adjacent to the $\text{Al}_7\text{Cu}_2\text{Fe}$ particles in the as-rolled microstructure proved a higher dislocation density around the particles, indicating high stored energy for recrystallisation. Upon annealing, these shear bands and $\text{Al}_7\text{Cu}_2\text{Fe}$ will act as nucleation sites for recrystallised grains, resulting in a homogeneous recrystallised grain size. Fine recrystallised grains (indicated with black arrows) at grain boundaries are shown in Fig. 6.7, suggesting that grain boundaries also acted as nucleation sites in the matrix alloy and the 0.2Ti alloy.

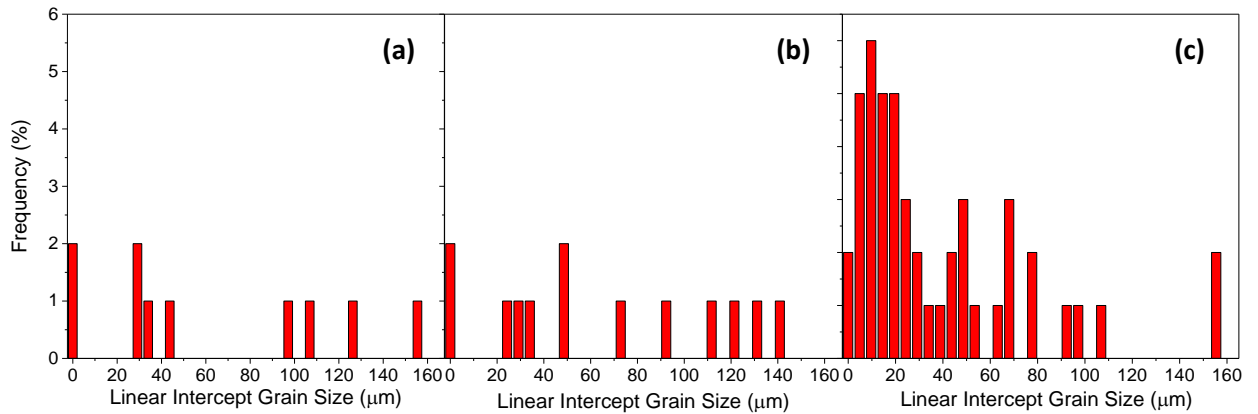


Fig. 6.9. Linear intercept grain size distribution of (a) matrix alloy; (b) 0.2Ti alloy and (c) 0.2Ti-4.5TiB₂ composite

In contrast to the matrix alloy, a heterogeneous recrystallised structure was observed in the 0.2Ti-4.5TiB₂ composite upon annealing and might be due to the heterogeneous structure obtained upon deformation. It has been explained before in Chapter 5 that Al_3Ti particles and TiB_2 clusters appeared occasionally in the deformed structure. Thus, nucleation sites were limited in the 0.2Ti-4.5TiB₂ composite, leading to the coarse recrystallised grains. Fine recrystallised grains observed in the 0.2Ti-4.5TiB₂ composite were believed to have nucleated in the vicinity of Al_3Ti particles (average size: 8.2 μm) and TiB_2 clusters (average size: 3.5 μm). This will, later on, be confirmed in a detailed examination in section 6.3.4.

Those above observations were reflected from their texture as shown in Fig. 6.10. Recrystallisation texture has been known to have a direct dependence on the orientation of nucleation sites for recrystallisation, which might be originated on the grain boundaries or intergranular sites [176]. In this study, the matrix alloy has the strongest texture of all as described from the $\{111\}$ pole figure in Fig. 6.10a. Its pole figure showed the least orientation spread with a maximum intensity of 12.37. As already described above, homogeneous shear bands and $\text{Al}_7\text{Cu}_2\text{Fe}$ were observed in the as-rolled microstructure, resulting in the least random orientation of recrystallised grains during annealing. Furthermore, 0.2Ti alloy exhibited a weaker texture and more random orientation spread than the matrix alloy with a maximum intensity of 11.49. This was attributed to the existence of Al_3Ti particles which were randomly distributed in the as-rolled microstructure as was explained in Chapter 5. On the other hand, the 0.2Ti-4.5TiB₂ composite exhibited the weakest texture and the most random orientation of all (max:

9.53). This could be explained since a random distribution of Al_3Ti particles as well as TiB_2 clusters existed in the 0.2Ti-4.5TiB₂ composite, resulting in heterogeneous recrystallised grains, leading to the random recrystallisation texture.

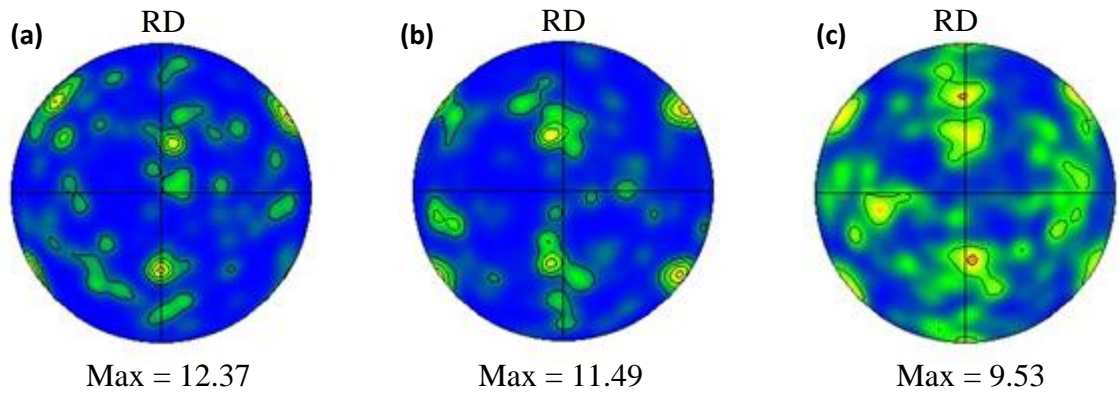
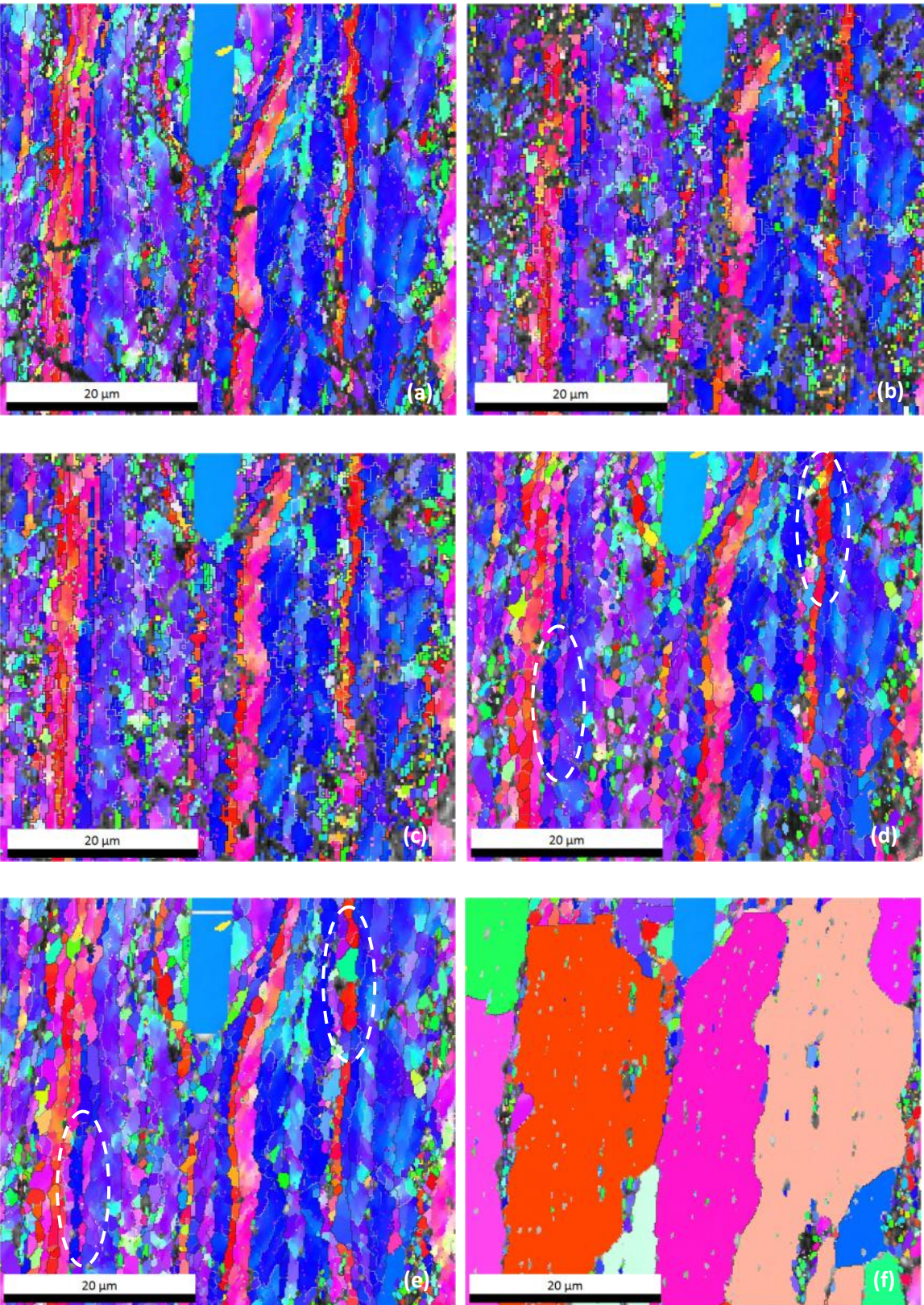


Fig. 6.10. $\{111\}$ pole figures of all alloys in the (a) matrix alloy; (b) 0.2Ti alloy and (c) 0.2Ti-4.5TiB₂ composite upon annealing at 540°C for 2 h

6.3.4. Recrystallisation Mechanism in 0.2Ti-4.5TiB₂ Composite

Fig. 6.11 shows the microstructural evolution of the 0.2Ti-4.5TiB₂ composite in a series of EBSD IPF maps for a heating rate of 5 K minute⁻¹ between room temperature and 375°C as well as the misorientation profile for each heating step. Similar to previous analysis, to differentiate between the substructure and grain boundaries, in this analysis low angle grain boundaries (LAGBs), 0 - 8° [102], are indicated with grey lines, medium-angle grain boundaries (MAGBs), 8 - 15° [102], are indicated with white lines and high-angle grain boundaries (HAGBs), >15° [102], are indicated with black lines.



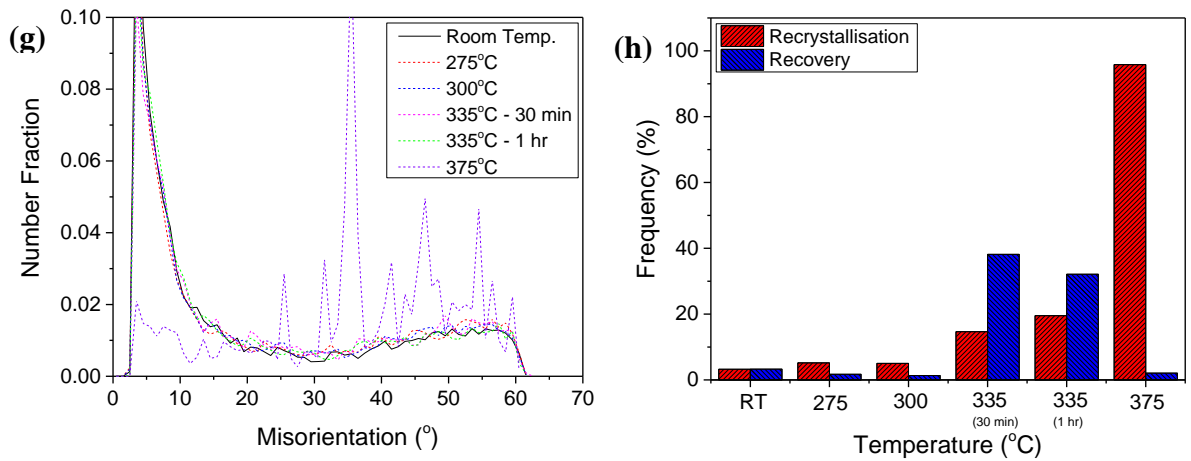


Fig. 6.11. IPF maps derived from in-situ experiments at temperatures of (a) room temperature, (b) 275 $^{\circ}\text{C}$, (c) 300 $^{\circ}\text{C}$, (d) 335 $^{\circ}\text{C}$ for 30 minutes, (e) 335 $^{\circ}\text{C}$ for 1 h, (f) 375 $^{\circ}\text{C}$ and (g) misorientation profile comparison, (h) SRX vs SRV percentage during in-situ EBSD scanning

As was explained before in Chapter 5, it can be clearly seen from Fig. 6.11 that highly misoriented boundaries were observed in the vicinity of Al_3Ti particles in the as-deformed microstructure (room temperature scanning). This suggested that a high localised stress was accumulated adjacent to the Al_3Ti particles. Further increasing temperature, it was noted that there were no significant changes observed in the microstructure until a temperature of 300 $^{\circ}\text{C}$. This was reflected from the misorientation (MO) profile which did not show any significant changes from room temperature (RT) until a temperature of 300 $^{\circ}\text{C}$. This was also supported by the SRV and SRX percentage over that temperature range which did not reveal any significant changes, suggesting no significant changes in microstructure over that temperature range. Furthermore, although the MO profile did not exhibit any significant changes upon heating at 335 $^{\circ}\text{C}$ for 30 minutes, an increment of SRV degree was evident from Fig. 6.11d, suggesting annihilation of dislocations. Upon being subjected to the temperature of 335 $^{\circ}\text{C}$ for 1 hour, localised recrystallisation was observed in some areas (indicated with white circles). And finally, following heating at 375 $^{\circ}\text{C}$, large and elongated fully recrystallised grains, similar with the observation in section 6.3.2 were obtained. In addition to that, fine recrystallised grains were clearly observed in the vicinity of Al_3Ti particles and TiB_2 clusters, indicating high energy stored in these areas upon deformation, leading to the higher degree of recrystallisation. In addition to that, grain

boundary pinning by TiB_2 particles was clearly observed in the microstructure (indicated by black circles in Fig. 6.12).

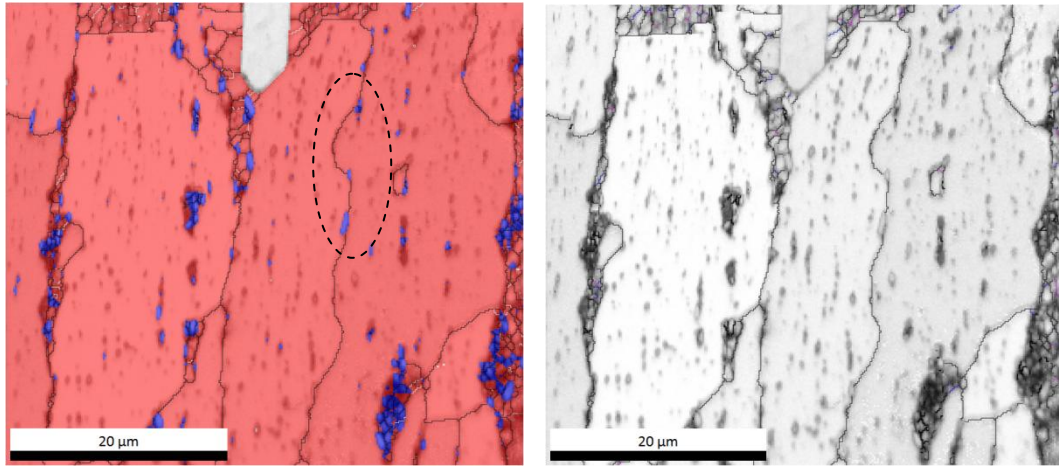


Fig. 6.12. Phase map (left) and band contrast map (right) of the 0.2Ti-4.5TiB₂ composite heated in the hot stage EBSD at 375 °C showing fine recrystallised grains in the vicinity of Al₃Ti particles and TiB₂ clusters

From the above observation, it can be concluded that a bimodal grain structure which consisted of large elongated and fine recrystallised grains was formed during annealing of the 0.2Ti-4.5TiB₂ composite. Nucleation of recrystallisation was always associated with the Al₃Ti particles and TiB₂ clusters. Matrix bowing observed in the vicinity of Al₃Ti particles and TiB₂ clusters in the as-deformed microstructure as explained in Chapter 5 indicated that local deformation occurred during deformation in these regions. Furthermore, the difference of thermal expansion between the matrix and TiB₂ clusters and Al₃Ti particles might cause additional local deformation at the interface. This led to the formation of dislocation cells around the particles which have a high misorientation with their neighbouring cells. During annealing, these dislocation cells will rearrange themselves into subgrain boundaries and hence convert to a recrystallised grain. Consequently, fine recrystallised grains were observed around Al₃Ti particles and TiB₂ clusters. Furthermore, grain boundary pinning by TiB₂ particles was evident as described in Fig. 6.12. Due to this pinning effect, grain boundary migration during annealing will be inhibited, leading to the retardation of recrystallisation. Consequently, in other areas where TiB₂ clusters and Al₃Ti particles were absent, large recrystallised grains were observed.

From the above observation, it could be concluded that large Al_3Ti particles and small TiB_2 particles have opposing effects as illustrated in Fig. 6.13. The net result will depend on parameters such as the size and interparticle spacing, initial grain size and the degree of deformation [197]. In this thesis, the Al_3Ti particles tend to accelerate recrystallisation, whilst TiB_2 particles tend to retard recrystallisation by pinning the grain boundaries, unless they are clustered.

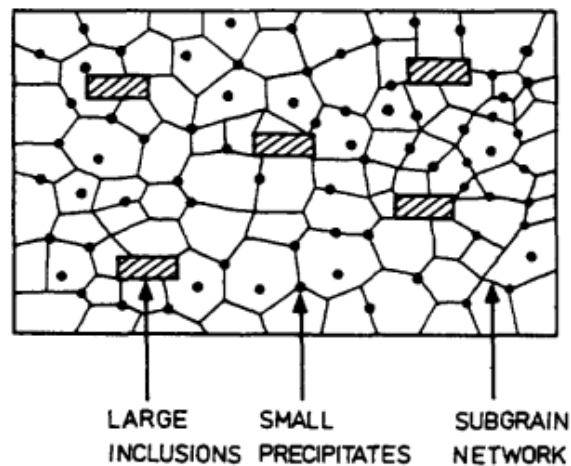


Fig. 6.13. Illustration of principal microstructural evolution during annealing of material containing bimodal particles, showing grain boundary pinning by small particles, whilst large particles accelerate recrystallisation [198]

6.4. Recrystallisation in Extruded Materials

Similar to sheet material, extruded materials were also subjected to annealing at 540°C for 2 h for SRX observation. Fig. 6.14 shows the IPF map of extruded materials upon annealing. Similar to previous examination, in this analysis, low angle grain boundaries (LAGBs), $0 - 8^\circ$ [102], are indicated with grey lines, medium-angle grain boundaries (MAGBs), $8 - 15^\circ$ [102], are indicated with white lines and high-angle grain boundaries (HAGBs), $>15^\circ$ [102], are indicated with black lines.

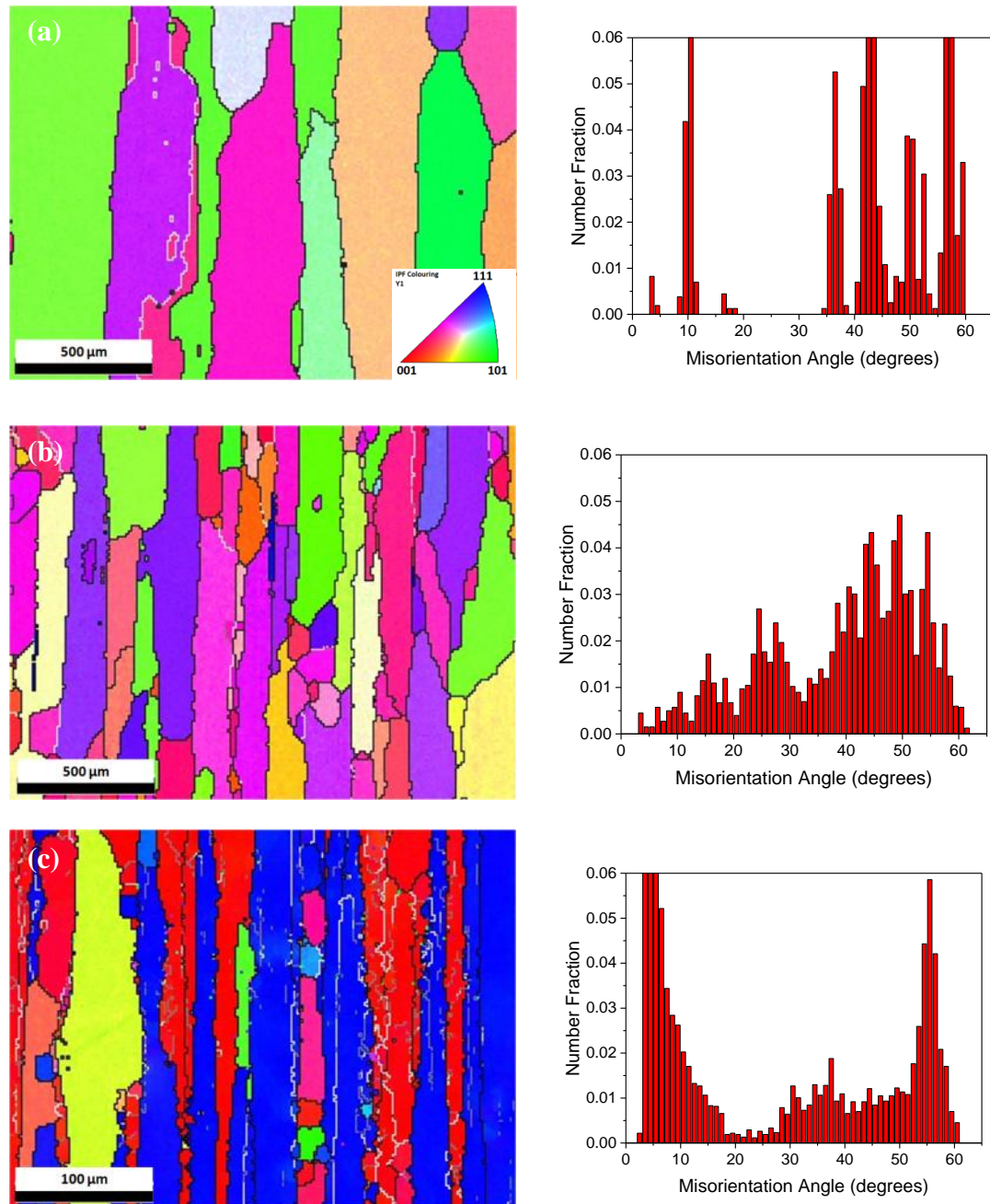


Fig. 6.14. IPF Maps of (a) matrix alloy; (b) 0.2Ti alloy and (c) 0.2Ti-4.5TiB₂ composite showing fully recrystallised structures upon annealing at 540°C for 2 h

It can be clearly seen that in contrast to the sheet product, all of the extruded materials exhibited large elongated grains parallel to the extrusion direction. Homogeneous large elongated grains were observed in the matrix alloy, while heterogeneous grains containing large elongated and fine grains were observed in the 0.2Ti alloy and the 0.2Ti-4.5TiB₂ composite. The fine grain observed in the 0.2Ti and the 0.2Ti-4.5TiB₂ composite were proposed due to the existence of Al_3Ti particles and TiB_2 clusters respectively.

Furthermore, an interesting finding was observed in which the deformed structure was retained in the 0.2Ti-4.5TiB₂ composite upon annealing, suggesting the inhibition of recrystallisation (Fig. 6.15). This was hypothesised due to the existence of TiB₂ particles which pinned the grain boundaries, causing inhibition of grain boundary migration which leads to the inhibition of recrystallisation. This result was also in accordance with the results from the compression tests which were deformed at high Z (high temperature and low strain rate) which also exhibited retardation of nucleation upon annealing at 540°C for 2 h.

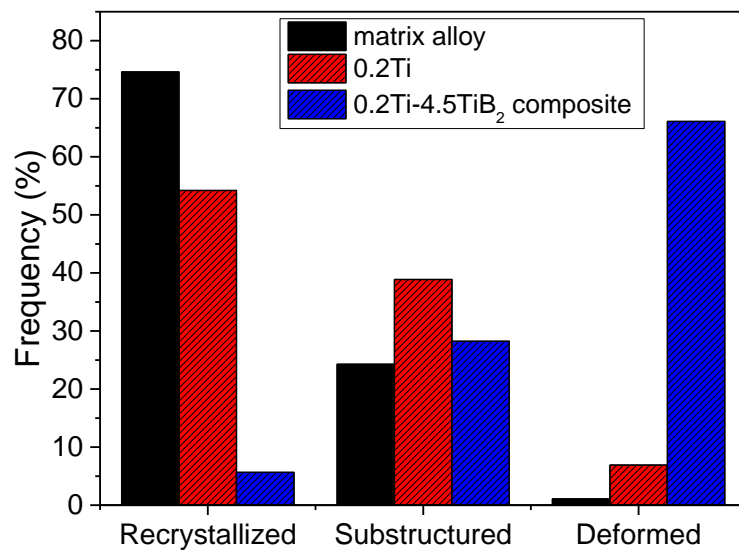


Fig. 6.15. Recrystallisation frequency comparison of the matrix alloy, 0.2Ti and 0.2Ti-4.5TiB₂ composite, showing inhibition of recrystallisation in the 0.2Ti-4.5TiB₂ composite

6.5. Summary of the Effect of TiB_2 on the Recrystallisation

Recrystallisation behaviour of the matrix alloy, the 0.2Ti alloy and the 0.2Ti-4.5TiB₂ composite was explored. The effect of the strain rates and temperature was investigated in terms of compression tests. The important result was found in which if the materials were deformed at high temperature and low strain rates, a coarse grain structure was obtained upon annealing, indicating retardation of recrystallisation. In contrast to that, a fine grain structure was obtained if the material was deformed at low temperature and high strain rate, indicating acceleration of recrystallisation. These were suggested as being due to

higher energy stored upon deformation at low temperature and high strain rate, leading to the higher driving force for recrystallisation. The higher flow stress achieved upon deformation at low temperature and high strain rate confirmed this postulation. Hence, it could be concluded that the flow stress achieved upon deformation is related to energy stored for SRX. This information could be of benefit to industry where if the material is deformed at a high flow stress, fine recrystallised grains will be achieved upon annealing, whilst if the material is deformed at a low flow stress, coarse grains will be achieved upon annealing.

Furthermore, a significant difference in sheet microstructure between the 0.2Ti-4.5TiB₂ composite and the other alloys was observed upon annealing. A bimodal grain structure was obtained in the 0.2Ti-4.5TiB₂ composite in which fine recrystallised grains were observed in the vicinity of Al₃Ti particles and TiB₂ clusters in addition to large elongated grains. The large elongated grains observed upon annealing of the 0.2Ti-4.5TiB₂ composite was proposed due to grain boundary pinning by TiB₂ particles in which inhibit grain boundary migration during annealing, leading to the coarse grain size.

Regarding extruded materials, it was observed that the deformed structure was retained following annealing at 540°C for 2 h in the 0.2Ti-4.5TiB₂ composite suggesting the retardation of recrystallisation. This was suggested as being due to the pinning effect of TiB₂ particles which inhibited grain boundary migration during annealing, resulting in a retardation of recrystallisation. In addition to that, localised recrystallised grains were also observed in the extruded materials which were postulated as being nucleating in the vicinity of Al₃Ti particles and TiB₂ clusters.

CHAPTER 7

EFFECT OF TiB₂ ON THE MECHANICAL PROPERTIES AND SUPERPLASTIC FORMING ABILITY

7.1. Introduction

This present chapter discusses mechanical property data, in this case tensile strength and a preliminary evaluation of superplastic behaviour. These results were secondary observations in this thesis so that the analysis was only carried out briefly. However, a significant influence of TiB₂ particles was observed on the superplastic behaviour as the existence of this particle limited its deformation to a certain temperature. The examination of superplasticity was studied using SEM and EBSD, while mechanical properties in tension were explored through room temperature and elevated temperature uni-axial tensile test and SEM.

7.2. Tensile Strength

The effect of the addition of TiB₂ particles on the mechanical properties of Al-Cu-Mg-Ag alloy was examined by means of tensile testing. All the samples were taken in the direction parallel to the deformation direction, in this case the rolling direction (RD) and extrusion direction (ED). Testing was conducted at room temperature and 200°C. However, due to limited samples, the extruded materials were only tested at room temperature. Examination under SEM was conducted after testing to analyse the effect of TiB₂ particles on the fracture mechanism.

7.2.1. Investigation on Ageing Behaviour

It is worth noting that owing to the most commonly used heat treatment process used in industry, only the T6 temper (solution treatment and artificial ageing) was explored in this study. The hardening response of the 0.2Ti-4.5TiB₂ composite was explored at several temperatures in the range of 175°C – 195°C after solution treatment for 2 h at 540°C with the aim of investigating optimum ageing conditions for the composite. This temperature range was chosen by considering the coarsening of the Ω phase which was observed at a

temperature of 250°C , leading to a decrement of strength [9–12,67]. This result was then used as a baseline for the other two materials. In this study, Vickers hardness was used to identify the peak ageing conditions.

Fig. 7.1a shows the hardness profiles against the ageing temperature. As we can see from the graph, the peak hardness and peak ageing duration decreased as the ageing temperature increased. This is commonly observed as the driving force for precipitation increases with decreasing temperature, allowing more finely dispersed precipitates to be formed. Additionally, the atom mobility/diffusion rates increase with increasing temperature, leading to a shorter duration of peak ageing [199]. The maximum hardening was achieved at an ageing temperature of 175°C and hence, this temperature was chosen as a baseline temperature for observing the ageing behaviour of the other two materials.

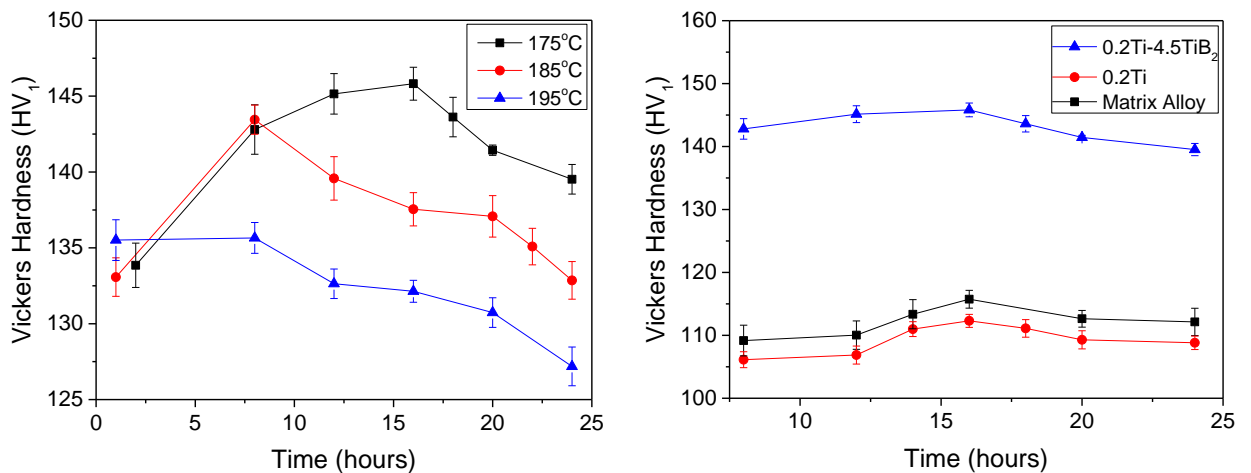


Fig. 7.1. (a) Ageing profile of the 0.2Ti-4.5TiB₂ composite aged at several temperatures; (b) Ageing behaviour comparison of the matrix alloy, 0.2Ti alloy and 0.2Ti-4.5TiB₂ at 175°C

Following this result, the other two materials were also subjected to an ageing temperature of 175°C and comparison between them was conducted. It was observed that there was no significant difference in the peak ageing duration with the addition of TiB_2 particles as is described in Fig. 7.1b. No enhancement of ageing kinetics was observed in the 0.2Ti-4.5TiB₂. This result is with good agreement with Lu *et al* [14] where no accelerated ageing behaviour was found on the Al- 4 wt.% Cu composite reinforced with in-situ TiB_2 particles when it was compared with the unreinforced alloy. In this study, the peak ageing time for

all the materials studied was obtained at a temperature of 175°C for 16 hours, thus, all the materials were heat-treated with this schedule. Of all of materials, the hardness value of $0.2\text{Ti}-4.5\text{TiB}_2$ was the highest, followed by the matrix alloy and 0.2Ti . This suggests that the existence of Ti did not give any significant change in the hardness as the hardness difference between the matrix alloy and 0.2Ti was less than 5% over all the temperatures which can be considered as the same hardness.

Furthermore, it is known that the high strength level achieved by the addition of trace Ag ($\sim 0.1\%$) to the high Cu:Mg ratio of an Al-Cu-Mg alloy was attributed to the existence of the Ω phase [48,200,201]. Fig. 7.2 confirmed the existence of finely dispersed Ω phase observed in the $0.2\text{Ti}-4.5\text{TiB}_2$ composite when it was aged at 175°C for 16 hours.

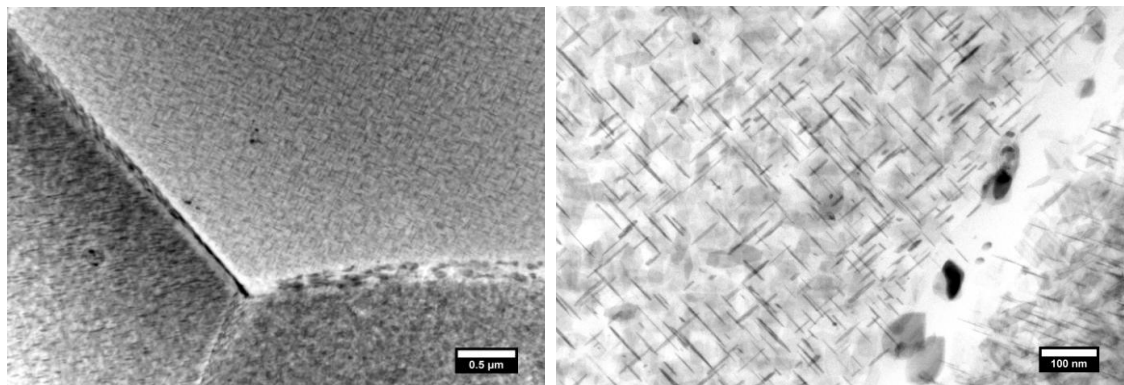


Fig. 7.2. Ω precipitate observed on the $0.2\text{Ti}-4.5\text{TiB}_2$ composites aged at 175°C for 16 hours

7.2.2. Measurement of Tensile Strength in Sheet Materials

Room temperature uniaxial tensile tests were carried out on all the materials in the T6 condition. As we can see from the engineering stress (S) vs engineering strain (e) in Fig. 7.3, it is evident that enhancement of yield strength (S_y) and ultimate tensile strength (UTS) was achieved with the addition of TiB_2 particles. As this compensate, the ductility declined with the addition of TiB_2 particles. This was an expected result since it is known that the existence of secondary particles, in this case TiB_2 particles, will hinder the dislocation movement during tensile deformation, leading to higher yield strength and ultimate tensile strength. Furthermore, as reflected from the hardness test, there was not much difference in yield strength and tensile strength values between the the 0.2Ti and matrix alloy, with a slightly higher value in the 0.2Ti alloy. This suggests that the higher strength level

achieved in the $0.2\text{Ti}-4.5\text{TiB}_2$ composite compared to the other two alloys was primarily attributed to the presence of TiB_2 particles. Furthermore, it could also be seen from the graph that the addition of TiB_2 particles had no or little, if any, effect on the modulus of elasticity of the matrix alloy since all three studied materials exhibited a somewhat similar slopes. Table 7.1 presents the tensile strength data and all the calculated values derived from the tensile data which will be explained in the paragraph below.

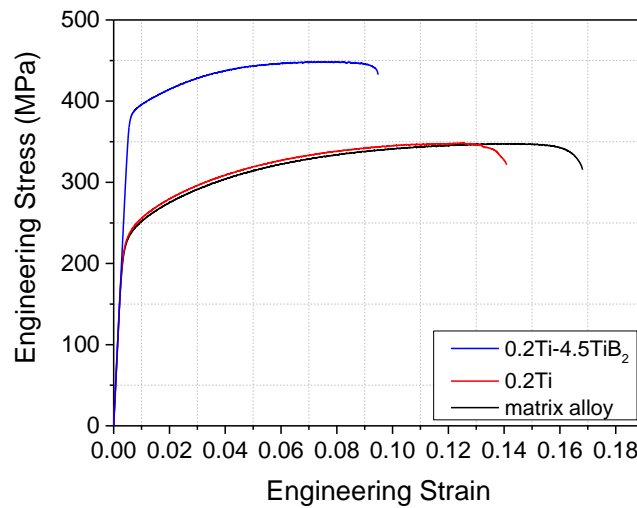


Fig. 7.3. Comparison of Engineering stress vs Engineering strain curves showing a higher ultimate tensile strength and lower ductility achieved by the addition of TiB_2 particles to the Al-Cu-Mg-Ag alloy

It is one of the interests in this study to approach industrial applications and hence it is worth investigating how the addition of TiB_2 affects the formability by calculating the strain hardening exponent (n), particularly in the sheet product. We know that yield strength and ultimate tensile strength values are not directly related to formability. However, it still can be predicted from the difference between these values where the closer the magnitude between these stresses, the more work hardened is the metal, suggesting a lower formability. From this, it can be suggested that the addition of TiB_2 particles to the Al-Cu-Mg-Ag alloy reduced the formability as the $0.2\text{Ti}-4.5\text{TiB}_2$ composite has the lowest difference in magnitude between the yield strength and ultimate tensile strength whereas the addition of Ti did not give a significant effect on the formability as

shown in Table 7.1. Nonetheless, it is still worth investigating the strain-hardening-exponent (n) value which defines the formability of the metal.

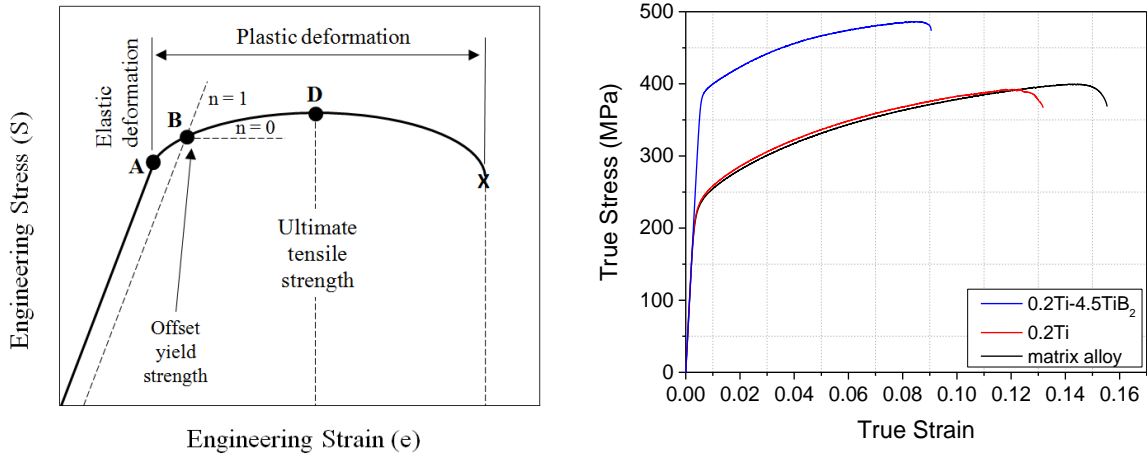


Fig. 7.4. (a) Illustration of data taken for the strain-hardening-exponent calculation; (b) True stress vs True Strain curves showing a higher flow stress of 0.2Ti-4.5TiB₂

The strain hardening exponent was calculated according to ASTM E646 in which the data was derived from the plastic region prior to necking, the region B - D as per the illustration in Fig. 7.4. The calculation utilised the true stress – true strain data calculated from engineering stress – engineering strain data using Eq (3-7) and (3-8). Subsequently, using these data, the n value for each of the materials was calculated based on Eq. (3-6).

Table 7.1. Comparison of tensile test data in the materials and commercial aircraft alloys

Material	Yield Strength (MPa)	UTS (MPa)	Ductility (%)	Strength Coefficient, K (MPa)	Strain hardening exponent, n
0.2Ti-4.5TiB ₂	385	445	9.3	619	0.10
0.2Ti	233	349	14	570	0.17
Matrix alloy	230	347	16.7	567	0.18
A 2024-T3	282 – 289	434 – 441	10 - 15	780	0.17

The strain hardening exponent explains how much strain could be performed prior to necking. This is related to the ability of the material to distribute the strain energy. It is

basically the true strain value at the onset of necking which can be explained by the following equations.

In the B – D region (Fig. 7.4a), the true stress and true strain values can be defined by

$$\sigma = \frac{P}{A_i} \quad (7-1)$$

$$\varepsilon = \frac{dL}{L_i} \quad (7-2)$$

Where A_i and L_i are the instantaneous area and gauge length respectively. We know that the load at the onset of necking (B – D region in the Fig. 7.4) will be pretty much constant and hence $dP = 0$. Substituting this value into Eq. (7-3) will give Eq. (7-4)

$$P = \sigma A \quad (7-3)$$

$$dP = \sigma dA + A d\sigma = 0 \quad (7-4)$$

Rearranging Eq. (7-4) gives us

$$\frac{d\sigma}{\sigma} = -\frac{dA}{A} \quad (7-5)$$

The specimen volume will remain constant in the plastic region, and hence Eq. (7-6) will be applied. Substituting this equation into Eq. (7-5) gives us the relation which is described in Eq. (7-7)

$$-\frac{dA}{A} = \frac{dL}{L} = d\varepsilon \quad (7-6)$$

$$\frac{d\sigma}{d\varepsilon} = \sigma \quad (7-7)$$

It is known that the plastic region of the true stress-true strain curve can be described with Eq. (7-7). And finally, by substituting Eq. (7-7) to Eq. (7-8) gives us the relationship which is described in Eq. (7-9).

$$\sigma = K \varepsilon^n \quad (7-8)$$

$$n K \varepsilon^{n-1} = K \varepsilon^n \quad (7-9)$$

Consequently, solving Eq. (7-9) gives us the relationship in which the true strain value at the onset of necking is equal to the strain hardening exponent (n) as described in Eq.(7-10)

$$n = \varepsilon \quad (7-10)$$

Therefore, it could be concluded that the higher the value of n , the higher the value of ϵ , meaning that more strain/stretching can be applied to the material prior to necking. Using this concept, it could be concluded that the addition of TiB_2 particles to the Al-Cu-Mg-Ag reduced the formability of the alloy as the 0.2Ti- TiB_2 composite ($n = 0.10$) showed a lower n value than the matrix alloy ($n = 0.18$) and the 0.2Ti alloy ($n = 0.17$) which shows a lower n value (Table 7.1). Furthermore, it is worth comparing the n value and other tensile properties of the 0.2Ti-4.5 TiB_2 composite with other commercial alloys to see the viability to be applied in industry. In this study, by considering its target application which is similar to Al 2024, comparison with that alloy was conducted. It was observed that the 0.2Ti-4.5 TiB_2 -T6 composite have a higher yield strength and *UTS* compared to commercial sheet Al 2024-T3 which shows a yield strength of 282 – 289 MPa and *UTS* of 434 – 441 MPa (Table 7.1) [202]. However the n and K value of Al 2024-T3, 0.17 and 780 MPa respectively [203], are higher than the 0.2Ti-4.5 TiB_2 composite. This means that Al 2024-T3 has a higher formability and is able to withstand a higher load before failure. These results suggest that there is a probability that 0.2Ti-4.5 TiB_2 could be applied in industry considering its high strength, however, further research needs to be done to improve its formability. Furthermore, owing to the high strength of the 0.2Ti-4.5 TiB_2 composite achieved in this study which falls within standard properties for aircraft applications, currently, Aeromet International Ltd is testing this material on a larger scale for Boeing. Apart from that, the 0.2Ti-4.5 TiB_2 composite developed in this study are currently being considered for the industrial certification for Boeing.

Besides room temperature tensile testing, tensile testing was also carried out at 200°C by considering its target application which can reach 215°C if there is a failure [204]. Similar to the behaviour at room temperature, the 0.2Ti-4.5 TiB_2 composite also demonstrated higher yield strength and *UTS* and lower ductility than the matrix alloy as described in Fig. 7.5. Comparing the properties between room temperature and 200°C showed that lower *UTS* were achieved at 200°C. This is commonly observed where increasing the temperature gives declining strength in a metal due to softening effect.

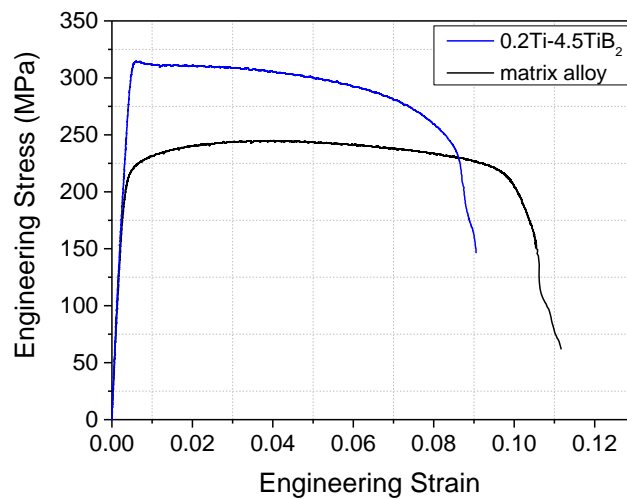


Fig. 7.5. Engineering stress vs engineering strain curve at 200°C

7.2.3. Measurement of Tensile Strength in Extruded Materials

As well as sheet products, the extruded products were also subjected to tensile testing. As already mentioned above due to limited specimens, only room temperature tensile testing was conducted. As expected, both the yield strength and *UTS* of the 0.2Ti-4.5TiB₂ composite are higher, while its ductility is lower than the other two materials as described in Fig. 7.6. The results of tensile strength achieved in the extruded product are described in Table 7.2.

Table 7.2. Comparison of tensile test data in the materials

Material	Yield Strength (MPa)	<i>UTS</i> (MPa)	Ductility (%)
0.2Ti-4.5TiB ₂	409	496	8
0.2Ti	115	204	18
Matrix alloy	202	323	38

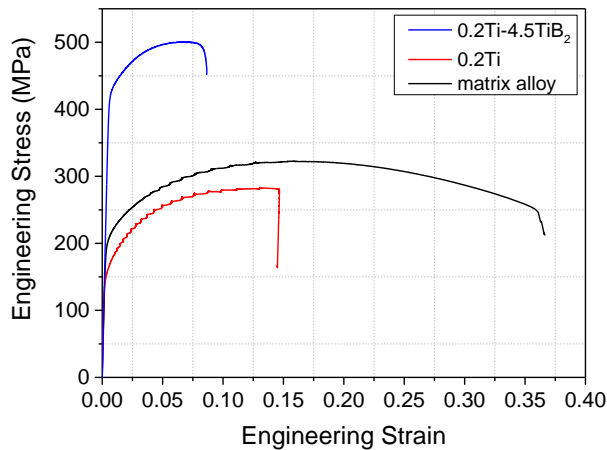


Fig. 7.6. Engineering stress vs engineering strain curve of extruded product showing a higher *UTS* was achieved in the 0.2Ti-4.5TiB₂ composite than the other two materials

7.2.4. Effect of TiB_2 on the Fracture Surface

In order to understand the effect of TiB_2 on the fracture behaviour, fractographic examination under SEM was conducted on the fracture surface. As can be seen from Fig. 7.7, a combination of coarse and fine dimples was observed in all of the materials studied. Coarse and deep dimples in the matrix and 0.2Ti alloy were attributed to the presence of coarse intermetallic $\text{Al}_7\text{Cu}_2\text{Fe}$ particles. Striation was created around the $\text{Al}_7\text{Cu}_2\text{Fe}$ intermetallic and occasionally, particle fracture was observed. Furthermore, the fine dimples observed in both materials was attributed to the Al_2Cu secondary phase. On the other hand, the coarse dimples present in the 0.2Ti-4.5TiB₂ composite were attributed to the existence of coarse Al_3Ti particles. Owing to the high volume fraction of TiB_2 particles and the fact that Al_2Cu and $\text{Al}_7\text{Cu}_2\text{Fe}$ tended to segregate to the TiB_2 interface during heat treatment results in a higher fraction of fine dimples in the 0.2Ti-4.5TiB₂ composite.

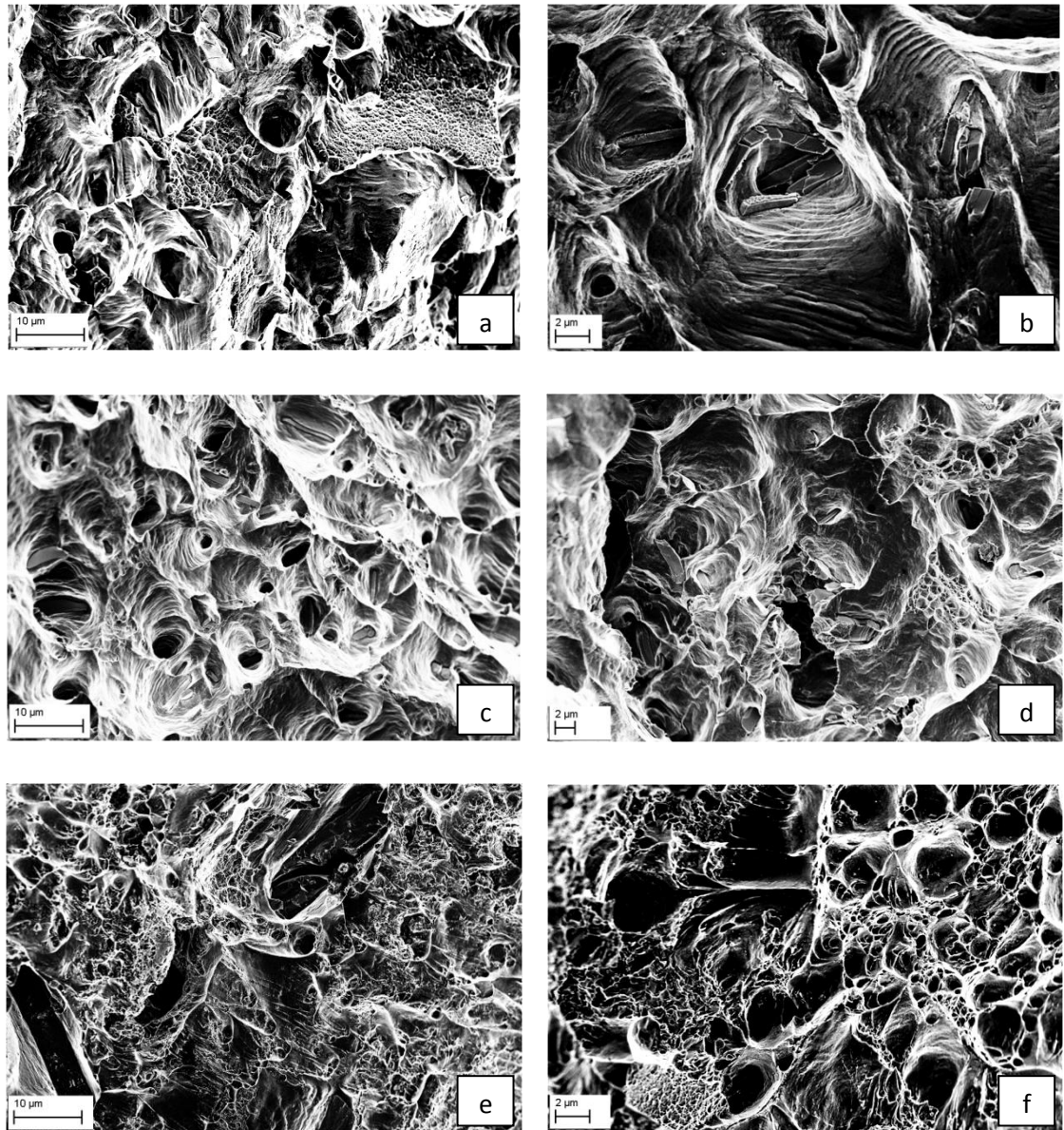


Fig. 7.7. Fractography of (a-b) matrix alloy; (c-d) 0.2Ti alloy and (e-f) 0.2Ti-4.5TiB₂ composite

7.3. Superplastic Forming Ability

It is of interest in this study to explore the superplastic potential of the 0.2Ti-4.5TiB₂ composite as recently superplastic forming has become one of the most attractive processes in industry especially in the aircraft industry. Hence, in this particular section, preliminary examination on the potentiality of superplastic forming of the 0.2Ti-4.5TiB₂ composite is reported. The comparison of its superplasticity with the two other materials studied and the

suspected phenomena occurring during deformation is explained very briefly in this particular section.

7.3.1. Superplastic Behaviour Dependence on the Strain Rate and Temperature

It is now well recognised that aluminium matrix composites (AMCs) produced by either powder metallurgy or mechanical alloying behave superplastic (elongation > 200%) when they are deformed with strain rates $\geq 10^{-2} \text{ s}^{-1}$ [19,134,143,205–209]. Based on these investigations, in this present research, the superplastic potential of the 0.2Ti-4.5TiB₂ composite was explored in the range of $5 \times 10^{-3} \text{ s}^{-1}$ to $5 \times 10^{-1} \text{ s}^{-1}$ in order to cover the range of lower and higher strain rates than 10^{-2} s^{-1} . The preliminary tests were conducted in the as-rolled specimens over a temperature range of 450°C – 550°C.

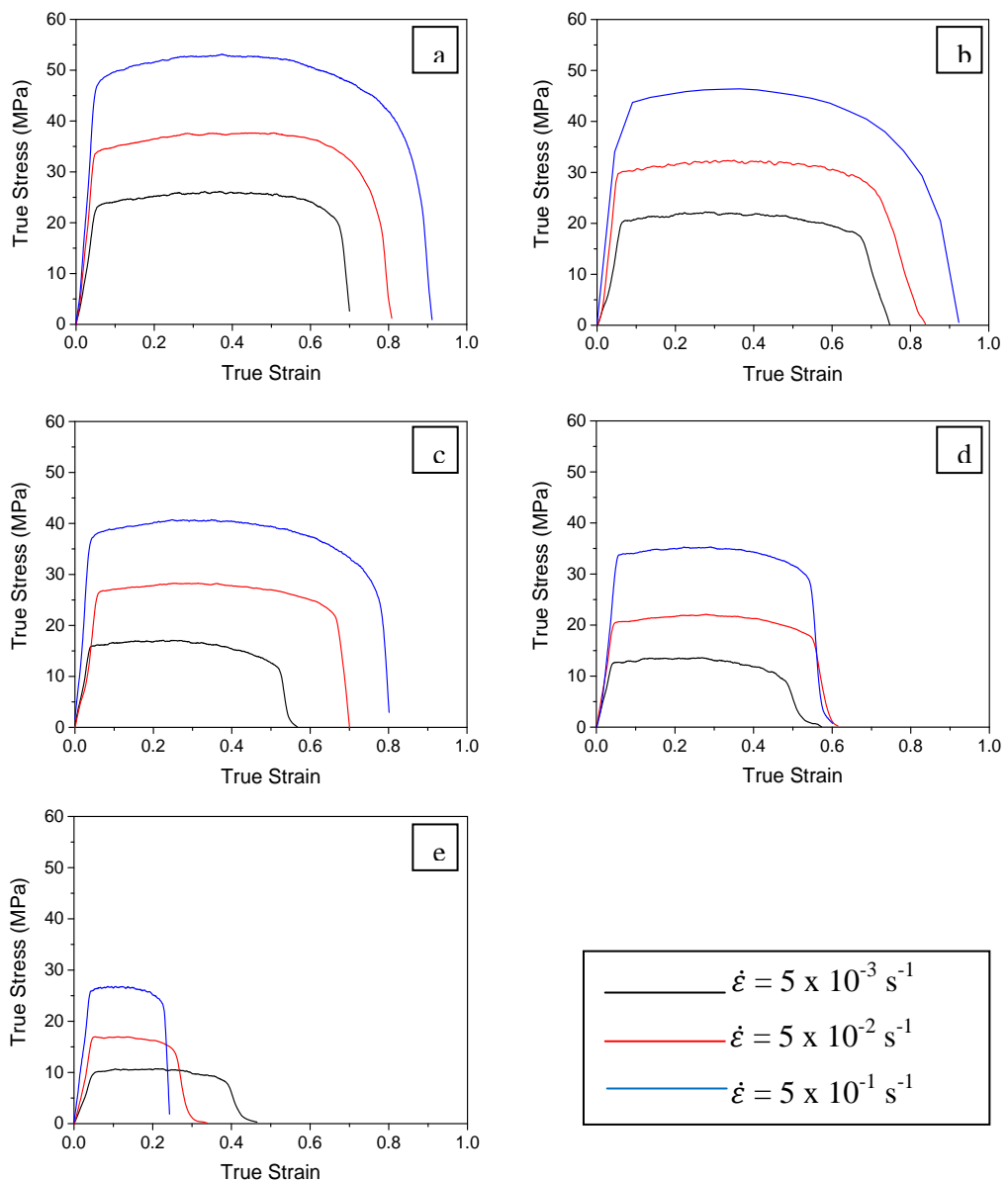


Fig. 7.8. The stress-strain relationship of 0.2Ti-4.5TiB₂ composite deformed at (a) 450°C, (b) 475°C, (c) 500°C, (d) 525°C and (e) 550°C

Fig. 7.8 presents a true stress-true strain curve of the 0.2Ti-4.5TiB₂ composite at various temperatures and strain rates. For brevity, the other two alloy graphs will be provided in Appendix D. It can be seen from the graph that in all deformation conditions, the stress-strain curve demonstrated a steady state flow stress until a certain strain and subsequently the flow stress reduces up to the point of fracture. It was noted that up to the deformation temperature of 475°C, in all the strain rates, a steady state flow stress was observed up to a true strain of typically 0.6. With further increasing the temperature to 525°C, however, the flow stress level dropped by 33 – 40% and strain to failure dropped by 25 – 30% which suggested microstructural instability at that temperature. This could be attributed to the partial melting of low melting point secondary intermetallic phases which will be discussed later. Following this, the flow stress was plotted against strain rate to understand the stress-strain rate dependency during superplastic deformation. Similar to the compression test, the stress characteristics derived from the tension test is usually utilised at the stress at a fixed strain [104,171]. In this thesis, a flow stress at a strain of 0.1 was chosen. It was observed that for all of the materials studied, the flow stress enhanced with increasing strain rate and decreasing temperature as described in Fig. 7.9.

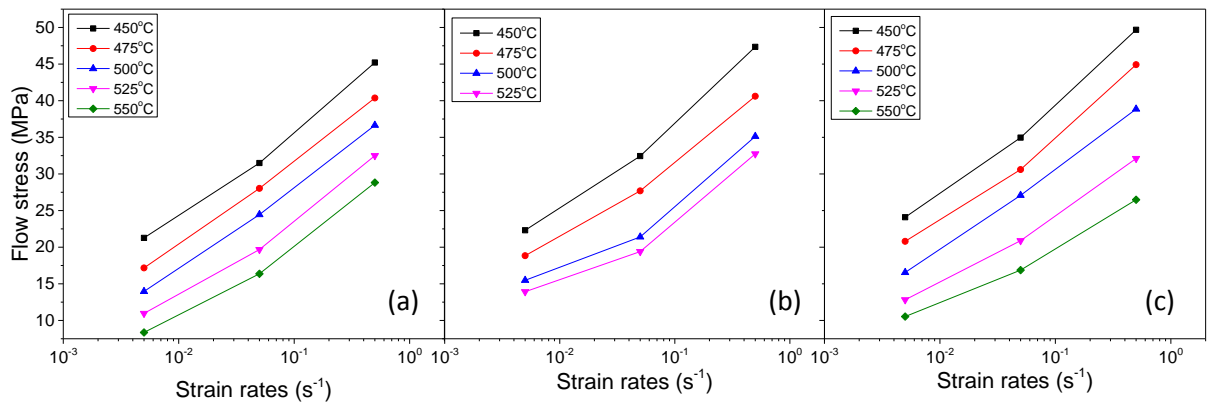


Fig. 7.9. Flow stress vs strain rate relationship of (a) matrix alloy, (b) 0.2Ti alloy and (c) 0.2Ti-4.5TiB₂ composite

Furthermore, from the plot of elongation versus strain rate in Fig. 7.10, it was noted that at a constant temperature, the ductility of the 0.2Ti-4.5TiB₂ composite increased with increasing strain rate until a temperature of 525°C, whilst better ductility was observed at lower strain rates at a temperature of 550°C. At constant strain rates, the ductility increased

with increasing temperature up to 475°C and subsequently decreased with further increase in temperature. This result suggested that the deformation of the 0.2Ti-4.5TiB₂ composite is limited to a temperature of 475°C since enhancement of brittleness was observed above this temperature. In this study, the highest elongation of 151% was obtained in the composite when it was deformed at a temperature of 475°C with a high strain rate of $5 \times 10^{-1} \text{ s}^{-1}$. Although this result is still far from superplasticity, it showed a higher elongation than existing reported results on the superplastic forming ability of TiB₂ reinforced 2xxx series Al alloys. Imai *et al* [210] in their experiment using TiB₂/2124 composites produced by powder metallurgy only achieved a highest elongation less than 150% when the composite was subjected to superplastic forming.

In contrast to that, the matrix alloy exhibited better ductility at lower strain rates over all deformation temperatures, although an anomaly was observed at a temperature of 475°C. This might be due to inhomogeneous inclusions present in the particular specimen. The highest elongation of 230% was attained in the matrix alloy at a temperature of 550°C when it was deformed at a low strain rate of $5 \times 10^{-3} \text{ s}^{-1}$, suggesting a potential of superplasticity. Regarding the ductility behaviour of the 0.2Ti alloy, unfortunately, it cannot be really concluded since it showed random variation of elongation over deformation strain rate and temperature. This random variation of ductility might be due to inhomogeneous distribution of Al₃Ti particles in the 0.2Ti alloy. However, further tests and investigations need to be done to clarify this hypothesis. Owing to this randomness, from this point, the 0.2Ti alloy will not be discussed further.

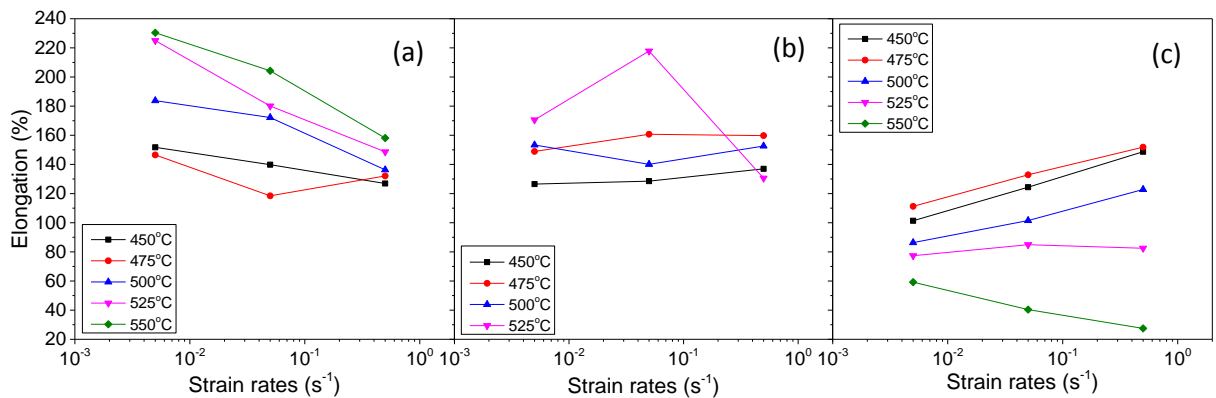


Fig. 7.10. Elongation vs strain rate relationship of (a) matrix alloy, (b) 0.2Ti alloy and (c) 0.2Ti-4.5TiB₂ composite

7.3.2. Strain Rate Sensitivity Parameter

Apart from the above analysis, one of the most important parameters in the SPF process is the value of the strain-rate sensitivity (m) which indicates a material's resistivity towards necking. Materials with high m values are able to withstand necking during deformation, resulting in a high elongation. As already described in section 2.6, to be amenable for superplastic forming, the m value has to be larger than 0.3. In superplastic forming, the relationship between the strain rate and flow stress could be described by Eq. (2-20) in which the m value could be derived by taking logarithms of that equation resulting in

$$m = \frac{\partial(\log \sigma)}{\partial(\log \dot{\epsilon})} \quad (7-11)$$

This is basically the slope of the $\log \sigma - \log \dot{\epsilon}$ curve. Hence, using Eq. (7-11), the m value for the matrix alloy and the 0.2Ti-4.5TiB₂ composite were calculated. The average of $m = 0.21$ and $m = 0.18$ was revealed for the matrix alloy and the 0.2Ti-4.5TiB₂ composite respectively suggesting that the matrix alloy has a better capability to be deformed. This was reflected in the higher elongation achieved in the matrix alloy.

7.3.3. Deformation Microstructure of 0.2Ti-4.5TiB₂ Composite

It is worth noting that since the 0.2Ti-4.5TiB₂ composite was the main material studied in this research, hence, from this point, the analysis will be limited only to the 0.2Ti-4.5TiB₂ composite. In order to identify the deformation mechanism, EBSD analysis was conducted on the specimen which exhibited the highest elongation during deformation. Fig. 7.11 shows the IPF map of the 0.2Ti-4.5TiB₂ specimen deformed at 475°C at $5 \times 10^{-1} \text{ s}^{-1}$, taken near the fracture area. Similar with other EBSD analysis, to differentiate between substructure and grain boundaries, in this map, low angle grain boundaries (LAGBs), 0 - 8°, are indicated with grey lines, medium-angle grain boundaries (MAGBs), 8 - 15°, are indicated with white lines and high-angle grain boundaries (HAGBs), >15°, are indicated with black lines.

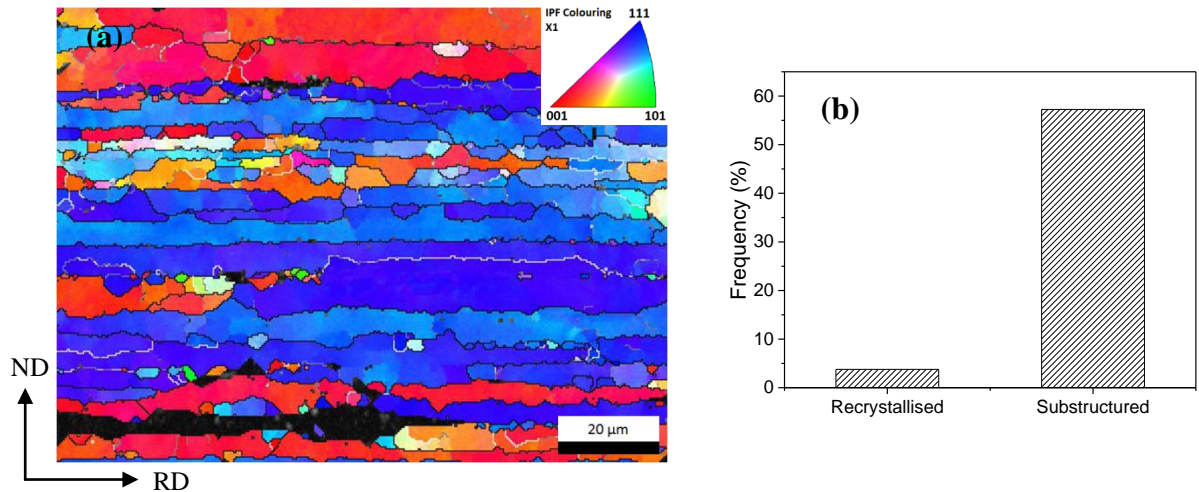


Fig. 7.11. (a) IPF map of 0.2Ti-4.5TiB₂ deformed at 475°C at a strain rate of $5 \times 10^{-1} \text{ s}^{-1}$; (b) Recrystallised vs subgrain structure percentage showing a higher percentage of substructure, indicating recovery was dominant during deformation

It can be clearly seen from Fig. 7.11 that the deformed microstructure exhibited a bimodal grain structure, similar to the as-annealed structure, which consisted of large grains elongated in the tensile direction as well as a fine grain structure. This observation indicated that recrystallisation was retarded during deformation. Owing to the fine TiB₂ particle size in which formed fine thickness strings in the as-rolled specimen as described in Chapter 5, it was postulated that at this particular temperature and strain rate, there was no adequate strain accumulated in the TiB₂ string zone to generate recrystallisation in this region during deformation. It was believed that the high level deformation experienced by matrix shearing in this TiB₂ string zone was recovered during deformation, leading to the coarse grain structure. This postulation was supported by Fig. 7.11b which shows a higher frequency of substructure, indicating recovery was dominant during deformation. Furthermore, grain boundary pinning by TiB₂ particles was also estimated to contribute to the retardation of recrystallisation by preventing grain boundary migration during deformation.

Apart from that, careful investigation observed grain boundary bulging in some areas as shown in Fig. 7.12 (indicated with a yellow arrow). Owing to the previous result on the EBSD hot stage (Chapter 6) in which TiB₂ was found to pin grain boundaries during heating, hence, the same behaviour was also expected during heating to the deformation temperature. The possible postulate for this is during the heating time, the grain boundary

migration was inhibited by TiB_2 particles pinning the grain boundaries, leading to the non-uniform migration. As a result, bulges were observed on the grain boundaries and the nucleation of new grains occurred by transformation of the bulge into nuclei due to straining [30,211]. These nuclei might grow and coalesce with neighbouring grains, resulting in large elongated grains (indicated with a yellow boundary in Fig. 7.12).

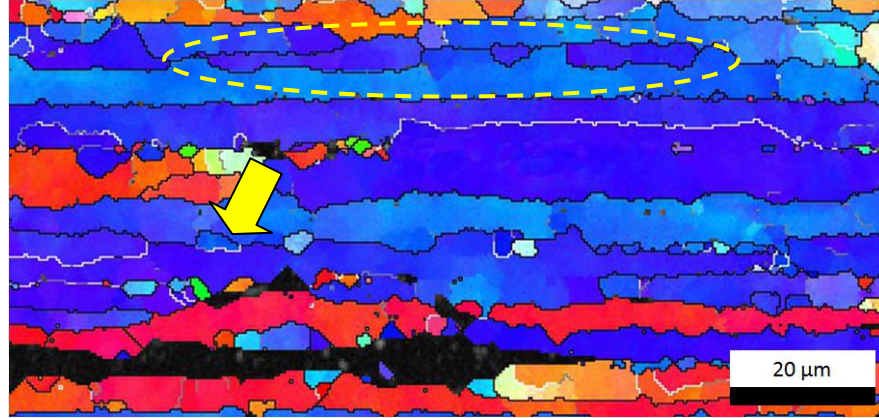


Fig. 7.12. Magnified area of the deformed structure showing grain boundary bulging

Consequently, based on the above observation, it can be understood why the 0.2Ti-4.5TiB₂ composite did not show superplastic properties since the recrystallisation was retarded during deformation, resulting in a large grain structure. Several ways have been suggested [176] to produce a fine recrystallised grain size in particulate composites. Apart from modification in the thermomechanical processing in which is usually produced by both foil processing and powder metallurgy processing [176], an internal stress superplasticity (ISS) mechanism was expected to be one of the methods to improve superplastic properties in this 0.2Ti-4.5TiB₂ composite. Owing to the large coefficient of thermal expansion (CTE) difference between TiB₂ string and/or TiB₂ clusters and the matrix, it is expected that a large dislocation densities will be created in these areas during thermal cycling of the composites. Consequently, a fine recrystallised grain size is expected to be formed during deformation, leading to the improvement of superplastic properties.

7.3.4. Cavitation Formation

Following microstructural examination under EBSD, the specimen deformed at 475°C with strain rate of $5 \times 10^{-1} \text{ s}^{-1}$ was subjected to optical microscope and SEM examination in order to investigate cavitation formation during deformation. An observation under the

optical microscope revealed that cavitations were nucleated primarily on secondary particles, in this case Al_3Ti and TiB_2 particles. Occasionally, crack propagation across Al_3Ti particles was also observed as shown in Fig. 7.13.

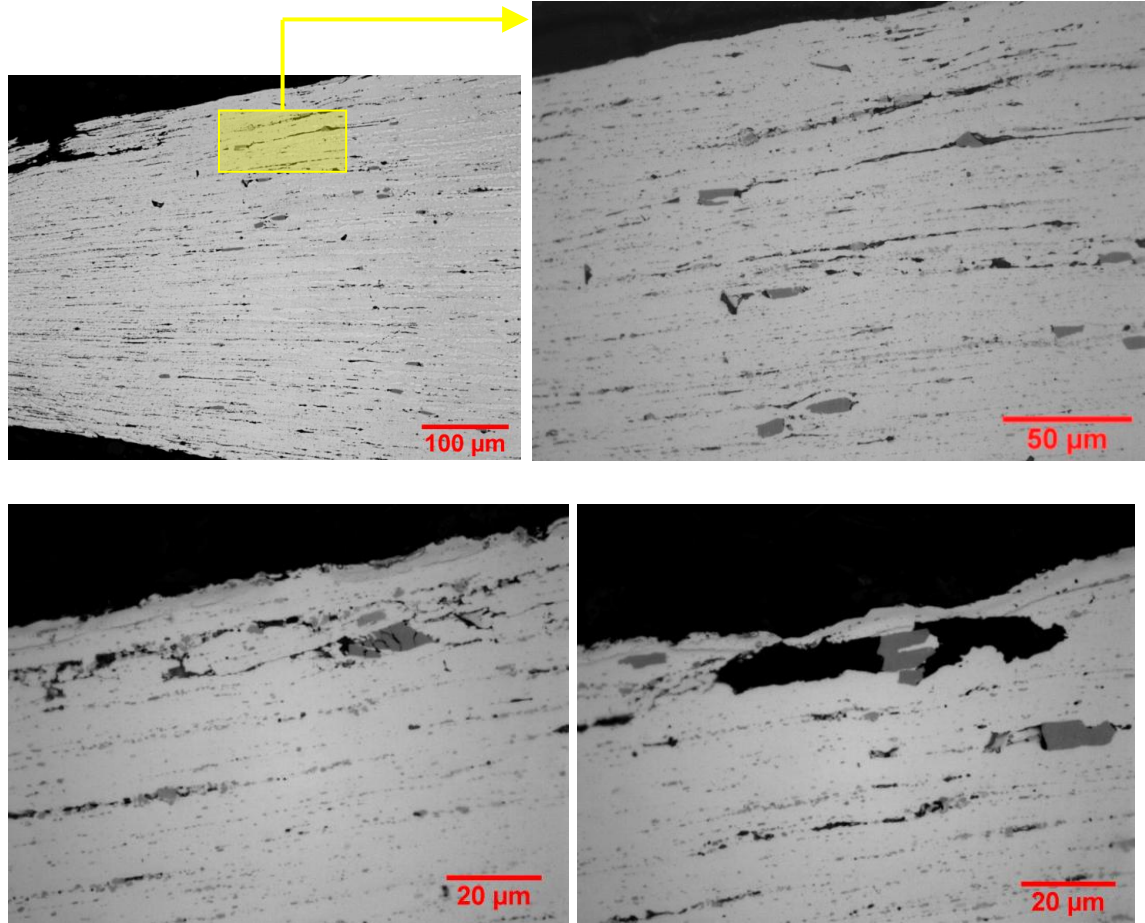


Fig. 7.13. Microstructure evaluation showing cavitations' nucleation on the Al_3Ti and TiB_2 particles; and crack propagation across Al_3Ti particle

Interestingly, from the SEM examination, it was noted that, in addition to Al_3Ti particles, the cavitations was mostly nucleated on the TiB_2 particles which were associated with Cu and Fe constituents. As was already explained in Chapter 5, the presence of this constituent originated from iron impurities present in the master alloy and tended to segregate to grain boundaries and/or particulate interfaces during casting. Cavitations were hardly seen nucleated on the TiB_2 particles which were not covered by Cu and Fe constituents. If any, it was mostly the prolongation of cavities formed on TiB_2 particles covered by Cu and Fe constituent. In Fig. 7.14, the TiB_2 particle covered by Cu and Fe constituent could be identified by its brighter appearance. It is known that this iron-bearing constituent is brittle.

And, in fact, the existence of this iron-bearing constituent in the vicinity of TiB_2 particles will enlarge the particle size and hence create more stress concentration, leading to the cavity nucleation. Cavitations were suspected to be nucleated around Al_3Ti and $\text{Al}_7\text{Cu}_2\text{Fe}$ intermetallic inclusions and the coalescence of such cavitations was aided by linkage of cavities nucleated around TiB_2 particles [176]. This was supported by the examination in which the cavities were mostly observed at the side of larger particles sizes and/or clusters, suggesting that the size of particles plays an important role during deformation. This could be explained since a higher dislocation density will be accumulated at the larger particles due to the inability of dislocations to climb around the particles. This leads to the higher stress concentration at the particle which initiates cavity formation [212].

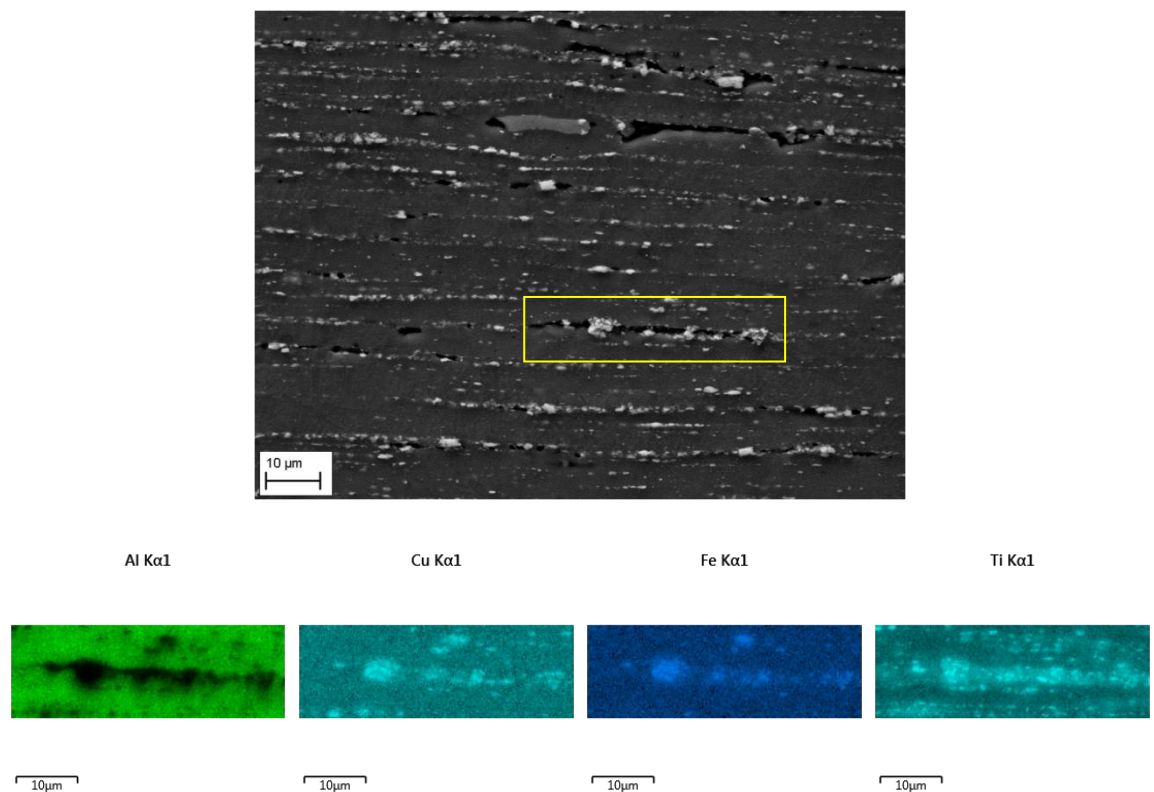


Fig. 7.14. SEM image and EDX map of Al, Cu, Fe and Ti showing cavities nucleated at Al_3Ti particles and TiB_2 particles which were associated with the Cu and Fe constituents

7.3.5. Fracture Dependence on the Deformation Strain Rate and Temperature of 0.2Ti-4.5TiB₂ Composite

Fig. 7.15 shows a comparison of the fracture behaviour of specimens with the highest ductility and low ductility. Large and deep voids with sharp edges were observed in the specimens with the highest elongation, suggesting ductile fracture. Occasionally, shear bands were observed when the fracture crossed Al_3Ti particles.

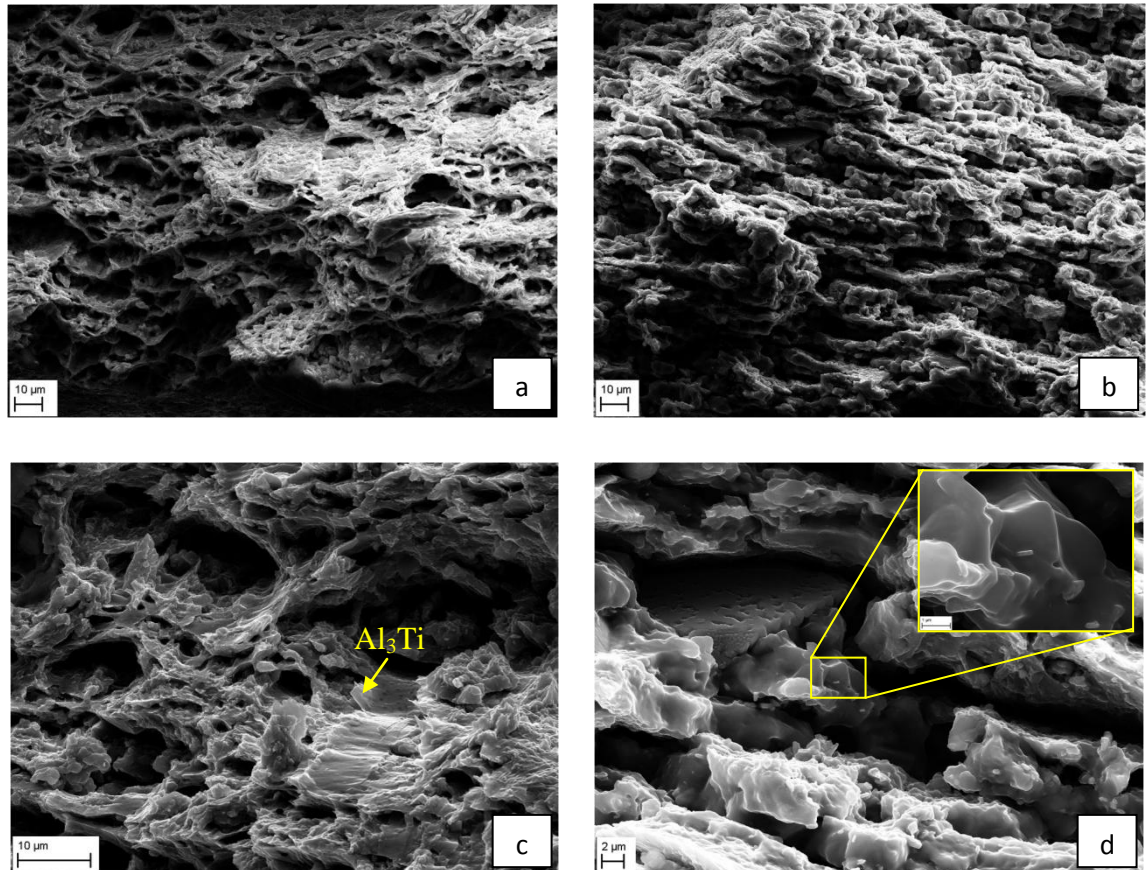


Fig. 7.15. Fracture surface on the specimens deformed at (a)-(c) 475°C , $5 \times 10^{-1} \text{ s}^{-1}$ which has the highest ductility and (b)-(d) 525°C , $5 \times 10^{-1} \text{ s}^{-1}$ which has low ductility

In contrast to the above observation, in the specimen with a low ductility, denser cavities with soft edges which were elongated in the direction of shear were observed (Fig. 7.15 b-d). The specimen was taken from the deformed specimen at a temperature of 525°C with a strain rate of $5 \times 10^{-1} \text{ s}^{-1}$. The author of this thesis postulated that liquid phase might be present at the interface of TiB_2 particles and the matrix due to segregation of solute to the particles – matrix interface and grain boundaries, lowering the local melting temperature.

Because of this liquid phase, the grain boundary can no longer sustain a tensile force and a shear stress could not be transferred across the boundary. Thus, a shear-fracture-feature surface was observed.

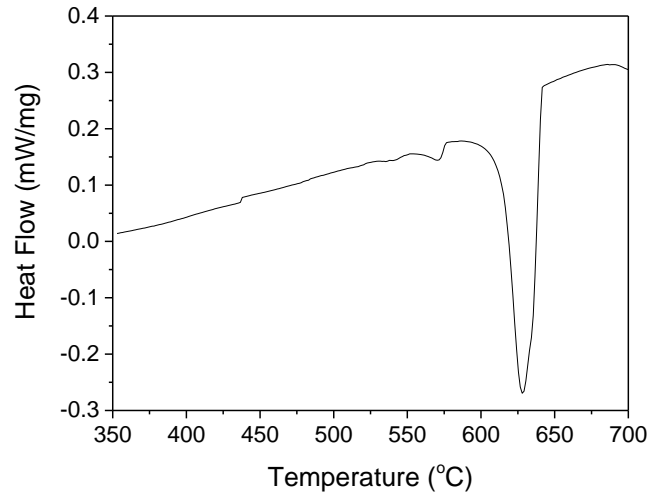


Fig. 7.16. DSC results of the 0.2Ti-4.5TiB₂ composite showing endothermic reaction at the temperature of 535°C

In order to confirm this postulation, DSC testing was carried out. However, the DSC results as shown in Fig. 7.16 did not reveal any significant endothermic reaction at a temperature below 535°C, suggesting that no liquid phase was involved at the temperature of 525°C. This might suggest that only local or isolated melting occurred during deformation which the DSC was not able to detect. However, further testing is needed to confirm this postulation. Apart from that, a bigger magnification on the fracture surface of the specimen with low ductility revealed the existence of particles, which later on were confirmed as TiB_2 particles by EDX analysis. This suggests that cavitation was generated on the TiB_2 particles. This also supported the above postulation in which a tensile force can no longer be sustained due to liquid phase presence at the interface of the TiB_2 and matrix, resulting in cavitation nucleation at the TiB_2 particles.

Following the above observation, EDX analysis was performed on both fracture surfaces. The existence of Cu and Fe constituents in the vicinity of TiB_2 particles on the fracture surface of the specimen with the highest elongation was evident from the EDX map. This observation confirms microstructural examination previously in which cavitations were

found nucleated on the TiB_2 particles which were covered by Cu and Fe constituents (Fig. 7.17). Furthermore, numbers of TiB_2 particles were revealed on the fracture surface on low ductility specimens which supports the previous postulation (Fig. 7.18). Apart from that, detailed examination needs to be conducted to confirm the postulation derived in this study.

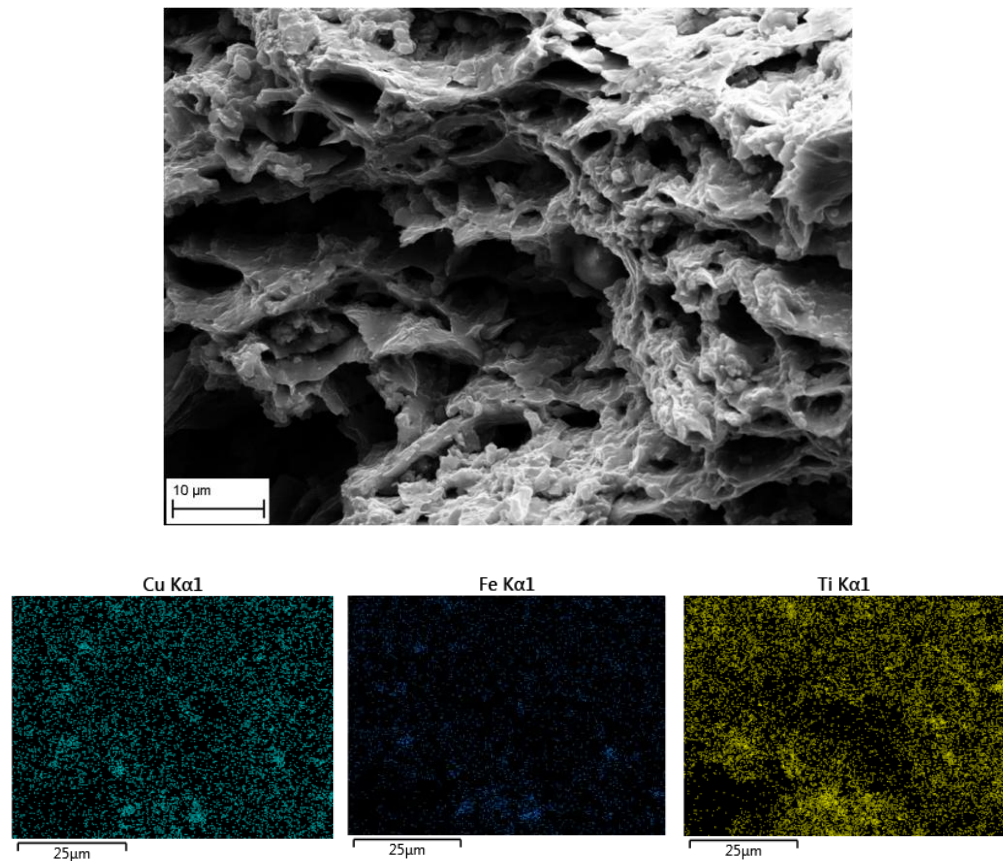


Fig. 7.17. EDX map (Cu, Fe and Ti map) of specimen with highest ductility which was deformed at 475°C with a strain rate of $5 \times 10^{-1} \text{ s}^{-1}$, showing the existence of Cu and Fe constituents in the vicinity of TiB_2

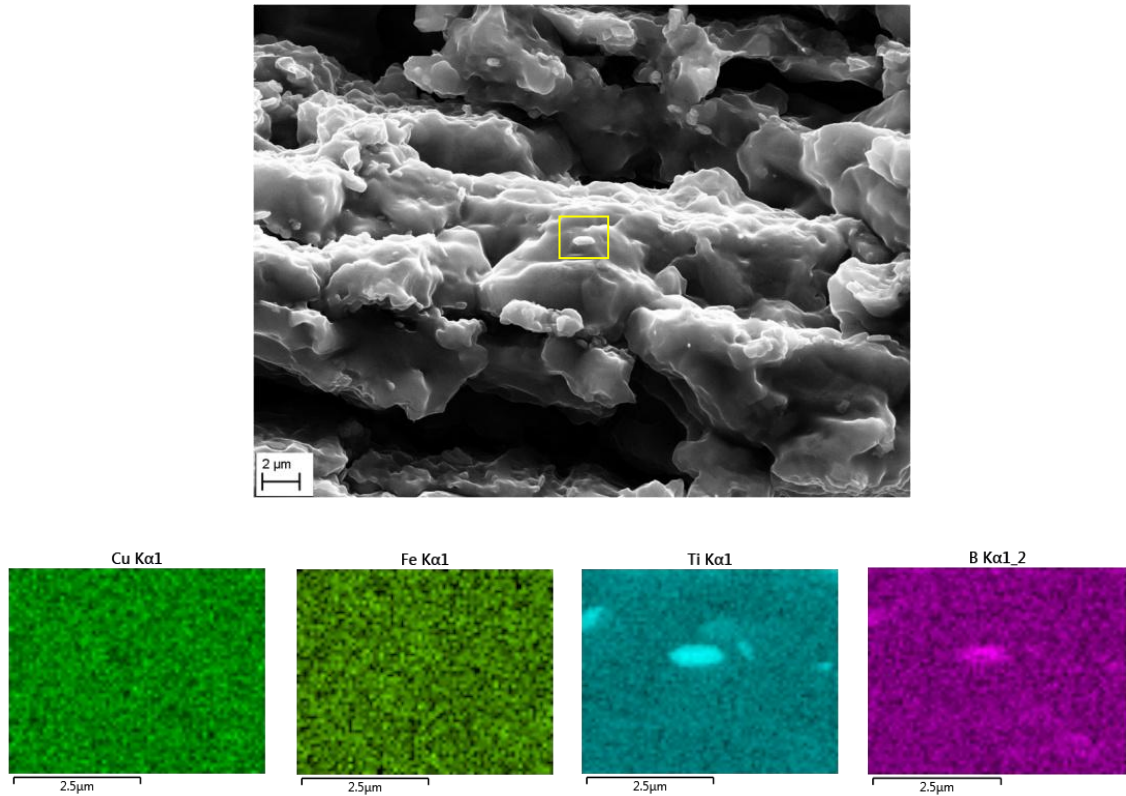


Fig. 7.18. Fracture surface of specimens with low ductility which was deformed at 525°C with a strain rate of $5 \times 10^{-1} \text{ s}^{-1}$

7.4. Summary of the Effect of TiB_2 on Superplasticity and Mechanical Properties

Mechanical properties in tension, both at room temperature and 200°C have been investigated on the matrix alloy, 0.2Ti alloy and the 0.2Ti-4.5TiB₂ composite. The 0.2Ti-4.5TiB₂ composite showed the highest tensile strength of all the materials, both at room temperature and 200°C , suggesting that the addition of TiB₂ particles will improve the tensile properties. A high UTS of 445 MPa with a yield strength of 385 MPa has been achieved in the peak aged condition (T6 temper) of sheet 0.2Ti-4.5TiB₂ composite. Compared with commercial aircraft alloy, A2024 – T3, the 0.2Ti-4.5TiB₂ composite exhibited higher tensile strength, suggesting its possibility of an aircraft application. Apart from that, high tensile properties were also achieved in the extruded product of the 0.2Ti-4.5TiB₂ composite (in T6 temper condition) with a UTS of 496 MPa and yield strength of 409 MPa.

Furthermore, superplasticity of the 0.2Ti-4.5TiB₂ composite has been investigated in which the highest elongation of 151% was observed with a high strain rate deformation, $5 \times 10^{-1} \text{ s}^{-1}$, at a temperature of 475°C. In contrast to the composite, the highest ductility of the matrix alloy, 230%, was investigated with slow strain rate deformation, $5 \times 10^{-3} \text{ s}^{-1}$, at temperature of 550°C. Furthermore, it was found that the ductility of the matrix alloy increased with increasing temperature, whilst the ductility of the composite decreased when specimens were deformed above a temperature of 475°C. This suggests that the deformation temperature of the composite is limited to 475°C.

Moreover, the size of the particles was found to have a significant influence during deformation. In this study it was observed that cavities were nucleated around large Al₃Ti particles and larger TiB₂ particles covered by Cu and Fe constituents and/or clusters. Fractography examination revealed large cavities with sharp edges in the highest elongation specimens, suggesting ductile fracture. In contrast to that, dense cavities with soft edges which were elongated in the shear direction were observed in lower ductility specimens deformed at a temperatures higher than 475°C, indicating that liquid phase might be present during deformation. However, further tests are needed to be carried out to confirm this postulation.

CONCLUSION

A. Effect of TiB₂ on the hot deformation behaviour

- Over all of the compression test parameters, the 0.2Ti-4.5TiB₂ composite exhibited higher flow stress than the matrix alloy and the 0.2Ti alloy.
- The addition of TiB₂ does not give significant influence on the deformation at high temperature and low strain rates as the flow stress discrepancy between the 0.2Ti-4.5TiB₂ composite and the other two alloys were decreased as the temperature increased and strain rates decreased
- Highest efficiency of 37 pct was achieved in the processing map of 0.2Ti-4.5TiB₂ composite at the domain of 500 °C in the range of strain rates 10⁻² s⁻¹ to 10⁻¹ s⁻¹
- Dynamic recovery (DRV) was found to be the sole mechanism over all test parameters in the matrix alloy and the 0.2Ti alloy
- Dynamic recrystallisation (DRX) was observed in the 0.2Ti-4.5TiB₂ composite following lower temperature and higher strain rates deformation. The existence of TiB₂ particles covering grain boundaries and triple junction areas as well as Al₃Ti particles were postulated to be responsible for this phenomenon. As the temperature increased and strain rate decreased, DRV was observed as the dominant mechanism in the 0.2Ti-4.5TiB₂ composite with localised DRX observed in the vicinity of TiB₂ clusters and Al₃Ti particles
- Regarding the mechanism during rolling in the 0.2Ti-4.5TiB₂ composite, local DRX in the vicinity of Al₃Ti particles was evident with DRV responsible in other areas.

B. Effect of TiB₂ on the static recrystallisation

- Following annealing of sheet material, recrystallisation was retarded in the 0.2Ti-4.5TiB₂ composite due to grain boundary pinning by TiB₂ particles which inhibited grain boundary migration during annealing. As a result, large and elongated recrystallised grains were achieved. However, fine recrystallisation grains were observed in the area adjacent to the Al₃Ti particles and TiB₂ clusters
- Regarding the extruded materials, the deformed structure was retained following subsequent annealing of the 0.2T-4.5TiB₂ composite. This was postulated due to the

pinning effect of TiB_2 particles which inhibited grain boundary migration during annealing, resulting retardation of recrystallisation. Furthermore, localised recrystallisation was also observed in the extruded 0.2Ti-4.5TiB₂ composite which was postulated nucleating in the vicinity of Al_3Ti particles and TiB_2 clusters

C. Effect of TiB_2 on the mechanical properties and superplastic forming ability

- A high tensile strength of 445 MPa and yield strength of 385 MPa was achieved in the peak aged (T6) condition of sheet material of the 0.2Ti-4.5TiB₂ composite. These properties are higher than commercial aircraft materials A2024-T3, suggesting a possibility to be applied in the aircraft application
- Regarding the superplastic forming ability of the 0.2Ti-4.5TiB₂ composite, highest elongation of 151% was achieved when it was deformed at 475°C with a strain rate of $5 \times 10^{-1} \text{ s}^{-1}$. The elongation was decreased with increasing temperature higher than 475°C. This suggests that the deformation of the 0.2Ti-4.5TiB₂ composite was limited to 475°C

FUTURE WORKS

Superplastic Forming Characterisation

- Conduct detailed investigation by DSC to confirm if the liquid phase plays a role during a SPF test
- Perform SPF tests by applying initial strain with high strain rates to induce dynamic recrystallisation prior to superplastic forming
- Perform SPF tests by applying a thermal cycle based on the ISS (internal stress superplasticity) method
- Perform detailed microstructural characterisation of the SPF specimens and compare it with the other two alloys
- Modify the thermomechanical process by applying a solution treatment, followed by overageing to generate coarse precipitates and subsequent warm rolling to produce a highly deformed structure (large local density of dislocations), hence, a fine recrystallised structure may develop during the SPF test, improving its superplasticity properties.

Microstructural Characterisation

- Perform texture analysis and correlate the TiB_2 pinning effect as well as Al_3Ti particles with certain grain orientations
- Perform EBSD analysis in other directions (transverse and longitudinal direction) to explore anisotropy of the materials
- Perform annealing with variation of times to investigate recrystallisation kinetics of the $0.2\text{Ti}-4.5\text{TiB}_2$ composite
- Owing to the high precipitate content in the matrix alloy, it would be beneficial to investigate the correlation between precipitates formed in the composite with TiB_2 particles which might influence the mechanical properties of the composites

Mechanical Testing

- Owing to the high tensile strength obtained in this study which showed promising properties for aircraft applications, it will be beneficial to conduct other important mechanical tests such as fracture toughness, fatigue and creep in order to approach an industrial application

REFERENCES

- [1] R.C. Dorward, T.R. Pritchett, Advanced aluminium alloys for aircraft and aerospace applications, *Mater. Des.* 9 (1988) 63–69. doi:10.1016/0261-3069(88)90076-3.
- [2] I.J.P. Polmear, *Light Alloys*, 2005. doi:10.1016/B978-075066371-7/50010-4.
- [3] I.J. Polmear, Recent developments in light alloys, *Mater. Trans.* 37 (1996) 12–31. doi:10.2320/matertrans1989.37.12.
- [4] A.J. Barnes, Superplastic forming 40 years and still growing, *J. Mater. Eng. Perform.* 22 (2013) 2935–2949. doi:10.1007/s11665-013-0727-4.
- [5] J.-P. Immarigeon, R.T. Holt, a. K. Koul, L. Zhao, W. Wallace, J.C. Beddoes, Lightweight materials for aircraft applications, *Mater. Charact.* 35 (1995) 41–67. doi:10.1016/1044-5803(95)00066-6.
- [6] J.R. Davis, ed., *Aluminum and Aluminum Alloys*, ASM International, 1993.
- [7] H.G. Salem, W.M. Lee, L. Bodelot, G. Ravichandran, M.A. Zikry, Quasi-Static and High-Strain-Rate Experimental Microstructural Investigation of a High-Strength Aluminum Alloy, *Metall. Mater. Trans. A.* 43 (2012) 1895–1901. doi:10.1007/s11661-011-1064-6.
- [8] B. Sofyan, K. Raviprasad, S. Ringer, Effects of microalloying with Cd and Ag on the precipitation process of Al–4Cu–0.3 Mg (wt%) alloy at 200° C, *Micron.* 32 (2001) 851–856.
- [9] B. Muddle, I. Polmear, The precipitate Ω phase in Al-Cu-Mg-Ag alloys, *Acta Metall.* 31 (1989) 777–789.
- [10] B.M. Gable, G.J. Shiflet, E.A. Starke Jr, Alloy development for the enhanced stability of Ω precipitate in Al-Cu-Mg-Ag alloys, *Metall. Mater. A.* 37 A (2006) 1091–1105.
- [11] S.P. Ringer, W. Yeung, B.C. Muddle, I.J. Polmear, Precipitate stability in Al-Cu-Mg-Ag alloys aged at high temperatures, *Acta Metall. Mater.* 42 (1994) 1715–1725.
- [12] Y.C. Chang, J.M. Howe, Composition and stability of Ω phase in an Al-Cu-Mg-Ag alloy, *Metall. Trans. A.* 24 A (1993) 1461–1470.
- [13] T.I. of Materials, *Materials in Aerospace*, n.d.
- [14] L. Lu, M. Lai, F. Chen, Al-4 wt% Cu Composite reinforced with in-situ TiB₂ particles, *Acta Mater.* 45 (1997) 4297 – 4309.
- [15] N. Rajasekaran, V. Sampath, Effect of In-Situ TiB₂ Particle Addition on the Mechanical Properties of AA 2219 Al Alloy Composite, *J. Miner. Mater. Charact. Eng.* 10 (2011) 527–534.
- [16] A. Mandal, M. Chakraborty, B.S. Murty, Effect of TiB₂ particles on sliding wear behaviour of Al–4Cu alloy, *Wear.* 262 (2007) 160–166. doi:10.1016/j.wear.2006.04.003.

- [17] T. Christman, S. Suresh, Microstructural development in an aluminum alloy-SiC whisker composite, *Acta Metall.* 36 (1988) 1691–1704. doi:10.1016/0001-6160(88)90236-2.
- [18] I. Sinclair, P.J. Gregson, S.M. Flitcroft, Effect of microstructure on mechanical properties of thermomechanically processed 2124-SiCp metal matrix composites, *Mater. Sci. Technol.* 10 (1994) 475 – 480.
- [19] G.H. Zahid, R.I. Todd, P.B. Prangnell, Superplasticity in an aluminium alloy 2124/SiCp composite, *Mater. Sci. Technol.* 14 (1998) 901–905.
- [20] S. Yadav, D.R. Chichili, K.T. Ramesh, The mechanical response of a 6061-T6 Al/Al₂O₃ metal matrix composite at high rates of deformation, *Acta Met. Mater.* 43 (1995) 4453–4464.
- [21] M. Ferry, P.R. Munroe, The effect of matrix temper on particulate integrity in an Al/Al₂O₃ metal matrix composite, *Scr. Metall. Mater.* 31 (1994) 143–148.
- [22] S.C. Tjong, Z.Y. Ma, R.K.Y. Li, The dynamic mechanical response of Al₂O₃ and TiB₂ particulate reinforced aluminum matrix composites produced by in-situ reaction, *Mater. Lett.* 38 (1999) 39–44.
- [23] K.L. Tee, L. Lu, M.O. Lai, In situ processing Al TiB₂ composite by stir casting technique, *J. Mater. Process. Technol.* 89 - 90 (1999) 513–519.
- [24] S. Suresh, N. Shenbag, V. Moorthi, Aluminium-Titanium Diboride (Al-TiB₂) Metal Matrix Composites: Challenges and Opportunities, *Procedia Eng.* 38 (2012) 89–97. doi:10.1016/j.proeng.2012.06.013.
- [25] I.G. Watson, M.F. Forster, P.D. Lee, R.J. Dashwood, R.W. Hamilton, A. Chirazi, Investigation of the clustering behaviour of titanium diboride particles in aluminium, *Compos. Part A Appl. Sci. Manuf.* 36 (2005) 1177–1187. doi:10.1016/j.compositesa.2005.02.003.
- [26] J. Forde, W. Stott, Aluminium-Copper Alloy for Casting, WO 2011/098813 A2, 2011.
- [27] T. Sheppard, *Extrusion of Aluminium Alloys*, 1st ed., Kluwer Academic Publishers, 1999. doi:10.1007/978-1-4757-3001-2.
- [28] M. Wang, D. Chen, Z. Chen, Y. Wu, F. Wang, N. Ma, et al., Mechanical properties of in-situ TiB₂/A356 composites, *Mater. Sci. Eng. A.* 590 (2014) 246–254. doi:10.1016/j.msea.2013.10.021.
- [29] J. Oñoro, High-temperature mechanical properties of aluminium alloys reinforced with titanium diboride (TiB₂) particles, *Rare Met.* 30 (2011) 200–205. doi:10.1007/s12598-011-0224-6.
- [30] F.J. Humphreys, M. Hatherly, *Recrystallization and Related Annealing Phenomena*, Elsevier, Oxford, 2004.
- [31] S. Lakshmi, L. Lu, M. Gupta, In situ preparation of TiB₂ reinforced Al based composites, *J. Mater. Process. Technol.* 73 (1998) 160–166.

- [32] I.G. Siddhalingeswar, M. a. Herbert, M. Chakraborty, R. Mitra, Effect of mushy state rolling on age-hardening and tensile behavior of Al-4.5Cu alloy and in situ Al-4.5Cu-5TiB₂ composite, *Mater. Sci. Eng. A.* 528 (2011) 1787–1798. doi:10.1016/j.msea.2010.11.027.
- [33] N. Charbhai, B. Murty, S. Sankaran, Characterization of microstructure and precipitation behavior in Al-4Cu-xTiB₂ in-situ composite, *Trans. Indian Inst.* 64 (2011) 117–121.
- [34] S. Guo, D. Li, D. Chen, H. Wang, Hot Deformation behaviour of insitu TiB₂ reinforced 6351 Al composite during compression at elevated temperatures, *Int. J. Mod. Phys. B* 23 (2009) 1432–1437.
- [35] S. Gourdet, S. Montheillet, An experimental study of the recrystallization mechanism during hot deformation of aluminium, *Mater. Sci. Eng. A.* 283 (2000) 274–288.
- [36] B. V Radhakrishna Bhat, Y.R. Mahajan, H.M. Roshan, Processing map for hot working of powder metallurgy 2124 Al-20 vol pct SiCp metal matrix composite, *Metall. Trans. A.* 23 A (1992) 2223–2230.
- [37] B.V. Radhakrishna, Y.R. Mahajan, H. Roshan, Y.V.R.K. Prasad, Processing map for hot working of 6061 Al-10 vol% Al₂O₃ metal matrix composite, *Mater. Sci. Technol.* 11 (1995) 167 – 173.
- [38] R. Raj, Development of a processing map for use in warm-forming and hot-forming processes, *Metall. Trans. A.* 12 (1981) 1089 – 1097.
- [39] S. Spigarelli, E. Cerri, An analysis of hot formability of the 6061+ 20% Al₂O₃ composite by means of different stability criteria, *Mater. Sci. Eng. A.* 327 (2002) 144–154.
- [40] N. Ravichandran, Y. Prasad, Dynamic recrystallization during hot deformation of aluminum: a study using processing maps, *Metall. Trans. A.* 22 (1990) 2339 – 2348.
- [41] P. Cavaliere, E. Cerri, P. Leo, Hot deformation and processing maps of a particulate reinforced 2618/Al₂O₃/20p metal matrix composite, *Compos. Sci. Technol.* 64 (2004) 1287–1291. doi:10.1016/j.compscitech.2003.10.007.
- [42] Y.V.R.K. Prasad, S. Sasidhara, eds., *Hot Working Guide: A Compendium of Processing Maps*, Second Edition, 2nd ed., ASM International, 2015.
- [43] I.J. Polmear, B.H. North, Wrought Al/Cu/Mg-type aluminum alloy of high strength in the temperature range between 0 and 250 degrees C, 4772342, 1988.
- [44] R.J. Chester, I. Polmear, *The Metallurgy of Light Metals*, Institute of Metals, London, England, 1983.
- [45] J.T. Vietz, I.J. Polmear, The influence of small additions of silver on the ageing aluminium alloys. Observation on Al-Cu-Mg-Ag alloys, *Inst Met. J.* 94 (1966) 410–419.
- [46] S.R. Arumulla, I.J. Polmear, Fatigue and creep behaviour of aged alloys based on Al-4%Cu-0.3%Mg, in: H.J. McQueen, J.-P. Bailon, J.I. Dickson, J.J. Jonas, M.G.

- Akben (Eds.), *Strength Met. Alloy. (ICSMA 7) Proc. 7th Int. Conf. Strength Met. Alloy.*, Elsevier, Montreal, 1985: pp. 453 – 548.
- [47] I. Polmear, M. Couper, Design and development of an experimental wrought aluminum alloy for use at elevated temperatures, *Metall. Trans. A.* 19 (1988) 1027–1035.
- [48] I.J. Polmear, G. Pons, Y. Barbaux, H. Octor, C. Sanchez, A. Morton, et al., After concorde: evaluation of creep resistant Al-Cu-Mg-Ag alloys, *Mater. Sci. Technol.* 15 (1999) 861–868.
- [49] S.P. Ringer, K. Hono, I.J. Polmear, T. Sakurai, Nucleation of precipitates in aged Al-Cu-Mg-(Ag) alloys with high Cu-Mg ratios, *Acta Mater.* 44 (1996) 1883–1898.
- [50] J. Metson, R. Lumley, *Fundamentals of Aluminium Metallurgy*, 2011. doi:10.1533/9780857090256.1.23.
- [51] A. Garg, J.M. Howe, Grain-boundary precipitation in an Al-4.0Cu-0.5Mg-0.5Ag Alloy, *Acta Met. Mater.* 40 (1992) 2451–2462.
- [52] J.H. Auld, Structure of a metastable precipitate in an Al-Cu-Mg-Ag alloy, *Acta Crystallogr.* (1972).
- [53] S. Kerry, V.D. Scott, Structure and orientation relationship of precipitates formed in Al-Cu-Mg-Ag alloys, *Met. Sci.* 18 (1984) 289–294.
- [54] H. Perlitz, A. Westgren, The crystal structure of Al₂CuMg, *Ark. Kemi Miner. Geol B16.* 13 (1943) 1 – 5.
- [55] A. Garg, J.M. Howe, Convergent-beam electron diffraction analysis of the Ω phase in an Al-4.0 Cu-0.5 Mg-0.5 Ag alloy, *Acta Metall. Mater.* 39 (1991) 1939–1946. doi:10.1016/0956-7151(91)90162-T.
- [56] K.M. Knowles, W.M. Stobbs, The structure of {111} age-hardening precipitates in Al–Cu–Mg–Ag alloys, *Acta Crystallogr. Sect. B Struct. Sci.* 44.3 (1988) 207 – 227.
- [57] J.A. Taylor, B.A. Parker, I.J. Polmear, Precipitation in Al-Cu-Mg-Ag casting alloy, *Met. Sci.* 12 (1978) 478–482. doi:10.1179/030634578790433341.
- [58] S.M. Cousland, G.R. Tate, Structural changes associated with solid-state reactions in Al–Ag–Mg alloys, *J. Appl. Crystallogr.* 19 (1986) 174–180. doi:10.1107/S0021889886089707.
- [59] K. Hono, N. Sano, S. Babu, Atom probe study of the precipitation process in Al-Cu-Mg-Ag alloys, *Acta Metall.* 41 (1993) 829–838.
- [60] A. Garg, Y. Chang, J. Howe, Precipitation of the Ω Phase in an Al-4.0 Cu-0.5 Mg alloy, *Scr. Metall. Mater.* 24 (1990) 677–680.
- [61] S. Abis, P. Mengucci, G. Riontino, A study of the high-temperature ageing of Al-Cu-Mg-Ag alloy 201, *Philos. Mag. B Phys. Condens. Matter; Stat. Mech. Electron. Opt. Magn. Prop.* 67 (1993) 465–484. doi:10.1080/13642819308207686.
- [62] S. Abis, P. Mengucci, G. Riontino, Influence of Si Additions on the Aging Process

- of an Al-Cu-Mg-Ag Alloy, *Philos. Mag. A-Physics Condens. Matter Struct. Defects Mech. Prop.* 70 (1994) 851–868. doi:10.1080/01418619408242935.
- [63] K. Hono, T. Sakurai, I. Polmear, Pre-precipitate clustering in an Al-Cu-Mg-Ag alloy, *Scr. Metall. Mater.* 30 (1994) 695–700.
- [64] A. Zhu, E.A. Starke, G.J. Shiflet, An FP-CVM calculation of pre-precipitation clustering in Al-Cu-Mg-Ag alloys, *Scr. Mater.* 53 (2005) 35–40. doi:10.1016/j.scriptamat.2005.03.023.
- [65] S.P. Ringer, B.C. Muddle, I.J. Polmear, Effects of cold work on precipitation in Al-Cu-Mg-(Ag) and Al-Cu-Li-(Mg-Ag) alloys, *Metall. Mater. A.* 26 A (1995) 1659–1671.
- [66] B. Skrotzki, G.J. Shiflet, E.A. Starke Jr, On the effect of stress on nucleation and growth of precipitate in Al-Cu-Mg-Ag alloy, *Metall. Mater. A.* 27 A (1996) 3431–3444.
- [67] C.R. Hutchinson, X. Fan, S.J. Pennycook, G.J. Shiflet, On the origin of the high coarsening resistance of omega plates in Al-Cu-Mg-Ag alloys, *Acta Mater.* 49 (2001) 2827–2841.
- [68] B.M. Gable, G.J. Shiflet, E.A. Starke, The effect of Si additions on Ω precipitation in Al-Cu-Mg-(Ag) alloys, *Scr. Mater.* 50 (2004) 149–153. doi:10.1016/j.scriptamat.2003.09.004.
- [69] A.K. Mukhopadhyay, On the nature of the second phase particles present in an as cast Al-Cu-Mg-Ag alloy, *Scr. Mater.* 41 (1999) 667–672.
- [70] A.K. Mukhopadhyay, Compositional characterization of Cu-rich phase particles present in As-cast Al-Cu-Mg-(Li) alloys containing Ag, *Metall. Mater. Trans. A.* 30A (1999) 1693–1704.
- [71] D. Xiao, J. Wang, D. Ding, S. Chen, Effect of Cu content on the mechanical properties of an Al-Cu-Mg-Ag alloy, *J. Alloys Compd.* 343 (2002) 77–81.
- [72] W.A. Cassada, M.F. Bartholomeusz, The Effect of Cu and Mg Content on Mechanical Properties of Al-Cu-Mg Alloys with and without Ag Additions, *Mater. Sci. Forum.* 217-222 (1996) 1765–1770.
- [73] I. Suh, J. Park, Influence of the elastic strain energy on the nucleation of Ω phase in Al-Cu-Mg (-Ag) alloys, *Scr. Metall. Mater.* 33 (1995) 205–211.
- [74] L. Reich, M. Murayama, K. Hono, Evolution of Omega phase in Al-Cu-Mg-Ag alloy - A Three dimensional atom probe study, *Acta Mater.* 46 (1998) 6053–6062.
- [75] S.P. Ringer, I.J. Polmear, T. Sakurai, Effect of additions of Si and Ag to ternary Al-Cu-Mg alloys in the alpha and S phase field, *Mater. Sci. Eng. A.* 217/218 (1996) 273–276.
- [76] D.H. Xiao, J.N. Wang, D.Y. Ding, Effect of titanium additions on mechanical properties of Al-Cu-Mg-Ag alloy, *Mater. Sci. Technol.* 20 (2004) 1199–1204. doi:10.1179/026708304225022106.

- [77] A. Mandal, R. Maiti, M. Chakraborty, B.S. Murty, Effect of TiB₂ particles on aging response of Al–4Cu alloy, *Mater. Sci. Eng. A.* 386 (2004) 296–300. doi:10.1016/j.msea.2004.07.026.
- [78] D.G. McCartney, Grain refining of aluminium and its alloys using inoculants, *International Mater. Rev.* 34 (1989) 247 – 260.
- [79] G. Jones, J. Pearson, Factors affecting the grain-refinement of aluminum using titanium and boron additives, *Metall. Trans. B.* 7 (1976) 223 – 234.
- [80] J.A.M. Antonio, L.F. Mondolfo, Grain refinement in aluminum alloyed with titanium and boron, *Metall. Trans.* 2 (1971) 465–471.
- [81] I. Maxwell, A. Hellawell, The constitution of the system Al-Ti-B with reference to aluminum-base alloys, *Metall. Trans.* 3 (1972) 1487 – 1493.
- [82] D.H. StJohn, M. Qian, M. a. Easton, P. Cao, The Interdependence Theory: The relationship between grain formation and nucleant selection, *Acta Mater.* 59 (2011) 4907–4921. doi:10.1016/j.actamat.2011.04.035.
- [83] M. Easton, D. StJohn, Grain refinement of aluminum alloys part I. the nucleant and solute paradigms, *Metall. Mater. Trans. A.* 30 A (1999) 1615–1623.
- [84] M. Easton, D. Stjohn, Grain Refinement of Aluminum Alloys: Part II . Confirmation of , and a Mechanism for , the Solute Paradigm, 30 (1999) 1625–1633.
- [85] P.S. Mohanty, J.E. Gruzleski, Mechanism of grain refinement in aluminium, *Acta Met. Mater.* 47 (1995) 2001–2012.
- [86] I. Maxwell, A. Hellawell, A simple model for grain refinement during solidification, *Acta Metall.* 23 (1975) 229 – 237.
- [87] I.G. Davies, J.M. Dennis, A. Hellawell, The Nucleation of Aluminum Grains in Alloys of Aluminum with Titanium and Boron, *Metall. Trans.* 1 (1970) 275 – 280.
- [88] L. Backerud, P. Gustafson, M. Johnsson, Grain refining mechanisms in aluminium as a result of additions of titanium and boron, *Aluminium.* 67 (1991) 910–915.
- [89] M. Vader, J. Noordegraaf, P.C. van Wiggeren, Aluminum master alloys with reduced intermetallic phase sizes open up windows for new applications, in: *Light Met. TMS*, New Orleans, LA, 1991: pp. 1123–1130.
- [90] Z. Fan, Y. Wang, Y. Zhang, T. Qin, X.R. Zhou, G.E. Thompson, et al., Grain refining mechanism in the Al/Al–Ti–B system, *Acta Mater.* 84 (2015) 292–304. doi:10.1016/j.actamat.2014.10.055.
- [91] C.D. Mayes, D.G. McCartney, G.J. Tatlock, Influence of microstructure on grain refining performance of Al–Ti–B master alloys, *Mater. Sci. Technol.* 9 (1993) 97–103.
- [92] B.S. Murty, S. a. Kori, M. Chakraborty, Grain refinement of aluminium and its alloys by heterogeneous nucleation and alloying, *Int. Mater. Rev.* 47 (2002) 3–29. doi:10.1179/095066001225001049.

- [93] M. Johnsson, L. Backerud, G.K. Sigworth, Study of the mechanism of grain refinement of aluminium after addition of Ti and B containing master alloy, *Metall. Trans. A*. 24 A (1993) 481–491.
- [94] M. a Easton, D.H. Stjohn, Partitioning of titanium during solidification of aluminium alloys, 16 (2000) 993–1000. doi:10.1179/026708300101508946.
- [95] A.M. Bunn, P. Schumacher, M.A. Kearns, C.B. Boothroyd, A.L. Greer, Grain refinement by Al – Ti – B alloys in aluminium melts : a study of the mechanisms of poisoning by zirconium, *Mater. Sci. Technol.* 15 (1999) 1115–1123.
- [96] J. V. Wood, P. Davies, J.L.F. Kellie, Properties of reactively cast aluminium–TiB₂ alloys, *Mater. Sci. Technol.* 9 (1993) 833–840.
- [97] I.G. Siddhalingeswar, a Behera, R. Mitra, M. Chakraborty, Composite Processed By Multiple Roll Passes in Mushy State, 62 (2009) 379–382.
- [98] I.G. Siddhalingeswar, D. Deepthi, M. Chakraborty, R. Mitra, Sliding wear behavior of in situ Al–4.5Cu–5TiB₂ composite processed by single and multiple roll passes in mushy state, *Wear*. 271 (2011) 748–759. doi:10.1016/j.wear.2011.03.017.
- [99] S.C. Tjong, Z.Y. Ma, Microstructural and mechanical characteristics of in situ metal matrix composites, *Mater. Sci. Eng. R Reports*. 29 (2000) 49–113. doi:10.1016/S0927-796X(00)00024-3.
- [100] X. Wang, R. Brydson, A. Jha, J. Ellis, Microstructural analysis of Al alloys dispersed with TiB₂ particulate for MMC applications, *J. Microsc.* 196 (1999) 137–145.
- [101] A20X by Aeromet International Ltd, (n.d.). <http://www.aeromet.co.uk/a20x/index.html>.
- [102] E. Evangelista, H.J. McQueen, M.E. Kassner, S. Spigarelli, *Hot Deformation and Processing of Aluminum Alloys*, CRC Press, 2011.
- [103] G.E. Dieter, H.A. Kuhn, S.L. Semiatin, eds., *Handbook of Workability and Process Design*, ASM International, 2003.
- [104] C.M. Sellars, W.J.M. Tegart, Hot Workability, *Int. Metall. Rev.* 17 (1972) 1–24. doi:10.1179/095066072790137765.
- [105] H.. McQueen, N.. Ryan, Constitutive analysis in hot working, *Mater. Sci. Eng. A*. 322 (2002) 43–63. doi:10.1016/S0921-5093(01)01117-0.
- [106] J.R. Cotner, W.J. McTegart, High-temperature deformation of aluminium-magnesium alloys at high strain rates, *J. Inst. Met.* 97 (1969) 73 – 79.
- [107] H.J. McQueen, Development of dynamic recrystallization theory, *Mater. Sci. Eng. A*. 387-389 (2004) 203–208. doi:10.1016/j.msea.2004.01.064.
- [108] M.E. Kassner, S.R. Barrabes, New developments in geometric dynamic recrystallization, *Mater. Sci. Eng. A*. 410-411 (2005) 152–155. doi:10.1016/j.msea.2005.08.052.

- [109] Y.V.R.K. Prasad, T. Seshacharyulu, Modelling of hot deformation for microstructural control, *Int. Mater. Rev.* 43 (1998) 243–258. doi:10.1179/095066098790105618.
- [110] Y.V.R.K. Prasad, Processing maps: A status report, *J. Mater. Eng. Perform.* 22 (2013) 2867–2874. doi:10.1007/s11665-013-0732-7.
- [111] M.F. Ashby, H.J. Frost, *Deformation-Mechanism Maps*, Pergamon Press, Oxford, 1982.
- [112] M.F. Ashby, A first report on deformation mechanism maps, *Acta Metall.* 20 (1972) 887 – 897.
- [113] F.J. Humphreys, A Unified theory of recovery, recrystallization and grain growth, based on the stability and growth of cellular microstructures-I. The basic model, *Acta Mater.* 45 (1997) 4231–4240.
- [114] R.D. Doherty, D. a. Hughes, F.J. Humphreys, J.J. Jonas, D. Juul Jensen, M.E. Kassner, et al., Current issues in recrystallization: A review, *Mater. Today.* 1 (1998) 14–15.
- [115] M.J. Luton, R.A. Petkovic, J.J. Jonas, Kinetics of recovery and recrystallization in polycrystalline copper, *Acta Metall.* 28 (1980) 729–743. doi:10.1016/0001-6160(80)90151-0.
- [116] M. Somerday, F. Humphreys, Recrystallisation behaviour of supersaturated Al-Mn alloys Part 1 - Al-0.3 wt-%Mn, *Mater. Sci. Technol.* 19 (2003) 30–35. doi:10.1179/026708303225008608.
- [117] E. Nes, N. Ryum, O. Hunderi, On the Zener drag, *Acta Metall.* 33 (1985) 11–22. doi:10.1016/0001-6160(85)90214-7.
- [118] G.N. Hassold, E. Holm, D.J. Srolovitz, Effect of particle size on inhibited grain growth, *Scr. Metall. Mater.* 24 (1990) 101 – 106.
- [119] T. Gladman, On the Theory of the Effect of Precipitate Particles on Grain Growth in Metals, *Proc. R. Soc. A Math. Phys. Eng. Sci.* 294 (1966) 298–309. doi:10.1098/rspa.1966.0208.
- [120] A. Rollett, F.J. Humphreys, G.S. Rohrer, M. Hatherly, Chapter 10 The Growth and Stability of Cellular, in: *Recryst. Relat. Annealing Phenom.*, 2004: pp. 321–331.
- [121] G. Giuliano, ed., *Superplastic Forming of Advanced Metallic Materials : Methods and Applications*, Woodhead Publishing Limited, 2011.
- [122] T.G. Nieh, J. Wadsworth, O.D. Sherby, *Superplasticity in Metals and Ceramics*, 1st ed., Cambridge University Press, New York, 1997. doi:10.1007/s13398-014-0173-7.2.
- [123] T.G. Langdon, Seventy-five years of superplasticity: Historic developments and new opportunities, *J. Mater. Sci.* 44 (2009) 5998–6010. doi:10.1007/s10853-009-3780-5.
- [124] J. Pilling, N. Ridley, *Superplasticity in crystalline Solids*, The Institute of Metals, London, England, 1989.

- [125] C.W. Humphries, N. Ridley, Effect of relatively hard particles on cavitation of microduplex Pb-Sn eutectic during superplastic flow, *J. Mater. Sci.* 12 (1977) 851 – 855.
- [126] D.W. Livesey, N. Ridley, Cavitation during superplastic flow of ternary alloys based on microduplex Pb-Sn eutectic, *J. Mater. Sci.* 13 (1978) 825 – 832.
- [127] C.I. Smith, B. Norgate, N. Ridley, Superplastic deformation and cavitation in a microduplex stainless steel, *J. Mater. Sci.* 10 (1976) 182 – 188.
- [128] B. Walser, O.D. Sherby, Mechanical behavior of superplastic ultrahigh carbon steels at elevated temperature, *Metall. Trans. A.* 10 (1979) 1461 – 1472.
- [129] N. Ridley, Superplastic microstructures, *Mater. Sci. Technol.* 6 (1990) 1145–1156.
- [130] P.K. Chaudhury, F.A. Mohamed, Effect of impurity content on superplastic flow in the Zn-22% Al alloy, *Acta Metall.* 36 (1988) 1099–1110. doi:10.1016/0001-6160(88)90163-0.
- [131] T.G. Langdon, The mechanical properties of superplastic materials, *Metall. Trans. A.* 13 (1982) 689–701. doi:10.1007/BF02642383.
- [132] T.G. Langdon, The physics of superplastic deformation, *Mater. Sci. Eng. A.* 137 (1991) 1–11. doi:10.1016/0921-5093(91)90312-B.
- [133] A.K. Mukherjee, The rate controlling mechanism in superplasticity, *Mater. Sci. Eng.* 8 (1971) 83–89.
- [134] T.G. Nieh, C.A. Henshall, J. Wadsworth, L. Palo, S. Operation, Superplasticity at high strain rates in a SiC whisker reinforced Al alloy, *Scr. Metall.* 18 (1984) 1405–1408.
- [135] J. Koike, M. Mabuchi, K. Higashi, In situ observation of partial melting in superplastic aluminum alloy composites at high temperatures, *Acta Metall. Mater.* 43 (1995) 199–206.
- [136] K. Higashi, T.G. Nieh, M. Mabuchi, J. Wadsworth, L. Livermore, Effect of Liquid Phases on the Tensile Elongation of Superplastic Aluminum Alloys and Composites, *Scr. Metall. Mater.* 32 (1995) 1079–1084.
- [137] M. Mabuehl, K. Hlgashi, Y. Okada, K. Kubo, Very high strain-rate superplasticity in a particulate Si₃N₄/6061 aluminum composite, *Scr. Metall. Mater.* 25 (1991) 2517–2522.
- [138] B.Q. Han, K.C. Chan, High-strain-rate superplasticity of an Al6061-SiCw composite, *Scr. Mater.* 36 (1997) 593–598.
- [139] T.G. Nieh, J. Wadsworth, Effect of liquid phase on superplasticity at high strain rates in metals and their composites, in: *Prop. Complex Inorg. Solids*, 1997: pp. 415–423.
- [140] K. Matsuki, H. Kawakami, M. Tokizawa, S. Murakami, High strain rate superplastic flow stress and post-deformation mechanical properties of mechanically alloyed 2024 aluminium alloy reinforced with SiC particles, *Mater. Sci. Technol.* 13 (1997)

1039 – 1044.

- [141] K. Higashi, M. Mabuchi, Experimental investigation of cavitation fracture at very high strain rates in superplastic aluminium alloy matrix composites, *Mater. Sci. Eng. A.* 176 (1994) 461–470.
- [142] H. Iwasaki, M. Mabuchi, K. Higashi, T.G. Langdon, The development of cavitation in superplastic aluminum composites reinforced with Si₃N₄, *Mater. Sci. Eng. A.* 208 (1996) 116–121. doi:10.1016/0921-5093(95)10088-1.
- [143] W.J. Kim, Y.S. Lee, C.W. An, Superplastic behavior of PM SiCp/6061 aluminum alloy composites at high strain rates, *Met. Mater. Int.* 8 (2002) 37–44. doi:10.1007/BF03027026.
- [144] H.E. Hu, L. Zhen, T. Imai, Strain rate sensitivity of a high strain rate superplastic TiNp/2014 Al composite, *J. Mater. Process. Technol.* 210 (2010) 734–740. doi:10.1016/j.jmatprotec.2009.12.011.
- [145] S.R. Nutt, R.W. Carpenter, Non-equilibrium Phase Distribution in an Al-SiC Composite, 75 (1985) 169–177.
- [146] M. Strangwood, C.A. Hipsley, J.J. Lewandowski, Segregation to SiC/Al interfaces in Al based metal matrix composites, *Scr. Metall. Mater.* 24 (1990) 1483 – 1487.
- [147] T. Imai, S. Kojima, G. L'Esperance, B. Hong, D. Jiang, Effect of volume fraction of SiC particle on superplasticity of AlN/6061 aluminum alloy composite, *Scr. Mater.* 35 (1996) 1199 – 1204.
- [148] M. Wu, O. Sherby, Superplasticity in a silicon carbide whisker reinforced aluminum alloy, *Scr. Metall.* 18 (1984) 6–9.
- [149] B. Derby, Internal stress superplasticity in metal matrix composites, *Scr. Metall.* 19 (1985) 703 – 707.
- [150] S.M. Pickard, B. Derby, The behaviour of metal matrix composites during temperature cycling, *Mater. Sci. Eng. A.* 135 (1991) 213 – 216.
- [151] T.W. Clyne, M.H. Robert, Stability of intermetallic aluminides in liquid aluminium and implications for grain refinement, *Met. Technol.* 7 (1980) 177–185. doi:10.1179/030716980803287314.
- [152] S. Tamotsu, S. Den, G. Ohira, The diffusion time required for dissolution of TiAl₃ crystals into pure aluminum liquid and the grain-refinement of α aluminum solid-solution by Ti addition, *Mater. Trans. JIM.* 20 (1979) 687 – 696.
- [153] M. Rajamuthamilselvan, Deformation Stability of Al 7075/20%SiCp (63 µm) Composites during Hot Compression, *Geomaterials.* 02 (2012) 121–127. doi:10.4236/gm.2012.24017.
- [154] S.V.S.N. Murty, B.N. Rao, B.P. Kashyap, On the hot working characteristics of 6061 Al-SiC and 6061 - Al₂O₃ particulate reinforced metal matrix composites, *Compos. Sci. Technol.* 63 (2003) 129–135.
- [155] A. El-Sabbagh, M. Soliman, M. Taha, H. Palkowski, Hot rolling behaviour of stir-

- cast Al 6061 and Al 6082 alloys – SiC fine particulates reinforced composites, *J. Mater. Process. Technol.* 212 (2012) 497–508. doi:10.1016/j.jmatprotec.2011.10.016.
- [156] H.J. McQueen, X. Xia, Y. Cui, B. Li, Q. Meng, Solution and precipitation effects on hot workability of 6201 alloy, *Mater. Sci. Eng. A.* 319–321 (2001) 420–424. doi:10.1016/S0921-5093(01)01099-1.
- [157] P. Wouters, B. Verlinden, H.J. McQueen, E. Aernoudt, L. Delaey, S. Cauwenberg, Effect of homogenization and precipitation treatments on the hot workability of an aluminium alloy AA2024, *Mater. Sci. Eng. A.* 123 (1990) 239–245. doi:10.1016/0921-5093(90)90289-F.
- [158] P. Leo, E. Cerri, H. Mcqueen, Hot workability of aluminum particulate composites, *Luglio.* 1–3 (2013) 245 – 254.
- [159] C. Shi, W. Mao, X.G. Chen, Evolution of activation energy during hot deformation of AA7150 aluminum alloy, *Mater. Sci. Eng. A.* 571 (2013) 83–91. doi:10.1016/j.msea.2013.01.080.
- [160] Y. Deng, Z. Yin, J. Huang, Hot deformation behavior and microstructural evolution of homogenized 7050 aluminum alloy during compression at elevated temperature, *Mater. Sci. Eng. A.* 528 (2011) 1780–1786. doi:10.1016/j.msea.2010.11.016.
- [161] H. McQueen, Deformation of aluminium at high temperatures and strain rates, *Can. J. Phys.* 45 (1967) 1225 – 1234.
- [162] N.D. Ryan, H.J. McQueen, Flow stress, dynamic restoration, strain hardening and ductility in hot working of 316 steel, *J. Mater. Process. Tech.* 21 (1990) 177–199. doi:10.1016/0924-0136(90)90005-F.
- [163] H.J. McQueen, Elevated-temperature deformation at forming rates of 10⁻² to 10² s⁻¹, *Metall. Mater. Trans. A.* 33 (2002) 345–362. doi:10.1007/s11661-002-0096-3.
- [164] F.J. Humphreys, P.N. Kalu, Dislocation-particle interactions during high temperature deformation of two-phase aluminum alloys, *Acta Metall.* 35 (1987) 2815–2829.
- [165] T. Sheppard, A. Jackson, Constitutive equations for use in prediction of flow stress during extrusion of aluminium alloys, *Mater. Sci. Technol.* 13 (1997) 203 – 309.
- [166] H. Shi, J. McLaren, C.M. Sellars, R. Shahani, R. Bolingbroke, Constitutive equations for high temperature flow stress of aluminium alloys, *Mater. Sci. Technol.* 13 (1997) 210–216.
- [167] H. McQueen, O. Celliers, Application of Hot Workability Studies to Extrusion Processing: Part II. Microstructural Development and Extrusion of Al, Al–Mg, and Al–Mg–Mn Alloys, *Can. Metall. Q.* 35 (1996) 305–319.
- [168] T. Sheppard, D. Wright, Determination of flow stress: Part 1 constitutive equation for aluminium alloys at elevated temperatures, *Met. Technol.* 6 (1979) 215–223. doi:10.1179/030716979803276264.
- [169] C. Zener, J.H. Hollomon, Effect of strain rate upon plastic flow of steel, *J. Appl.*

- Phys. 15 (1944) 22–32. doi:10.1063/1.1707363.
- [170] C.M. Sellars, W.J. McTegart, On the mechanism of hot deformation, *Acta Metall.* 14 (1966) 1136–1138. doi:10.1016/0001-6160(66)90207-0.
- [171] J.J. Jonas, C.M. Sellars, W.J.M. Tegart, Strength and structure under hot-working conditions, *Int. Mater. Rev.* 14 (1969) 1–24. doi:10.1179/095066069790138056.
- [172] X.Y. Liu, Q.L. Pan, Y. Bin He, W. Bin Li, W.J. Liang, Z.M. Yin, Flow behavior and microstructural evolution of Al–Cu–Mg–Ag alloy during hot compression deformation, *Mater. Sci. Eng. A.* 500 (2009) 150–154. doi:10.1016/j.msea.2008.09.028.
- [173] X. Xia, P. Sakaris, H.J. McQueen, Hot deformation, dynamic recovery, and recrystallisation behaviour of aluminium 6061–SiCp composite, *Mater. Sci. Technol.* 10 (1994) 487–496. doi:10.1179/mst.1994.10.6.487.
- [174] H.J. McQueen, M. Myshlyaev, E. Konoplevat, P. Sakarist, High temperature mechanical and microstructural behaviour of A356/15 vol % SiCp and A356 alloy, *Can. Metall. Q.* 37 (1998) 125–139.
- [175] M. Ferry, P.R. Munroe, Microstructure and kinetics of recrystallisation hot deformed Al–Al₂O₃ particulate reinforced metal matrix composite, *Mater. Sci. Technol.* 11 (1995) 734–740.
- [176] S. Suresh, A. Mortensen, A. Needleman, *Fundamentals of Metal Matrix Composites*, Butterworth-Heinemann, Massachusetts, 1993.
- [177] M.R. Drury, J.L. Urai, Deformation-related recrystallization processes, *Tectonophysics*. 172 (1990) 235–253. doi:10.1016/0040-1951(90)90033-5.
- [178] H. McQueen, N. Ryan, Formation and application of grain boundary serrations, *Can. Metall.* 34 (1995) 219–229.
- [179] G.K. Sigworth, Communication on mechanism of grain refinement in aluminum, *Scr. Mater.* 34 (1996) 919–922.
- [180] F. Wang, Z. Liu, D. Qiu, J. a. Taylor, M. a. Easton, M.X. Zhang, Revisiting the role of peritectics in grain refinement of Al alloys, *Acta Mater.* 61 (2013) 360–370. doi:10.1016/j.actamat.2012.09.075.
- [181] P. Schumacher, A.L. Greer, *Studies of the action of grain - refining particles in aluminium alloys*, (1995).
- [182] M. Easton, D. StJohn, Theoretical advances leading to improvement in commercial grain refinement practices in Al alloys, *Mater. Forum.* 31 (2007) 57–62.
- [183] G.K. Sigworth, T.A. Kuhn, Grain refinement of aluminium casting alloy, *AFS Trans.* 07-067(02) (2007) 1–12.
- [184] R.W.K. Honeycombe, *The Plastic Deformation of Metals*, Second Edi, Edward Arnold Ltd, London, England, 1984.
- [185] G.M. Owolabi, D.T. Bolling, A.A. Tiamiyu, R. Abu, A.G. Odeshi, H.A. Whitworth,

- Shear strain localization in AA 2219-T8 aluminum alloy at high strain rates, *Mater. Sci. Eng. A.* 655 (2016) 212–220. doi:10.1016/j.msea.2015.12.100.
- [186] H. Paul, A. Tarasek, W. Wajda, K. Berent, Shear bands formation after a strain path change for AA1050 alloy pre-deformed by ECAP and subsequently plane strain compressed, *IOP Conf. Ser. Mater. Sci. Eng.* 63 (2014) 012145. doi:10.1088/1757-899X/63/1/012145.
- [187] M. Hatherly, A.S. Malin, Shear bands in deformed metals, *Scr. Metall.* 18 (1984) 449–454. doi:10.1016/0036-9748(84)90419-8.
- [188] S. Mahesh, Deformation banding and shear banding in single crystals, *Acta Mater.* 54 (2006) 4565–4574.
- [189] A.A. Ridha, W.B. Hutchinson, Recrystallisation mechanisms and the origin of cube texture in copper, *Acta Metall.* 30 (1982) 1929–1939. doi:10.1016/0001-6160(82)90033-5.
- [190] P.K. Saha, *Aluminum Extrusion Technology*, 1st ed., ASM International, Ohio, 2000.
- [191] T. Sheppard, R.P. Vierod, Effect of Preheat Modification on Extrusion Characteristics of Aluminium Alloy 2014, *Mater. Sci. Technol.* 1 (1985) 321–324. doi:10.1179/mst.1985.1.4.321.
- [192] M. Ferry, P.R. Munroe, The effect of subgrain size on the static recrystallization behaviour of an aluminium-based metal-matrix composite, *Scr. Metall. Mater.* 33 (1995) 857–862. doi:10.1016/0956-716X(95)00319-Q.
- [193] F.J. Humphreys, The nucleation of recrystallization at second phase particles in deformed aluminium, *Acta Metall.* 25 (1977) 1323 – 1344.
- [194] M. Ferry, P.R. Munroe, Recrystallization kinetics and final grain size in a cold rolled particulate reinforced Al-based MMC, *Compos. Part A Appl. Sci. Manuf.* 35 (2004) 1017–1025. doi:10.1016/j.compositesa.2004.03.014.
- [195] F.J. Humphreys, Local lattice rotations at second phase particles in deformed metals, *Acta Metall.* 27 (1979) 1801–1814. doi:10.1016/0001-6160(79)90071-3.
- [196] C.W. Corti, P. Cotterill, G. a. Fitzpatrick, The Evaluation of the Interparticle Spacing in Dispersion Alloys, *Int. Mater. Rev.* 19 (1974) 77–88. doi:10.1179/095066074790137088.
- [197] N. Hansen, B. Bay, Initial stages of recrystallization in aluminium containing both large and small particles, *Acta Metall.* 29 (1981) 65–77. doi:10.1016/0001-6160(81)90087-0.
- [198] E. Nes, On the effect of finely dispersed second-phase particles on nucleation in recrystallization, *Scr. Metall.* 10 (1976) 1025 – 1028.
- [199] Hatch J.E., *Aluminum Properties and Physical Metallurgy*, 1984. doi:10.1361/appm1984p001.
- [200] N. Sano, K. Hono, T. Sakurai, K. Hirano, Atom-probe analysis of Ω and θ' phases in

- an Al-Cu-Mg-Ag alloy, *Scr. Metall. Mater.* 25 (1991) 491–496.
- [201] I.J. Polmear, R.J. Chester, Abnormal age hardening in an Al-Cu-Mg alloy containing silver and lithium, *Scr. Metall.* 23 (1989) 1213–1218.
- [202] Alcoa, Alloy 2024 Sheet and Plate, Excellent fatigue properties-consistent performance, n.d.
- [203] W.D.C. Jr., *Fundamentals of Materials Science and Engineering*, 2nd additi, John Wiley & Sons, United States of America, 2005.
- [204] H. Phull, Personal Conversation, (2015).
- [205] T. Hikosaka, T. Imai, T.G. Nieh, J. Wadsworth, High strain rate superplasticity of a SiC particulate reinforced aluminium alloy composite by vortex method, *Scr. Metall. Mater.* 31 (1994) 1181–1186.
- [206] M. Mabuchi, T. Imai, K. Kubo, K. Higashi, Y. Okada, S. Tanimura, Superplasticity in as-extruded Si₃N₄/6061 aluminum composites processed at a ratio of 100: 1, *Mater. Lett.* 11 (1991) 339–342.
- [207] M. Mabuchi, K. Higashi, S. Tanimura, T. Amai, K. Kubo, Superplasticity behavior at high strain rates in a particulate Si₃N₄/6061 aluminum composites, *Scr. Metall. Mater.* 25 (2006) 2003–2006.
- [208] R.S. Mishra, A.K. Mukherjee, On superplasticity in silicon carbide reinforced aluminum composites, *Scr. Metall. Mater.* 25 (1991) 271–275.
- [209] K.C. Chan, B.Q. Han, High-strain-rate superplasticity of particulate reinforced aluminium matrix composites, *Int. J. Mech. Sci.* 40 (1998) 305–311.
- [210] T. Imai, G. L'Esperance, B. Hong, S. Kojima, J. Kusui, Tms, High strain rate superplasticity of ceramic particulate reinforced aluminium alloy composites, *Proc. 1995 124th TMS Annu. Meet.* 364 (1995) 145–152. doi:10.1016/j.msea.2003.08.051.
- [211] T. Sakai, A. Belyakov, R. Kaibyshev, H. Miura, J.J. Jonas, Dynamic and post-dynamic recrystallization under hot, cold and severe plastic deformation conditions, *Prog. Mater. Sci.* 60 (2014) 130–207. doi:10.1016/j.pmatsci.2013.09.002.
- [212] R.S. Mishra, T.R. Bieler, A.K. Mukherjee, Mechanism of high strain rate superplasticity in aluminium alloy composites, *Acta Mater.* 45 (1997) 561–568.

APPENDIX A

FLOW STRESS DATA FROM COMPRESSION TEST

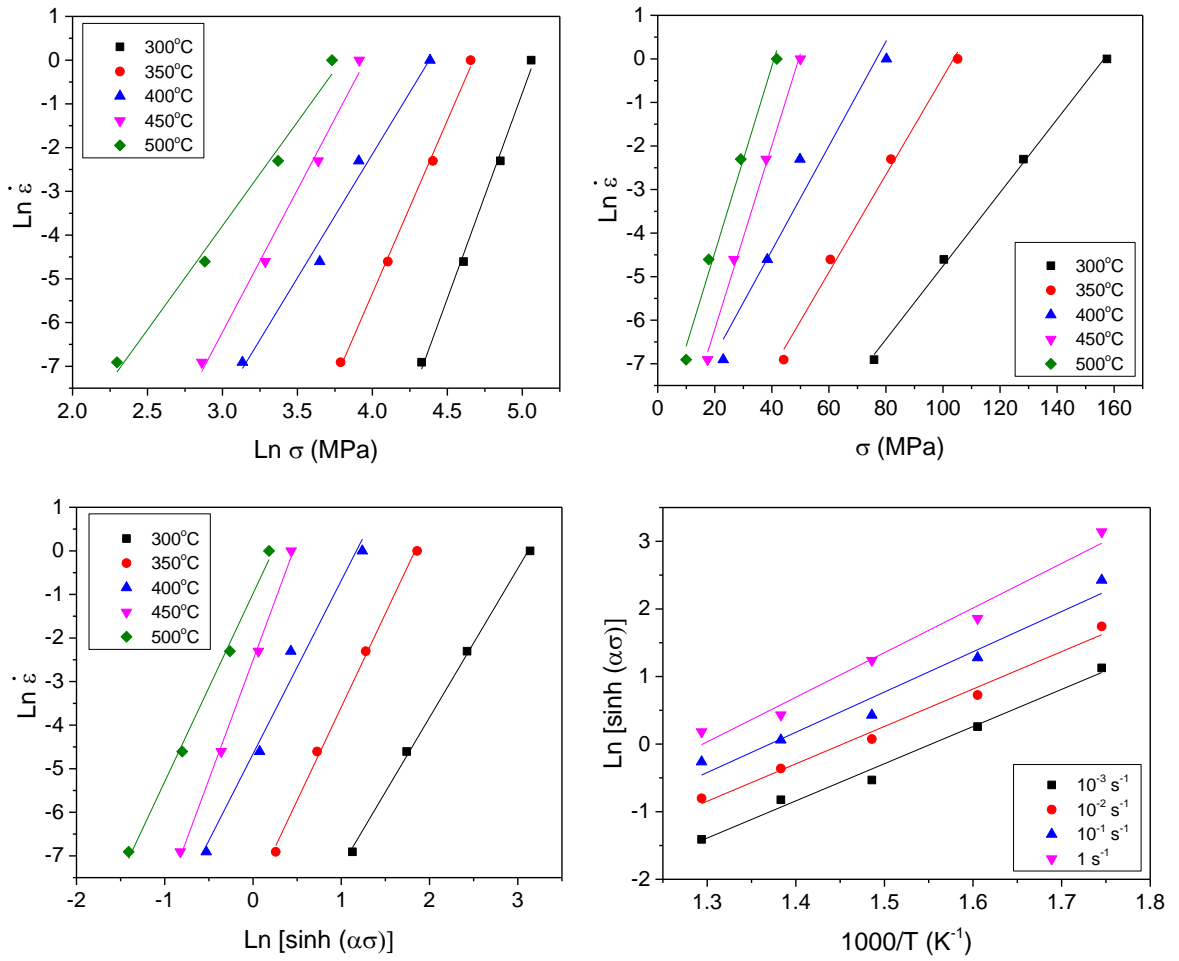
A.1. Flow stress (MPa) data of matrix alloy at different temperature, strain rate and strain

Strain	Strain Rate	Temperature (°C)				
		300	350	400	450	500
0.1	0.001	86.8	50.6	24.6	18.3	9.7
	0.01	115.4	69.7	42.0	26.5	17.6
	0.1	141.0	92.8	52.2	38.1	28.8
	1	173.1	116.3	86.2	51.3	41.3
0.2	0.001	79.7	46.7	25.4	17.7	9.7
	0.01	106.0	64.0	40.3	26.4	17.9
	0.1	134.2	85.7	51.0	37.7	28.7
	1	165.7	111.3	82.5	50.1	41.2
0.3	0.001	75.8	44.2	23.0	17.5	9.9
	0.01	100.3	60.5	38.4	26.7	17.9
	0.1	128.2	81.7	49.9	38.0	29.1
	1	157.5	105.1	80.2	50.0	41.7
0.4	0.001	72.8	41.5	22.2	17.2	9.7
	0.01	96.6	57.9	39.0	26.4	17.6
	0.1	123.7	78.3	49.0	37.3	28.6
	1	151.5	100.6	77.9	49.8	41.5
0.5	0.001	71.4	40.9	21.7	17.9	10.2
	0.01	93.0	57.0	37.0	26.5	17.1
	0.1	120.6	76.6	49.1	37.4	28.8
	1	148.9	98.6	77.3	49.8	41.0
0.6	0.001	69.4	39.9	22.5	17.6	10.0
	0.01	91.7	55.5	36.9	26.8	17.3
	0.1	120.2	75.5	48.1	37.6	28.6
	1	149.0	98.0	77.3	50.0	40.9

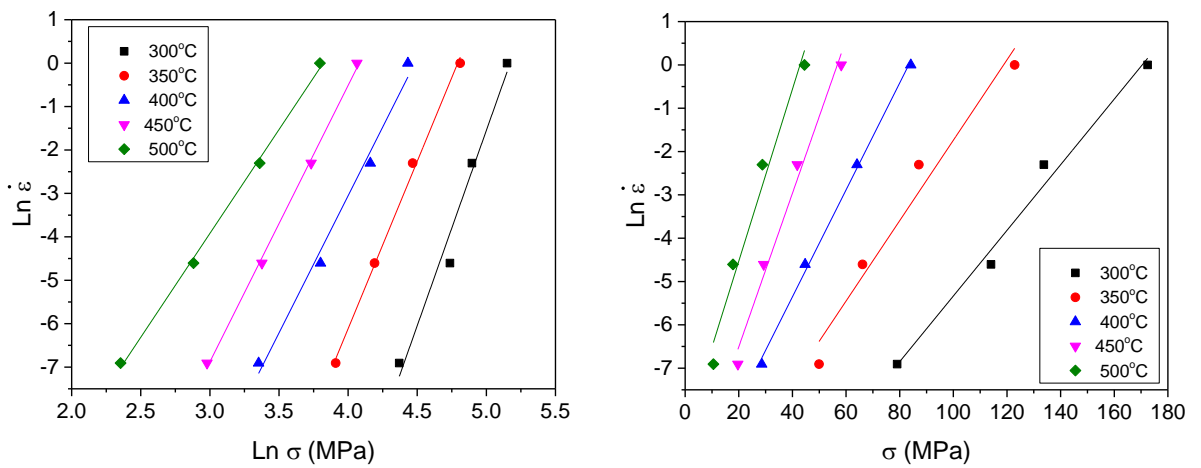
A.2. Flow stress (MPa) data of 0.2Ti alloy at different temperature, strain rate and strain

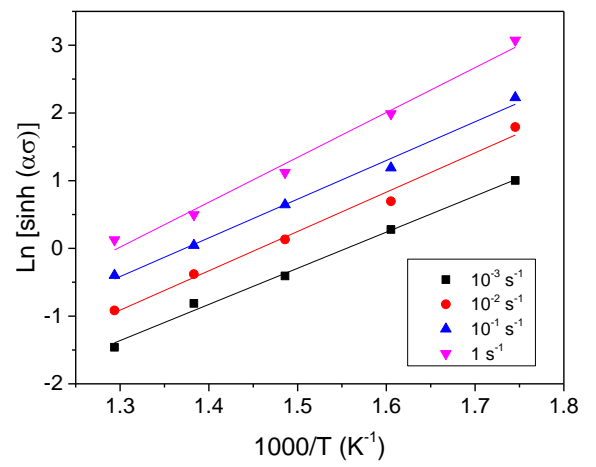
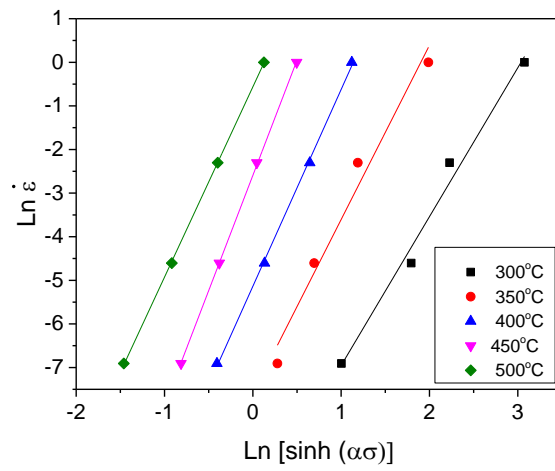
Strain	Strain Rate $\dot{\epsilon}$	Temperature (°C)				
		300	350	400	450	500
0.1	0.001	87.0	58.1	31.4	19.7	10.5
	0.01	125.6	74.5	48.5	31.0	16.1
	0.1	140.3	94.2	68.7	41.9	28.6
	1	187.5	134.3	87.5	57.7	43.8
0.2	0.001	82.5	53.0	30.8	20.0	10.4
	0.01	119.1	69.6	45.7	30.1	17.5
	0.1	137.6	89.2	65.7	41.9	28.8
	1	181.4	130.2	85.8	58.2	44.8
0.3	0.001	79.1	49.9	28.6	19.7	10.5
	0.01	114.1	66.1	44.7	29.3	17.8
	0.1	133.7	87.1	64.1	41.8	28.8
	1	172.4	122.9	84.2	58.2	44.5
0.4	0.001	75.7	46.9	27.8	19.5	10.9
	0.01	110.0	63.2	42.7	29.7	18.0
	0.1	131.2	84.1	62.9	41.1	28.9
	1	165.4	116.7	82.7	57.7	45.0
0.5	0.001	74.7	45.6	27.2	19.7	10.9
	0.01	106.4	62.1	42.6	29.4	17.4
	0.1	129.4	81.8	61.6	41.7	28.4
	1	161.8	113.4	81.4	58.1	44.5
0.6	0.001	74.6	43.8	26.8	20.1	11.2
	0.01	104.4	60.1	41.5	29.6	17.5
	0.1	128.8	81.4	61.4	41.2	28.8
	1	159.0	111.0	81.7	57.9	44.7

A.3. Constitutive calculation of matrix alloy



A.4. Constitutive calculation of 0.2Ti alloy

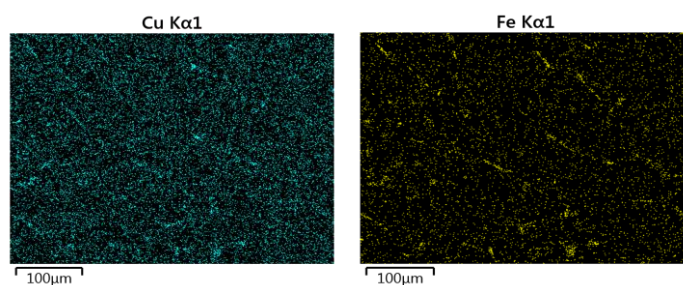
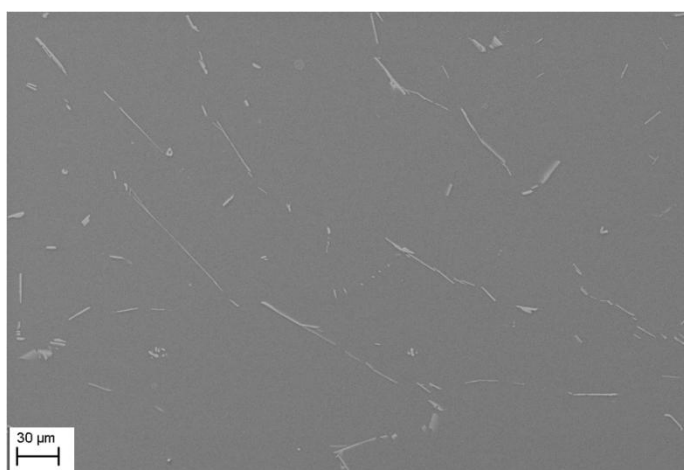




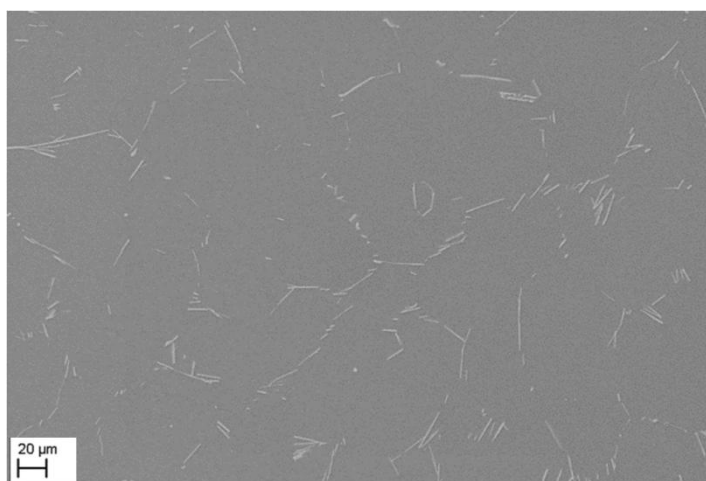
APPENDIX B

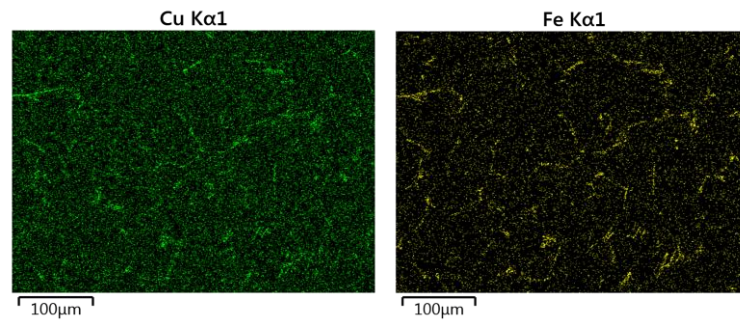
PHASE DISTRIBUTION OF HOMOGENISED MATERIALS

B.1. As-homogenised phase distribution of matrix

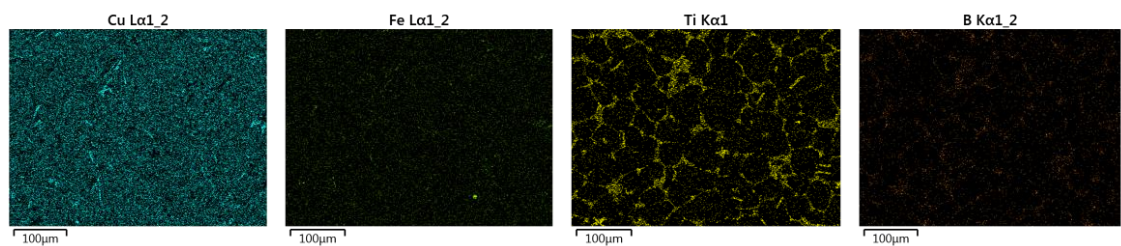
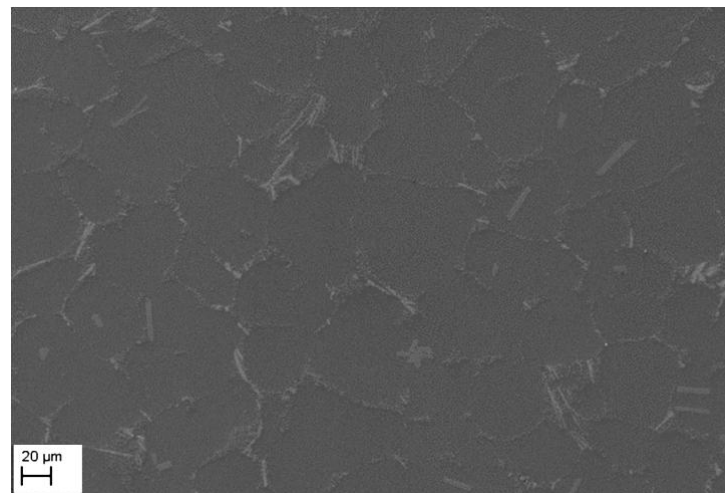


B.2. As-homogenised phase distribution of 0.2Ti alloy



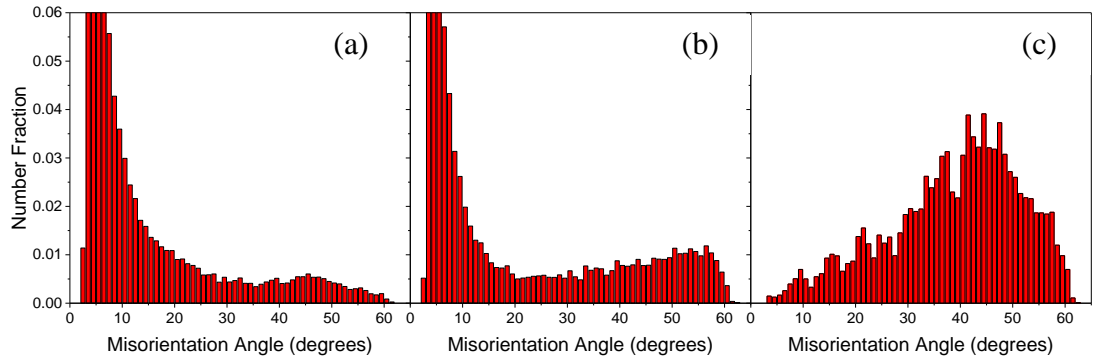


B.3. As-homogenised phase distribution of 0.2Ti-4.5TiB₂ composite

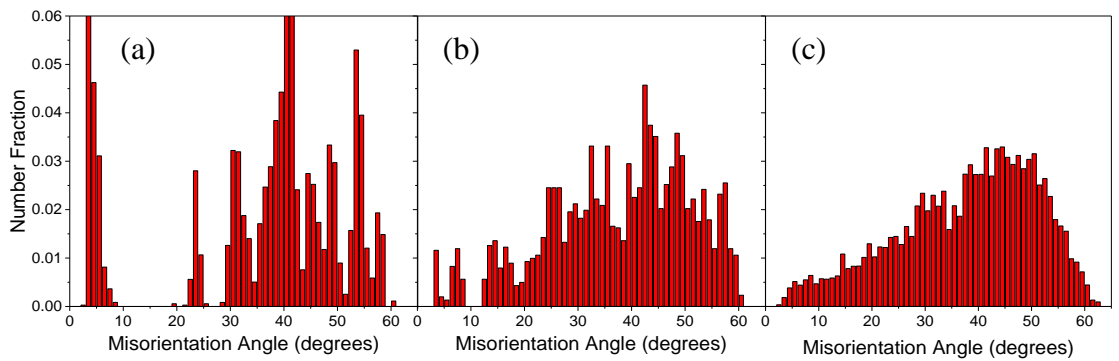


APPENDIX C

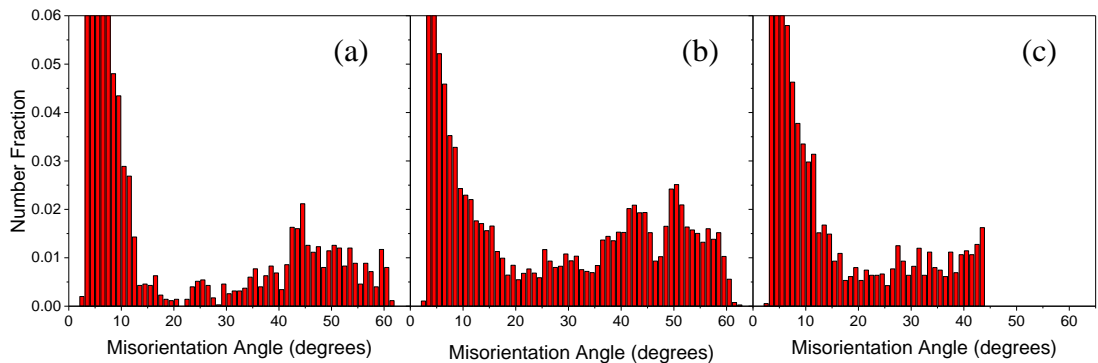
MISORIENTATION PROFILE COMPARISON OF COMPRESSED SPECIMEN



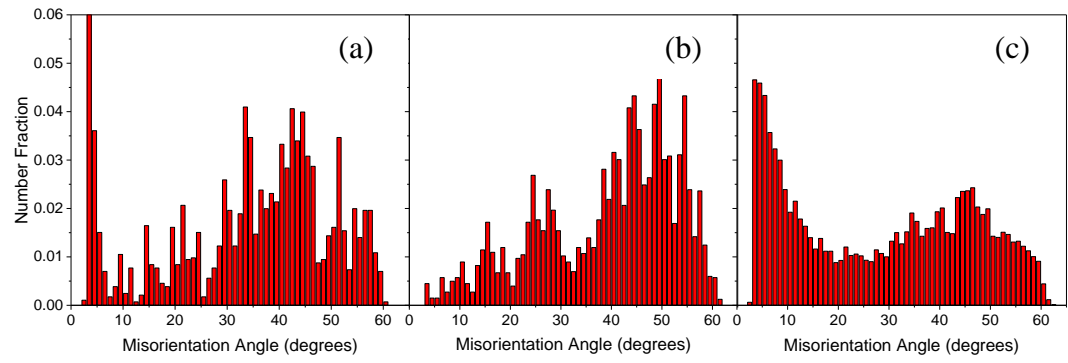
Misorientation profile of as-compressed specimen deformed at 300°C, 10^{-1} s^{-1} of (a) matrix alloy, (b) 0.2Ti alloy and (c) 0.2Ti-4.5TiB₂ composite



Misorientation profile of as-annealed specimen deformed at 300°C, 10^{-1} s^{-1} of (a) matrix alloy, (b) 0.2Ti alloy and (c) 0.2Ti-4.5TiB₂ composite



Misorientation profile of as-compressed specimen deformed at 500°C, 10^{-3} s^{-1} of (a) matrix alloy, (b) 0.2Ti alloy and (c) 0.2Ti-4.5TiB₂ composite

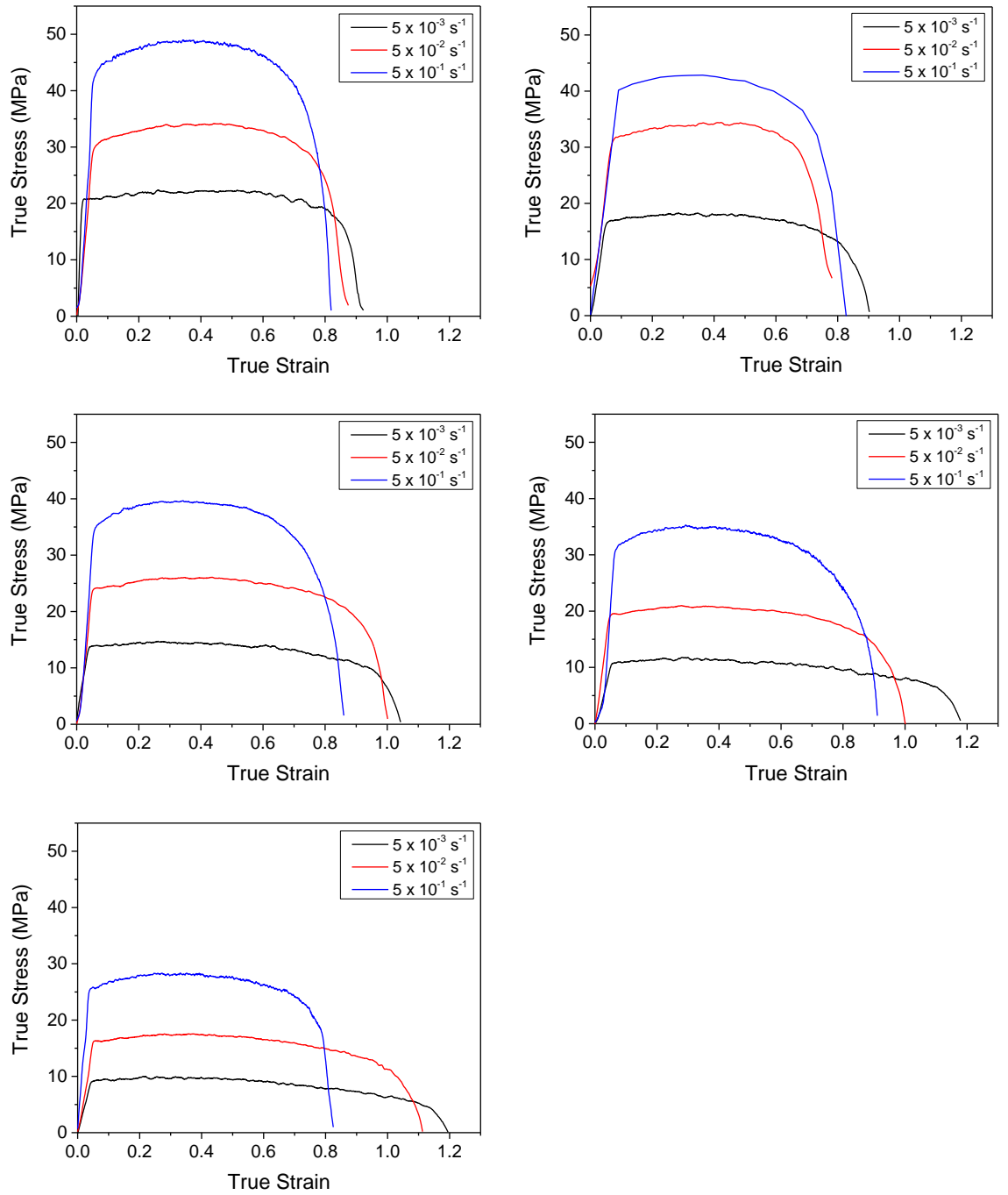


Misorientation profile of as-annealed specimen deformed at 500°C, 10^{-3} s^{-1} of (a) matrix alloy, (b) 0.2Ti alloy and (c) 0.2Ti-4.5TiB₂ composite

APPENDIX D

SUPERPLASTIC FORMING (SPF) GRAPH

D.1. True stress – true strain curves from SPF test of matrix alloy



D.2. True stress – true strain curves from SPF test of 0.2Ti alloy